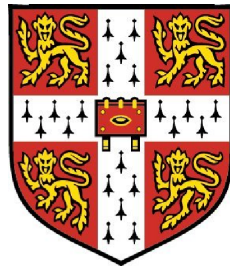


Skidding and Fault Detection in the Bearings of Wind-Turbine Gearboxes



A dissertation submitted to the University of Cambridge
for the degree of Doctor of Philosophy

by

Sharad Jain
Churchill College

December 2012

To the memory of Amma and Baba

Preface

This thesis is submitted for the degree of Doctor of Philosophy, at the University of Cambridge. The work presented in this thesis is carried out at the Department of Engineering, University of Cambridge between October 2009 and October 2012 under the supervision of Dr. Hugh Hunt.

This dissertation is the result of my own work and includes nothing which is the outcome of work done in collaboration except where specifically indicated in the text. This document, in whole or in parts, has not been submitted for any other degree, diploma or qualification.

This thesis contains approximately 48000 words, 69 figures and 6 tables, in accordance with the specifications laid down by the Board of Graduate Studies.

Sharad Jain
Cambridge, UK
December 2012

Acknowledgements

I express my deep sense of gratitude to my supervisor Dr. Hugh Hunt for his invaluable guidance, constant encouragement and insightful suggestions through out the course of this research. My sincere thanks go to Prof. John Williams for his interest in this project and helpful discussions.

Experimental validation of work on planet-bearing-fault detection is done in collaboration with Mr. Peter Whiteley, who designed the planetary test-rig. I would like to thank Peter for this collaboration. It has been a pleasure to work with him. I am grateful to Mr. Gareth Ryder and Mr. Mark Rainer for their help in the construction of the test rig. I am also thankful to Dr. David Cole and Dr. Derek Smith for some useful discussions.

The work is funded by Romax Technology Ltd., for which I am very much indebted. I would like to thank Dr. Peter Poon, CEO of Romax Technology Ltd., for his continuous support and helpful suggestions. I am grateful to Dr. Ashley Crowther, Dr. Jamie Pears, Dr. John Coultate, Mr. Won Shin, Dr. Evgenia Golysheva, Dr. Xiaoqin Ma and Mr. Daniel Edwards of Romax Technology Ltd. for maintaining a keen interest in this work and for some useful discussions.

I would also like to thank Dr. Chris Halse, Mr. Nawazish Zaidi and Mr. Maik Hoppert for some very helpful technical discussions.

Finally, I would like to express my most sincere gratitude to my parents for their never-ending support and inspiration.

Abstract

Wind-turbine gearboxes continue to exhibit a high rate of premature failure despite use of the best in current design practices. Since gearbox is one of the most expensive components of a wind turbine, higher-than-expected failure rates increase cost of energy. Most of the problems in wind-turbine gearboxes appear to emanate from bearings. High-speed bearings and planet bearings exhibit a high failure rate and are identified as two of the most critical components. This dissertation addresses two key issues associated with these bearings: skidding in high-speed bearings and fault detection in planet bearings.

First part of this dissertation focuses on skidding in high-speed bearings. High-speed bearings operate under low loads and high speeds and therefore, are prone to skidding. Skidding can lead to premature failure, long before classical fatigue failure. Yet the mechanism of skidding in ball bearings is poorly understood, especially under combined axial and radial loads and time-varying operating conditions. We develop a dynamic model to analyse the skidding behaviour of angular-contact ball-bearings under axial and radial loads and time-varying speeds. The model includes gyroscopic effect. The traction forces between rolling elements and raceways are calculated using elasto-hydrodynamic lubrication theory. The analysis suggests that the skidding mechanism changes with operating condition, and any skidding criterion developed for thrust bearings cannot be applied to bearings operating under combined loading conditions or time-varying speeds. We derive simple analytical equations to predict the occurrence of skidding under axial as well as combined loading conditions. These equations are computationally cheap and provide an insight into the influence of different geometrical and operational parameters on the skidding behaviour.

Second part of this dissertation focuses on understanding vibration signatures of planet bearings containing localized faults. Various models are available in the literature to simulate vibration signatures of bearings with localized faults, but all of these models are limited to fixed-axis bearings. Vibration signature of a planet bearing is different from a fixed-axis bearing because of the complicated and time-varying vibration transmission path caused by the epicyclic drivetrain. We develop an analytical model of a planetary drivetrain to simulate this complicated transmission path. The model includes a flexible ring-gear and a planet bearing with localized faults. The findings show that the vibration signatures contain multiple modulation sidebands around fault frequency and its harmonics. We identify the sources of these sidebands and provide a mathematical explanation of their formation. The vibration signatures are also validated against experimental measurements. An assumption commonly made in the literature on bearing-fault detection

is that the impulse due to a bearing fault is proportional to the load acting on a rolling element at the time of impact. In this dissertation, we show theoretically and experimentally that these impulses depend on the rolling-element speed not load. There is some load dependence but it is secondary compared to the speed dependence.

The findings from this dissertation will: improve the reliability of high-speed bearings by estimating the amount of skidding at the design stage; improve the condition-monitoring and fault-detection algorithms for planet bearings.

Contents

1	Introduction	1
1.1	Motivation and Research Objectives	1
1.2	Thesis Outline	3
2	Literature Review	5
2.1	Failures in Wind Turbines	5
2.2	Skidding in Bearings	9
2.2.1	Simulating the Skidding Behaviour	9
2.2.1.1	Models for Ball Bearings	10
2.2.1.2	Models for Roller Bearings	13
2.2.2	Criteria to Predict Onset of Skidding	14
2.3	Elastohydrodynamic Lubrication Theory	16
2.4	Vibration Behaviour of Healthy Planetary-Drives	22
2.4.1	Sources of Vibration	22
2.4.2	Modelling Vibration in Healthy Planetary-Drives	24
2.5	Detecting Faults in Bearings Using Vibration Measurements	26
2.5.1	Faults in Fixed-Axis Bearings	26
2.5.2	Faults in Planet Bearings	28
2.6	Conclusions	29
3	Skidding in High-Speed Bearings	31
3.1	Introduction	31
3.2	Numerical Model Description	33
3.2.1	Quasi-Static Analysis of Internal Load Distribution	33
3.2.2	Dynamic Analysis to Analyze Rolling-Element Motion	37
3.2.3	EHD Lubrication Model to Determine Traction Forces	40
3.3	Skidding Under Constant Axial Loads and Constant Speeds	44

3.3.1	Mechanism of Skidding Under Constant Axial Loads and Constant Speeds	46
3.3.2	Derivation of Skidding Criterion for Constant Axial Loads and Constant Speeds	49
3.4	Skidding Under Combined Axial and Radial Loads	54
3.4.1	Mechanism of Skidding Under Combined Loads	56
3.4.2	A Simple Analytical Method to Determine the Extent of the Skidding Region Inside the Load Zone	59
3.4.2.1	Extent of the Sliding-Contact Region at Entry	60
3.4.2.2	Extent of the Spin-Contact Region	66
3.4.2.3	Influence of the Applied Load on the Extent of the Skidding Region	68
3.5	Skidding Under Constant Axial Loads and Time-Varying Speeds	73
3.5.1	Skidding Mechanism Under Time-Varying Speeds	73
3.5.2	Derivation of Skidding Criterion for Constant Axial Loads and Time-Varying Speeds	76
3.6	Conclusions	77
4	Fault Detection in Planet Bearings	79
4.1	Introduction	79
4.2	Analytical Model Description	81
4.2.1	Equation of Motion for a Flexible Ring Gear	82
4.2.2	Equation of Motion for Planet Gears	86
4.2.3	Equation of Motion for the Inner Race of Defective Bearing	87
4.2.4	Equations of Motion for Carrier and Sun Gear	87
4.2.5	Equation of Motion for the Combined System	88
4.3	Derivation of Frequency-Response Function	89
4.4	Vibration Signatures of Planet-Bearing Faults	93
4.4.1	Fault Located on an Inner Race	98
4.4.2	Fault Located on an Outer Race	100
4.4.3	Fault Located on a Rolling Element	101
4.4.4	Sources of Modulation Sidebands	101
4.5	Influence of Ring-Gear Flexibility on the Sideband Behaviour	104
4.6	Experimental Validation of Fault Signatures	109
4.7	Impulse Generated by a Localized Bearing-Fault	114
4.7.1	Theoretical Impulse Calculation	114

4.7.2	Experimental Determination of Impacts Generated by a Localized Fault	118
4.7.3	Reason Behind Secondary Load-Dependence	119
4.7.3.1	Nonlinear Contact-Stiffness	120
4.7.3.2	Interaction Between Cage and Rolling-Elements	125
4.7.4	Effect of Impulse Calculation on the Vibration Signatures of Planet-Bearing Faults	129
4.8	Conclusions	132
5	Conclusions and Future Work	135
5.1	Conclusions	135
5.1.1	Skidding in high-speed bearings	135
5.1.2	Detection of localized faults in planet bearings	137
5.2	Future work	138
5.2.1	Future work on bearing skidding	138
5.2.2	Future work on planet-bearing fault-detection	140
A	Comparison of Minimum Loads Required to Avoid Drag-Sliding and Gyroscopic-Spinning	143
B	Equations of Motion of a Continuous Elastic Ring	145
C	Matrices of the Planetary Model	149
D	Effect of Coriolis and Centripetal Terms on the Natural Frequencies	151
E	Critical Speed of a Rolling Element Passing Through a Fault	155
	References	159

List of Figures

- 1.1 Layout of a typical wind turbine gearbox 2
- 2.1 Trend of geared and gearless turbine installations during 1995-2005. Data taken from Hansen and Hansen^[51] 6
- 2.2 (a) Distribution of failures caused by various wind-turbine components, (b) Distribution of wind-turbine downtime due to various failures. Data taken from McMillan and Ault^[92] 7
- 2.3 Typical smearing wear on bearing raceways. Source: NSK new bearing doctor catalogue^[2]. 8
- 2.4 Acceptable operating region, for a bearing, bounded by the fatigue limit and minimum load required to prevent skidding. 9
- 2.5 Forces acting on a ball according to raceway control hypothesis. M_g is the gyroscopic torque, μ is the friction coefficient, F_{inn} and F_{out} are the inner and outer contact forces. 11
- 2.6 Pressure distribution and film-thickness variation in an EHD contact . . . 18
- 2.7 Typical traction curve in EHD contact showing three regions: linear (for shear stress values below Eyring stress, τ_0), nonlinear and thermal. 19
- 2.8 Variation of traction coefficient with film parameter, showing different regimes of lubrication. 21
- 2.9 Contact pressure shared between asperity contacts and EHD film in a mixed-EHD lubrication regime. 22
- 2.10 Vibration signature of a bearing with fixed outer-race in the presence of a localized outer-race fault. 27
- 3.1 (a) Forces acting on a rolling element; (b) Geometrical compatibility between ball and raceways 33
- 3.2 Geometry and contact dimensions of two elastic solids in contact 34
- 3.3 Quasi-static model to determine the internal load distribution under combined axial and radial loads 36

3.4	(a) Two reference frames used in the dynamic model formulation; (b) components of the angular velocity of a rolling element in the rotating reference frame.	38
3.5	Cage model used in the current analysis	39
3.6	Coordinate system ($x''y''z''$) used to formulate EHD lubrication model showing the contact-patch ellipses for inner-race and outer-race contacts.	40
3.7	Elliptical contact patch and lubricant film inside the contact zone	42
3.8	Comparison of simulation results with the experimental data published by Pasdari and Gentle ^[99] under constant axial load and constant speed	45
3.9	Simulation results for a bearing operating under constant axial loads and a constant speed of $\omega_i = 1500$ rpm	47
3.10	Axes governing the motion of a rolling element	48
3.11	Variation in the ball orientation angles with the applied load in a bearing operating under constant axial loads and constant speed of 1500 rpm. Orientation of the rotation axis of a rolling element at low and at high loads (P_1 and P_2) are also shown.	49
3.12	Variation in traction coefficient with slip speed	51
3.13	(a) Contour plot showing variation in sliding speed (m/s) at inner-race contact (Δu_i^A) with applied axial load and inner-race speed, along with the Kliman's criterion (equation 3.40), Hirano's criterion (equation 3.39) and new proposed drag-sliding criterion (equation 3.38a) (b) Contour plot showing variation in spin speed (rad/s) at inner-race contact (ω_s^A) with applied axial load and inner-race speed along with proposed gyroscopic-slip criterion (equation 3.38b) (c) Skidding map for axially loaded bearing showing different regimes of skidding	53
3.14	Slip speed variation with axial load for two lubricants (L_1 and L_2) with different viscosity-pressure coefficients; remaining properties of both lubricants are same (table 3.3). Skidding criteria predicted by Hirano and Kliman along with the new proposed method are shown.	54
3.15	(a) Graphical representation of rolling-element motion under combined loading condition and formation of five regions; (b) Variation in the angular-momentum vector of a rolling element with its angular position	55
3.16	(a) Variation in the maximum slip speed at the inner-race contact with the orbital position of a rolling element; (b),(c),(d) Slip speed distributions on the inner contact patches at three orbital positions P_1 , P_2 and P_3 ; $F_a = 4.3$ kN, $F_r = 4$ kN, $\omega_i = 1500$ rpm	57

3.17	Variation in the rotational speed of a rolling element with orbital position of a rolling element under combined loading condition; $F_a = 4.3$ kN, $F_r = 4$ kN, $\omega_i = 1500$ rpm	59
3.18	Angular momentum of a rolling element at the boundaries of different skidding regions inside load zone	60
3.19	State of moment acting on a rolling element in different skidding regions. Directions of angular-momentum vectors are consistent with figure 3.18.	61
3.20	Normalized lengths of the skidding regions (sliding-contact and spin-contact) inside load zone calculated using both full numerical simulations (circles and crosses) and simple analytical solution (continuous lines). Slip speed at inner-race contact is also shown for the two cases: P1 - applied load is less than \tilde{F}_e and rolling-contact region is not present inside the load zone, P2 - applied load is greater than \tilde{F}_e and rolling-contact region is present	69
3.21	Variation in the cage speed with applied load under combined axial and radial loads	70
3.22	Skidding under constant axial load and time-varying speed; $F_a = 3.5$ kN, $\omega_0 = 1500$ rpm	74
4.1	Analytical model of a planetary drivetrain with a flexible ring-gear and a defective planet-bearing	81
4.2	Sun-planet and ring-planet meshes	83
4.3	An example of the frequency-response function of a planet-bearing fault with (A,B,C,D,E) five dominant mode-shapes for $\theta = \frac{\pi}{2}$, $\theta^* = \frac{\pi}{3}$ and $\gamma = -\frac{\pi}{4}$. Ring gear deforms in all the five dominant modes.	91
4.4	(a) Free-body diagram of a planet bearing showing formation of load zone; (b) A train of impulses due to bearing fault; (c) Impulse-train function showing non-zero impulse value inside a load zone and zero impulse value outside a load zone.	94
4.5	(a) Impulse train with impulse proportional to rolling-element load, (b) Impulse train with impulse proportional to rolling-element speed	95
4.6	Analytical vibration signature of a planet-bearing inner-race fault located at an angle $\gamma_0 = -\pi/4$, (a) frequency response, (b) clusters of peaks separated by ω_d , (c) sidebands within a cluster separated by carrier frequency ω_c	97

4.7	Analytical vibration signature of a planet-bearing outer-race fault, (a) frequency response, (b) clusters of peaks separated by ω_d , (c) sidebands within a cluster separated by the planet frequency relative to carrier ω_{pc} and the carrier frequency ω_c	99
4.8	Analytical vibration signature of a planet-bearing rolling-element fault, (a) frequency response, (b) clusters of peaks separated by ω_d , (c) sidebands within a cluster separated by the frequency of the planet-bearing cage relative to carrier Ω and the carrier frequency ω_c	102
4.9	(a) An elastic ring excited by an impulse train moving with a constant speed ω_c . (b) Impulse train with frequency ω_d exciting the elastic ring. . .	104
4.10	Frequency response of an elastic ring excited by a moving impulse-train. Clusters of sidebands along with their envelope functions show that the amplitude of n^{th} sideband is governed by the n^{th} ring mode	106
4.11	Variation in the sideband behaviour of a planet-bearing inner-race fault with frequency. n^{th} sideband dominates near the n^{th} ring-gear mode. Examples are shown for A ($n = 1$), B ($n = 2$) and C ($n = 3$) with respective mode shapes.	107
4.12	Influence of ring-gear thickness on the sideband pattern. Higher-order sidebands disappear as we increase the ring-gear thickness: (a) three dominant sidebands for a thickness of 75 mm; (b) two dominant sidebands for a thickness of 2.5×75 mm; and (c) only one dominant sideband for a thickness of 5×75 mm.	108
4.13	(a) Planetary test rig; (b) Epicyclic drivetrain used in the test rig; (c) Planet bearing with a localized outer-race fault (a through rectangular hole)	110
4.14	(a) Measured vibration response of a healthy planet ball-bearing. (b) Measured vibration signature of a planet bearing inner-race defect, for a carrier speed of 72 rpm, containing clusters of peaks separated by ω_d . (c) Sidebands within a cluster.	111
4.15	Measured vibration signature of a planet-bearing (cylindrical roller) inner-race fault for a carrier speed of 72 rpm (a) Clusters of peaks separated by ω_d (b) Sidebands within a cluster	112
4.16	Measured vibration signature of a planet bearing outer-race defect for a carrier speed of 96 rpm (a) Clusters of peaks separated by ω_d (b) Sidebands within a cluster	112

4.17	Different stages of a rolling element passing through a narrow localized fault with a constant horizontal speed: (a) before entering the fault; (b) after entering the fault; and (c) at the time of impact.	114
4.18	Effect of static axle-load on the peak impact-sound pressure-level for a rail joint (reproduced from Ver et. al. ^[125]). At low speeds, sound pressure is independent of axle load. At high speeds, sound pressure depends on axle load.	116
4.19	Experimental setup used to measure the impulse generated by a localized bearing-fault. Lever mechanism is used to vary the applied load and the shaft in the small rig is driven by a hand drill.	117
4.20	Typical acceleration signal measured by an accelerometer located near the outer race of the faulty bearing. Each peak represents an impulse response due to a bearing fault.	118
4.21	Measured variation in the impulse generated by a bearing fault with the applied load at two rolling-element speeds. Theoretical impulse values predicted from the speed-dependence (dotted blue) and load-dependence (dotted black) theories are also shown.	119
4.22	A rolling element of radius r with nonlinear contact springs passing through a narrow fault of width d and depth h such that $d < 2\sqrt{2rh}$, i.e., the rolling element never touches the bottom of the fault.	120
4.23	An impact-force pulse due to a bearing fault	122
4.24	Variation in the vertical velocity of a rolling element with its position angle as it passes through the fault	123
4.25	Qualitative variation in the impulse due a bearing fault with the applied load. The regime in which experiments of section 4.7.2 were conducted is also shown.	124
4.26	A spring representing a rolling element passing through a fault. (a) Initial compression in the spring is more than the maximum vertical displacement of the rolling element. (b) Initial compression in the spring is less than the maximum vertical displacement of the rolling element.	125
4.27	Acceleration and forces acting on a rolling element as it enters the fault (before impact).	126
4.28	A rolling element passing through a bearing fault and connected to a cage pillar with a linear spring	128

4.29	Measured variation in the impulse generated by a bearing fault with the applied load (black) along with the impulse variation predicted by the cage-interaction model for two values of cage stiffness (blue).	129
4.30	Load-dependent impulse-train function	130
4.31	Analytical vibration signature of a planet-bearing outer-race defect: (a) calculated using speed-dependent impulse-train, (b) calculated using load-dependent impulse-train. The frequencies of sidebands are same in both cases (a) and (b), but the amplitudes are different.	131
5.1	A real bearing fault with non-rectangular profile. Source: Kuhnell ^[80] . . .	140
B.1	(a) Free-body diagram of a ring showing all the forces acting on a section; (b) Differential element at a distance x from the neutral axis of the ring. .	146
B.2	Vibration modes of an elastic ring. Top row represents inextensional modes. Bottom row represents extensional modes.	147
D.1	Variation in the natural frequencies of a planetary drive with carrier speed caused by the Coriolis and the centripetal terms.	153
E.1	(a) A rolling element passing through a narrow localized fault; (b) Forces acting on a rolling element after it enters the fault.	155

List of Tables

- 3.1 Bearing properties used by Pasdari and Gentle^[99] in their skidding tests . . . 44
- 3.2 Geometrical properties of a typical wind-turbine high-speed bearing 46
- 3.3 Lubricant parameters 46

- 4.1 Model parameters for a typical 2MW wind-turbine planetary drivetrain
 (number of planets, $z = 3$). Symbols r , R , m and I take the subscript s
 for sun, p_i for i^{th} planet, r for ring and c for carrier. 90
- 4.2 Parameters of the planetary gearbox used in the test rig 110

- B.1 Comparison of natural frequencies of the ring of table 4.1 calculated using
 complete theory (inextensional and extensional, equation B.8) and inex-
 tentional only theory (equation B.10). 148

Chapter 1

Introduction

Premature failures of wind-turbine gearboxes increase cost of energy. Most gearbox failures initiate in bearings. High-speed bearings and planetary bearings exhibit a high rate of premature failure. This chapter introduces the motivation behind studying these bearing failures, introduces the objectives of this research, and outlines the chapters comprising this thesis.

1.1 Motivation and Research Objectives

Most modern wind turbines use a gearbox (figure 1.1) to convert low rotational speed of the rotor (10-15 rpm) to high rotational speed of the generator (1200-1800 rpm). As the power generation capacity of wind turbines is going up, failure rate of these gearboxes is increasing. Wind turbines are designed to last 20 years, but average life of a wind-turbine gearbox is only 5 years^[128]. Since gearbox is one of the most expensive components of a wind turbine, higher-than-expected failure rate increases cost of energy. Most of the problems in wind turbine gearboxes appear to emanate from bearings. High-speed bearings and planetary bearings (figure 1.1) exhibit a high rate of premature failure and are identified as two of the most critical components^[94]. This calls for development of methods to understand failure modes and to detect faults in these components in order to increase the average life of a wind-turbine gearbox.

This research has two main objectives:

1. to investigate skidding in high-speed bearings;
2. to understand the vibration signatures of planet-bearing faults.

High-speed bearings are susceptible to skidding failure as they operate under high speeds and low loads. Many methods have been developed over the years to predict

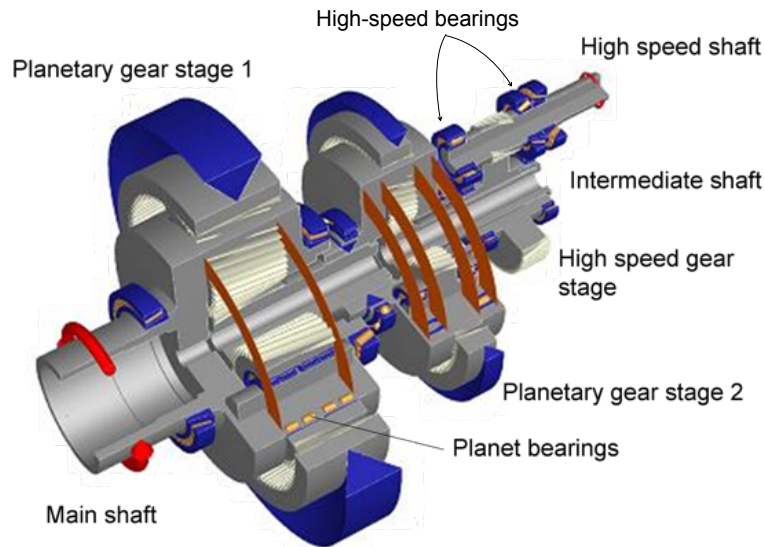


Figure 1.1: Layout of a typical wind turbine gearbox (modelled in RomaxWIND^[3])

skidding in ball bearings, but most of these methods are quasi-static, computationally expensive, and limited to thrust bearings. Since wind-turbine bearings operate under combined axial and radial loads, a computationally-cheap method is required to predict skidding under these conditions at the design stage. This research addresses the following questions on bearing skidding:

- is skidding mechanism under combined-loading condition different from the skidding mechanism under axial loading condition;
- is it possible to predict the occurrence of skidding under axial as well as combined loading conditions using simple analytical methods;
- how do time-varying operating conditions influence skidding behaviour;
- is a skidding prevention criterion, developed for axially loaded bearings, applicable for combined loading conditions or time-varying speeds?

Planet bearings, located inside the planetary drives of wind-turbine gearboxes, exhibit a high failure rate despite the use of best in current design practices. Vibration based methods are used to detect faults in wind-turbine gearboxes. Various methods are available to detect localized faults (spalls or pits) in fixed-axis bearings, but few methods are available to detect faults in planet bearings. Detecting faults in planet bearings is difficult because of their complicated vibration-transmission path. In this research, we find out if it is possible to detect planet-bearing faults using vibration measurements. The work addresses the following questions:

- how does the presence of a localized planet-bearing fault change the vibration response of a planetary drive;
- how do different planet-bearing faults (inner race, outer race and rolling element) manifest themselves in a vibration spectrum;
- how does ring-gear flexibility influence the vibration signatures of planet-bearing faults;
- how does the impulse due to a bearing fault change with operating speed and load?

Answers to all these questions will improve the current understanding of skidding and fault detection in wind-turbine bearings, and will help to improve reliability of wind-turbine gearboxes.

1.2 Thesis Outline

This thesis comprises of three main chapters: review of the previous work relevant to this research, prediction of skidding in high-speed bearings, and detection of localized faults in planet bearings.

Chapter 2 reviews the previous work on bearing skidding and planetary-fault diagnostics. It contains: failures in wind-turbine gearboxes, various bearing skidding models, elasto-hydrodynamic lubrication theory, and various models to simulate planetary-drive dynamics.

Chapter 3 investigates the skidding behaviour of angular-contact ball-bearings. A numerical model, which includes gyroscopic effects, is developed to predict skidding under various operating conditions. Rolling-element motion and skidding mechanism is studied in detail for bearings operating under axial loads, combined axial and radial loads, and time-varying speeds. Simple analytical equations are also derived to predict the occurrence of skidding for the operating conditions mentioned above.

Chapter 4 describes a dynamic model, which includes a flexible ring-gear and a planet bearing containing with a localized defect, used to determine vibration signatures of planet bearing faults. Sources of modulation sidebands present in the fault signatures are identified and an explanation of their formation is provided. Theoretically predicted vibration signatures of planet-bearing faults are validated against the experiments conducted in collaboration with Whiteley^[127]. Speed and load dependence of the impulse due to a bearing fault is also investigated theoretically as well as experimentally.

Chapter 5 summarises the key conclusions of this research and provides some suggestions for the future work which directly follows from this research.

Chapter 2

Literature Review

This chapter reviews the previous work done in the areas relevant to this research. The chapter provides an overview of gearbox failures in wind turbines; reviews various methods available to predict skidding in bearings; provides an overview of elastohydrodynamic lubrication theory; briefly explains vibration behaviour of healthy planetary drives; and reviews methods to simulate and detect localized faults in fixed-axis and planet bearings.

2.1 Failures in Wind Turbines

Wind energy is the fastest growing renewable energy sector with an average annual growth rate of around 30 % during the last 10 years. In order to harvest energy most efficiently and reliably, various wind-turbine design concepts have been developed over the years^[83,101]. Modern wind turbines are enormous with power capacity of 2.5-5 MW, rotors of 100-120 m diameter and tower heights upto 100 m^[74,87]. Most of the modern industrial designs of wind turbines utilize a gearbox which connects the rotor shaft to high-speed shaft and increases rotational speed from 10-15 rpm (at rotor) to 1200-1800 rpm – the speed required by most generators to produce electricity. Direct-drive technology has also gained much attention recently. In direct-drive turbines traditional gearboxes and high-speed generators are replaced with bigger low-speed generators. The rotor hub is directly attached to a generator avoiding multiple rotating components like gears and bearings and hence possibly improving the system reliability. The trend began in smaller turbines and is now being incorporated in turbines size upto 3 MW. The downside is their low torque to weight ratio, larger diameter and difficulty in maintaining air gap in such large diameters^[83]. In spite of eliminating gearboxes, direct-drive wind-turbines do not appear to have lower failure rate than geared wind-turbines. The aggregate failure rates

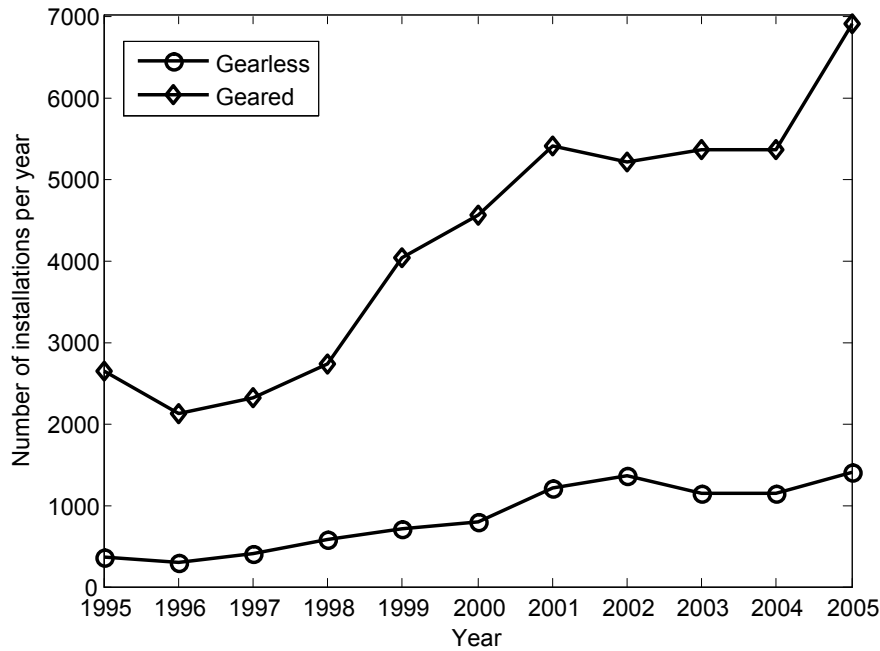


Figure 2.1: Trend of geared and gearless turbine installations during 1995-2005. Data taken from Hansen and Hansen^[51]

of inverter and electronics in direct-drive wind-turbines are greater than the failure rate of gearboxes in geared wind-turbines^[120,124]. For this reason wind-turbine market is still dominated by geared-turbine concepts (figure 2.1).

The wind energy industry has experienced high gearbox failure rates from its inception. Since gearboxes are one of the most expensive components of a wind turbine (about 13% of the total cost^[4,12]), higher-than-expected failure rates are adding to the cost of energy production. There are more failures associated with generators and turbine electronics than gearboxes (figure 2.2a) but still gearbox is considered as a critical component because of higher downtime per failure compared to other components^[47,92,107,115] (figure 2.2b). For a typical turbine, 20% of the downtime is due to gearbox failures and an average gearbox failure takes about 250 hours to repair^[109]. Major reasons behind long downtime per gearbox-failure include requirement of big and cumbersome replacement equipments such as cranes etc. and sometimes unavailability of spare parts also contributes to prolong repair time. Figure 1.1 shows the layout of a typical wind turbine gearbox modelled in RomaxWIND^[3] software. There are two planetary stages followed by a parallel-gear stage transmitting power to the high-speed shaft which is connected to a generator. Most of the problems in wind-turbine gearboxes are generic in nature i.e. not specific to a single manufacturer or turbine design and majority of these failures appear to initiate in bearings, which may later advance to gears due to excessive vibrations and

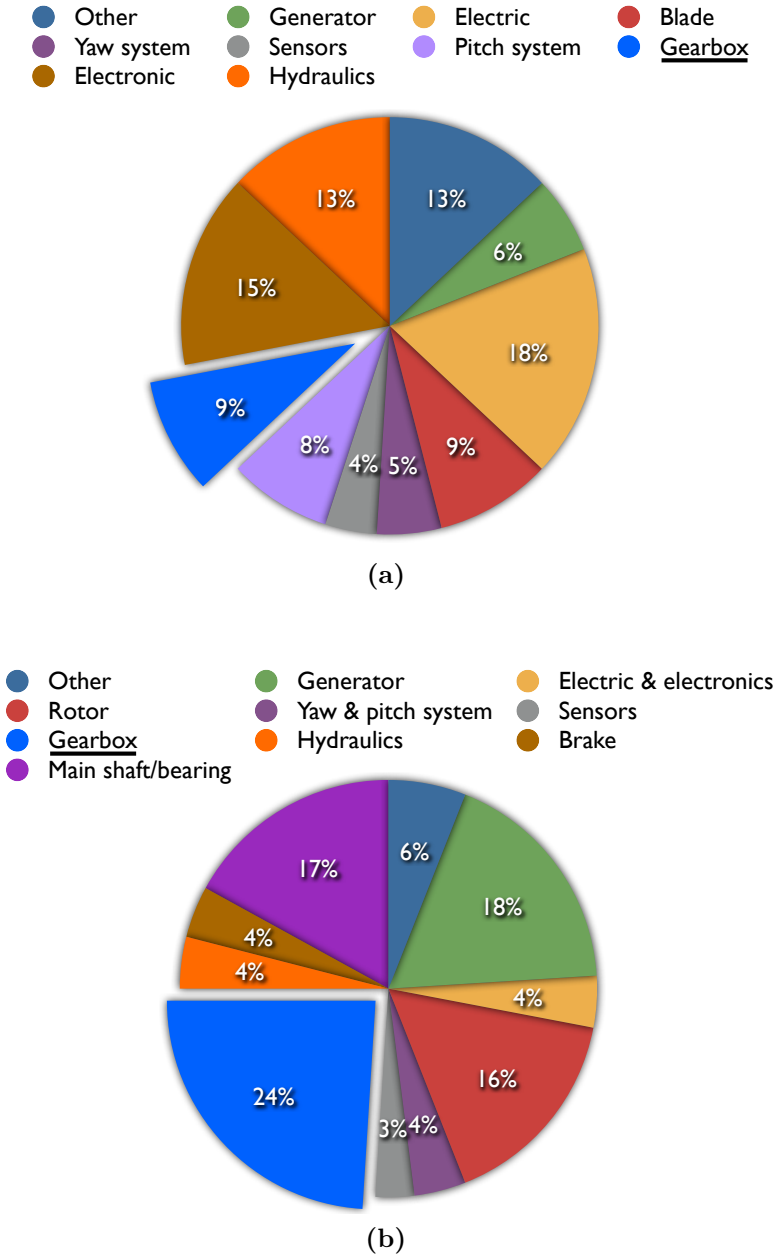


Figure 2.2: (a) Distribution of failures caused by various wind-turbine components, (b) Distribution of wind-turbine downtime due to various failures. Data taken from McMillan and Ault [92]



Figure 2.3: Typical smearing wear on bearing raceways. Source: NSK new bearing doctor catalogue^[2].

misalignments^[94]. High-speed bearings, planet bearings and intermediate-shaft bearings (figure 1.1) exhibit a high rate of premature failure and are considered to be some of the most critical components^[94,109].

The root cause of failures in high-speed bearings is not fully understood so far, but it is not classical fatigue failure as these bearings fail well before their L_{10} life*^[33]. A commonly observed wear mode in these bearings is smearing^[33] (like the one shown in figure 2.3). One of the main causes of smearing wear is sliding or skidding between rolling elements and raceways^[1]. Since high-speed bearings of a wind-turbine gearbox operate under high speeds and low loads, these bearings are prone to skidding. Skidding behaviour of a bearing depends on the traction forces generated in the lubricant film trapped between two contacting surfaces. In section 2.2 we discuss the skidding behavior of bearings in detail followed by a brief overview of elastohydrodynamic lubrication theory in section 2.3.

Planet-bearings failures in wind-turbine gearboxes can be caused by many factors such as low lubricant-film thickness due to low speeds and high loads, and poor internal load-distribution due to planet deformation and misalignment^[96]. Detection of planet-bearing faults using vibration measurement requires a thorough understanding of their vibration behavior. In section 2.4 we discuss the vibration behaviour of healthy planetary-drives. Various methods have been developed over the years to detect localized faults in fixed-axis bearings using vibration measurements. An overview of these methods is presented in section 2.5.

* L_{10} life is the fatigue life attained by 90% of the bearings from a group containing identical bearings operating under identical conditions.

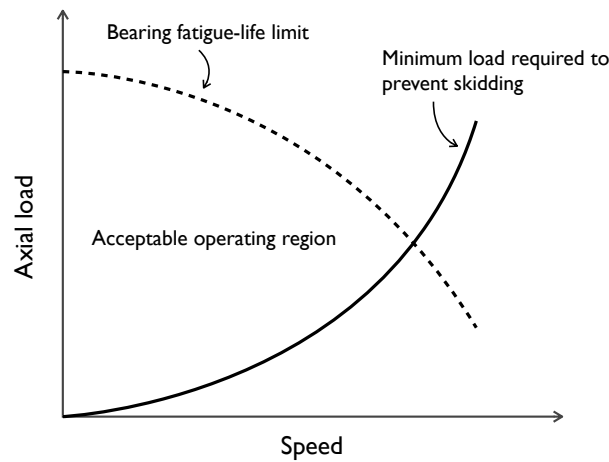


Figure 2.4: Acceptable operating region, for a bearing, bounded by the fatigue limit and minimum load required to prevent skidding.

2.2 Skidding in Bearings

Skidding in bearings is the gross sliding of rolling elements on raceways. Skidding occurs when the traction forces between rolling elements and raceways are not enough to overcome viscous drag and inertial forces. Gross sliding in bearings could lead to high subsurface shear stress and eventually to premature failure long before the classical fatigue failure. A minimum load must be applied to a bearing in order to avoid skidding. The value of this minimum load increases with speed due to the increase in both the drag and the inertial forces with speed. Load corresponding to the fatigue-life limit of a bearing decreases as the operating speed increases. Therefore, the acceptable operating region of a bearing is bounded by the fatigue-life limit and the minimum load required to prevent skidding (figure 2.4). In order to determine the extent of this acceptable operating region, methods to predict skidding under various operating conditions are required. This section outlines various simulation methods available in the literature to analyze rolling-element motion inside a bearing and skidding criteria proposed by various researchers based on analytical calculations and experimental observations.

2.2.1 Simulating the Skidding Behaviour

Much work has been done to understand the skidding behaviour of ball and roller bearings. Researchers have developed various analytical and numerical models of varying complexity to simulate rolling-element motion inside a bearing. These models can be split into two broad categories: quasi-static models and dynamic models. The quasi-static models are

based on force equilibrium and neglect inertial effects while the dynamic models capture inertial effects but require a time integration scheme to achieve a solution because of the nonlinear nature of friction between rolling elements and raceways. The following paragraphs describe different modelling approaches attempted in the past, their underlying assumptions and limitations.

2.2.1.1 Models for Ball Bearings

Jones^[72] provides the first mathematical theory to analyze the motion of rolling elements in ball bearings. He derives the expressions for friction forces resulting from interfacial slip at ball-race contacts. The normal pressure distribution over the elliptical contact area is determined in accordance with Hertz theory of elastic contact^[57] and a dry friction model is employed to evaluate the friction forces. Jones later extends his theory for arbitrarily loaded ball and roller bearings constraint in an elastic supporting structure^[73]. He solves the entire assembly of bearings, shaft and supporting structure as a single elastic system. This work discretizes a shaft into multiple nodes. Each node represents either a bearing connection or an applied-load point. The elastic compliance of these nodes is defined with respect to the supporting structure using influence coefficients in five degrees of freedom to determine the exact internal load distribution in all the bearings in a system.

One of the limitations of Jones' theory^[72,73] is its dependence over raceway control hypothesis to achieve a solution. At high rotational speeds, centrifugal force acting on a rolling element becomes significant and is balanced by the inner and outer race contact forces. This force balance condition leads to different contact angles at the inner and outer races (figure 2.5). According to this hypothesis, a ball is assumed to roll without spin on one raceway and roll with spin on another. The raceway at which no spin occurs is said to be the controlling raceway which controls the motion of the ball about its own axis and the bearing axis. It is also further assumed that the gyroscopic moment acting on a ball is resisted by frictional forces acting at the controlling raceway only and gyroscopic slippage does not occur in a plane normal to the bearing plane as shown in figure 2.5.

The validity of the raceway control hypothesis is questioned by Harris^[55,56]. In a lubricated ball-bearing, a lubricant film is formed in between rolling elements and raceways. In order to generate viscous traction in a lubricant film, relative sliding between contacting surfaces is required. A relative sliding on either inner or outer raceway would require ball to rotate in the plane normal to the bearing plane, this would lead to sliding on both inner and outer raceways. Therefore, gyroscopic motion is resisted at both the inner and outer raceways and not at the controlling raceway alone. Harris^[56] develops an improved model to predict rolling-element slippage in angular-contact ball-bearings

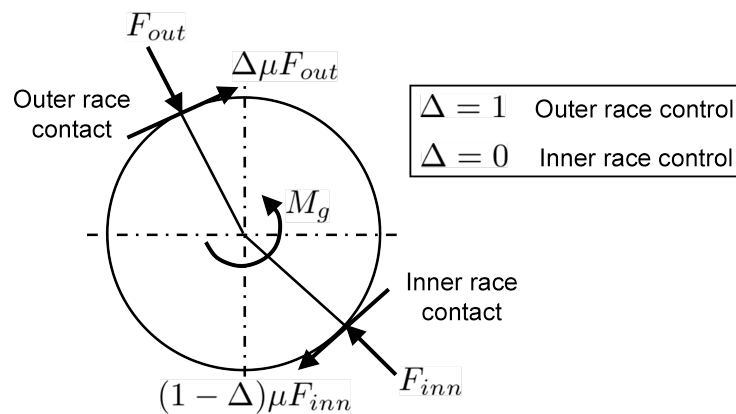


Figure 2.5: Forces acting on a ball according to raceway control hypothesis. M_g is the gyrosopic torque, μ is the friction coefficient, F_{inn} and F_{out} are the inner and outer contact forces.

under constant axial load without using the raceway control assumption. He finds that the results obtained from his analytical model more closely approximate the measured data (reported by Poplawski and Mauriello^[103]) than the raceway control method, which further proves the inadequacy of raceway control hypothesis. Harris also investigates the raceway control hypothesis for dry bearings with Coulomb friction conditions and finds if the ball rotation due to gyrosopic moment is resisted by static friction forces at the contact interfaces, then the raceway control theory is adequate to analyze ball motion and bearing performance^[56].

The quasi-static analysis techniques proposed by Jones^[72,73] and Harris^[55,56] give a good insight into the frictional behaviour of ball bearings and also show the existence of skidding. However, these methods cannot be used to analyze combined radial and axial loads or time-varying operating conditions both of which are important for wind turbine applications. The inadequacy of quasi-static models for these operating conditions is because of two main reasons: absence of any ball-cage interaction and no consideration of dynamic effects.

Under combined radial and axial loads, a load zone is formed inside a bearing. The rolling elements lying inside the load zone are loaded and drive the cage, whereas the rolling elements outside the load zone are unloaded and are driven by the cage. Hence ball-cage interaction is important under these conditions. A detailed understanding of dynamic behaviour of rolling elements and cage is required to calculate these interaction forces. Meeks and Tran^[93] propose a six degree of freedom model to simulate cage transient motion in a bearing. They adopt the quasi-static methods of Jones^[72] and Harris^[55] to determine the internal load distribution in a bearing, and a dynamic formulation is used to obtain ball-cage collision forces. The gyrosopic effects are considered in the quasi-static

model to calculate internal loads but the dynamic model lacks gyroscopic coupling terms in the equations governing the ball motion. Their model might be suitable for predicting cage dynamics and its failure modes, but it is not suitable to predict skidding under combined loading conditions because of the absence of gyroscopic terms in the dynamic model formulation.

Houpert^[61,62] proposes a novel equivalent-stiffness methodology to calculate impact forces between rolling elements and cage pillars which take into account the Hertzian contact stiffness as well as the structural stiffness of a cage pillar. He also demonstrates the influence of hydrodynamic effects on bearing internal load distribution which in turn affects ball-cage forces. He finds that consideration of hydrodynamic effects increases the size of the load zone and reduces the peak load values, especially if the applied load is low.

Gupta^[42] proposes a dynamic model to study the ball motion and the skidding characteristics in thrust ball bearings. He later extends his model for combined axial and radial loads by including the cage dynamics^[43], but his model ignores the variation in slip speed and traction properties along the minor axis of the contact ellipse between rolling elements and raceways. Traction force and moment calculations adopted by Gupta are based on a semi-empirical EHD lubrication model. From the numerical analysis, Gupta^[44] finds that the slip speed between rolling elements and raceways increases with radial to axial load ratio. The ball motion and underlying skidding mechanism under combined axial and radial loads is not studied in detail.

Tu et. al.^[123] study the effect of inner-race acceleration on the skidding behaviour of deep-groove ball-bearings using a dynamic model. As with previous studies, they find that skidding decreases with increasing load. Their model does not include the gyroscopic effects which is a reasonable assumption for deep-groove ball-bearings as the theoretical spin-axis of a rolling element is parallel to the bearing axis. For an angular-contact ball-bearing, spin axis of a rolling element is not aligned with the bearing axis and gyroscopic effects are important.

At high operating speeds, centrifugal force acting on the rolling elements amplifies the difference between inner and outer race contact angles and therefore, increases the risk of scuffing damage due to excessive spinning at the contact interfaces^[82]. Harris^[54] finds that by reducing the ball mass by 50% significant improvements in bearing life could be achieved due to lower centrifugal force generation. This is achieved by making the balls hollow. Another solution is to use an arched or four contact-point ball-bearings because of their high load carrying capacity as the applied load is distributed among four contact points.

Hamrock and Aderson^[49] perform the first analysis of an arched ball-bearing. A quasi-static axial-load analysis method is developed considering centrifugal effects. Ignacio Amasorrain et al.^[64] propose a more generic calculation procedure to obtain internal load distribution for four contact-point ball-bearings operating under combined loading conditions. More recently, Leblanc and Nelias^[81,82] extend Jones theory^[71] of bearing internal kinematics from two to four contact points.

Four contact-point ball-bearings, in general, are assumed to have more fatigue life compared to a conventional bearing with two contact points because of load sharing between two outer-race contacts. However, under certain operating conditions, this benefit is counterbalanced by increase in sliding within contact interfaces^[81]. Thus, careful investigation of dynamic characteristics of these bearings must be done before selection.

2.2.1.2 Models for Roller Bearings

Harris presents an analytical method^[53] for predicting skidding in cylindrical-roller bearings which allows designers to investigate skidding phenomenon at the initial design stage. He uses a semi-empirical EHD lubrication theory to obtain traction forces between rolling elements and raceways. It is shown that skidding occurs when drag forces acting on a rolling element exceed frictional driving forces. In order to establish equilibrium between these forces, cage speed decreases and inner race skids past the roller surface. Slip-speed results obtained from Harris' model^[53] show good agreement with test data, except at low load conditions. This discrepancy between analytical results and test data is attributed to the break down of empirical relationships for EHD contacts, used in the analysis, at low loads. The analysis also shows that skidding can be reduced by increasing the contact force on rolling elements, but increasing the contact force reduces the fatigue life of a bearing. Hence, a balance must be achieved between the load required to avoid skidding and the load which limits the bearing fatigue-life.

Chang et al.^[22] find the same inconsistency while comparing their skidding model with experimental data at low load, despite use of an analytical rather than empirical EHD lubrication model. They suggest that one possible reason behind this variation is the influence of cage dynamics on roller slippage which is neglected in their model. They also suggest that at low loads test data can involve large uncertainties because of the sensitivity of cage slip to lubricant supply rate.

Dynamic models developed by Gupta^[45] make it possible to simulate dynamic performance of roller bearings in time domain, but the complexity involved requires long computational times. Creju et al.^[26,27] propose a simpler and relatively cheap method to consider roll-slip dynamics of taper-roller bearings. Their analysis follows a two step

approach: the first step uses static equilibrium to determine load distribution on rolling elements, and the second step uses a dynamic model to determine rolling-element motion inside a bearing. Tractive forces are calculated using slicing technique. According to slicing technique, contact area along a roller length is divided into number of strips or slices, and analysis is performed on each slice separately. This skidding model is later extended to double-row taper-roller bearings to investigate fatigue life and heat generation^[11,95].

Selvaraj and Marappan^[112] carry out an experimental investigation on some of the factors influencing the skidding behaviour in cylindrical-roller bearings. Experimental analysis reveals that: (i) skidding increases with increasing speed and decreasing load, which is consistent with the findings of Harris^[53] and Gupta^[45]; (ii) skidding increases with increase in lubricant viscosity because of the reduction in traction forces between rolling elements and raceways caused by increase in film thickness at high lubricant viscosities; (iii) skidding increases with increase in number of rolling elements, because the contact force on a rolling element decreases as we increase the number of rolling elements in a bearing.

2.2.2 Criteria to Predict Onset of Skidding

Kliman^[79] introduces a simple equation to calculate the minimum axial load required to prevent skidding in thrust bearings by minimizing the difference between inner and outer raceway contact angles. According to Kliman, skidding occurs when a non-dimensional parameter zF_c/F_a exceeds $\cot\beta$; where z is the number of rolling elements, F_c is the centrifugal force, and F_a is the applied axial force.

Hirano and Tanoue^[60] devised an experiment to investigate ball motion in an angular-contact ball-bearing by using magnetized balls and by measuring the alternating current induced by change in magnetic flux caused by these magnetized balls. The findings for bearings under pure radial load suggest that: (i) skidding occurs at unloaded region and it increases with radial clearance, and (ii) skidding decreases with increase in applied load. Hirano^[59] later carries out a similar experimental investigation for angular-contact ball-bearings under pure thrust load. Measured data of angular velocities of balls and cage suggest that the skidding occurs when the parameter zF_c/F_a exceeds 0.1. Hirano does not provide any analytical justification for this empirical criterion. For Hirano's test bearing, Kliman's criterion gives $zF_c/F_a = \cot\beta = 1.22$ which is different from the value proposed by Hirano (0.1). So, we can see that the two criteria are not in agreement. Poplawski and Mauriello^[103] later establish that the parameter zF_c/F_a alone is not sufficient to predict onset of skidding.

Boness and Gentle^[14] also propose a ball-bearing force-equilibrium model using an

EHD traction equation, derived by Gentle and Cameron^[37]. Using this model, Boness^[13] develops the following empirical equation to calculate the minimum load required to avoid skidding in thrust ball bearings.

$$\sigma_{\max} = 0.00733(2\omega_i^2 R)^{0.22}(2Rz\eta)^{-0.175} \text{ GPa}, \quad (2.1)$$

where σ_{\max} is the contact pressure, ω_i is the inner-race speed (rpm), R is the pitch radius (mm), z is the number of rolling elements and η is the lubricant viscosity at operating temperature (Pa.s).

Poplwaski et al.^[102] use SHABERTH^[25], a computer program developed by SKF Industries, to perform a parametric study on the influence of rolling-element size, number of rolling elements, contact angle, raceway curvature, lubricant type and bearing preload on contact stress, fatigue life and load required to prevent skidding. This work serves as a design guide for bearing selection and performance evaluation based on skidding.

Most of the criteria described above to determine onset of skidding are limited to bearings operating under constant axial loads. Recently, Liao and Lin^[84] develop a method to calculate rolling-element forces in ball bearings by taking into account contact angle variation with ball position angle. They create the skidding maps for ball bearings operating under combined axial and radial loads using Hirano's skidding criterion^[59]. They later expand their model to evaluate thermal effects on skidding^[85]. Their slip speed calculation is based on the raceway control hypothesis (with outer race as controlling raceway), and their model does not include any dynamic effects. Since the skidding maps produced by Liao and Lin^[84] for bearings operating under combined axial and radial loads are based on the empirical criterion proposed by Hirano^[59] which is derived for bearings operating under pure axial loads, their use can often be limited.

The methods described above are useful to predict onset of skidding in bearings, but they do not tell us anything about how much skidding is allowable before serious wear will occur. Under stable operating conditions considerable slip may occur without significant surface damage. Under some unfavourable operating conditions, however, lubricant film might collapse due to skidding resulting in surface damage^[48]. Very few criteria are available to predict onset of damage caused by skidding. More recently, an experimental study is performed by Bujoreanu et al.^[17] to estimate scuffing limits in angular-contact ball-bearings. Scuffing is a complex wear phenomenon which involves sudden collapse of lubricant film and results in metal-to-metal contact. The variables used in the experimental procedure to study scuffing damage are sliding speed and normal load. They perform two tests: one with twin discs and another with an angular-contact ball-bearing. The test data indicates that scuffing damage is related to the amount of heat generated inside a

fluid film due to traction forces. Based on these tests, they derive an empirical equation describing the onset of scuffing, which is given by

$$\mu\sigma\Delta u^{0.8} = 1.5 \times 10^8, \quad (2.2)$$

where μ is the friction coefficient, σ is the contact stress, and Δu is the slip speed. This critical value ($1.5 \times 10^8 \text{ W/m}^2$) of frictional heat is enough to initiate scuffing damage. The empirical criterion described by equation 2.2 is derived for a particular test bearing (7206), and more experimental investigation must be performed on bearings with different geometry and lubricants to generalize this result.

2.3 Elastohydrodynamic Lubrication Theory

At the end of the 19th century, Beauchamp Tower (a railway engineer) noticed oil leak out of a hole located beneath the load in a journal bearing. When he tried to plug the hole with a wooden bung, pressure slowly pushed the bung out. Tower then carefully measured the oil pressure over the surface of the bearing by drilling more holes and found that the pressure was asymmetrical and that a fluid film of finite thickness was formed in the loaded region of the bearing which separated the sliding surfaces by a hydraulic force^[121,122]. Tower's work provides the first experimental confirmation of hydrodynamic lubrication.

Based on Tower's experiments, Osborne Reynolds^[108] formulates the first analytical theory of hydrodynamic lubrication. According to the theory, a viscous liquid can physically separate two sliding surfaces by hydrodynamic pressure resulting in low friction and theoretically zero wear. The occurrence of hydrodynamic lubrication requires^[116]:

- the contacting surfaces to move relative to each other with a speed sufficient to create a lubricant film;
- the contacting surfaces to be inclined at some angle relative to each other or to have parallel-stepped profiles, otherwise a pressure field will not form in the lubricating film to support the applied load.

Elastohydrodynamic lubrication is a form of hydrodynamic lubrication where elastic deformation of contacting solids and change in viscosity with pressure become important. Hydrodynamic lubrication theory explains the lubrication mechanisms in conformal contacts such as those found in hydrostatic bearings, but it does not explain the lubrication mechanism in non-conformal contacts such as those found in rolling bearings, gears etc.

The film thickness values predicted by hydrodynamic theory for non-conformal contacts are so small that it is not possible to physically separate the contacting surfaces, which is in contradiction with the experimental observations. This contradiction is the result of change in lubrication regime from hydrodynamic to elastohydrodynamic.

Lubricant behaviour in an EHD contact is effected by the elastic deformation of contacting solids and change in lubricant viscosity due to pressure. Based on these two factors Johnson^[69] identifies four lubrication regimes in EHD contacts.

1. *Isoviscous rigid*. In this regime, elastic deformations of the contacting solids are small compared to the lubricant-film thickness and lubricant viscosity does not change with pressure. This is comparable to hydrodynamic lubrication regime.
2. *Piezoviscous rigid*. In this regime, elastic deformations of the contacting solids are small and can be neglected, but the contact pressure is sufficiently high to increase the lubricant viscosity significantly.
3. *Isoviscous elastic*. In this regime, elastic deformations of the contacting solids have considerable influence on film thickness, but the contact pressure is too small to change the lubricant viscosity significantly.
4. *Piezoviscous elastic*. In this regime, both the elastic deformations of contacting solids and the rise in lubricant viscosity influence the lubricant-film thickness (figure 2.6). This regime is also known as full EHD regime. Gears and rolling-element bearings mostly operate in this regime.

Contact pressure in a static non-conformal contact can be defined by Hertzian theory^[57]. If the contact surfaces are moving relative to each other and the lubricant film is in full EHD (piezoviscous elastic) regime then the pressure distribution slightly deviates from the Hertzian theory, especially at the entry and exit regions of the contact (figure 2.6). The contact region at entry in an EHD contact is slightly larger than the Hertzian contact because of the combined effect of rolling and hydrodynamic-film formation. Thickness of the lubricant film roughly stays constant over an appreciable fraction of the contact region. At exit, a constriction is formed and the film thickness reduces. This results in a spike in the contact pressure just before the constriction as shown in figure 2.6. The lubricant viscosity increases with pressure as it enters the contact and then decreases to the ambient viscosity level at exit. The constriction is formed to compensate for the decline in lubricant viscosity at exit and to maintain the continuity of flow^[67,116]. Grubin^[40] provides an approximate analytical treatment of the mechanism of

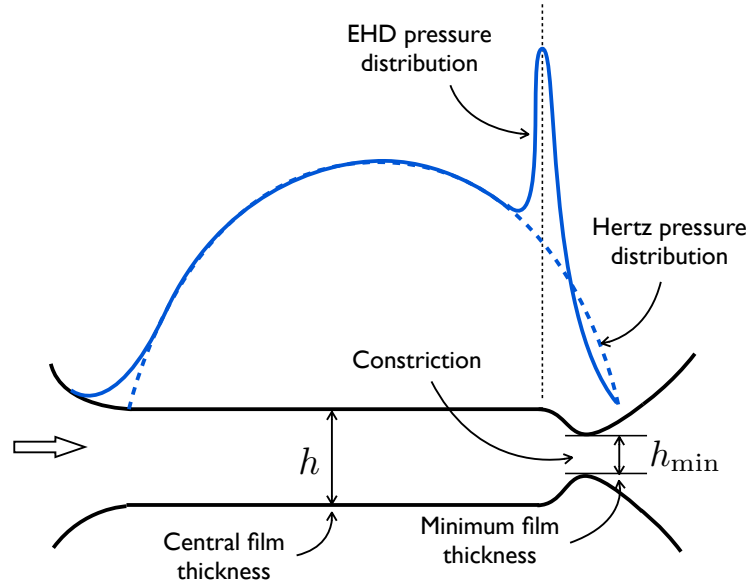


Figure 2.6: Pressure distribution and film-thickness variation in an EHD contact

film formation and pressure distribution in an EHD contact, and Greenwood^[38] extends Grubin's analysis to cover the constriction formation at exit zone.

Hamrock and Dowson^[50] derive the formulae for the central and the minimum film thickness (as shown in figure 2.6) in an EHD contact. The formulae for a point contact are

$$h = 2.69 \left(\frac{\eta_0 u_{\text{ent}}}{E' R'} \right)^{0.67} (E' c_{\eta P})^{0.53} \left(\frac{F}{E' R'^2} \right)^{-0.067} (1 - 0.61 \exp(-0.73\kappa)) R' \quad (2.3a)$$

and

$$h_{\text{min}} = 3.63 \left(\frac{\eta_0 u_{\text{ent}}}{E' R'} \right)^{0.68} (E' c_{\eta P})^{0.49} \left(\frac{F}{E' R'^2} \right)^{-0.073} (1 - \exp(-0.68\kappa)) R', \quad (2.3b)$$

where η_0 is the lubricant viscosity at atmospheric pressure, u_{ent} is the fluid-entrainment speed, E' is the effective Young's modulus, R' is the effective radius of curvature in the rolling direction, $c_{\eta P}$ is the pressure-viscosity coefficient, F is the contact force and κ is the ellipticity parameter.

Crook^[28,29,31] performs some experimental studies on the effect of bearing operating parameters on film thickness and lubricant viscosity. Film thickness is found to be sensitive to rise in surface temperature. Few degrees of temperature rise could reduce the film thickness by as much as 50 %^[28]. Crook also shows that there is no considerable reduction in film thickness with the increase in relative sliding between contacting surfaces despite the accompanying increase in frictional heating^[29].

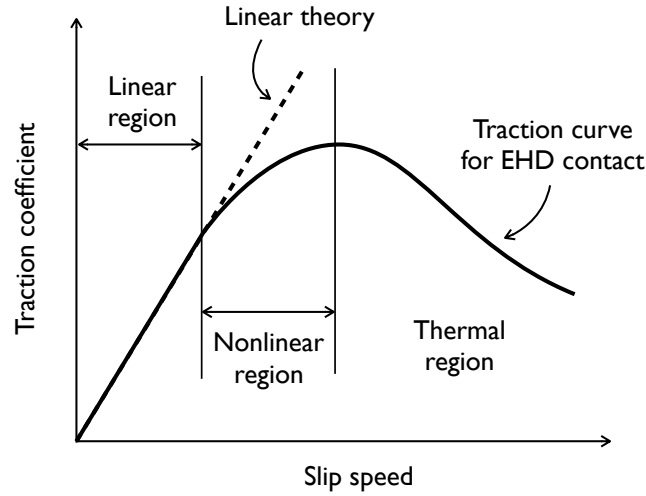


Figure 2.7: Typical traction curve in EHD contact showing three regions: linear (for shear stress values below Eyring stress, τ_0), nonlinear and thermal.

In order to calculate traction force in EHD contacts some simplified assumptions are commonly made. The first simplification is to assume a constant film thickness throughout the contact zone, and the second simplification is to approximate the pressure distribution in the contact zone by Hertz pressure distribution. For a Newtonian fluid, shear stress is proportional to the shear-strain rate, i.e.

$$\tau = \eta \dot{\gamma} = \eta \frac{\Delta u}{h}, \quad (2.4)$$

where τ is the shear stress, $\dot{\gamma}$ is the shear-strain rate and $\Delta u/h$ is the velocity gradient across the film thickness. If the contact area is A and applied load is F then traction coefficient can be obtain from equation 2.4 as

$$\mu = \frac{\tau A}{F} = \frac{\eta A}{F} \frac{\Delta u}{h}. \quad (2.5)$$

This simple relationship gives a linear relationship between traction coefficient and slip speed. Figure 2.7 shows a typical traction curve for EHD contact. For low slip speeds, traction behaviour is linear as predicted by equation 2.5. Traction curve starts to deviate from the linear behaviour at higher slip speeds, reaches a maximum value and then gradually decline. This decline in the traction coefficient is caused by the reduction in viscosity due to shear heating of lubricant. Based on this traction behaviour, traction curve can be divided into linear, nonlinear and thermal regions.

The extent of the linear regime in a traction curve depends on the contact pressure. At

high contact pressures, lubricant traction shows a deviation from the Newtonian theory and behaves nonlinearly. Evans and Johnson^[35] find four regimes and their appropriate constitutive equations describing lubricant traction behaviour in EHD contacts. These regimes are: Newtonian, Eyring, Viscoelastic and Elastic-plastic (in increasing order of pressure). At low pressures, lubricant behaviour is Newtonian and can be described by equation 2.4. At high pressures when shear stress exceeds the Eyring stress (τ_0), lubricant starts to behave nonlinearly and its behaviour can be modelled by the Eyring equation,

$$\dot{\gamma} = \frac{\tau_0}{\eta} \sinh\left(\frac{\tau}{\tau_0}\right). \quad (2.6)$$

Further increase in pressure results in viscoelastic^[70] and then elastic-plastic regimes. To construct boundaries between these regimes, variation of viscosity and Eyring stress (τ_0) with temperature and pressure must be known. Some of these rheological properties for few lubricants can be found in the paper by Evans and Johnson^[36].

Many empirical and analytical models are available in the literature to describe pressure and temperature dependency of lubricant viscosity but their accuracy is often limited to certain operating regimes. A commonly used empirical expression describing this dependency is well known Barus equation^[10] given by

$$\eta = \eta_0 \exp\{c_{\eta_P} \sigma - c_{\eta_T} (T - T_R)\}, \quad (2.7)$$

where η_0 is the reference viscosity at reference temperature T_R and T is the temperature. This equation accurately predicts viscosity for a certain range of temperature and pressure, but for a slightly wider range the equation can be corrected by introducing additional terms in powers of $(T - T_R)$ and p to fit the measured data. The problem with this approach is that at further wider range of temperature and pressure the correction terms may dominate and introduce behaviour that is not intended in the correction process^[9]. Further information regarding pressure-temperature-viscosity models can be found in the book by Bair^[9].

In the EHD traction calculations described above, it is assumed that the contacting surfaces are smooth and a lubricant film always separates the contacting surfaces. In practice, however, all surfaces are rough and are covered with asperities. Depending on their size, surface asperities could influence the mechanism of fluid-film formation in a contact. A film parameter (Λ) is generally used to establish a lubrication regime in a contact zone and it is defined as

$$\Lambda = \frac{h}{(\lambda_A^2 + \lambda_B^2)^{1/2}}, \quad (2.8)$$

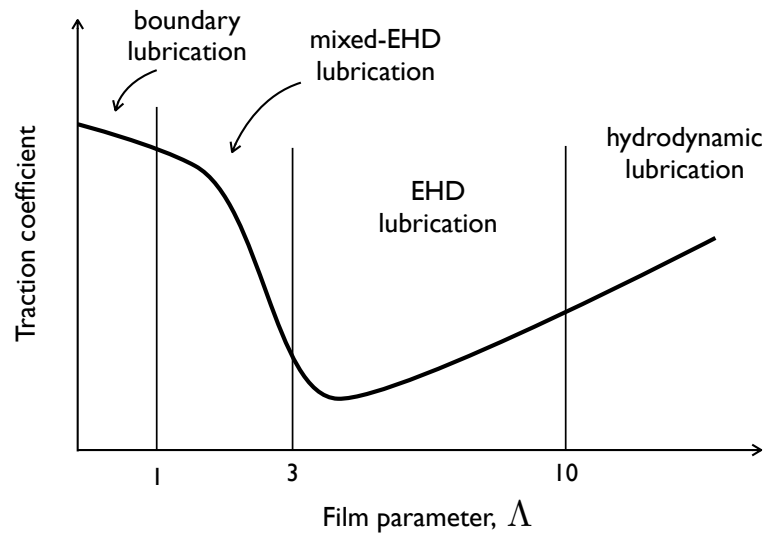


Figure 2.8: Variation of traction coefficient with film parameter, showing different regimes of lubrication.

where h is the minimum film thickness, λ_A and λ_B are the RMS surface roughness of two contacting bodies.

When the lubricant film-thickness is sufficient to prevent contact between surface asperities of contacting solids, lubrication regime is hydrodynamic ($\Lambda > 10$) as shown in figure 2.8. EHD lubrication is a form of hydrodynamic lubrication where elastic deformation of contacting solid surfaces becomes significant. Film thickness is smaller but is enough to prevent asperity contact ($3 \leq \Lambda < 10$). If Λ is less than 1 then surface contact takes place resulting in high friction coefficient, and the regime of contact is known as boundary lubrication. The friction behaviour in this regime is similar to dry contact. If Λ is between 1 and 4 then asperity contact might take place along with the lubricant-film formation. The contact force is supported by both asperities and lubricant film (figure 2.9). This lubrication regime is known as partial or mixed EHD lubrication.

Johnson, Greenwood and Poon^[68] develop a theory to describe the mechanism of asperity contact in mixed EHD lubrication regime. They find that if the major part of the applied load is carried by EHD film then the separation between two rough surfaces is about the same as the film thickness between two smooth surfaces under the same load. They also find that average asperity pressure depends primarily on the ratio of theoretical film thickness and combined roughness of two surfaces (Λ).

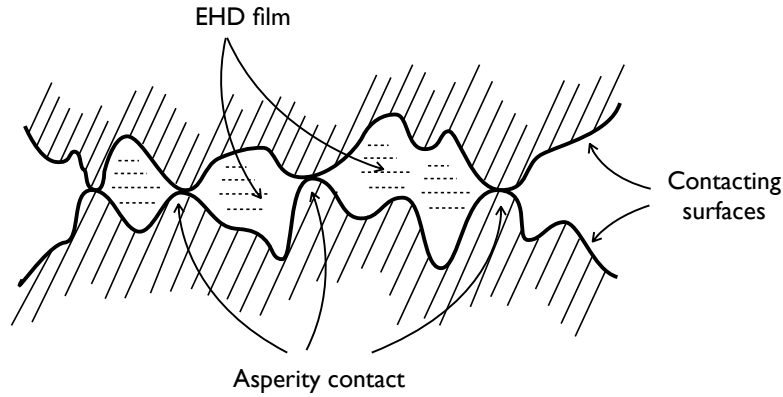


Figure 2.9: Contact pressure shared between asperity contacts and EHD film in a mixed-EHD lubrication regime.

2.4 Vibration Behaviour of Healthy Planetary-Drives

In this section we present different sources of vibration in a planetary-drive and review various mathematical models available in the literature to simulate the vibration response of healthy planetary-drives.

2.4.1 Sources of Vibration

Primary source of vibration in any involute-gear drive is the variation of the contact force between a gear pair during the meshing process. The variation in the contact force can be caused by: profile modification of a gear tooth, elastic deflection of a gear tooth and change in number of teeth in contact during meshing. This type of excitation during meshing process of gears originated the idea of “transmission error”. The first significant work on prediction and measurement of dynamic transmission error was carried out at the Department of Engineering, University of Cambridge in the late 1950s by Gregory, Harris and Munro^[39,52].

Transmission error (Δe) is defined as the difference between actual and theoretical rotations of a driven gear. The theoretical rotation assumes an ideal gear with rigid teeth and no profile modification operating in a perfect mesh. Mathematically, it can be described as

$$\Delta e = \theta_B - \frac{z_A}{z_B} \theta_A, \quad (2.9)$$

where θ_A and θ_B are the angular rotations of gears A and B, z_A and z_B are the number of teeth on gears A and B, and gear A is driving gear B. This deviation of actual rotation from its corresponding theoretical value gives rise to a periodic excitation forces with excitation

frequency equal to meshing or tooth-passing frequency. Friction forces acting between contacting teeth also result in a directional change in the resultant contact force but this effect is small (less than $\pm 3^\circ$) and can be neglected in most industrial applications^[114].

Another possible source of vibration in a gear drive is the presence of manufacturing errors inside gears. Manufacturing error could be either radial run-out/eccentricity of one of the gears or profile error. All these errors alter the dynamic behaviour of the system and modulate the actual vibration signature. Chaari et al.^[21] develop a discrete dynamic-model of a planetary drive to predict the influence of manufacturing errors on the force excitation caused by transmission error. They find that the presence of gear eccentricity or profile error results in amplitude modulation of the original mesh-force signal and generates modulation sidebands, separated by gear-rotation frequency, around meshing frequency and its harmonics. This is because of the change in transmission-error caused by the manufacturing errors. Inalpolat and Kahraman^[66] also study the effects of manufacturing errors on the vibration characteristics of healthy planetary-drives. They find that a run-out error causes the contact point of the two meshing gears to change with the gear rotation in a meshing cycle. This results in amplitude as well as frequency modulation of the contact force.

In a planetary drive, vibration due to transmission-error excitation is greatly effected by planet-gear phasing. If multiple gear-meshes are running in parallel, each mesh will have its own transmission error and the overall vibration response is determined by the relative phasing between these individual transmission error components. For example, in a planetary drive containing three planets, if the number of teeth on sun gear is divisible by three then three meshes will contact at their pitch points simultaneously and the three transmission error excitations will be in-phase. This will produce a strong torsional excitation to the sun but no net radial forcing. Whereas if there is a relative phase difference of 120° between the three meshes then there will be no net torsional excitation but a radial excitation at the sun. The direction of this radial excitation force changes with meshing frequency^[114]. Parker^[97] utilizes planet mesh phasing to suppress the vibration of a planetary drive at certain harmonics of mesh frequency based on physical forces acting at sun-planet and ring-planet meshes. He deduces simple rules of harmonic suppression. The suppression phenomenon is also demonstrated using a dynamic finite-element/contact-mechanics simulation.

In most planetary-drive applications, like wind turbines, ring gear remains stationary and power is transmitted either from sun to planet carrier or the other way around. In such an arrangement, a transducer mounted on ring gear housing experiences a periodic variation in vibration amplitudes as planets pass through this fixed transducer location.

This results in amplitude modulation of vibration signal and creates modulation sidebands around meshing frequency and its harmonics. The separation between these sidebands is given by $z_p\omega_c$, where z_p is the number of planets and ω_c is the carrier-rotation frequency. Variation in the vibration amplitudes, as seen by the stationary transducer, is due to varying vibration transmission path between vibration source (planet-ring mesh) and measurement point (fixed transducer) as carrier rotates. McFadden and Smith^[91] propose a simple analysis technique to predict the vibration response of a planetary drive at a fixed point on a ring gear by considering the variation in vibration transmission path caused by carrier rotation. Their study is the first to explain the underlying reasons for asymmetric distribution of modulation sidebands about meshing frequency and its harmonics. Their model is able to predict the frequencies associated with dominant sidebands but is unable to predict their relative amplitudes.

Inalpolat and Kahraman^[65] perform a theoretical and experimental investigation on modulation sidebands of a planetary set due to carrier rotation. The analytical model developed in their study is capable of predicting amplitudes as well as frequencies of these modulation sidebands. They show that based on the vibration behaviour a planetary drive can be classified into one of five distinct groups: (i) equally spaced and in-phase planets, (ii) equally spaced and sequentially phased planets, (iii) unequally spaced and in-phase planets, (iv) unequally spaced and sequentially phased planets, and (v) unequally spaced and arbitrarily phased planets. General sideband behaviour unique to each of these cases is characterized using simulations.

The studies mentioned above provide a good insight into the modulation mechanisms in healthy planetary-drives, but they do not include a flexible ring-gear to model the vibration transmission path. In all these models, the vibration transmission path between a ring-planet mesh and a measurement-point fixed on the ring gear is approximated by a Hann function, which limits their applicability.

2.4.2 Modelling Vibration in Healthy Planetary-Drives

Modelling of vibration characteristics of healthy planetary-drives attracted significant attention of various researchers in the past. Majority of the proposed models are based on lumped-parameter approach in which gear wheels are treated as rigid bodies and gear mesh flexibility is represented as a linear or a non-linear spring inserted between these rigid gears. Based on number of degrees of freedom, lumped-parameter models can be split into three categories: pure torsional models^[76], planar models^[21,75,86] and three-dimensional models^[34].

Most of the lumped-parameter models use a time-invariant mesh-stiffness neglect-

ing the change in mesh stiffness caused by varying number of teeth in contact [8,15,32,58]. Kahraman [75] extends these models by employing a non-linear time-varying stiffness formulation which allows consideration of both backlash and transmission-error excitation to investigate the dynamic load sharing characteristics of a planetary drive. Lin and Parker [86] perform an analytical investigation of natural frequencies and vibration modes of planetary drive. They adopt a linear mesh-stiffness model and solve the corresponding eigenvalue problem to obtain vibration modes. Their findings suggest that due to the cyclic symmetry of a planetary drive, its vibration modes can be classified into three categories: rotational modes (contain pure rotation of all components), translational modes (contain pure translation of components) and planet modes (no motion of carrier, ring and sun). Another group of planetary models use more sophisticated contact mechanics algorithms based on finite-element analysis [77,98]. These models eliminate the need of user defined gear-mesh parameters (as required by lumped-parameter models) as gear-meshes are modelled as individual nonlinear contact problems. In addition, the influence of tooth-base flexibility and rim deflections is also taken into account. However, the solver time required by these finite element based models is significantly higher than lumped-parameter models.

A common assumption made in lumped-parameter models is that the ring gear is treated as rigid body. In practice, however, flexibility of ring gear plays an important role in vibration measurement specially if transducer is located at ring gear housing, which is common in wind-turbine gearboxes. Very limited research has been done to include ring-gear deformation in analytical models. Wu and Parker [129] address this problem by developing a planar elastic-discrete model, where ring gear is modelled as a continuous elastic body while all other gears are represented as rigid bodies. Modal properties are derived for the combined system using eigenvalue perturbation and candidate mode approaches.

Recently, Eritenel and Parker [34] study the modal properties of a planetary drive containing helical gears. They extend the existing planar lumped-parameter models in three dimensions and each gear is represented by six degrees of freedom. The model includes the tilting effect of gears but lacks ring gear flexibility. Their study shows that for helical gears, pure-rotational and pure-translational modes are replaced by rotational-axial and translational-tilting modes due to additional degrees of freedom.

2.5 Detecting Faults in Bearings Using Vibration Measurements

Vibration based techniques are commonly used to detect bearing faults in wind turbines. In order to detect bearing faults effectively and to develop more sophisticated vibration-based algorithms for fault detection, a thorough understanding of vibration signatures of bearings with faults is required. In this section we discuss various methods available in the literature to detect faults and to simulate their vibration signatures in both fixed-axis and planet bearings.

2.5.1 Faults in Fixed-Axis Bearings

A fixed-axis bearing is a bearing whose axis of rotation remains stationary with respect to a measurement point located on the bearing housing. A lot of work has been done on the detection of localized faults (spalls or pits) in fixed-axis bearings. McFadden and Smith^[88] and Tandon and Choudhury^[119] provide a review of some of the methods developed for vibration monitoring of rolling-element bearings.

In a bearing containing a localized fault, each time a rolling element passes through the fault it generates an impulse. These impulses are periodic if the bearing speed remains constant, and the frequency at which these impulses occur is known as the characteristic fault frequency (ω_d). The characteristic fault frequency for a bearing fault is a function of fault location, bearing geometry and operating speed. For a bearing with stationary outer-race and rolling-element radius r , pitch radius R , number of rolling elements z , contact angle β and inner-race speed ω_i , characteristic fault frequency can be defined as^[46]

$$\omega_d = \begin{cases} \frac{z\omega_i}{2} \left(1 - \frac{r}{R} \cos\beta\right) & \text{for outer-race fault} \\ \frac{z\omega_i}{2} \left(1 + \frac{r}{R} \cos\beta\right) & \text{for inner-race fault} \\ \frac{R\omega_i}{r} \left(1 - \left(\frac{r}{R}\right)^2 \cos^2\beta\right) & \text{for rolling-element fault.} \end{cases} \quad (2.10)$$

The impulses occurring at characteristic fault frequency excite the system resonance frequencies and the frequency spectrum contains peaks separated by characteristic fault frequency. System resonance frequencies act as an envelope to these peaks as shown in figure 2.10. Depending on the location of the fault and measurement point, some modulation sidebands can also be present around the fault frequency and its higher harmonics. McFadden and Smith^[89,90] provide a good insight into the formation of these sidebands. They propose that the sources of these sidebands are the amplitude modulations of vibration signal occurring inside the bearing. The first modulation is caused by the contact

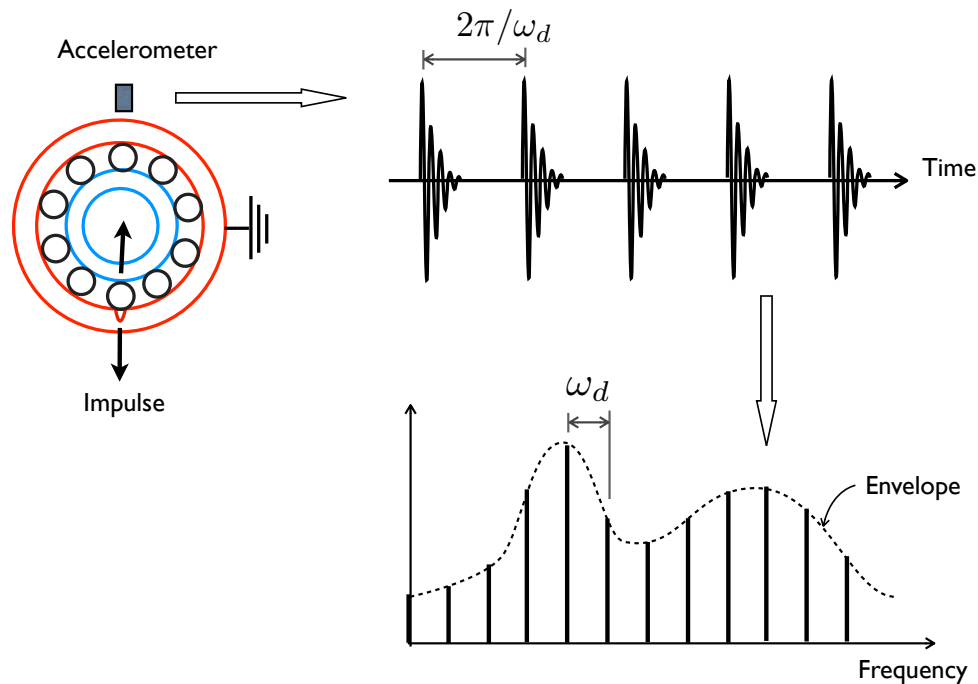


Figure 2.10: Vibration signature of a bearing with fixed outer-race in the presence of a localized outer-race fault.

load variation on a rolling element as it passes through a load zone. The second modulation is due to varying vibration transmission path between a fault and a transducer fixed on outer-race housing. This modulation is similar to the one caused by carrier rotation in planetary drives (section 2.4.1). If outer race of a bearing is stationary then these modulations are only present if a fault is located either on inner race or on a rolling element.

Tandon and Choudhary^[118] also develop an analytical model to investigate the effect of localized faults on bearing vibration behaviour. They model the inner and outer raceways as uncoupled continuous elastic rings with in-plane vibration modes and they use a mode summation approach to obtain the bearing vibration response. They model the force excitation due to a localized fault as an impulse-train with periodic impulses occurring at characteristic fault frequency. The width of these impulse pulses is obtained from the time taken by a rolling-element to cross a fault. They discuss that pulse height changes with severity and age of a fault, but no analytical or empirical relationship is provided to simulate this dependency.

Sassi et al.^[110] calculate the excitation force generated by a fault by splitting it into static and dynamic components. Static component is obtained from the contact load acting between a rolling element and a raceway while the dynamic component is obtained

by solving contact mechanics between fault and other contacting body. They apply energy conservation approach to calculate the shock velocity at the time of impact and this shock velocity is then used to determine dynamic excitation force. Instead of using a mode summation approach Sassi et al.^[110] calculate the vibration response at a fixed transducer location by considering only the first vibration mode of outer race. Based on the first mode shape, they establish a geometric relationship between impact and measurement points to obtain the dynamic response.

In all the above mentioned studies, it is assumed that the impulse due to a localized bearing-fault is proportional to the contact force acting on a rolling element at the time of impact. None of the papers provide any theoretical or experimental justification to this assumption.

If a bearing is operating at low speeds or the fault size is small then it is difficult to detect the characteristic fault frequencies and associated sidebands especially at low frequencies because the noise from other components like gears mask the fault vibration-signal^[106,111,113]. Chaturvedi and Thomas^[23] use adaptive noise-cancellation to enhance the signal-to-noise ratio for bearing faults by reducing the unwanted noise coming from other components. Antoni and Randall^[5,6] show that it is possible to separate bearing fault signals from gear signals in a gearbox using unsupervised noise-cancellation.

High-frequency resonance technique is also commonly used to identify bearing faults by extracting characteristics fault frequencies. According to this technique, measured signal is first band-pass filtered around a high-frequency resonance to remove unwanted gear noise and this filtered signal is then demodulated by using envelope analysis. The envelope signal contains characteristic fault frequencies.

2.5.2 Faults in Planet Bearings

Detection of localized faults in planet bearings is difficult than fixed-axis bearings because of the complicated and time-varying vibration transmission path between the fault and a measurement point on a ring gear. No published work has been found which simulates this time-varying transmission path and determines the vibration signature of a planetary drive containing a localized planet-bearing fault.

Some literature is available on gear-tooth faults in planetary drives. Presence of a gear-tooth fault alters the gear-mesh stiffness. Finite-element analysis is commonly used for gear-mesh stiffness evaluation^[7,100] but high computation times required to solve refined meshes limit its use. Some analytical methods^[78,130] are also developed to obtain mesh stiffness of a healthy gear and they prove to be a good substitute for finite-element based methods. Choy et al.^[24] shows, using numerical simulations and experimental results,

that gear tooth damage due to wear and pitting can be simulated by amplitude and phase changes in the gear-mesh stiffness. Chaari et al.^[18] derive an analytical expression for tooth and gear-mesh stiffness taking into account tooth bending, local Hertzian contact and fillet-foundation deflections. He modifies this expression to investigate the effect of tooth breakage, spalling and root cracks^[20] on mesh-stiffness curve. Chaari et al.^[19] also studies the dynamic response of a planetary drive subjected to tooth pitting and cracking defects. A joint time-frequency method of Wigner-Ville is used to characterize the signature of each of these faults. They find that whenever a faulty tooth passes through a contact mesh, an increase in sideband activity around meshing frequency and its harmonics can be observed in the joint time-frequency distribution. They do not discuss the sources behind this sideband activity and frequencies associated with sidebands.

2.6 Conclusions

Gearbox failures in wind turbines continue to be a major source of downtime and repair costs. Average life of a wind-turbine gearbox is about 5 years, which is significantly less than the 20 years design life of a wind turbine. Following conclusions can be drawn from the literature review.

- Most of the problems in wind-turbine gearboxes initiate in bearings. Bearings supporting the high-speed shaft and planet gears exhibit a high rate of premature failure and are two of the most critical components in a wind-turbine gearbox.
- High-speed bearings operate under low loads and high speeds, which make them susceptible to skidding. A commonly observed wear mode in these bearings is smearing, and skidding is one of the main causes of smearing and scuffing wear.
- Much work has been done to understand the skidding behaviour of angular-contact ball-bearings, but most of the work is based on quasi-static analysis and is limited to axially-loaded bearings. Almost all the models require time-consuming numerical simulations and hence are not suited for use as design tools. Some empirical and semi-empirical skidding criteria are also derived to predict the occurrence of skidding in ball bearings, but these criteria are not in agreement with each other and are limited to axially-loaded bearings.
- The skidding models available in the literature could be used to predict the onset of skidding in axially-loaded bearings. These models, however, do not tell us anything about how much skidding is allowable before serious wear will take place.

- Vibration behaviour of healthy planetary drives is well understood and many models exist in the literature to simulate the vibration behaviour of healthy planetary drives. Vibration behaviour of a planetary drive containing bearing or gear faults, however, is poorly understood. Very few models exist to simulate the vibration response of a faulty planetary drive and all of these models focus on gear tooth faults.
- Many methods have been developed to detect localized faults in fixed-axis bearings and to simulate their vibration signature. Detecting localized faults in planet bearings is more difficult than fixed-axis bearings because of their complicated vibration transmission path. No published work has been found in the literature which simulates this complicated transmission path and determines the vibration signature of a planetary drive containing localized planet-bearing faults.
- An assumption commonly made in the bearing-fault-detection literature is that the impulse due to a localized bearing-fault is proportional to the contact force acting on a rolling element during impact. None of the published work provides any scientific justification to this assumption.

Chapter 3

Skidding in High-Speed Bearings

High-speed bearings in a wind-turbine gearbox continue to exhibit a high rate of premature failure. As high-speed bearings operate under low loads and high speeds, these bearings are prone to skidding. Yet, most of the existing methods for analyzing skidding in ball bearings are quasi-static in nature and are limited to axially loaded bearings. In this chapter we propose a dynamic model, considering elasto-hydrodynamic (EHD) lubrication theory and gyroscopic effects, to understand the skidding behaviour of angular-contact ball-bearings under axial and radial loads, and time-varying speeds. We also derive novel analytical equations to predict the onset of skidding under these operating conditions. This work will help bearing engineers to predict the occurrence of skidding at the design stage for axial as well as radial loading conditions and make suitable design changes to improve bearing reliability.

3.1 Introduction

Bearings operating under high speeds and low loads are prone to skidding, i.e., gross sliding of rolling elements on raceways. Skidding occurs when the tractive forces between rolling elements and raceways are not enough to overcome drag and inertial forces. Skidding is known to cause excessive frictional heat generation and high surface shear stress. This can lead to premature bearing failure, long before classical fatigue failure. For a given speed and bearing geometry, a minimum load must be applied on the bearing to prevent it from skidding.

Various skidding models are available in the literature to calculate this minimum load, but most of these models are quasi-static and are limited to axially-loaded bearings. A brief review of these models is provided in chapter 2. The review suggests that almost all the skidding prediction methods in literature are based on time-consuming numerical

models. Some empirical criteria are also available to predict the minimum load required to avoid skidding, but these criteria are also limited to axially-loaded bearings. Wind-turbine bearings operate under combined axial and radial loads. This calls for development of simple methods to predict the occurrence of skidding at the design stage in bearings operating under these conditions.

Skidding models for ball bearings available in the literature provide a good understanding of the skidding behaviour of bearings operating under constant axial loads and steady speeds. However, limited amount of work has been done on skidding under combined axial and radial loads, and skidding behaviour under time-varying speeds has not been studied so far. In this chapter, we explore the skidding characteristics of angular-contact ball-bearings under both axial and radial loads as well as time-varying speeds. There are five main contributions of this chapter.

1. A mathematical model to analyze the skidding behaviour of angular-contact ball bearings (section 3.2). The model includes gyroscopic effects. The traction forces between rolling elements and raceways are calculated using full EHD lubrication theory. We also consider the variation of slip speed and traction forces along both the major and minor axes of the contact ellipse.
2. A simple equation to calculate the minimum load required to prevent skidding in bearings operating under constant axial loads and constant speeds (section 3.3.2). The benefits of the proposed equation are evaluated against the skidding criteria of Hirano^[59] and Kliman^[79].
3. Description of rolling-element motion and underlying skidding mechanism in a bearing operating under combined axial and radial loads (section 3.4). We also demonstrate that the skidding mechanism under combined loading conditions is different from that under axial loading conditions, and any skidding criterion developed for thrust bearings does not work for bearings operating under combined loads.
4. Derivation of a simple analytical method to predict the extent of skidding region inside the load zone of a bearing operating under combined axial and radial loads (section 3.4.2). The proposed method also gives us the minimum load required to create a rolling-contact region (where no skidding takes place) inside the load zone.
5. For bearings operating under time-varying speeds, we show how amplitude and frequency of speed fluctuation influence the skidding behaviour. We also derive an analytical equation to predict onset of skidding in bearings operating under time-varying speeds (section 3.5.1).

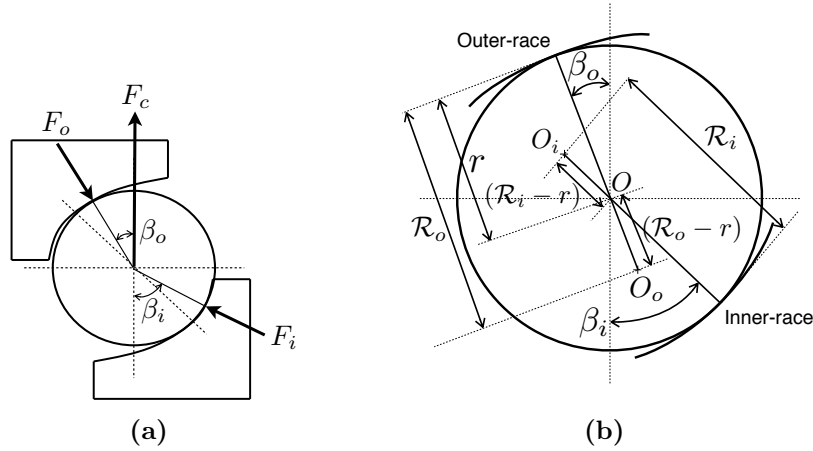


Figure 3.1: (a) Forces acting on a rolling element; (b) Geometrical compatibility between ball and raceways

3.2 Numerical Model Description

We perform the skidding analysis in two steps. In the first step we use a quasi-static model to calculate load distribution on the individual rolling elements. In the second step, we use a dynamic model along with an EHD lubrication model to analyze the motion of rolling elements inside a bearing. EHD model utilizes the load distribution, calculated in the first step, to determine traction forces and moments acting between rolling elements and raceways. The analysis steps are described in detail in the following paragraphs.

3.2.1 Quasi-Static Analysis of Internal Load Distribution

An external load applied to a bearing raceway is distributed among the rolling elements. If an axial load is applied to a bearing then all the rolling elements share equal load. From figure 3.1a, we can write the force balance equations for a single rolling element as

$$F_i \cos \beta_i + F_c = F_o \cos \beta_o \quad (3.1a)$$

and

$$F_i \sin \beta_i = F_o \sin \beta_o = \frac{F_a}{z}, \quad (3.1b)$$

where F_i and F_o are the contact forces acting between a rolling element and inner and outer raceways respectively, β_i and β_o are inner and outer contact angles, F_c is the centrifugal force, F_a is the axial force acting on the bearing, and z is the number of rolling elements.

Geometrical compatibility between a rolling element and raceway grooves (figure 3.1b)

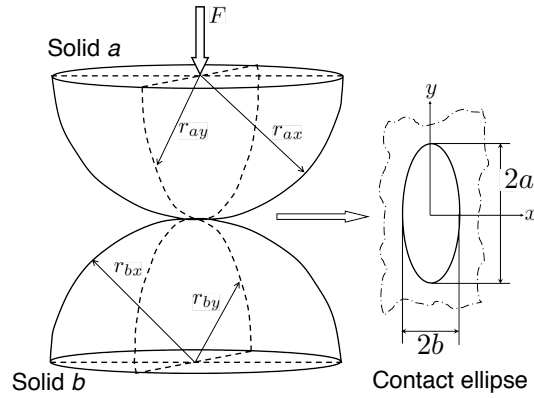


Figure 3.2: Geometry and contact dimensions of two elastic solids in contact

gives

$$(\mathcal{R}_o - r)\cos\beta_o + (\mathcal{R}_i - r)\cos\beta_i = \cos\beta(\mathcal{R}_o + \mathcal{R}_i - 2r), \quad (3.2)$$

where r is the rolling-element radius, β is the theoretical contact angle, \mathcal{R}_i and \mathcal{R}_o are the inner and outer raceway curvatures. During the derivation of equation 3.2, we neglect the effect of elastic deformation between rolling elements and raceways. We solve equations 3.1 and 3.2 numerically to get the contact angles (β_i and β_o) and the contact forces (F_i and F_o) for bearings operating under pure axial loads.

In case of a bearing operating under combined axial and radial loads the magnitude of the force carried by an individual rolling element depends upon the internal geometry of a bearing, the number of rolling elements in contact and the instantaneous location of the rolling element inside the load zone.

In this study, we use Hertz elastic theory^[57] to determine the contact force between rolling elements and raceways. According to Hertz theory, the contact force (F) between two elastic solids can be expressed in terms of the maximum deformation (δ) at the centre of a contact ellipse as

$$F = K\delta^{3/2}. \quad (3.3)$$

Here K is the stiffness parameter given by

$$K = \frac{\pi\kappa E'}{3\xi} \sqrt{\frac{3\varepsilon R}{\xi}}. \quad (3.4)$$

In equation 3.4, κ is the ellipticity parameter, ξ and ε are the elliptical integral of first and second kind, R is the effective radius of curvature of contacting bodies, and E' is the

effective Young's modulus defined as

$$E' = \frac{2}{\frac{1-\nu_a^2}{E_a} + \frac{1-\nu_b^2}{E_b}}, \quad (3.5)$$

where ν is the poisson's ratio, E is the Young's modulus, and subscripts a and b represent the two contacting bodies. If the contacting bodies are of same material, i.e., $\nu_a = \nu_b = \nu$ and $E_a = E_b = E$ then from equation 3.5 effective Young's modulus becomes

$$E' = \frac{E}{1 - \nu^2}. \quad (3.6)$$

Effective radius of curvature R for an elastic contact is defined in terms of the effective radii of curvatures in x and y directions (R_x and R_y), such that

$$\frac{1}{R} = \frac{1}{R_x} + \frac{1}{R_y}. \quad (3.7)$$

Effective radii of curvatures R_x and R_y are defined as

$$\frac{1}{R_x} = \frac{1}{r_{ax}} + \frac{1}{r_{bx}} \quad (3.8a)$$

and

$$\frac{1}{R_y} = \frac{1}{r_{ay}} + \frac{1}{r_{by}}, \quad (3.8b)$$

where r_{ax} , r_{ay} , r_{bx} and r_{by} are the radii of curvatures of the contacting bodies in the x and y directions as shown in figure 3.2. For the case of a ball bearing these radii of curvatures can be calculated as: (i) $r_{ax} = r_{ay} = r$, $r_{bx} = r_i$ and $r_{by} = -\mathcal{R}_i$ (for the contact between a ball and inner race); (ii) $r_{ax} = r_{ay} = r$, $r_{bx} = -r_o$ and $r_{by} = -\mathcal{R}_o$ (for the contact between a ball and outer race). Here solid a is the ball, solid b is the contacting raceway, and r_i and r_o are the radii of inner race and outer race.

Brewe and Hamrock^[16] derive simplified expressions for κ , ξ and ε using linear regression, which are given by

$$\kappa = 1.0339 \left(\frac{R_y}{R_x} \right)^{0.6360}, \quad (3.9a)$$

$$\varepsilon = 1.0003 + \frac{0.5968}{R_y/R_x}, \quad (3.9b)$$

and

$$\xi = 1.5277 + 0.6023 \ln \left(\frac{R_y}{R_x} \right). \quad (3.9c)$$

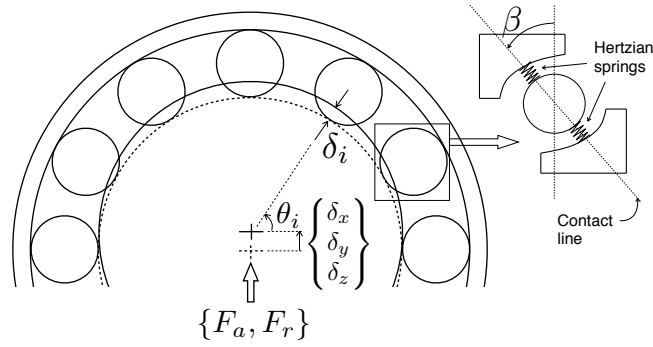


Figure 3.3: Quasi-static model to determine the internal load distribution under combined axial and radial loads

Now, we have all the ingredients to calculate the combined effective stiffness parameter for a rolling element as^[50]

$$K_{\text{eff}} = \frac{1}{\left\{ \left(\frac{1}{K_{\text{inn}}} \right)^{2/3} + \left(\frac{1}{K_{\text{out}}} \right)^{2/3} \right\}^{3/2}}, \quad (3.10)$$

where K_{inn} and K_{out} are the stiffness parameters for inner- and outer-race contacts defined by equation 3.4. In order to derive equation 3.10 we assume that the contact angles between a rolling element and inner and outer raceways are same, i.e., $\beta_i = \beta_o = \beta$. This assumption is valid for the bearings operating at low or medium speeds. Since wind turbine bearings operate at the maximum speed of 1500-1800 rpm, it is reasonable to make this assumption. For the bearings operating at very high speeds, difference between contact angles can be substantial because of large centrifugal force acting on a rolling element and the quasi-static formulation described here might not be adequate.

The next step is to calculate the contact deformation of the rolling elements. Assuming that the raceways are rigid and there are no clearances between rolling elements and raceways, the deformation along the contact line of a rolling element located at an angle θ_i (figure 3.3) can be calculated as

$$\delta_i = (C_{\theta_i} C_\beta, \quad S_{\theta_i} C_\beta, \quad S_\beta) \begin{pmatrix} \delta_x \\ \delta_y \\ \delta_z \end{pmatrix}, \quad (3.11)$$

where $C_\alpha = \cos(\alpha)$, $S_\alpha = \sin(\alpha)$, and $(\delta_x, \delta_y, \delta_z)^T$ is the displacement vector of the inner race.

Contact forces between the rolling element located at θ_i and raceways are

$$F_i = F_o = F_e = K_{\text{eff}} \langle \delta_i \rangle^{3/2}, \quad (3.12)$$

where $\langle \rangle$ is the Macaulay's bracket defined as

$$\langle \delta_i \rangle = \begin{cases} \delta_i & \text{for } \delta_i \geq 0 \\ 0 & \text{for } \delta_i < 0. \end{cases} \quad (3.13)$$

A positive value of δ_i represents the deformation of the contacting surfaces, which gives non-zero contact force; while a negative value of δ_i represents the separation between the contacting surfaces, which gives zero contact force.

Now we can calculate the reaction forces (F_x , F_y and F_z) at the inner race by adding the individual contact forces acting on the rolling elements. Therefore,

$$\begin{pmatrix} F_x \\ F_y \\ F_z \end{pmatrix} = - \sum_{i=1}^z K_{\text{eff}} \langle \delta_i \rangle^{3/2} (C_{\theta_i} C_\beta, S_{\theta_i} C_\beta, S_\beta)^T. \quad (3.14)$$

Axial and radial forces acting on the inner race are $F_a = -F_z$ and $F_r = \sqrt{F_x^2 + F_y^2}$, respectively.

Internal load distribution on the rolling elements is determined by using an iterative approach. At each iteration, equations 3.11 to 3.14 are solved numerically to get the axial and the radial forces (F_a and F_r). These forces are then compared to the applied forces on the inner race. Iterations terminate when the calculated axial and radial forces are equal to the applied ones. The method outlined above does not account for changes in the bearing stiffness caused by the movement of the rolling elements inside a load zone. In his detailed study While^[126] finds that the fluctuations in the stiffness due to these factors are less than 0.5% of the total value. The influence of friction forces between rolling elements and raceways on the internal load distribution is also ignored in the current analysis as these friction forces are significantly small compared to the contact forces.

3.2.2 Dynamic Analysis to Analyze Rolling-Element Motion

The dynamic model consists of two reference frames (figure 3.4). The first reference frame (xyz) is fixed at the centre of the bearing, and the second reference frame ($x'y'z'$) is a moving frame with its centre attached to a rolling element. Each rolling element has four degrees of freedom: three rotational degrees of freedom about its centre in moving

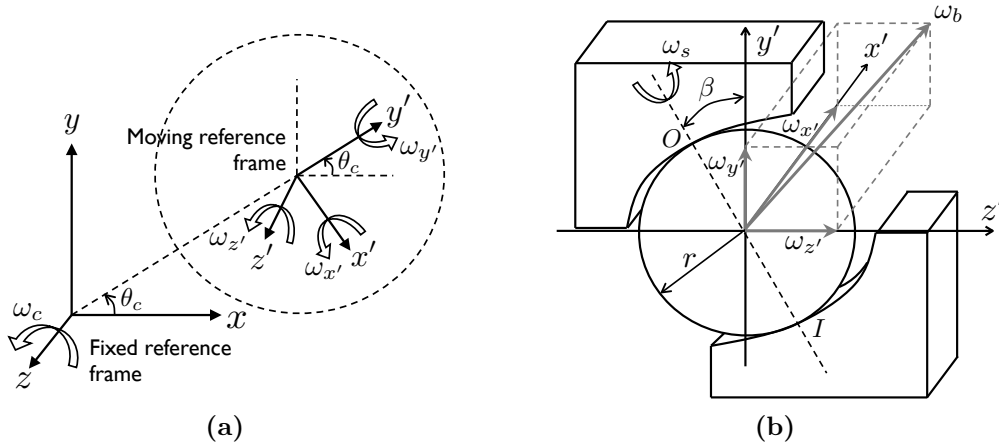


Figure 3.4: (a) Two reference frames used in the dynamic model formulation; (b) components of the angular velocity of a rolling element in the rotating reference frame.

reference frame ($\omega_{x'}$, $\omega_{y'}$ and $\omega_{z'}$), and one rotational degree of freedom about bearing centre (ω_c). The equations governing the motion of a rolling element are derived using Euler's equations and are given by

$$\begin{pmatrix} M_{x'} \\ M_{y'} \\ M_{z'} \end{pmatrix} = \text{diag} \left[\frac{2}{5}mr^2 \right] \begin{pmatrix} \dot{\omega}_{x'} \\ \dot{\omega}_{y'} \\ \dot{\omega}_{z'} \end{pmatrix} + \begin{pmatrix} 0 & -\omega'_z & \omega'_y \\ \omega'_z & 0 & -\omega'_x \\ -\omega'_y & \omega'_x & 0 \end{pmatrix} \text{diag} \left[\frac{2}{5}mr^2 \right] \begin{pmatrix} \omega_{x'} \\ \omega_{y'} \\ \omega_{z'} \end{pmatrix}, \quad (3.15)$$

where $M_{x'}\underline{i}' + M_{y'}\underline{j}' + M_{z'}\underline{k}'$ is the friction-moment vector acting on a ball, $\omega_{x'}\underline{i}' + \omega_{y'}\underline{j}' + \omega_{z'}\underline{k}'$ ($= \underline{\omega}_b$) is the ball angular-velocity in $x'y'z'$ frame, $\omega'_x\underline{i} + \omega'_y\underline{j} + \omega'_z\underline{k}$ is the angular velocity of the moving reference frame $x'y'z'$ with respect to the fixed reference frame xyz and $\dot{\omega} = \frac{\partial \omega}{\partial t}$. For the system shown in figure 3.4, reference frame $x'y'z'$ is constrained to rotate about the z axis with the rolling-element's orbital speed ω_c . Therefore, $\omega'_x = \omega'_y = 0$ and $\omega'_z = \omega_c$. Putting these values into equation 3.15 gives

$$M_{x'} = I(\dot{\omega}_{x'} - \omega_c \omega_{y'}) \quad (3.16a)$$

$$M_{y'} = I(\dot{\omega}_{y'} + \omega_c \omega_{x'}) \quad (3.16b)$$

$$M_{z'} = I\dot{\omega}_{z'}, \quad (3.16c)$$

where I is the moment of inertia of a rolling element ($= \frac{2}{5}mr^2$) and m is the mass of a rolling element.

Now, we determine the equation governing the motion of a rolling element about the bearing axis (z -axis in the fixed reference frame xyz). To derive this equation, the inter-

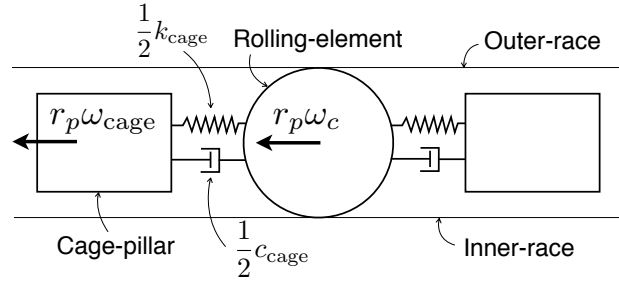


Figure 3.5: Cage model used in the current analysis

action between the rolling elements and the cage must be taken into account. Figure 3.5 shows how the cage interaction is modelled in the current analysis. The cage has one rotational degree of freedom about the bearing-axis and we ignore the clearance between the rolling elements and the cage pillars. We also ignore the radial movement of the cage. The contact between the cage pillars and the rolling elements is modelled by a spring-damper system. We can write the equation of motion for the cage as

$$I_{\text{cage}}\dot{\omega}_{\text{cage}} = \sum_{i=1}^z F_{\text{cage}}^{(i)} r_p, \quad (3.17)$$

where I_{cage} is the moment of inertia of the cage, ω_{cage} is the rotational speed of the cage and r_p is the pitch radius. $F_{\text{cage}}^{(i)}$ is the force between a cage pillar and i^{th} rolling element given by

$$F_{\text{cage}}^{(i)} = k_{\text{cage}}\delta_{\text{cage}}^{(i)} + c_{\text{cage}}\dot{\delta}_{\text{cage}}^{(i)}, \quad (3.18)$$

where k_{cage} is the cage stiffness, c_{cage} is the cage damping, $\delta_{\text{cage}}^{(i)} = r_p\{\theta_c - \theta_{\text{cage}} - 2\pi(i-1)/z\}$ is the relative displacement of i^{th} rolling element with respect to cage, $\dot{\delta}_{\text{cage}}^{(i)} = r_p(\omega_c - \omega_{\text{cage}})$ is the relative speed of i^{th} rolling element with respect to cage, $\theta_c = \theta_c^0 + \int_0^t \omega_c dt$ where θ_c^0 is the initial position angle of the i^{th} rolling element, and $\theta_{\text{cage}} = \int_0^t \omega_{\text{cage}} dt$.

In addition to the cage force, rolling elements must also overcome a viscous drag force imposed by the lubricant within the bearing cavity. This viscous force (F_{drag}) is

$$F_{\text{drag}} = \frac{\pi}{2} C_D \rho (\omega_c r_p)^2 r^2, \quad (3.19)$$

where C_D is the drag coefficient, and ρ is the lubricant density.

By considering the cage and the drag forces, we can now formulate the remaining differential equation governing the orbital motion of a rolling element as

$$I_c \dot{\omega}_c = -(\underline{f}_i \cdot \underline{\dot{r}}_i + \underline{f}_o \cdot \underline{\dot{r}}_o) - F_{\text{cage}}^{(i)} r_p - F_{\text{drag}} r_p, \quad (3.20)$$

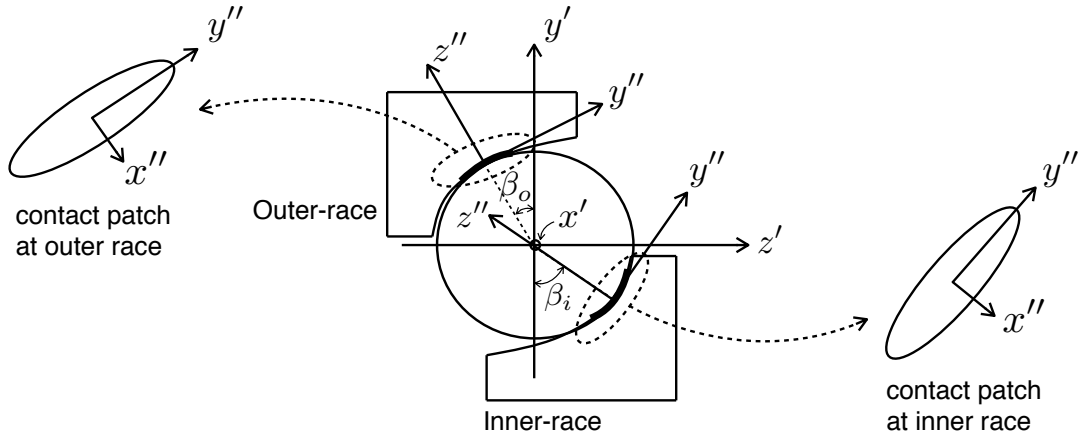


Figure 3.6: Coordinate system $(x''y''z'')$ used to formulate EHD lubrication model showing the contact-patch ellipses for inner-race and outer-race contacts.

where I_c is the moment of inertia of a rolling element about bearing axis ($= I + mr_p^2$), f is the friction force, and subscripts i and o represent the inner-race and the outer-race contacts respectively. Equations 3.16 and 3.20 define the complete motion of a rolling element inside a bearing. We solve these equations for each rolling element, along with the cage equation 3.17. In order to solve these equations, we need to know the traction forces acting between rolling elements and raceways.

3.2.3 EHD Lubrication Model to Determine Traction Forces

In this section we use an EHD lubrication model to calculate the friction forces (f_i, f_o) and moments ($M_{x'}, M_{y'}, M_{z'}$) required to solve equations 3.16 and 3.20. For the calculation, we introduce a new moving coordinate system $x''y''z''$ with x'' and y'' axes lying in the plane of the contact-patch and z'' axis parallel to the contact line (figure 3.6). Note that the coordinate system $x''y''z''$ is used for both the inner- and outer-race contacts, and care must be taken to use the correct contact angle (β_i for inner race and β_o for outer race).

Let us consider an elliptical contact patch between a rolling element and inner or outer raceway (figure 3.7). If we take a point $P(x'', y'')$ on this contact patch, then the shear stress (τ) in the Newtonian fluid film trapped between the two contacting solids can be described as

$$\tau(x'', y'') = \eta(x'', y'') \frac{\Delta u(x'', y'')}{h}, \quad (3.21)$$

where η is the lubricant viscosity, h is the film thickness, and Δu is the slip speed between

the two contacting surfaces.

Shear stress is the result of the lubricant film shearing, which also generates frictional heat (given by the product of the shear stress and strain rate). The rise in the lubricant temperature due to frictional heat changes its effective viscosity. The dependency of lubricant viscosity on pressure and temperature can be described by the Barus equation^[10]

$$\eta(x'', y'') = \eta_0 \exp [c_{\eta P} \sigma(x'', y'') - c_{\eta T} \{T(x'', y'') - T_R\}], \quad (3.22)$$

where η_0 is the lubricant viscosity at atmospheric pressure and reference temperature T_R , $c_{\eta P}$ and $c_{\eta T}$ are viscosity-pressure and viscosity-temperature coefficients respectively, T is the lubricant temperature, and σ is the contact pressure.

According to the Hertzian theory, the pressure distribution over an elliptical contact area has an ellipsoidal profile. However, the actual pressure distribution in an EHD contact is slightly different from the Hertzian pressure because of the relative motion of the contacting bodies and the hydrodynamic effects. Large differences in the pressure profile occur at entry and exit of the contact zone. A constriction is formed near the exit of the contact zone (figure 2.6), which results in a large pressure peak on the upstream side of this constriction. In the analysis described here, we ignore the changes in the pressure profile caused by the relative motion and hydrodynamic effects, and use the Hertzian theory to calculate it. Hertzian pressure distribution over an elliptical contact area is

$$\sigma = \sigma_{\max} \sqrt{1 - \left(\frac{x''}{b}\right)^2 - \left(\frac{y''}{a}\right)^2}, \quad (3.23)$$

where a and b are the dimensions of the elliptical contact patch given by

$$a = \left(\frac{6\kappa^2 \varepsilon F R}{\pi E'}\right)^{1/3} \quad (3.24a)$$

and

$$b = \left(\frac{6\varepsilon F R}{\pi \kappa E'}\right)^{1/3}. \quad (3.24b)$$

Maximum contact pressure σ_{\max} is given by

$$\sigma_{\max} = \frac{3F}{2\pi ab}. \quad (3.25)$$

Crook^[30,31] investigates the effect of temperature rise due to film shearing on the lubricant traction properties. The investigation was based on a Newtonian fluid model according to which the shear stress in a lubricant film is proportional to the shear-strain

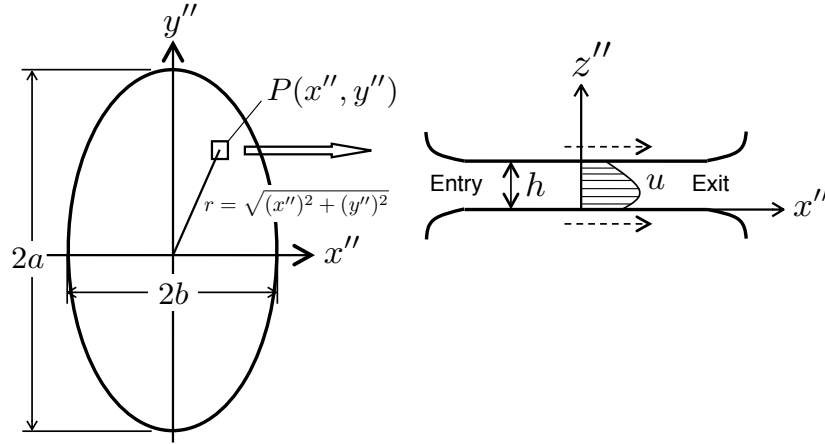


Figure 3.7: Elliptical contact patch and lubricant film inside the contact zone

rate. Using the Newtonian fluid assumption and equation 3.22, Crook derives a closed-form expression for the lubricant viscosity, which is given by

$$\eta(x'', y'') = \eta_0 \exp\{c_{\eta_P} \sigma(x'', y'')\} \frac{\ln(\sqrt{\psi+1} + \sqrt{\psi})}{\sqrt{\psi(\psi+1)}}, \quad (3.26)$$

where $\psi = \eta_0 \exp\{c_{\eta_P} \sigma(x'', y'')\} c_{\eta_T} \Delta u^2 / (8K_c)$ and K_c is the lubricant thermal conductivity (see Crook^[30] for the derivation).

In the traction equation 3.21, we assume that the film thickness (h) between the contacting surfaces is constant throughout the contact patch, and is calculated using the central film-thickness formula provided by Hamrock and Dowson^[50]

$$h = 2.69 \hat{U}^{0.67} \hat{G}^{0.53} \hat{W}^{-0.067} (1 - 0.61 \exp(-0.73\kappa)) R_{x''}, \quad (3.27)$$

where $\hat{U} (= \frac{\eta_0 u_{\text{ent}}}{E' R_{x''}})$, $\hat{G} (= E' c_{\eta_P})$, and $\hat{W} (= \frac{F}{E' R_{x''}^2})$ are the dimensionless parameters for speed, material and load respectively, $u_{\text{ent}} = r_i r_o \omega_i / (r_i + r_o)$ and ω_i is the inner-race speed.

In order to determine the traction forces acting on the contact patches, we must first calculate sliding and spin speeds at the inner and the outer contact interfaces. The sliding velocities at the centres of the inner and the outer contact-patches due to translational speed-differential are

$$\Delta \underline{u}_i^l = \{r(\omega_{y'} \sin \beta_i + \omega_{z'} \cos \beta_i) + r_i(\omega_i - \omega_c)\} \underline{i}' - r\omega_{x'} \sin \beta_i \underline{j}' - r\omega_{x'} \cos \beta_i \underline{k}' \quad (3.28a)$$

and

$$\Delta \underline{u}_o^l = \{r(\omega_{y'} \sin \beta_o + \omega_{z'} \cos \beta_o) + r_o \omega_c\} \underline{i}' + r\omega_{x'} \sin \beta_o \underline{j}' + r\omega_{x'} \cos \beta_o \underline{k}'. \quad (3.28b)$$

The spin velocities caused by the rotational speed-differential are

$$\underline{\omega}_i^s = (\omega_{y'} \cos \beta_i - \omega_{z'} \sin \beta_i) \underline{k}'' \quad (3.29a)$$

and

$$\underline{\omega}_o^s = (\omega_{y'} \cos \beta_o - \omega_{z'} \sin \beta_o) \underline{k}'' \quad (3.29b)$$

Let us now determine the expression for the slip velocity at point P (figure 3.7). Spin velocity at the contact interface results in slip at point $P(x'', y'')$ along both x'' and y'' directions. These slip speeds are $-\omega^s y''$ along x'' axis and $\omega^s x''$ along y'' axis. Combining these slip speeds along with the sliding velocities of equations 3.28 gives the resultant slip velocity at point P as

$$\Delta \underline{u}_{i/o}(x'', y'') = \Delta \underline{u}_{i/o}^l - \omega_{i/o}^s y'' \underline{i}'' + \omega_{i/o}^s x'' \underline{j}'' \quad (3.30)$$

By this point we have calculated all the parameters required to solve equation 3.21: viscosity in equation 3.26; film thickness in equation 3.27; and slip speed in equation 3.30.

For a contact patch shown in figure 3.7, the resultant traction force ($\underline{f}_{i/o} = f_{i/o}^{x''} \underline{i}'' + f_{i/o}^{y''} \underline{j}'' + f_{i/o}^{z''} \underline{k}''$) and the traction moment ($\underline{M}_{i/o} = M_{i/o}^s \underline{k}''$) can be calculated by integrating equation 3.21. Therefore,

$$\underline{f}_{i/o} = -\frac{1}{h_{i/o}} \int_{-a}^a \int_{-b}^b \eta_{i/o}(x'', y'') \Delta \underline{u}_{i/o}(x'', y'') dx'' dy'' \quad (3.31a)$$

and

$$\underline{M}_{i/o} = -\frac{1}{h_{i/o}} \int_{-a}^a \int_{-b}^b \eta_{i/o}(x'', y'') (x'' \underline{i}'' + y'' \underline{j}'') \Delta \underline{u}_{i/o}(x'', y'') dx'' dy'' \quad (3.31b)$$

Finally, we can calculate the friction moment terms of equation 3.16 from the traction forces and moments defined in equations 3.31 as

$$M_{x'} = r \left(f_o^{y''} - f_o^{y''} \right), \quad (3.32a)$$

$$M_{y'} = r \left(f_o^{x''} \sin \beta_o - f_i^{x''} \sin \beta_i \right) + M_i^s \cos \beta_i + M_o^s \cos \beta_o, \quad (3.32b)$$

$$M_{z'} = r \left(f_o^{x''} \cos \beta_o - f_i^{x''} \cos \beta_i \right) - M_i^s \sin \beta_i - M_o^s \sin \beta_o. \quad (3.32c)$$

Substitution of equations 3.31 and 3.32 into equations 3.16 and 3.20 gives us the four

Table 3.1: Bearing properties used by Pasdari and Gentle^[99] in their skidding tests

Parameter	Value
Number of rolling elements (z)	11
Contact angle (β)	25°
Ball radius (r)	6.745 mm
Pitch radius (r_p)	28.3 mm
Ball mass (m)	10 grams
Raceway curvature radius ($\mathcal{R}_{i/o}$)	7.05 mm
Material	Steel

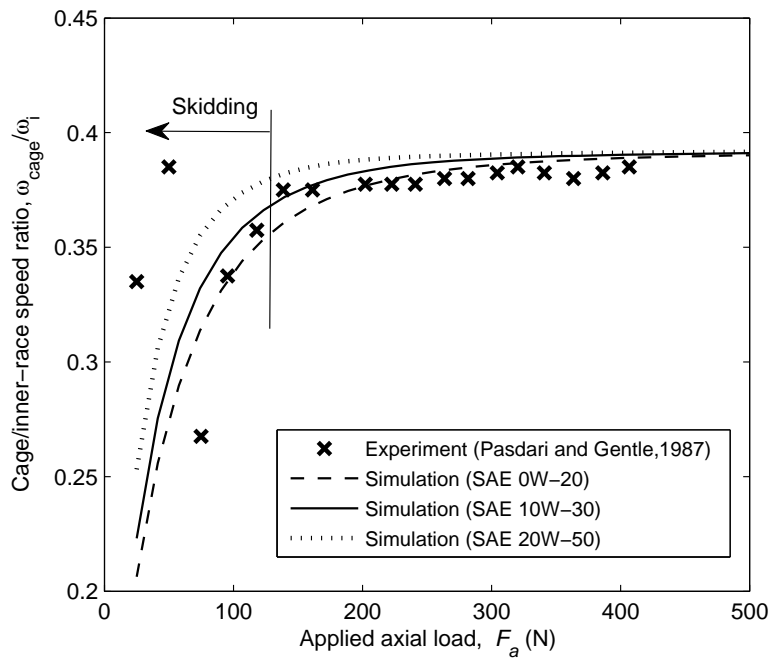
first-order nonlinear differential equations, which we solve numerically along with the cage equation 3.17 using a Runge-Kutta solver.

Although the dynamic model formulation described in this section is developed for an EHD lubrication regime, it is also valid for any other lubrication regime, e.g. mixed lubrication. We just have to change the traction model and all the equations of motion remain unchanged.

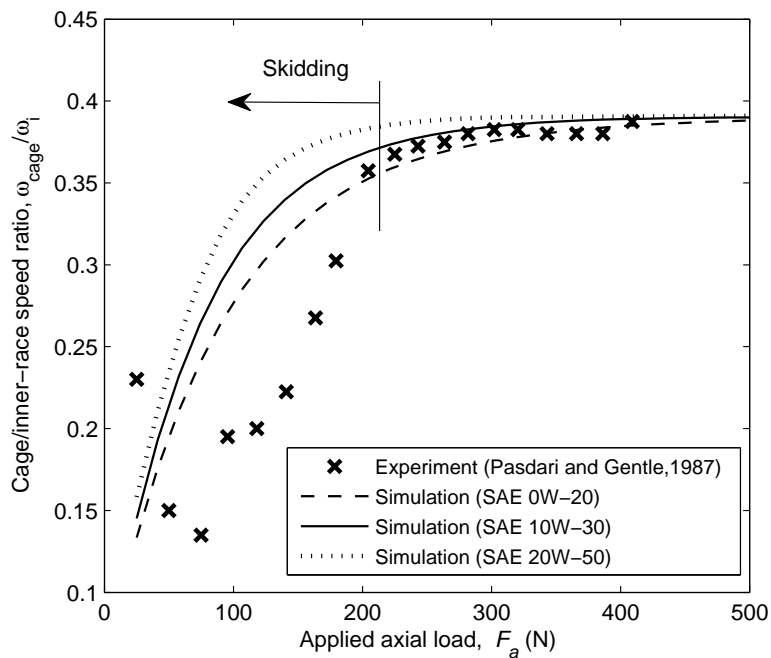
3.3 Skidding Under Constant Axial Loads and Constant Speeds

The first case we consider is skidding under constant axial loads and constant speeds. Before we discuss the underlying skidding mechanism for this case, let us first validate the numerical model described in section 3.2. Figure 3.8 shows the variation in the cage/inner-race speed ratio (ω_{cage}/ω_i) with the applied axial load. It can be observed that at low values of the applied load, the actual speed ratio is less than its corresponding theoretical value; and the difference increases as we reduce the applied load. This difference between the actual and the theoretical speed ratios means that the cage is rotating slower than what is required for pure-rolling motion, which results in skidding. The experimental data is taken from Pasdari and Gentle^[99]. The geometrical properties of the bearing used by Pasdari and Gentle are listed in table 3.1, and the lubricant used by them during skidding tests was a multi-grade motor oil. They do not provide the exact composition of the lubricant. Therefore, we carry out the analysis for three multi-grade motor oils (SAE 0W-20, SAE 10W-30 and SAE 20W-50). Simulation results are mostly in agreement with the experimental data.

In figure 3.8, as we decrease the applied load to a very low value the simulation



(a) Inner-race speed $\omega_i = 2000$ rpm



(b) Inner-race speed $\omega_i = 4000$ rpm

Figure 3.8: Comparison of simulation results with the experimental data published by Pasdari and Gentle^[99] under constant axial load and constant speed

Table 3.2: Geometrical properties of a typical wind-turbine high-speed bearing

Parameter	Value
Number of rolling elements (z)	16
Contact angle (β)	40°
Ball radius (r)	12.5 mm
Pitch radius (r_p)	77.5 mm
Ball mass (m)	64 grams
Raceway curvature radius ($\mathcal{R}_{i/o}$)	13.125 mm
Material	Steel

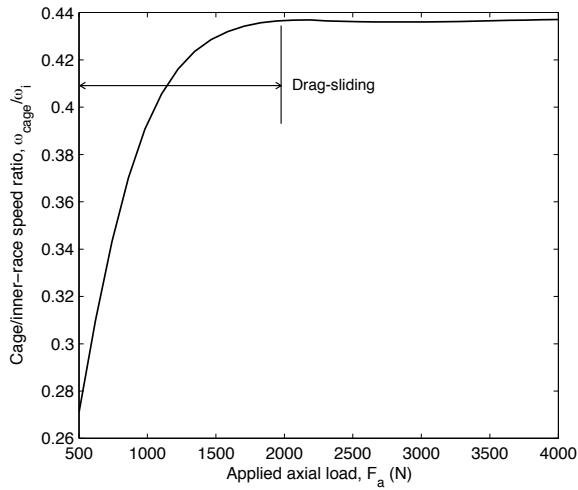
Table 3.3: Lubricant parameters

Parameter	Value
Dynamic viscosity (η_0)	0.05 Pa.s
Reference temperature (T_R)	30°C
Viscosity-Pressure coefficient (c_{η_P})	$1.2 \times 10^{-8} \text{ Pa}^{-1}$
Viscosity-Temperature coefficient (c_{η_T})	0.04°C^{-1}
Thermal conductivity (K_c)	0.125 J/(kgK)
Density (ρ)	890 kg/m ³

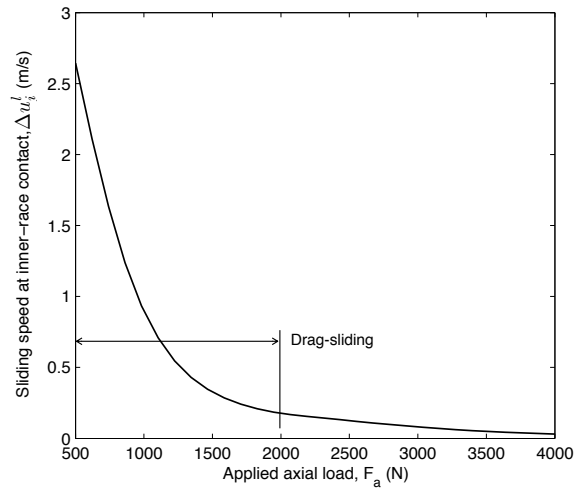
results start to deviate from the experimental data. There can be many reasons behind this deviation. One possible reason can be the nonlinear behaviour of lubricant film. The maximum shear stress over the contact patch varies from 3 to 9 MPa for the given range of applied loads. These values of shear stress are slightly above the Eyring stress. Therefore, lubricant might behave nonlinearly; and the linear EHD model used in the current analysis might not be adequate. Another possible reason can be the effect of cage-clearance on the cage and the rolling-element motion. This is particularly important at low loads as cage becomes unstable^[41]. This will also explain scatter in the measured data at low loads. But our main interest here is to determine the minimum load required to avoid skidding, and the numerical simulations are able to determine this value quite accurately.

3.3.1 Mechanism of Skidding Under Constant Axial Loads and Constant Speeds

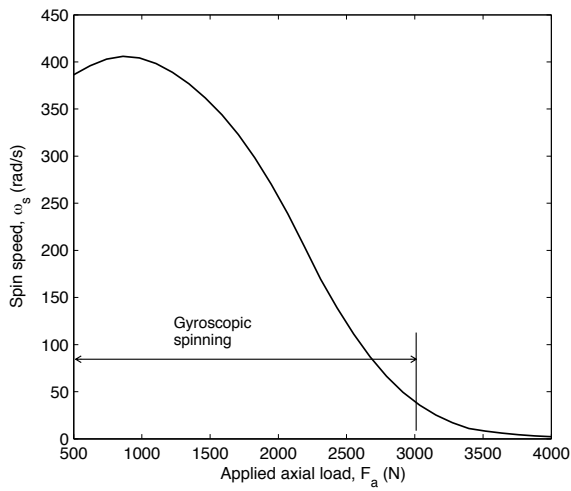
All the results presented in this chapter hereafter are for an example with the bearing and the lubricant parameters listed in tables 3.2 and 3.3. Skidding mechanism under constant



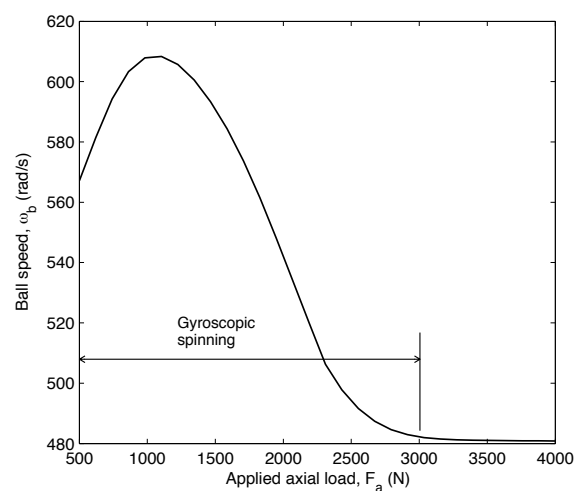
(a) Variation of cage/inner-race speed ratio with the applied axial load



(b) Sliding speed at the centre of the inner contact patch (Δu_i^t)



(c) Spin speed (ω_s) variation with applied load



(d) Variation in the rotational speed of a ball (ω_b) with the applied load

Figure 3.9: Simulation results for a bearing operating under constant axial loads and a constant speed of $\omega_i = 1500$ rpm

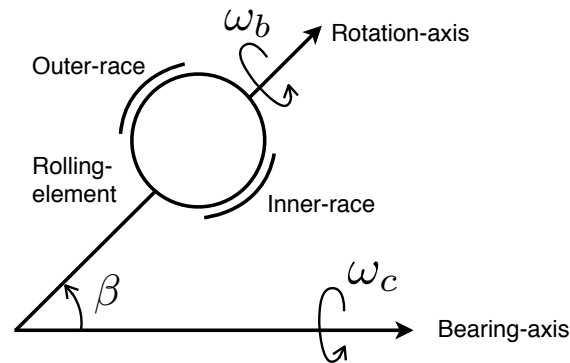


Figure 3.10: Axes governing the motion of a rolling element

axial loads and constant speeds can be divided into two types.

1. *Drag-Sliding.* This occurs when the applied load is not enough to generate traction forces required to overcome the viscous drag acting on a rolling element. Figure 3.9a shows the variation in the cage/inner-race speed ratio with the applied load. At low loads, the traction forces at the contact interfaces are not enough to overcome the drag force, hence the cage speed decreases. Since the drag force is proportional to the square of the cage speed (equation 3.19), a decrease in the cage speed results in the drag force reduction. This reduced drag force is balanced by the traction forces. Decrease in the cage speed from the theoretical speed required for pure-rolling motion results in gross sliding at the contact interfaces (figure 3.9b). As we increase the applied load, the cage speed approaches its theoretical value and the sliding speed decreases. The sliding speed in figure 3.9b approaches zero asymptotically and never actually becomes zero. This is for the reason that in order to generate traction forces, some amount of relative slip is required between the contacting bodies.
2. *Gyroscopic-Spinning.* In an angular contact ball bearing, a rolling element spins about an axis (rotation axis in figure 3.10) passing through its centre at an angle β from the bearing axis. This spinning rolling-element is also forced to rotate about the bearing axis. As the rolling element rotates around the bearing axis, the direction of its angular momentum changes continuously. This change in angular momentum generates a gyroscopic torque which is balanced by the traction forces acting at the contact interfaces. At low loads, traction forces are not enough to provide the required gyroscopic torque and rotation axis of the rolling element changes its orientation and becomes almost parallel to the bearing axis, thereby reducing the required gyroscopic torque (figure 3.11). Rotational speed of the rolling element (ω_b)

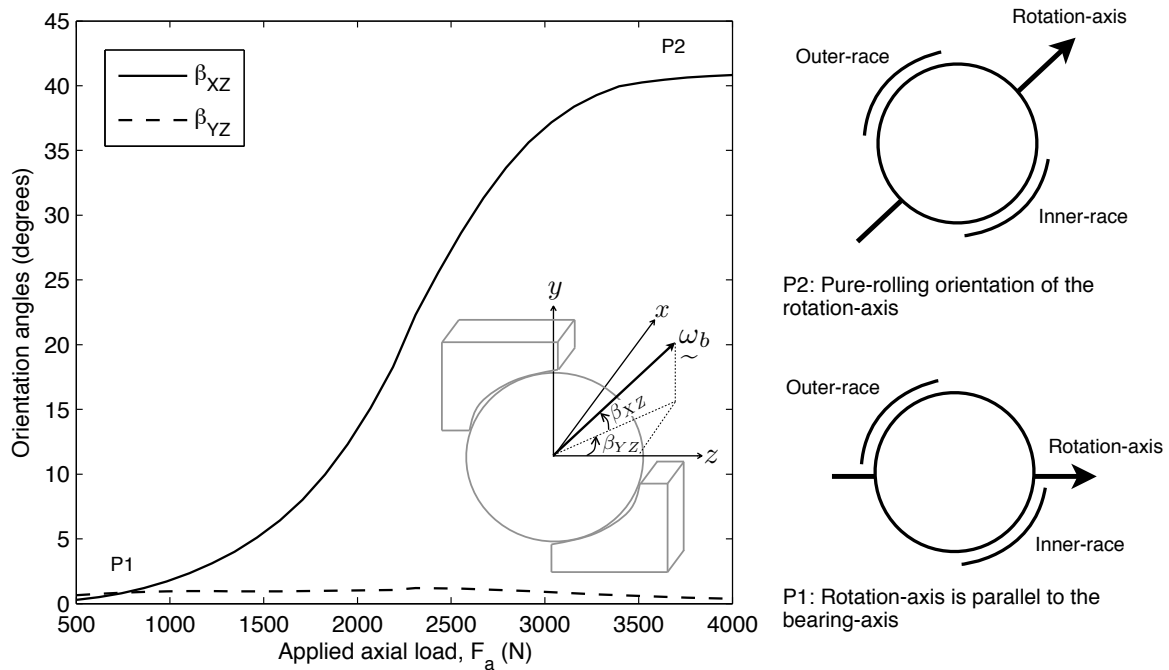


Figure 3.11: Variation in the ball orientation angles with the applied load in a bearing operating under constant axial loads and constant speed of 1500 rpm. Orientation of the rotation axis of a rolling element at low and at high loads (P₁ and P₂) are also shown.

also increases to eliminate the translational speed differential between the rolling element and the raceways (figure 3.9d). However, the low-load orientation (P₁ in figure 3.11) of the rotation axis causes the rolling element to spin on the raceways, which results in skidding (figure 3.9c). As we increase the applied load, the traction forces increase as well, and the rotation axis of the rolling element approaches its theoretical pure-rolling orientation (P₂ in figure 3.11), thereby reducing the spin speed and skidding.

From the above discussion we can conclude that an axial load applied on a thrust bearing must be able to overcome the drag force as well as it must be able to provide the required gyroscopic torque to avoid skidding.

3.3.2 Derivation of Skidding Criterion for Constant Axial Loads and Constant Speeds

In the previous section we observe that for any given rotational speed a minimum load is required to prevent skidding. In this section, we derive a simple expression to calculate this minimum load without having to run the full numerical model of section 3.2. The

derivation is based on the two assumptions.

1. Contact forces between a rolling element and inner and outer raceways are same, i.e., $F_i = F_o (= F_e)$; where $F_e = F_a/(z\sin\beta)$.
2. Contact angles at the inner and the outer contact interfaces are same, i.e., $\beta_i = \beta_o (= \beta)$.

If the friction coefficient between a rolling element and raceways is μ_e then the maximum friction force at the contact interfaces would be $\mu_e F_e$, and the maximum friction moment acting on the rolling element to provide the gyroscopic torque will be $2r\mu_e F_e$. In order to avoid gyroscopic-spinning, this friction moment must be able to provide the required gyroscopic torque. Therefore,

$$\begin{aligned} 2r\mu_e F_e &\geq |I\omega_c \times \omega_b| \\ &\geq |I\omega_c \omega_b \sin\beta|. \end{aligned} \quad (3.33)$$

Substitution of $\omega_c = \omega_c^{\text{th}} = \left(1 - \frac{\cos\beta}{r_p/r}\right) \frac{\omega_i}{2}$, $\omega_b = -\omega_b^{\text{th}} = -\left(\frac{r_p}{r} - \frac{\cos^2\beta}{r_p/r}\right) \frac{\omega_i}{2}$, $F_e = F_a/(z\sin\beta)$ and $I = \frac{2}{5}mr^2$ into equation 3.33 gives

$$F_a \geq \frac{zmr_p\omega_i^2}{20\mu_e} \left(1 - \frac{\cos\beta}{r_p/r}\right)^2 \left(1 + \frac{\cos\beta}{r_p/r}\right) \sin^2\beta. \quad (3.34)$$

ω_c^{th} and ω_b^{th} mentioned above are the theoretical values of cage and ball speeds.

The friction forces at the contact interfaces must also be able to balance the drag force in order to avoid drag-sliding. Hence,

$$2\mu_e F_e \geq F_{\text{drag}}. \quad (3.35)$$

Since $F_e = F_a/(z\sin\beta)$, and substituting F_{drag} from equation 3.19 into 3.35 yields

$$F_a \geq \frac{\pi C_D \rho (\omega_c^{\text{th}} r_p)^2 r^2}{4\mu_e} z \sin\beta. \quad (3.36)$$

To calculate the minimum load from equations 3.34 and 3.36, we require the value of the friction coefficient μ_e . Figure 3.12 shows the variation of the friction coefficient with slip speed calculated using the EHD lubrication model (described in section 3.2.3). Initially the friction coefficient increases with slip; but as we increase the slip speed beyond a certain value (Δu_{peak}), the friction coefficient starts to decrease due to the reduction in viscosity caused by shear heating. Peak value of the friction coefficient (μ_{peak}) will

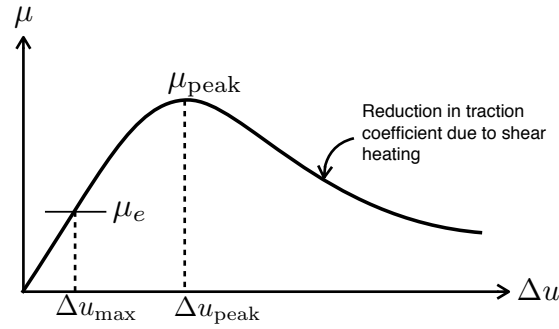


Figure 3.12: Variation in traction coefficient with slip speed

give us the maximum available friction force. If this friction force is not able to satisfy the drag-sliding and the gyroscopic-spinning conditions, the rolling elements will skid. So, one option is to use this peak value (μ_{peak}) as μ_e ; but the slip speed corresponding to the peak value of the traction curve (Δu_{peak} in figure 3.12) could be larger than the maximum permissible slip, which will not fulfill our aim of avoiding skidding. To overcome this problem, we define a maximum permissible slip speed Δu_{max} and use the friction coefficient at this slip speed as μ_e (figure 3.12). Therefore, following from equation 3.31a,

$$\mu_e = \frac{|\underline{f}(\Delta u_{\text{max}})|}{F_e} = \frac{\Delta u_{\text{max}}}{hF_e} \int_{-a}^a \int_{-b}^b \eta(x'', y'') dx'' dy''. \quad (3.37)$$

Here $\eta(x'', y'')$, defined by equation 3.26, is a function of F_e .

To derive equation 3.37 from 3.31a, we make some simplifications: first, we assume that the slip speed over the contact patch is constant, $\Delta u(x'', y'') = \Delta u_{\text{max}}$ for all x'' and y'' ; second, we assume that the film thickness and viscosity at outer contact is same as inner contact, $h_o = h_i (= h)$ and $\eta_o = \eta_i (= \eta)$. For the results presented in this section we use 1% of rolling speed as the maximum permissible slip, $\Delta u_{\text{max}} = 0.01r\omega_b$. Substituting equation 3.37 into 3.34 and 3.36 give the following two conditions.

$$\int_{-a}^a \int_{-b}^b \eta(x'', y'') dx'' dy'' \geq \frac{\pi h C_D \rho (\omega_c^{\text{th}} r_p)^2 r^2}{4 \Delta u_{\text{max}}} \quad (\text{condition to avoid drag-sliding}) \quad (3.38a)$$

and

$$\int_{-a}^a \int_{-b}^b \eta(x'', y'') dx'' dy'' \geq \frac{G_0 h}{\Delta u_{\text{max}}} \quad (\text{condition to avoid gyroscopic-spinning}). \quad (3.38b)$$

Here $G_0 = \frac{mr_p\omega_i^2}{20} \left(1 - \frac{\cos\beta}{r_p/r}\right)^2 \left(1 + \frac{\cos\beta}{r_p/r}\right) \sin\beta$. In equations 3.38, $\eta(x'', y'')$, a , b and h are functions of the applied load F_a . We solve equations 3.38 numerically to get the values of the minimum applied loads. Equation 3.38a represents the criterion to avoid drag-sliding, and equation 3.38b represents the criterion to avoid gyroscopic-spinning.

Figures 3.13a and 3.13b show the contour plots of the sliding (Δu_i^l) and the spin (ω_i^s) speeds at the inner-race contact. Darker regions in the plots represent sliding/spinning while the white regions represent no-sliding/no-spinning. It is clear from the plots that skidding occurs at low loads and high speeds. Minimum loads required to avoid drag-sliding and gyroscopic-spinning, obtained from equations 3.38, are also plotted on top of the numerical results (thick black lines). Clearly, the skidding criteria defined by equations 3.38 are successfully able to identify the regions with skidding. Figure 3.13c shows a skidding map with different regimes of skidding. In order to avoid the skidding damage, a bearing must operate in the no-skidding zone of the map.

Using equations 3.38, we can quickly generate the skidding map (like the one shown in figure 3.13c) for any bearing without having to run the time-consuming full numerical model. According to the map shown in figure 3.13c, load required to prevent drag-sliding is always smaller than the load required to prevent gyroscopic-spinning. But, this might not always be the case. Depending on the bearing geometry, it is possible to have a case in which load required to prevent drag-sliding is more than the load required to prevent gyroscopic-spinning (see appendix A).

Now, let us compare the proposed skidding criterion (equations 3.38) with the following conventional criteria found in the literature.

1. Hirano's^[59] criterion to avoid skidding in ball bearings under axial load,

$$F_a \geq \frac{zF_c}{0.1}. \quad (3.39)$$

2. Kliman's^[79] criterion to avoid skidding in ball bearings under axial load,

$$F_a \geq zF_c \tan\beta. \quad (3.40)$$

Figures 3.13a and 3.13b show the minimum load predicted by the three skidding criteria (Hirano, Kliman and the one proposed here) along with the numerical simulations results. Skidding zones predicted by the new proposed criteria are better than the Hirano's and Kliman's criteria for both the drag-sliding and the gyroscopic-spinning regimes. Another advantage of the proposed criteria over Hirano and Kliman is its dependency over the lubricant traction properties. Figure 3.14 shows the skidding behaviour of the exam-

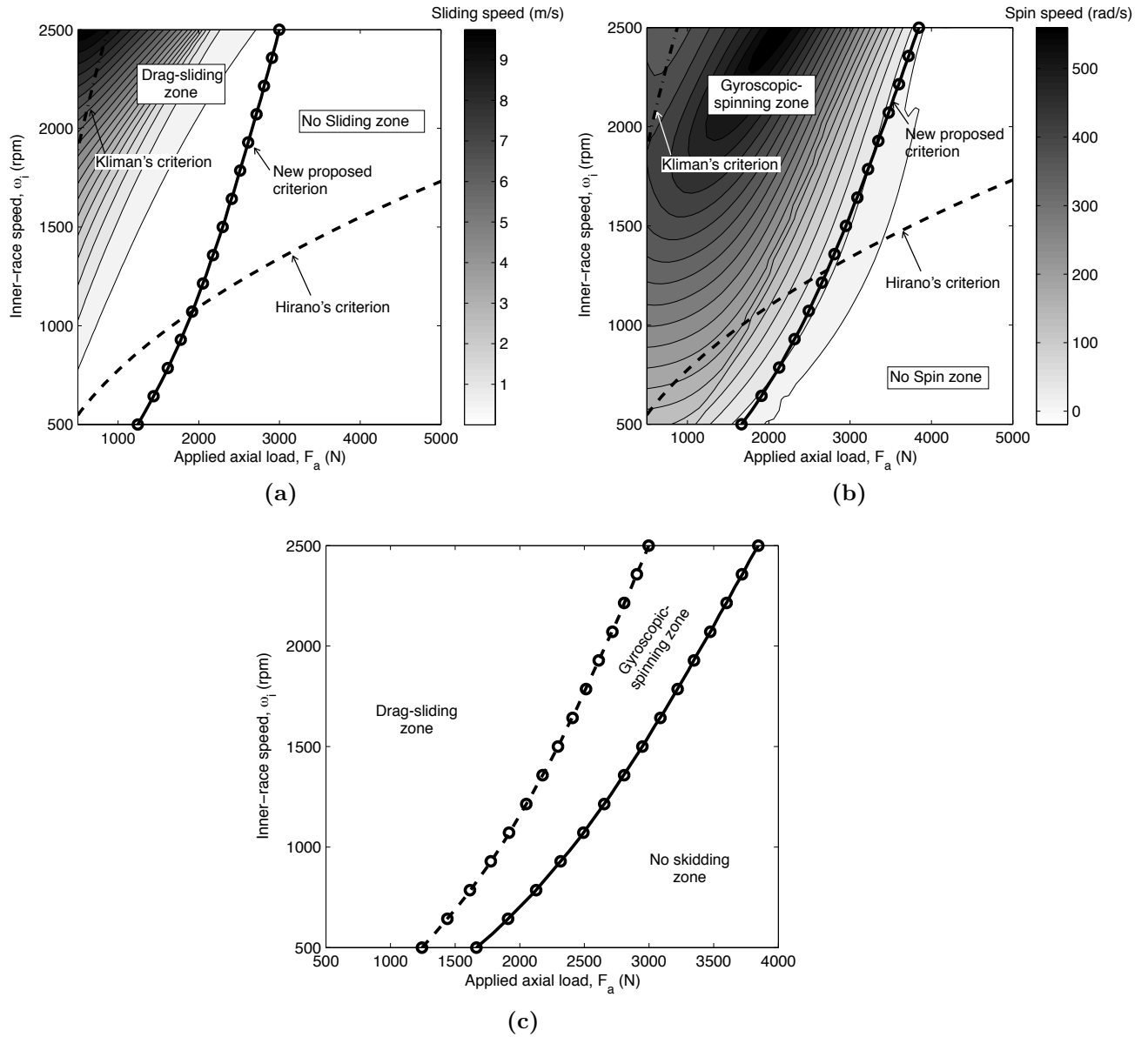


Figure 3.13: (a) Contour plot showing variation in sliding speed (m/s) at inner-race contact (Δu_i^A) with applied axial load and inner-race speed, along with the Kliman's criterion (equation 3.40), Hirano's criterion (equation 3.39) and new proposed drag-sliding criterion (equation 3.38a) (b) Contour plot showing variation in spin speed (rad/s) at inner-race contact (ω_s^A) with applied axial load and inner-race speed along with proposed gyroscopic-slip criterion (equation 3.38b) (c) Skidding map for axially loaded bearing showing different regimes of skidding

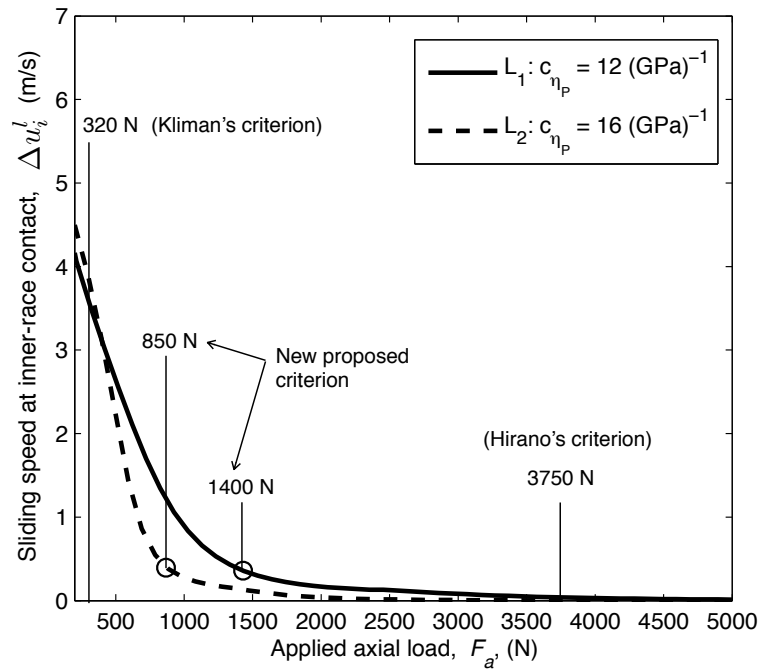


Figure 3.14: Slip speed variation with axial load for two lubricants (L_1 and L_2) with different viscosity-pressure coefficients; remaining properties of both lubricants are same (table 3.3). Skidding criteria predicted by Hirano and Kliman along with the new proposed method are shown.

ple bearing with two lubricants having different viscosity-pressure coefficients. Since the criteria provided by Hirano and Kliman do not take into account lubricant traction behaviour, they predict the same minimum load for both cases; while the skidding criterion proposed here predicts different minimum load for each case and the predicted loads are close to the minimum loads required to avoid skidding for the slip-curves calculated using the numerical simulations.

3.4 Skidding Under Combined Axial and Radial Loads

In the presence of both axial and radial loads, a load zone is formed inside a bearing and the contact force is not uniformly distributed among the rolling elements. The rolling elements lying inside this load zone are loaded while those outside are unloaded. Due to the formation of this load zone, motion of a rolling element and its skidding behaviour are different from what we observed in the previous section where load was uniformly distributed on the rolling elements.

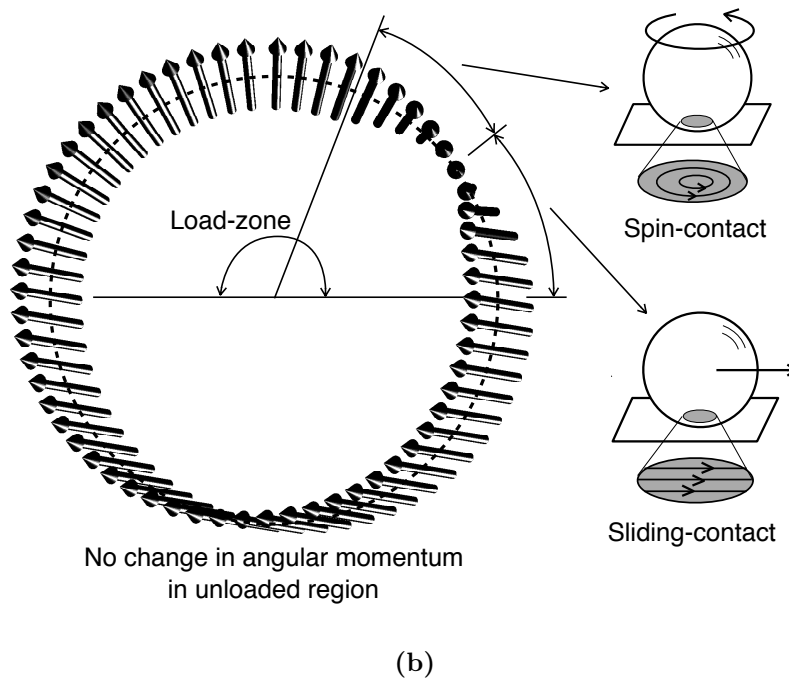
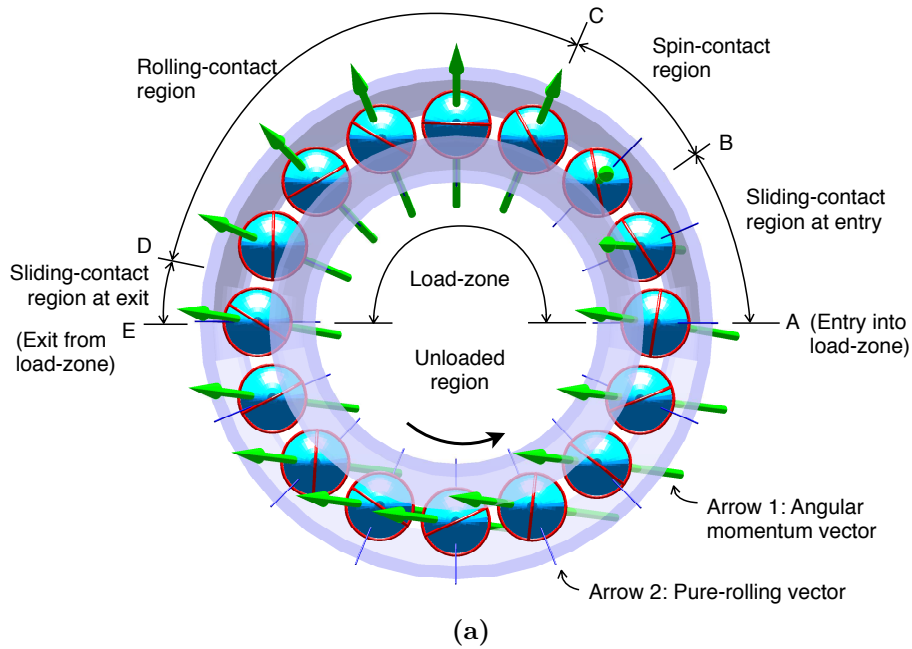


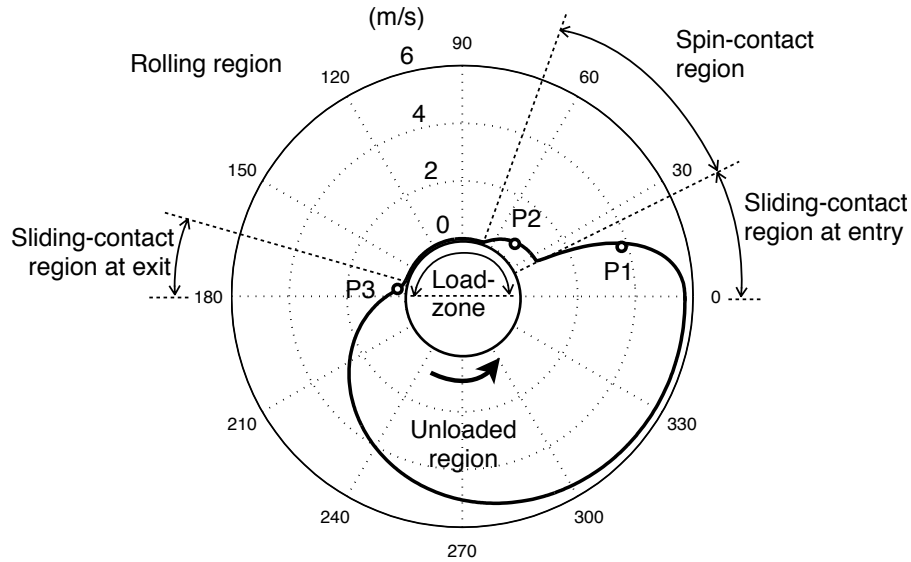
Figure 3.15: (a) Graphical representation of rolling-element motion under combined loading condition and formation of five regions; (b) Variation in the angular-momentum vector of a rolling element with its angular position

3.4.1 Mechanism of Skidding Under Combined Loads

To explain the skidding mechanism under combined loading conditions, we take an example where the bearing of table 3.2 is operating under an axial load of 4.3 kN and a radial load of 4 kN. The maximum contact force on a rolling element is 1300 N and the size of the load zone is 180° ; rotational speed of the inner race is 1500 rpm.

Figure 3.15 shows the motion of a rolling element during one complete rotation. Arrow 1 (figure 3.15a) represents the actual angular momentum of a rolling element or its instantaneous rotation-axis and arrow 2 is the “pure-rolling” vector which represents the motion of a rolling element without any skidding. If arrow 1 is aligned with arrow 2 then skidding does not take place. Motion of the rolling element can be divided into following five regions.

1. *Sliding-contact region at entry* (A to B). When a rolling element enters the load zone, its rotation-axis (arrow 1) is not aligned with the pure-rolling vector (arrow 2) which results in gross slip between the rolling element and the raceways. This gross slip is primarily caused by the translational speed differential between the contacting bodies (rolling element and raceways). Therefore, we call this region sliding-contact at entry (point A to B in figure 3.15). Figure 3.16a shows the variation of the maximum slip speed at the inner contact patch (Δu_i) with the orbital position of a rolling element. A high value of slip speed can be observed in the sliding-contact region at entry. By looking at the sliding velocity distribution over the contact patch between the rolling element and the inner race (figure 3.16b), it is clear that the sliding velocity is nearly constant in both the direction and the magnitude throughout the contact patch - which shows the existence of the translational speed differential between the contacting surfaces. As the rolling element moves further into the load zone, friction torque acting on it starts to increase and its rotation axis begins to align itself with the bearing axis. At point B (end of the sliding-contact region) the rotation axis becomes parallel to the bearing axis. The rotational speed of the rolling element (ω_b) also starts to increase from its theoretical value (ω_b^{th}) and at point B it becomes ω'_b ($\approx \omega_b^{\text{th}}/\cos\beta$) (see figure 3.17) which is the speed required to eliminate the translational speed differential between the rolling element and the raceways. Translational-sliding does not take place beyond this point.
2. *Spin-contact region* (B to C). At point B, the rotation axis of the rolling element is parallel to the bearing axis, which produces a spin component of the rotational speed along the contact line (z'' axis in figure 3.6). The magnitude of this spin speed is $\omega'_b \sin\beta$ (at point B). The rolling element spins between points B and C



(a) Maximum slip speed

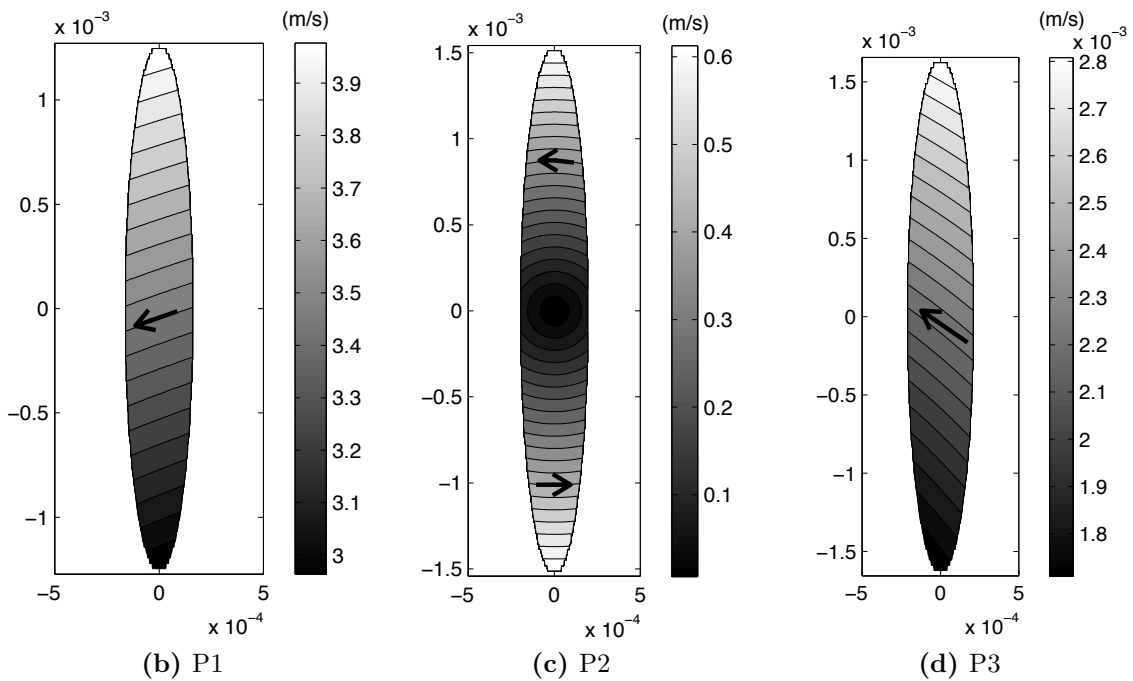


Figure 3.16: (a) Variation in the maximum slip speed at the inner-race contact with the orbital position of a rolling element; (b),(c),(d) Slip speed distributions on the inner contact patches at three orbital positions P1, P2 and P3; $F_a = 4.3$ kN, $F_r = 4$ kN, $\omega_i = 1500$ rpm

on the inner and the outer contact patches, which results in gross slip. Therefore, we call this region spin-contact region as slip is caused by relative spinning of the contacting surfaces rather than the translational speed differential. Figure 3.16c shows the distribution of the slip velocity over the inner contact patch. A circular pattern of the slip lines clearly shows the existence of the relative spinning between the contacting surfaces and absence of any translational speed differential. As the rolling element moves from point B to C, the rotation-axis starts to rotate towards the pure-rolling vector (arrow 2) in the radial plane ($y'z'$) and the slip speed starts to decrease (figure 3.16a). At point C, the rotation-axis aligns itself with the pure-rolling vector, and neither translational sliding nor spinning takes place beyond this point. The magnitude of the maximum slip speed at the contact patch in this region is less than that at the sliding-contact region at entry but significantly more than the rolling-contact region.

3. *Rolling-contact region (C to D)*. In this region, no gross slip takes place between the rolling elements and the raceways. Although some slippage is needed between the contacting surfaces to generate the required traction forces, but the magnitude of such slip speed is much less than what we observe in the previous two skidding regions (figure 3.16a). The rotation-axis is aligned with the pure-rolling vector throughout this region.
4. *Sliding-contact region at exit (D to E)*. At point D, the contact force acting on the rolling element is just enough to provide frictional torque required for rolling without skidding. As the rolling element moves beyond this point towards E (load-zone exit), the contact force decreases and the frictional torque is no longer able to provide the gyroscopic torque required for pure-rolling motion. This results in gross slip. Since this slip occurs when the rolling element is about to leave the load zone, we call this region sliding-contact region at exit. Figure 3.16d shows the distribution of slip velocity over the inner contact patch. The distribution is similar to what we observed during the sliding-contact at entry, and shows the existence of translational speed differential.
5. *Unloaded region (E to A)*. In this region, there is no contact force acting on the rolling element. Therefore, in the absence of any frictional torque, angular momentum of the rolling element remains constant throughout this region (figure 3.15b). Since arrow 2 is not aligned with arrow 1, high gross slip occurs at the contact interfaces (figure 3.16a). However, damage caused by this slippage in the absence of any contact force is negligible compared to the skidding damage inside the load zone.

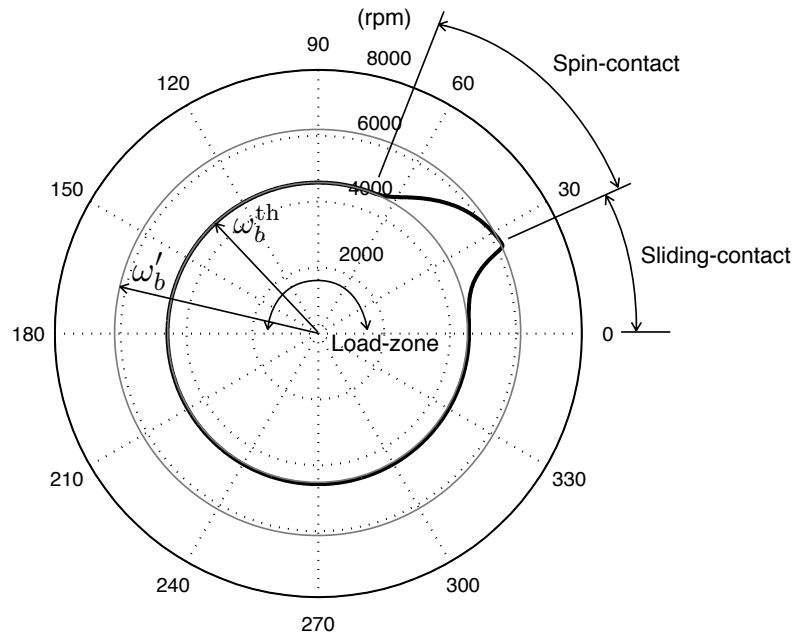


Figure 3.17: Variation in the rotational speed of a rolling element with orbital position of a rolling element under combined loading condition; $F_a = 4.3$ kN, $F_r = 4$ kN, $\omega_i = 1500$ rpm

We observe that the skidding mechanism under combined loading condition is different from the skidding under pure axial loads. For the case of a bearing operating under axial loads, if the load is less than a minimum required value then the rolling elements skid all through their orbital motion uniformly. On the other hand, skidding pattern changes with the location of a rolling element inside the bearing operating under the combined loading conditions. Sliding-contact and spin-contact regions are the two critical zones where substantial damage to the rolling elements and raceways can take place. Therefore, it is important for a bearing designer to know their size for a given set of loads and bearing geometry.

3.4.2 A Simple Analytical Method to Determine the Extent of the Skidding Region Inside the Load Zone

In the previous section we have investigated bearing skidding under combined axial and radial loads. The maximum skidding occurs within the two regions formed inside the load zone: (i) sliding-contact region at entry, and (ii) spin-contact region. We calculate the extents of these regions using the full numerical model of section 3.2, which is time

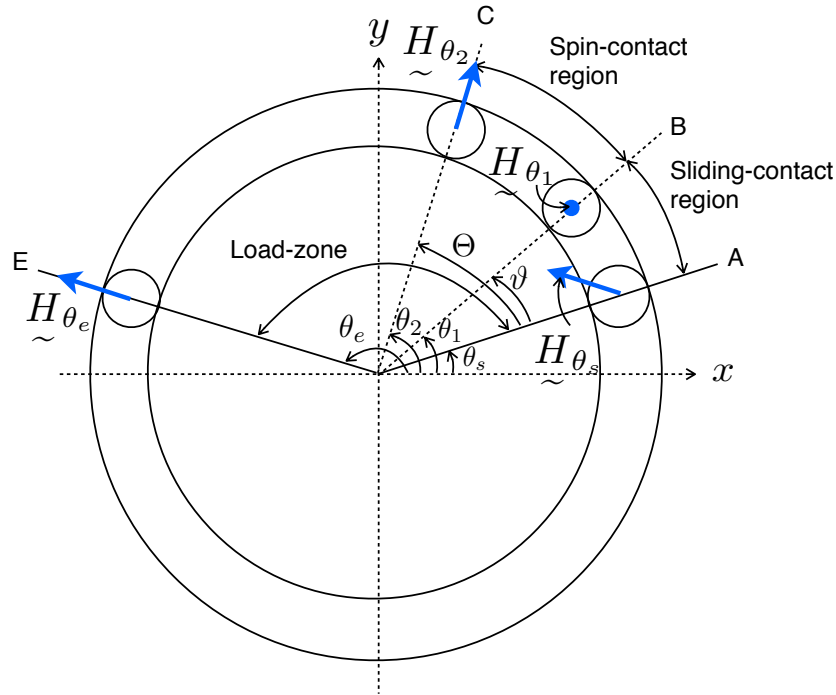


Figure 3.18: Angular momentum of a rolling element at the boundaries of different skidding regions inside load zone

consuming. In this section we derive a simple analytical method to calculate the length* of sliding-contact and spin-contact regions for a given bearing geometry and applied load and speed. The approach is based on Newton's second law of motion. We know the angular momentum of a rolling element at the boundaries of different skidding regions inside a load zone (figures 3.18 and 3.19), but we do not know quantitatively how this angular momentum changes inside these skidding regions. Therefore, according to Newton's second law of motion, we calculate the change in the angular momentum caused by a skidding region and we equate it to the impulse due to friction moment acting on a rolling element in that skidding region. This gives us the extent of the skidding region.

3.4.2.1 Extent of the Sliding-Contact Region at Entry

Figure 3.18 shows the sliding-contact and the spin-contact regions represented by the angles θ_1 and θ_2 respectively. Let us first consider the sliding-contact region. In the previous section we have observed when a rolling element passes through an unloaded region, its angular momentum remains unchanged because of the absence of any contact force. Therefore, the angular momentum of a rolling element when it enters the load zone

*'length' suggests a distance in metres, but the calculated 'extent' is in radians. We will use the terms 'extent' and 'length' interchangeably.






Region	Angular momentum vector	Moment
E		zero, hence angular momentum is conserved
A		moment due to sliding and spinning
B		moment due to spinning
C		rolling moment (no slip)
E		

Figure 3.19: State of moment acting on a rolling element in different skidding regions. Directions of angular-momentum vectors are consistent with figure 3.18.

at point A (\underline{H}_{θ_s}) is approximately equal to the angular momentum at the point of exit from the load zone, point E (\underline{H}_{θ_e}). This gives

$$\underline{H}_{\theta_s} = \underline{H}_{\theta_e}, \quad (3.41)$$

where θ_s and θ_e are the angles corresponding to the start and the end of the load zone.

If we ignore the change in angular momentum caused by the sliding-contact region at exit (as it is small compared to the sliding-contact region at entry) then the angular momentum at point E can be approximated by pure-rolling angular-momentum[†]. In the moving reference frame $x'y'z'$ (figure 3.4), pure-rolling angular-momentum is $-I\omega_b^{\text{th}}(\sin\beta\underline{j}' + \cos\beta\underline{k}')$. Using this expression and by transforming equation 3.41 from the moving reference frame $x'y'z'$ to the fixed reference frame xyz , we get

$$\begin{aligned} \underline{H}_{\theta_s} &= \underline{H}_{\theta_e} \\ &= -I\omega_b^{\text{th}}(\sin\beta\underline{j}' + \cos\beta\underline{k}') \\ &= -I\omega_b^{\text{th}}(\sin\beta\cos\theta_e\underline{i} + \sin\beta\sin\theta_e\underline{j} + \cos\beta\underline{k}). \end{aligned} \quad (3.42)$$

At point B (transition point between sliding-contact region at entry and spin-contact region), rotation-axis of the rolling element becomes parallel to the bearing axis and

[†]By pure-rolling angular-momentum, we mean the theoretical value of the angular momentum required for pure-rolling motion

rotational speed of the rolling element increases from ω_b^{th} to $\omega'_b (= \omega_b^{\text{th}}/\cos\beta)$ in order to eliminate the translational gross sliding (see section 3.4.1 for the detailed explanation). Thus, the angular momentum at point B can be calculated as

$$\underline{H}_{\theta_1} = -I\omega'_b \underline{k}. \quad (3.43)$$

The change in angular momentum between points A and B is

$$\begin{aligned} \Delta \underline{H}_{AB} &= \underline{H}_{\theta_1} - \underline{H}_{\theta_s} \\ &= -I\omega'_b \underline{k} + I\omega_b^{\text{th}} (\sin\beta \cos\theta_e \underline{i} + \sin\beta \sin\theta_e \underline{j} + \cos\beta \underline{k}) \\ &= -I\omega_b^{\text{th}} (-\sin\beta \cos\theta_e \underline{i} - \sin\beta \sin\theta_e \underline{j} + \tan\beta \sin\beta \underline{k}). \end{aligned} \quad (3.44)$$

This change in angular momentum must be provided by the moment due to friction forces acting on the rolling element. In order to determine the frictional moment acting on the rolling element between points A and B, we must know the direction as well as the magnitude of the friction forces acting at the contact interfaces. We make the following simplifications/assumptions to calculate the direction and the magnitude of these friction forces.

- We assume that the variation in the contact force between rolling elements and raceways inside a load zone is parabolic, i.e.,

$$F_e(\theta) = \begin{cases} \frac{4F_e^{\text{max}}}{\theta_L}(\theta - \theta_s) \left(1 - \frac{\theta - \theta_s}{\theta_L}\right) & \text{for } \theta_s \leq \theta \leq \theta_e \\ 0 & \text{for } \theta < \theta_s \text{ or } \theta > \theta_e, \end{cases} \quad (3.45)$$

where $\theta_L = \theta_e - \theta_s$ and F_e^{max} is the maximum contact force acting on a rolling element inside a load zone.

- When a rolling element enters a load zone, its rotation-axis is not aligned with the pure-rolling vector. Therefore, the translational velocity of the inner contact-point (located on the rolling element) along the rolling direction[‡] is less than the translational velocity of the corresponding contact point located on the inner race. This results in sliding along the $-x''$ axis. Similarly, the translational speed of the outer contact-point (located on the rolling element) along the rolling direction is greater than the corresponding contact point located on the outer race, which results in sliding along the x'' axis. Hence, friction forces will act in the x'' axis[§] at

[‡]Rolling direction is parallel to the minor axis x'' of the contact ellipse (figure 3.7)

[§]Direction of the friction force is opposite to the slip velocity

the inner-race contact and in the $-x''$ axis at the outer-race contact. Mathematically these friction forces can be written as

$$\underline{\tilde{f}}_i = \underline{\tilde{f}}_i \underline{\tilde{i}}'' = -\underline{\tilde{f}}_i \underline{\tilde{i}}' \quad (3.46a)$$

and

$$\underline{\tilde{f}}_o = -\underline{\tilde{f}}_o \underline{\tilde{i}}'' = \underline{\tilde{f}}_o \underline{\tilde{i}}', \quad (3.46b)$$

where f_i and f_o are the magnitudes of the friction forces acting at the inner-race and the outer-race contacts. Equation 3.46 gives us the directions of the friction forces. The direction of the friction force changes continuously as a rolling element passes through the sliding-contact region. At any location inside the sliding-contact region, the friction force will have components along both the minor and the major axes of the contact ellipse. It is difficult to calculate the precise direction at a given location inside the sliding-contact region without knowing the instantaneous slip velocities. Therefore, we assume that the friction force will act in the same direction (defined by equation 3.46) throughout the sliding-contact region. The directions defined by equation 3.46 are along the rolling direction (minor axis of a contact ellipse), and the friction forces acting along the major axis of a contact ellipse are ignored.

- In order to determine the magnitude of these friction forces, we must first calculate the coefficient of friction acting between rolling elements and raceways in the sliding-contact region. As observed in section 3.3, value of the friction coefficient between rolling elements and raceways depends upon the contact force (F_e) and the sliding speed (Δu). Therefore, as the contact force and sliding speed vary inside a load zone, friction coefficient also varies. We know the contact load variation (equation 3.45) but we do not know how the sliding speed varies inside the load zone. Therefore, to simplify the analysis we assume that the friction coefficient will remain constant throughout the sliding-contact region. In order to determine its value we use the average contact force ($F_{\text{avg}} = 2F_e^{\text{max}}/3$)[¶] and sliding speed at point A (Δu_A). Thus,

$$\mu_{AB} = \frac{|\underline{\tilde{f}}(\Delta u_A)|}{F_{\text{avg}}} = \frac{\Delta u_A}{h F_{\text{avg}}} \int_{-a}^a \int_{-b}^b \eta(x'', y'') dx'' dy''. \quad (3.47)$$

Using equation 3.47 and assuming that the inner- and outer-race contact forces are

[¶]Average contact force: $F_{\text{avg}} = \frac{1}{\theta_L} \int_{\theta_s}^{\theta_e} F_e(\theta) d\theta = \frac{2}{3} F_e^{\text{max}}$

same, we can calculate the magnitude of friction forces as

$$f_i = f_o = \mu_{AB} F_e(\theta). \quad (3.48)$$

Our next step is to calculate the sliding speed at point A (Δu_A in equation 3.47). The rotational velocity of a rolling element at point E is

$$\begin{aligned} \underline{\omega}_{\theta_e} &= -\omega_b^{\text{th}} \left(\cos\beta \underline{k}' + \sin\beta \underline{j}' \right) \\ &= -\omega_b^{\text{th}} \left(\sin\beta \cos\theta_e \underline{i} + \sin\beta \sin\theta_e \underline{j} + \cos\beta \underline{k} \right). \end{aligned} \quad (3.49)$$

This velocity remains unchanged between points E and A, and by transforming equation 3.49 from fixed to moving reference frame we can calculate the rotational velocity at point A as

$$\underline{\omega}_{\theta_s} = -\omega_b^{\text{th}} \left\{ \sin\beta \cos\theta_e \left(\sin\theta_s \underline{i}' + \cos\theta_s \underline{j}' \right) + \sin\beta \sin\theta_e \left(-\cos\theta_s \underline{i}' + \sin\theta_s \underline{j}' \right) + \cos\beta \underline{k}' \right\}. \quad (3.50)$$

Substituting equation 3.50 into the sliding speed equation 3.28a gives the three components of the sliding speed at the inner-race contact patch

$$\Delta u_A^{x'} = -r\omega_b^{\text{th}} \left\{ \sin^2\beta (\cos\theta_e \cos\theta_s + \sin\theta_e \sin\theta_s) + \cos^2\beta \right\} + r_i (\omega_i - \omega_c) \quad (3.51a)$$

$$\Delta u_A^{y'} = r\omega_b^{\text{th}} \sin^2\beta (\cos\theta_e \sin\theta_s - \sin\theta_e \cos\theta_s) \quad (3.51b)$$

$$\Delta u_A^{z'} = r\omega_b^{\text{th}} \cos\beta \sin\beta (\cos\theta_e \sin\theta_s - \sin\theta_e \cos\theta_s). \quad (3.51c)$$

From equations 3.51 we can calculate the sliding speed at point A as

$$\Delta u_A = \sqrt{(\Delta u_A^{x'})^2 + (\Delta u_A^{y'})^2 + (\Delta u_A^{z'})^2}. \quad (3.52)$$

By substituting the value of Δu_A from equation 3.52 into equation 3.47 we can calculate the friction coefficient in the sliding-contact region (μ_{AB}), which gives us the magnitude of the friction forces acting at the contact interfaces.

At this point, we have all the ingredients required to calculate the friction moment acting on the rolling element as it passes through the sliding-contact region at entry. Using equations 3.46, we obtain the expression for the friction moment as

$$\underline{M}_{AB} = \underline{p}_i \times \underline{f}_i + \underline{p}_o \times \underline{f}_o, \quad (3.53)$$

where \underline{p}_i and \underline{p}_o are the position vectors of the inner- and outer-race contact points given

by

$$\underline{p}_i = r(\sin\beta\underline{k}' - \cos\beta\underline{j}') \quad (3.54a)$$

and

$$\underline{p}_o = r(-\sin\beta\underline{k}' + \cos\beta\underline{j}'). \quad (3.54b)$$

Substitution of equations 3.54 into equation 3.53 and using equation 3.48 yields

$$\begin{aligned} \underline{M}_{AB}(\theta) &= -2r\mu_{AB}F_e(\theta)(\sin\beta\underline{j}' + \cos\beta\underline{k}') \\ &= -2r\mu_{AB}F_e(\theta)(\sin\beta\cos\theta\underline{i} + \sin\beta\sin\theta\underline{j} + \cos\beta\underline{k}). \end{aligned} \quad (3.55)$$

The impulse due to this friction torque is

$$\underline{\mathfrak{S}}_{AB} = \frac{1}{\omega_c^{\text{th}}} \int_{\theta_s}^{\theta_1} \underline{M}_{AB}(\theta) d\theta, \quad (3.56)$$

using $\theta = \omega_c^{\text{th}}t$ and provided ω_c^{th} stays constant. We assume that the primary component of the friction forces (equation 3.46) is acting along the rolling direction (minor axis of the contact ellipse), and neglect the friction forces acting along the major axis. Friction forces along the major axis will generate a friction moment acting along the x' axis (moving reference frame), and this friction moment will influence the impulse in x and y directions (fixed reference frame). But, the impulse calculation in the z direction will not be influenced by the friction moment acting along the x' axis, because $\underline{k} \cdot \underline{i}' = 0$. Therefore, substituting equation 3.55 into 3.56 and taking the z -component of the impulse gives

$$\begin{aligned} \underline{\mathfrak{S}}_{AB} \cdot \underline{k} &= \frac{1}{\omega_c^{\text{th}}} \int_{\theta_s}^{\theta_1} -2r\mu_{AB}F_e(\theta)\cos\beta d\theta \\ &= -\frac{2r\mu_{AB}\cos\beta}{\omega_c^{\text{th}}} \int_{\theta_s}^{\theta_1} F_e(\theta) d\theta. \end{aligned} \quad (3.57)$$

We integrate equation 3.57 by using the parabolic load approximation defined in equation 3.45, which yields

$$\underline{\mathfrak{S}}_{AB} \cdot \underline{k} = -\frac{8r\mu_{AB}F_e^{\text{max}}\cos\beta}{3\omega_c^{\text{th}}\theta_L^2} \left(-\vartheta^3 + \frac{3}{2}\theta_L\vartheta^2 \right), \quad (3.58)$$

where ϑ ($= \theta_1 - \theta_s$) is the size of the sliding-contact region at entry.

This impulse produced by the friction moment must provide the required change in angular momentum between points A and B. This condition gives

$$|\mathfrak{S}_{AB} \cdot \underline{k}| \geq |\Delta \underline{H}_{AB} \cdot \underline{k}|. \quad (3.59)$$

Inserting equations 3.58 and 3.44 into equation 3.59 gives the following inequality.

$$\left| -\vartheta^3 + \frac{3}{2}\theta_L\vartheta^2 \right| \geq \frac{3I\omega_b^{\text{th}}\omega_c^{\text{th}}\tan^2\beta\theta_L^2}{8r\mu_{AB}F_e^{\text{max}}}. \quad (3.60)$$

Solution of equation 3.60 gives us the length of the sliding-contact region at entry (ϑ).

3.4.2.2 Extent of the Spin-Contact Region

Spin-contact region is the region between points B and C in figure 3.18. Point C is the transition point between the spin-contact and the rolling-contact regions. Angular momentum at C (\underline{H}_{θ_2}) can be calculated from the pure-rolling angular-momentum, i.e.,

$$\begin{aligned} \underline{H}_{\theta_2} &= -I\omega_b^{\text{th}}(\sin\beta\dot{j}' + \cos\beta\dot{k}') \\ &= -I\omega_b^{\text{th}}(\sin\beta\cos\theta_2\dot{i} + \sin\beta\sin\theta_2\dot{j} + \cos\beta\dot{k}). \end{aligned} \quad (3.61)$$

We have already calculated the angular momentum at point B (equation 3.43). Thus, the change in angular momentum between points B and C is

$$\begin{aligned} \Delta \underline{H}_{BC} &= \underline{H}_{\theta_2} - \underline{H}_{\theta_1} \\ &= -I\omega_b^{\text{th}}(\sin\beta\cos\theta_2\dot{i} + \sin\beta\sin\theta_2\dot{j} - \tan\beta\sin\beta\dot{k}). \end{aligned} \quad (3.62)$$

Like the sliding-contact region, we assume that the friction coefficient between rolling elements and raceways remains constant throughout the spin-contact region. In order to determine the value of this friction coefficient, we use the average contact force (F_{avg}) and the average slip speed acting on the contact patch at point B. From section 3.4.1, we know that at point B the rolling element is spinning on the contact patch with a speed of $\omega_b' \sin\beta$ ($= \omega_b^{\text{th}} \tan\beta$). Due to this spinning, slip speed at any point P(x'' , y'') on the contact patch (figure 3.7) is $\sqrt{(x'')^2 + (y'')^2}$ times the spin speed. The slip speed is maximum at the two edges lying on the major axis of the contact ellipse, and the value of this maximum slip speed is $a\omega_b^{\text{th}} \tan\beta$. Slip speed at the centre of the contact ellipse is zero. Hence, the

average slip speed over the contact patch at point B is

$$\Delta u_B = \frac{1}{2} a \omega_b^{\text{th}} \tan \beta. \quad (3.63)$$

Using the slip speed described by equation 3.63 and the average contact force (F_{avg}) acting on the rolling elements, we calculate the friction coefficient for the spin-contact region as

$$\mu_{BC} = \frac{|\underline{f}(\Delta u_B)|}{F_{\text{avg}}} = \frac{\Delta u_B}{h F_{\text{avg}}} \int_{-a}^a \int_{-b}^b \eta(x'', y'') dx'' dy''. \quad (3.64)$$

We now calculate the spin moment acting on the rolling element during the spin-contact region. If the contact pressure^{||} at a point P(x'', y'') on the contact-ellipse is $\sigma(x'', y'', \theta)$, the friction force over a differential element ($dx'' dy''$) is $\mu_{BC} \sigma(x'', y'', \theta) dx'' dy''$; and the spin-moment generated by this differential friction force is

$$\mu_{BC} \sigma(x'', y'', \theta) \sqrt{(x'')^2 + (y'')^2} dx'' dy''.$$

By integrating this differential spin-moment over the entire contact ellipse, we obtain the total spin-moment acting on the rolling element as

$$\begin{aligned} \underline{M}_{BC}(\theta) &= 2 \int_{-a}^a \int_{-b}^b \mu_{BC} \sigma(x, y, \theta) \sqrt{x^2 + y^2} dx dy \underline{k}'' \\ &= 2 \int_{-a}^a \int_{-b}^b \mu_{BC} \frac{3F_e(\theta)}{2\pi ab} \sqrt{1 - \left(\frac{x}{b}\right)^2 - \left(\frac{y}{a}\right)^2} \sqrt{x^2 + y^2} dx dy \underline{k}'' \\ &= \frac{3\mu_{BC} \Phi(a, b)}{\pi ab} F_e(\theta) (\cos \beta \cos \theta \underline{i} + \cos \beta \sin \theta \underline{j} - \sin \beta \underline{k}), \end{aligned} \quad (3.65)$$

where $\Phi(a, b) = \int_{-a}^a \int_{-b}^b \sqrt{1 - \left(\frac{x}{b}\right)^2 - \left(\frac{y}{a}\right)^2} \sqrt{x^2 + y^2} dx dy$. A factor of two in the above equation comes from the spin moment contributions by both the inner-race and the outer-race contacts. The contact patch dimensions (a and b) vary with the contact force, but in equation 3.65 these are treated as constants and their values are calculated at the average contact force (F_{avg}) acting on a rolling element. The z -component of the impulse due to

^{||}Under combined loading conditions, contact pressure varies with θ , because of the variation in the contact force inside the load zone

this spin-moment is

$$\begin{aligned}
\mathfrak{S}_{BC} \cdot \underline{k} &= \frac{1}{\omega_c^{\text{th}}} \int_{\theta_1}^{\theta_2} \underline{M}_{BC} \cdot \underline{k} d\theta \\
&= \frac{3\mu_{BC}\Phi(a,b)\sin\beta}{\pi ab\omega_c^{\text{th}}} \int_{\theta_1}^{\theta_2} F_e(\theta) d\theta \\
&= \frac{4\mu_{BC}F_e^{\text{max}}\Phi(a,b)\sin\beta}{\pi ab\omega_c^{\text{th}}\theta_L^2} \left(\frac{3}{2}\theta_L\Theta^2 - \Theta^3 + \vartheta^3 - \frac{3}{2}\theta_L\vartheta^2 \right), \quad (3.66)
\end{aligned}$$

where $\Theta (= \theta_2 - \theta_s)$ is the total size of skidding region (sliding-contact region + spin-contact region) and ϑ is obtained from equation 3.60.

The impulse due to the spin moment must provide the required change in angular momentum. Thus, substitution of equations 3.62 and 3.66 into the condition $|\mathfrak{S}_{BC} \cdot \underline{k}| \geq |\Delta \underline{h}_{BC} \cdot \underline{k}|$ yields the following inequality.

$$\left| \frac{3}{2}\theta_L\Theta^2 - \Theta^3 + \vartheta^3 - \frac{3}{2}\theta_L\vartheta^2 \right| \geq \frac{\pi ab I \omega_b^{\text{th}} \omega_c^{\text{th}} \theta_L^2 \tan\beta}{4\mu_{BC} F_e^{\text{max}} \Phi(a,b)}. \quad (3.67)$$

Solution of equation 3.67 gives us the combined length (Θ) of the sliding-contact and the spin-contact regions.

3.4.2.3 Influence of the Applied Load on the Extent of the Skidding Region

In the previous two sections, we derive two analytical equations (equations 3.60 and 3.67) to calculate the lengths of the skidding regions inside the load zone. In this section we compare these analytical equations with the full numerical model, and we also analyze the influence of the applied load on the lengths of these skidding regions.

Figure 3.20 shows the variation in the lengths of the sliding-contact region at entry (ϑ) and the combined sliding- and spin-contact regions (Θ) with the maximum contact force acting on a rolling element (F_e^{max}). Lengths of the skidding regions in the figure are normalized by the length of load zone, i.e., $\hat{\Theta} = \Theta/\theta_L$ and $\hat{\vartheta} = \vartheta/\theta_L$. The values of Θ and ϑ are determined using both the full numerical analysis of section 3.2 and the simple analytical method described in sections 3.4.2.1 and 3.4.2.2. For each load-case** shown in figure 3.20, numerical analysis takes around 30 minutes to compute the lengths of the skidding regions. On the other hand, analytical method takes just a few seconds to calculate these lengths for all the load-cases. We can make the following observations

**Each data point (circle or cross) in figure 3.20 represents a load-case

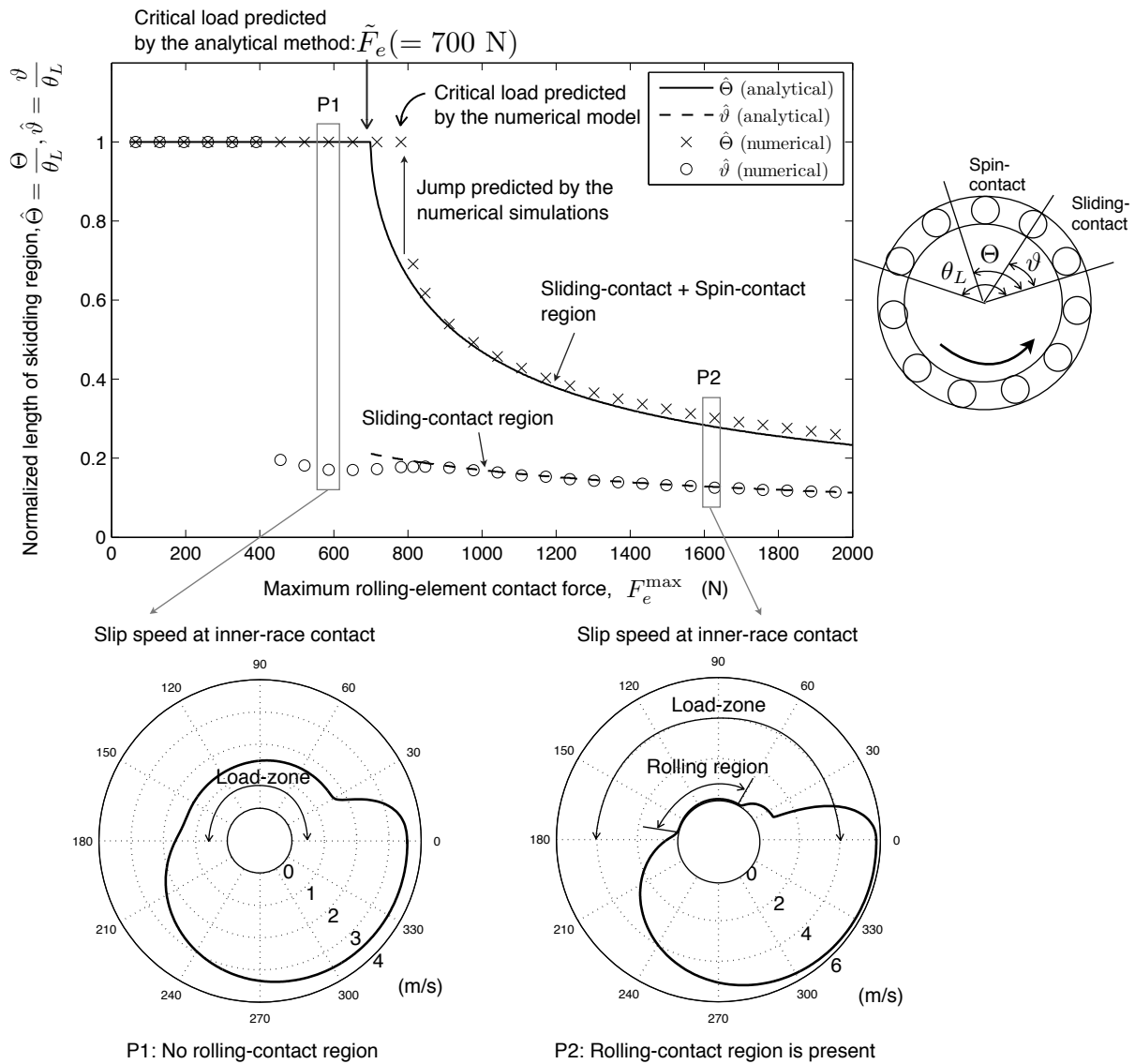


Figure 3.20: Normalized lengths of the skidding regions (sliding-contact and spin-contact) inside load zone calculated using both full numerical simulations (circles and crosses) and simple analytical solution (continuous lines). Slip speed at inner-race contact is also shown for the two cases: P1 - applied load is less than \tilde{F}_e and rolling-contact region is not present inside the load zone, P2 - applied load is greater than \tilde{F}_e and rolling-contact region is present

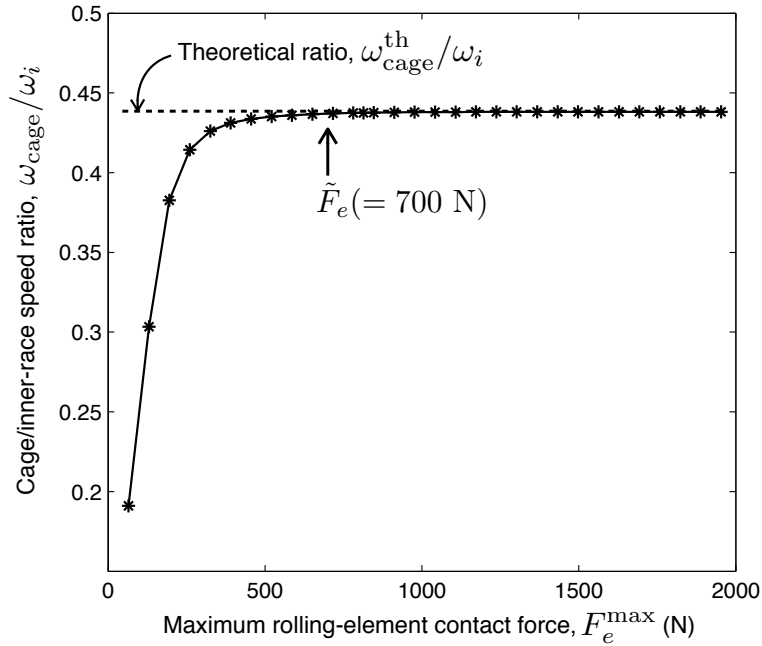


Figure 3.21: Variation in the cage speed with applied load under combined axial and radial loads

from figure 3.20.

- The lengths of the sliding-contact and the spin-contact regions predicted by the analytical equations are in close agreement with the numerical simulations. This validates the proposed analytical method.
- The lengths of both the sliding- and the spin-contact regions decrease as we increase the applied load, and they approach zero value asymptotically. This means that it is possible to reduce the lengths of these skidding regions by increasing the applied load. Though, it is not possible to completely eliminate skidding, no matter how high the applied load is.
- There is a critical load (\tilde{F}_e) below which $\Theta = \theta_L$ (or $\hat{\Theta} = 1$), i.e., the total length of the skidding region is equal to the length of the load zone. Therefore, rolling-contact region does not exist in bearings operating below \tilde{F}_e (e.g. P1 in figure 3.20), and skidding takes place throughout the load zone. Figure 3.21 shows the variation of the cage speed with the maximum contact force acting on a rolling element. Clearly, if the maximum contact force is below \tilde{F}_e , the cage speed is lower than its corresponding theoretical value. This is because in the absence of a rolling-contact region, all the rolling elements skid inside the load zone; and none of them is able to drive the cage at the required speed. In the presence of a rolling-contact

region, all the rolling elements which are within this region do pure-rolling motion. Consequently these rolling elements are able to drive the cage at the theoretical pure-rolling speed. For a bearing designer, it is crucial to know the value of this critical load \tilde{F}_e for a given bearing. Using equations 3.60 and 3.67 we can easily calculate this critical load. Since ϑ is always less than θ_L , $\vartheta^3 < \frac{3}{2}\theta_L\vartheta^2$. Therefore, equation 3.60 becomes

$$\frac{3}{2}\theta_L\vartheta^2 - \vartheta^3 = \dagger\dagger \frac{3I\omega_b^{\text{th}}\omega_c^{\text{th}}\tan^2\beta\theta_L^2}{8r\mu_{AB}F_e^{\text{max}}}. \quad (3.68)$$

Similarly, $\Theta \leq \theta_L$ which means $\Theta^3 < \frac{3}{2}\theta_L\Theta^2$, and $\Theta > \vartheta$ (combined length of the sliding-contact and the spin-contact regions is always greater than the length of the spin-contact region). Hence equation 3.67 becomes

$$\frac{3}{2}\theta_L\Theta^2 - \Theta^3 - \left(\frac{3}{2}\theta_L\vartheta^2 - \vartheta^3\right) = \frac{\pi ab I\omega_b^{\text{th}}\omega_c^{\text{th}}\theta_L^2 \tan\beta}{4\mu_{BC}F_e^{\text{max}}\Phi(a, b)}. \quad (3.69)$$

Substituting equation 3.68 into 3.69 and solving for F_e^{max} yields

$$F_e^{\text{max}} = \frac{I\omega_b^{\text{th}}\omega_c^{\text{th}}\theta_L^2 \tan\beta}{\frac{3}{2}\theta_L\Theta^2 - \Theta^3} \left(\frac{\pi ab}{4\mu_{BC}\Phi(a, b)} + \frac{3\tan\beta}{8r\mu_{AB}} \right). \quad (3.70)$$

If a bearing is operating at the critical load (\tilde{F}_e), the length of the combined sliding- and spin-contact region is equal to the length of the load zone. To determine the expression for the critical load we substitute $\Theta = \theta_L$ into equation 3.70, which gives

$$\tilde{F}_e = \frac{2I\omega_b^{\text{th}}\omega_c^{\text{th}}\tan\beta}{\theta_L} \left(\frac{\pi ab}{4\mu_{BC}\Phi(a, b)} + \frac{3\tan\beta}{8r\mu_{AB}} \right). \quad (3.71)$$

Equation 3.71 gives us the value of the critical load required for the formation of a rolling-contact region inside the load zone. The contact-ellipse dimensions a and b , and friction coefficients μ_{AB} and μ_{BC} in equation 3.71 are functions of the applied load. Therefore, equation 3.71 must be solved iteratively.

- Deviation in the cage-speed from its pure-rolling value is often used as an indicator of skidding, which is true for the bearings operating under axial loads. However, for the bearings operating under combined axial and radial loads, deviation in the cage speed does not provide us the complete information about the skidding behaviour. That is even if there is no deviation in the cage speed (for loads greater than \tilde{F}_e),

^{††}Inequality (\geq) in equation 3.60 is replaced by equality ($=$) as we are interested in the minimum length of the skidding region required to provide the desired change in angular momentum

skidding can take place in the sliding- and spin-contact regions.

- Equation 3.60, used to calculate the length of the sliding-contact region, is not valid if $F_e^{\max} < \tilde{F}_e$ or $\Theta > \theta_L$. This is because under this condition a rolling-contact region does not get created inside the load zone and angular momentum at point E cannot be approximated by the pure-rolling value. Hence, the derivation described in section 3.4.2.1 breaks down.
- The value of the critical load (\tilde{F}_e) predicted by the analytical method is slightly different from the one predicted by the numerical analysis (figure 3.20). As we approach the critical load from a higher load value, the normalized length of the combined skidding region predicted by the analytical method increases smoothly; but the normalized length predicted by the numerical model suddenly jumps to 1. This is because while deriving the analytical solution, we ignore the formation of a sliding-contact region at exit. As we move towards the critical load from a higher load, the length of the rolling-contact region decreases. At a certain load, the rolling-contact region completely disappears and the rolling element transits from the spin-contact region directly into the sliding-contact region at exit, and the length of the skidding region becomes equal to the length of the load zone. Hence, at this load, the value of the normalized length of the skidding region predicted by the numerical model jumps to 1. On the other hand, the analytical method does not take into account the formation of a sliding-contact region at exit. In this case, the rolling-contact region extends up to the end of the load zone. As we decrease the load further, the length of the rolling-contact region decreases smoothly until it reaches zero. This explains the smooth increase in the normalized length and a small error in the prediction of the critical load.

The analytical method proposed here tells us the extent of the skidding region as well as the minimum load required to establish a rolling-contact region inside a load zone. The assumptions made during the derivation limit the scope of the method, but they also allow us to obtain some interesting new analytical results. One limitation of the analytical solution is that it does not tell us anything about the variation in the slip speeds inside the skidding region, which is important to calculate the amount of damage caused by skidding. We should note here that although the analytical method is derived for a Newtonian fluid under an EHD lubrication regime, the method is applicable to a non-Newtonian fluid or a mixed lubrication regime. We have to change only the way the friction coefficients in the skidding regions are calculated.

3.5 Skidding Under Constant Axial Loads and Time-Varying Speeds

So far we have considered skidding under constant speed conditions; but in some cases, for example wind turbines, bearing speed might vary with time. Therefore, in this section, we will analyze the skidding behaviour of bearings operating under constant axial loads and time-varying speeds to understand the effect of speed variation on skidding behaviour. For simplicity, we assume that the speed variation is sinusoidal, i.e.,

$$\omega_i = \omega_0 + \Delta\omega \sin(\Omega t), \quad (3.72)$$

where ω_0 is the mean speed, $\Delta\omega$ is the amplitude of speed fluctuation, and Ω is the frequency of speed-fluctuation.

3.5.1 Skidding Mechanism Under Time-Varying Speeds

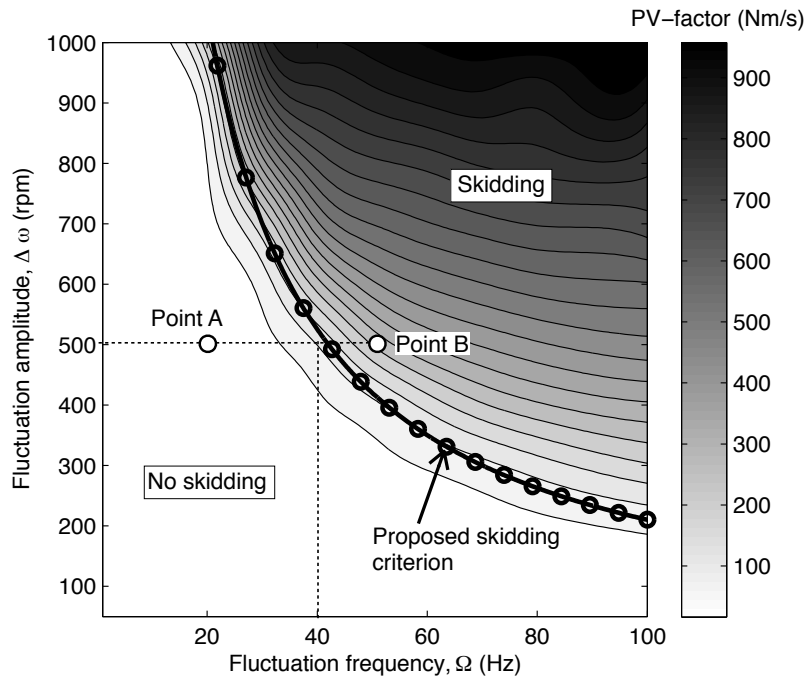
In order to quantify the effect of speed-fluctuation amplitude $\Delta\omega$ and frequency Ω on the skidding behaviour, we solve the numerical model of section 3.2 along with the inner-race speed profile described by equation 3.72 to calculate the slip speeds at the contact interfaces for various values of $\Delta\omega$ and Ω . Figure 3.22a shows a skidding map for the example bearing obtained from the numerical simulations under a mean speed (ω_0) of 1500 rpm and a constant axial load of 3.5 kN. The Z-axis of the map represents the ‘‘PV-factor’’, which is defined as the product of the contact force and sliding speed. If a bearing is operating under a time-varying speed, then the PV-factor will also vary with time. Therefore, we calculate a time-averaged value of the PV-factor over n cycles of speed-fluctuation. Mathematically, it is calculated as

$$\text{PV-factor} = \frac{1}{nT_c} \int_0^{nT_c} F_c(s) |\Delta\underline{u}(s)| ds \quad (3.73)$$

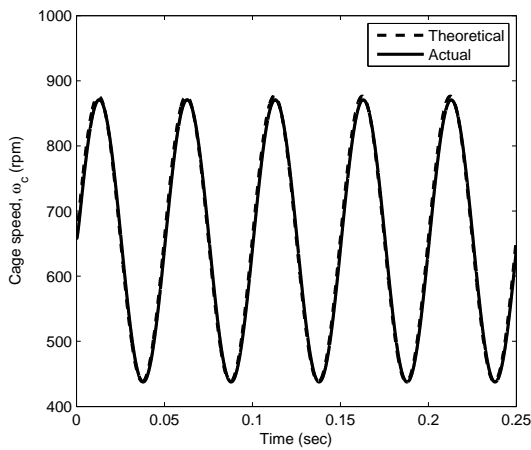
where T_c is the time-period of speed fluctuation ($= 2\pi/\Omega$). For the skidding map of figure 3.22a, PV-factor is averaged over five cycles i.e., $n = 5$.

Higher values of the PV-factor represent the possibility of skidding damage. Therefore, based on PV-factor values, the skidding map of figure 3.22a can be divided into two regions: ‘‘Skidding zone’’ with high PV-factor and ‘‘No-skidding zone’’ with almost zero PV-factor. We can make the following observations from the skidding map of figure 3.22a.

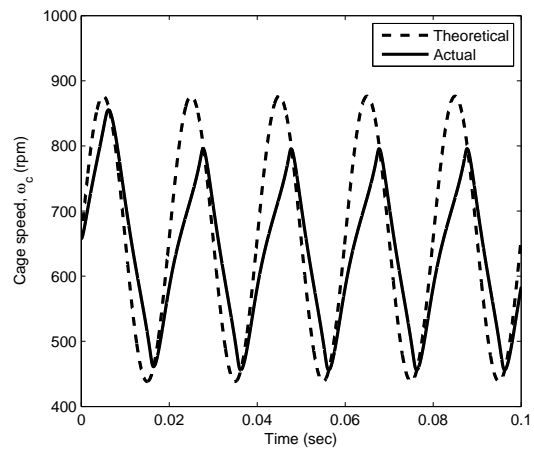
1. Skidding behaviour of a bearing under time-varying speeds depends on the ampli-



(a) Contour plot showing the variation in the PV-factor (Nm/s) with the frequency and amplitude of inner-race speed fluctuation; along with the proposed skidding criterion for constant axial loads and time-varying speeds (equation 3.78)



(b) Cage speed with time for $\Delta\omega = 500$ rpm, $\Omega = 20$ Hz (Point A)



(c) Cage speed with time for $\Delta\omega = 500$ rpm, $\Omega = 50$ Hz (Point B)

Figure 3.22: Skidding under constant axial load and time-varying speed; $F_a = 3.5$ kN, $\omega_0 = 1500$ rpm

tude and frequency of speed fluctuation.

2. For a given fluctuation amplitude ($\Delta\omega$), PV-factor suddenly increases as we increase the fluctuation frequency beyond a critical value. For example, in the skidding map of figure 3.22a high values of PV-factor can be observed when the fluctuation frequency is increased above 40 Hz for the fluctuation amplitude of 500 rpm. Let us call this critical frequency the “skidding onset frequency”. If the fluctuation frequency is above this value then the bearing will start to skid. Similarly, we can also define the “skidding onset amplitude” for a given fluctuation frequency.
3. Skidding onset frequency decreases as we increase the speed-fluctuation amplitude and likewise skidding onset amplitude decreases as we increase the fluctuation frequency. In other words, skidding occurs at high values of the speed-fluctuation frequency and amplitude.
4. To avoid skidding, speed-fluctuation frequency and amplitude must be less than their corresponding skidding onset values as defined above.

In order to understand the mechanism of skidding under time-varying speeds in detail, let us first take a point *A* ($\Delta\omega = 500$ rpm, $\Omega = 20$ Hz) which lies inside the no-skidding zone of the skidding map of figure 3.22a. Figure 3.22b shows the cage speed variation with time for the bearing operating at point *A*. The actual cage speed calculated using the numerical model follows the applied theoretical speed profile (calculated using equation 3.72), and hence no skidding takes place. Let us take another point *B* ($\Delta\omega = 500$ rpm, $\Omega = 50$ Hz) which lies inside the skidding zone. In this case, the cage is struggling to catch up with the applied speed variation (figure 3.22c) because the applied fluctuation frequency is much higher than the skidding-onset frequency for the fluctuation amplitude of 500 rpm. Therefore, the traction forces are not able to provide enough acceleration to the rolling elements to maintain the input speed profile. This results in skidding.

The skidding mechanism under constant axial load and sinusoidal speed variation, explained here, is different from the skidding mechanism under constant load and constant speed. Under time-varying speeds, skidding is primarily caused by the variation in the orbital speed of a rolling element; whereas under constant speed, skidding is caused by the viscous drag and gyroscopic effects. Now, if we apply the skidding criterion derived for constant axial load and constant speed (section 3.3.2) to the example considered here then according to the skidding map of figure 3.13c, the bearing should not skid at the mean speed of 1500 rpm and axial load of 3.5 kN. However, figure 3.22a clearly shows that the bearing will skid if $\Delta\omega$ or Ω are larger than certain values. This proves that

the skidding criterion derived for stationary operating conditions is not applicable for the time-varying speeds.

3.5.2 Derivation of Skidding Criterion for Constant Axial Loads and Time-Varying Speeds

In the previous section, we observe that the occurrence of skidding under constant axial loads and time-varying speeds depends on the frequency and amplitude of speed-fluctuation. Skidding takes place if the values of fluctuation frequency and amplitude are greater than the skidding-onset frequency and amplitude. In this section we will derive a simple analytical expression to determine the skidding-onset frequency and amplitude for a given bearing geometry and operating conditions. From the applied inner-race speed profile (equation 3.72), we can obtain the rolling-element orbital speed and its first derivative as

$$\omega_c = \frac{\omega_i}{2} \left(1 - \frac{\cos\beta}{r_p/r} \right) = G_1 \{ \omega_0 + \Delta\omega \sin(\Omega t) \} \quad (3.74a)$$

and

$$\dot{\omega}_c = G_1 \Delta\omega \Omega \cos(2\pi\Omega t), \quad (3.74b)$$

where $G_1 = \frac{1}{2} \left(1 - \frac{\cos\beta}{r_p/r} \right)$. Equations 3.74 explain why rolling elements skid at high speed-fluctuation frequencies and amplitudes. Since the orbital acceleration ($\dot{\omega}_c$) is proportional to $\Delta\omega$ and Ω , large values of these parameters result in large orbital acceleration. This acceleration must be provided by the friction forces acting between the rolling elements and the raceways. If the friction forces are not enough to provide the required orbital acceleration, rolling elements will skid.

Orbital motion of a rolling element inside a bearing is governed by equation 3.20. Bearing is operating under an axial load, therefore, all the rolling elements will have the same loading conditions and the cage forces can be ignored. Substitution of $F_{\text{cage}} = 0$ and $\dot{\omega}_c$ from equation 3.74 into equation 3.20 yields

$$- (f_i^{x'} r_i + f_o^{x'} r_o) = I_c G_1 \Delta\omega \Omega \cos(2\pi\Omega t) + F_{\text{drag}} r_p. \quad (3.75)$$

If the maximum friction coefficient between rolling elements and raceways is μ_e then the maximum value of the friction force between a rolling element and inner or outer raceway would be μ_e times the contact-force; therefore, $|f_i^{x'}| \leq \mu_e F_i$ and $|f_o^{x'}| \leq \mu_e F_o$. We also assume that the contact forces between a rolling element and inner- and outer-race are

same i.e. $F_i = F_o = F_e$. Using these conditions we can rewrite equation 3.75 as

$$\mu_e F_e (r_i + r_o) \geq |I_c G_1 \Omega \Delta \omega \cos(2\pi \Omega t) + F_{\text{drag}} r_p|. \quad (3.76)$$

We use the peak value of the traction curve (μ_{peak} in figure 3.12) as the maximum friction coefficient, i.e.,

$$\mu_e = \frac{|\underline{f}(\Delta u_{\text{peak}})|}{F_e} = \frac{\Delta u_{\text{peak}}}{h F_e} \int_{-a}^a \int_{-b}^b \eta(x'', y'') dx'' dy'', \quad (3.77)$$

where film thickness h and lubricant viscosity $\eta(x'', y'')$ are calculated at the mean operating speed ω_0 .

We can further simplify equation 3.76 by substituting the maximum value of $\{\cos(2\pi \Omega t)\}$ as 1, $F_{\text{drag}} = \frac{\pi}{2} C_D \rho (G_1 \omega_0 r_p)^2 r^2$ (from equation 3.19) and $F_e = F_a / (z \sin \beta)$, which leads to

$$\Omega \Delta \omega \leq \frac{2\mu_e F_a (r_i + r_o)}{z I_c \sin \beta \left(1 - \frac{\cos \beta}{r_p/r}\right)} - \frac{C_D}{2I_c} \pi \rho r_p^3 r^2 \omega_0^2 \left(1 - \frac{\cos \beta}{r_p/r}\right). \quad (3.78)$$

Equation 3.78 gives us the skidding-onset values of speed-fluctuation amplitude and frequency for a given bearing geometry and operating conditions, using which we can calculate the boundary between the skidding and no-skidding regions of the skidding map shown in figure 3.22a without running the full numerical model. Skidding boundary calculated by equation 3.78 are plotted on top of the skidding map generated using numerical simulations (figure 3.22a). The proposed equation is successfully able to identify the skidding region in the map.

3.6 Conclusions

We present a dynamic model, which uses EHD lubrication theory and includes gyroscopic effects, to study the roll-slip behaviour of angular-contact ball-bearings. We also discuss the skidding characteristics of these bearings under various operating conditions. Based on these discussions, we can draw the following conclusions.

- For the case of a bearing operating under constant axial load and constant speed, a minimum load is required to prevent skidding. The value of this minimum load depends on the bearing geometry, rotational speed and lubricant properties. We propose a simple equation to calculate this load without having to run the time consuming numerical model.

- We study the ball motion inside a bearing operating under combined axial and radial loads in detail, and show that the skidding mechanism under these conditions is different from the skidding mechanism under axially loaded bearings due to the formation of a load zone. Maximum skidding occurs when a rolling element enters the load zone. We also identify different regions of skidding inside the load zone.
- We show that it is possible to predict the extents of different skidding regions formed inside the load zone of a bearing operating under combined axial and radial loads using a simple analytical method. We derive equations governing the extents of the sliding-contact and the spin-contact regions. The proposed analytical solution does not require much computational power and therefore, it can be used as a design tool.
- For the case of a bearing operating under combined axial and radial loads, a minimum load is required for the formation of a rolling-contact region (skidding does not take place inside this region). If the applied load is below this minimum load then rolling elements skid through out the load zone, causing the maximum damage to the bearing. We derive an equation to predict this minimum load for a given bearing geometry and operating speeds.
- We analyze the skidding behaviour under constant axial loads and sinusoidal speed fluctuations. For a given fluctuation amplitude, rolling elements start to skid when the fluctuation frequency is increased above a critical value (skidding-onset frequency). We derive an analytical equation to predict this skidding-onset frequency.
- We also establish that any skidding criteria derived for axial loading conditions cannot be applied to a bearing operating under combined loading conditions or time-varying speeds. This is because the underlying skidding mechanism is completely different in the three cases.

Chapter 4

Fault Detection in Planet Bearings

Planet bearings of wind-turbine gearboxes exhibit a high failure rate and are considered as one of the most critical components. In order to detect localized faults in planet bearings using vibration measurements, a detailed knowledge of their vibration signature is required. In this chapter, we develop a dynamic model of a wind-turbine planetary-drivetrain. The model includes a flexible ring-gear and a planet bearing with localized faults. We determine the vibration signatures of planet-bearing faults located on inner race, outer race and rolling elements. We also calculate the impulse due to a bearing fault, explore its dependence on load and speed, and investigate how it influences the vibration signatures of faults. The findings from this chapter will improve the existing detection techniques for planet-bearing faults in wind-turbine gearboxes.

4.1 Introduction

Planet bearings are considered as one of the most critical components with very high failure rate^[94]. Vibration based techniques are mostly used to detect bearing faults in wind-turbine gearboxes. In order to detect planet-bearing faults using vibration measurements, a thorough understanding of their vibration signature is required. For example, we must know how the presence of a planet-bearing fault alters the vibration behaviour of a planetary drivetrain.

In chapter 2, we review various models available in the literature to simulate vibration behaviour of bearing containing localized faults. The review suggests that most of these models are limited to fixed-axis bearings, i.e., bearings whose rotation axes are stationary with respect to vibration sensors mounted on gearbox housing. The rotation axis of a planet bearing changes with time due to carrier rotation. Thus, the vibration signature of a planet bearing is different from a fixed-axis bearing because of the complicated

and time-varying vibration transmission-path. No published work has been found in the literature which simulates this complicated transmission path and determines the vibration signature of a planetary drive containing localized planet-bearing faults.

In order to determine the vibration characteristics of planet bearings, dynamics of a planetary drivetrain containing these bearings must also be considered. Researchers have developed numerous models of varying complexity to simulate the vibration response of a healthy planetary drive. We discuss some of these model in chapter 2. Most of these models do not include a flexible ring-gear and the vibration transmission path between a ring-planet mesh and a measurement-point fixed on the ring gear is approximated by a Hann function. Very few analytical models take into account ring-gear deformation. One such model is proposed by Wu and Parker^[129].

Literature review also suggests that an assumption commonly made in the bearing-fault-detection literature is that the impulse due to a localized bearing-fault is proportional to the contact force acting on a rolling element during impact, and none of the published work provide any scientific justification to this assumption.

Bearing-fault and planetary models available in the literature provide a good understanding of the vibration behaviour of defective fixed-axis bearings and healthy planetary-drivetrains. However, vibration response of a planetary drivetrain containing a non-fixed-axis planet bearing with localized faults (spalls or pits) has not been studied so far. In this chapter, we determine the vibration signatures of planet-bearings faults using an analytical model. The main contributions of this chapter are:

1. an analytical planetary-drivetrain model which includes a deformable ring-gear and localized planet-bearing faults (section 4.2);
2. a closed-form expression for the frequency response of ring gear, in the presence of different planet-bearing faults, in terms of modal properties of the system (section 4.3);
3. the vibration signatures of planet bearings containing localized inner-race, outer-race and rolling-element faults (section 4.4), validated using experimental results (section 4.6);
4. identification of different sources of modulation sidebands providing an explanation for their formation (section 4.4.4);
5. an investigation of the influence of ring-gear flexibility on the vibration signatures of planet-bearing faults (section 4.5);

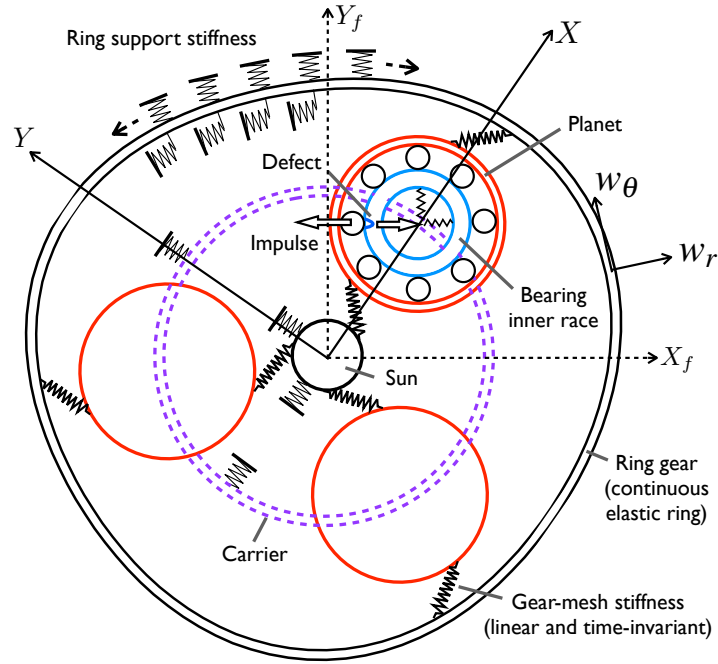


Figure 4.1: Analytical model of a planetary drivetrain with a flexible ring-gear and a defective planet-bearing

6. calculation of the impulse due to a localized bearing fault and quantification of the effect of rolling-element speed and load on the impulse value (section 4.7).

4.2 Analytical Model Description

The analytical model (figure 4.1) is developed for spur gears and only considers the in-plane dynamics of drivetrain components. Sun gear, planet gears and carrier are modelled as rigid bodies (similar to Lin and Parker^[86]) with coordinates $\mathbf{q}_{(\bullet)} = (x_{(\bullet)}, y_{(\bullet)}, \theta_{(\bullet)})^T$, where $x_{(\bullet)}$ and $y_{(\bullet)}$ are the translational degrees-of-freedom in x and y directions, $\theta_{(\bullet)}$ is the rotational degree-of-freedom (DOF) about z axis. Subscript (\bullet) is s for sun gear; p_i for i^{th} planet gear; and c for carrier. Variables written in bold letters represent matrices in this chapter. In addition to gears, planet bearing containing a localized fault (also referred as “defective bearing”) is also included in the model. The planet gear containing this bearing serves as the outer race and the inner race is modelled as a rigid body with coordinates $\mathbf{q}_{\mathbf{b}} = (x_b, y_b, \theta_b)^T$. Inner and outer raceways of the defective bearing are connected together with linear springs representing bearing stiffness k_{bp} . Contact between two meshing gears is represented by a linear time-invariant spring which acts along the line-of-action of a gear-pair. Ring gear is modelled as a continuous elastic ring. w_r and w_θ are the radial and tangential DOFs of the ring gear. Equations of motion described in the

following sections are derived in the XYZ coordinate system which is rotating with the carrier. The Coriolis and centripetal terms due to the rotation of the coordinate system are small and can be neglected while deriving the equations of motion for the individual components. The justification for choosing a rotating coordinate-system is provided later (section 4.2.5) when we write the equation of motion for the combined system.

4.2.1 Equation of Motion for a Flexible Ring Gear

Equations governing the dynamics of a continuous elastic ring in the radial and the tangential directions are^[63]

$$\frac{Eh^3\ell}{12R_r^3}(w_r''' - w_\theta'') - \frac{Eh\ell}{R_r}(w_r' + w_\theta'') + \rho AR_r\ddot{w}_\theta + K_\theta\ell R_r w_\theta = f_\theta(\theta, t) \quad (4.1a)$$

and

$$\frac{Eh^3\ell}{12R_r^3}(w_r'''' - w_\theta''') + \frac{Eh\ell}{R_r}(w_\theta' + w_r) + \rho AR_r\ddot{w}_r + K_r\ell R_r w_r = f_r(\theta, t), \quad (4.1b)$$

where $(\dot{\bullet}) = \partial(\bullet)/\partial t$, $(\bullet)' = \partial(\bullet)/\partial\theta$, K_r and K_θ are the distributed support stiffness in the radial and tangential directions, R_r is the pitch radius of the ring gear, h is the ring gear thickness, ℓ is the ring gear width, A is the cross-section area ($= \ell h$), E is the young's modulus, and $f_r(\theta, t)$ and $f_\theta(\theta, t)$ are the external forces acting on the ring in radial and tangential directions. See appendix B for the derivation of equations 4.1.

Equation 4.1 can be simplified by representing the ring gear DOFs in terms of the vibration modes of an elastic ring using Fourier series expansion as

$$w_r(\theta, t) = \sum_{n=0}^{\Phi} a_n(t)\cos(n\theta) + b_n(t)\sin(n\theta) \quad (4.2a)$$

and

$$w_\theta(\theta, t) = \sum_{n=0}^{\Phi} c_n a_n(t)\sin(n\theta) - c_n b_n(t)\cos(n\theta), \quad (4.2b)$$

where a_n and b_n are the modal participation factors for the n^{th} mode, n is the ring-mode index, Φ is the highest ring mode considered, and $c_n = -1/n$ for $n > 0$ and $c_n = -1$ for $n = 0$. For the results presented in this chapter Φ is equal to 6; however, the methodology developed here puts no upper limit on its value. Equation 4.2 is based on the assumption that the ring gear is inextensional (see appendix B for a discussion on extensional and

where ϕ is the pressure angle, r_p is the planet base radius, r_r is the ring base radius, $\theta_i = \alpha_i + \phi - \cos^{-1}(r_r/R_r)$, and α_i is the position angle of the i^{th} planet in the rotating coordinate system. Forces acting in the radial ($F_{r_i}^{(r)}$) and tangential ($F_{r_i}^{(\theta)}$) directions on the ring gear due to the i^{th} planet can be calculated in terms of the ring-planet mesh force F_{rp} ($= k_{rp}\Delta_{rp}$), where k_{rp} is the ring-planet mesh stiffness. Therefore,

$$\begin{aligned} (F_{r_i}^{(r)}, F_{r_i}^{(\theta)})^T &= F_{rp} \left(\sqrt{1 - \left(\frac{r_r}{R_r}\right)^2}, -\frac{r_r}{R_r} \right)^T \\ &= k_{rp}\Delta_{rp} \left(\sqrt{1 - \left(\frac{r_r}{R_r}\right)^2}, -\frac{r_r}{R_r} \right)^T, \end{aligned} \quad (4.6)$$

where $(\bullet)^T$ is the transpose of the matrix (\bullet) . f_r and f_θ in equation 4.3 can now be expressed in terms of the point loads $F_{r_i}^{(r)}$ and $F_{r_i}^{(\theta)}$ as

$$f_r = \sum_{i=1}^z F_{r_i}^{(r)} \delta(\theta - \theta_i) \quad (4.7a)$$

and

$$f_\theta = \sum_{i=1}^z F_{r_i}^{(\theta)} \delta(\theta - \theta_i), \quad (4.7b)$$

where $\delta(\bullet)$ is the delta function and z is the number of planets.

Substituting equations 4.7 into 4.3 and expressing w_r and w_θ in terms of a_n and b_n , using equation 4.2, leads to the following equation of motion for the ring gear

$$\begin{aligned} \begin{pmatrix} \mathbf{M}_r & 0 \\ 0 & \mathbf{M}_r \end{pmatrix} \begin{pmatrix} \ddot{\mathbf{a}} \\ \ddot{\mathbf{b}} \end{pmatrix} + \begin{pmatrix} \boldsymbol{\omega}_r & 0 \\ 0 & \boldsymbol{\omega}_r \end{pmatrix} \begin{pmatrix} \mathbf{a} \\ \mathbf{b} \end{pmatrix} \\ + k_{rp} \left\{ \mathbf{K}_{21}^{\text{rp}} \mathbf{q}_p + \mathbf{K}_{22}^{\text{rp}} \begin{pmatrix} \mathbf{a} \\ \mathbf{b} \end{pmatrix} \right\} = 0. \end{aligned} \quad (4.8)$$

In equation 4.8 the sub-matrices are defined as follows

$$\mathbf{M}_r = \text{diag}(M_0, M_1, \dots, M_\Phi), \quad (4.9a)$$

$$\mathbf{a} = (a_0, a_1, \dots, a_\Phi)^T, \quad (4.9b)$$

$$\mathbf{b} = (b_0, b_1, \dots, b_\Phi)^T, \quad (4.9c)$$

$$\boldsymbol{\omega}_r = \text{diag}(M_0\omega_0'^2, M_1\omega_1'^2, \dots, M_\Phi\omega_\Phi'^2), \quad (4.9d)$$

$$\mathbf{q}_p = (\mathbf{q}_{p_1}, \mathbf{q}_{p_2}, \dots, \mathbf{q}_{p_z})^T, \quad (4.9e)$$

$$\mathbf{q}_{p_i} = (x_{p_i}, y_{p_i}, \theta_{p_i})^T. \quad (4.9f)$$

In addition,

$$\mathbf{K}_{21}^{\text{rp}} = ((\mathbf{K}_{21}^{\text{rp}})_1, (\mathbf{K}_{21}^{\text{rp}})_2, \dots, (\mathbf{K}_{21}^{\text{rp}})_z), \quad (4.10a)$$

$$(\mathbf{K}_{21}^{\text{rp}})_i = (A_0^i, A_1^i, \dots, A_\Phi^i, B_0^i, B_1^i, \dots, B_\Phi^i)^T (\sin\phi, \cos\phi, r_p), \quad (4.10b)$$

$$\mathbf{K}_{22}^{\text{rp}} = \sum_{i=1}^z \begin{pmatrix} \bar{\mathbf{A}}_{11}^i & \bar{\mathbf{A}}_{12}^i \\ \bar{\mathbf{A}}_{21}^i & \bar{\mathbf{A}}_{22}^i \end{pmatrix}. \quad (4.10c)$$

Also,

$$\bar{\mathbf{A}}_\odot^i = \begin{pmatrix} A_\odot^{(0,0)} & A_\odot^{(0,1)} & \dots & A_\odot^{(0,\Phi)} \\ A_\odot^{(1,0)} & A_\odot^{(1,1)} & \dots & A_\odot^{(1,\Phi)} \\ \vdots & \vdots & \ddots & \vdots \\ A_\odot^{(\Phi,0)} & A_\odot^{(\Phi,1)} & \dots & A_\odot^{(\Phi,\Phi)} \end{pmatrix} \text{ for } \odot = 11, 12, 21, 22, \quad (4.11a)$$

$$A_{11}^{(j,k)} = A_k^i A_j^i, A_{12}^{(j,k)} = B_k^i A_j^i, A_{21}^{(j,k)} = A_k^i B_j^i, A_{22}^{(j,k)} = B_k^i B_j^i, \quad (4.11b)$$

with

$$A_{(\bullet)}^i = \left(\sqrt{1 - \left(\frac{r_r}{R_r}\right)^2} \cos(\bullet)\theta_i - \frac{r_r}{R_r} c_j \sin(\bullet)\theta_i \right) \quad (4.12a)$$

and

$$B_{(\bullet)}^i = \left(\sqrt{1 - \left(\frac{r_r}{R_r}\right)^2} \sin(\bullet)\theta_i + \frac{r_r}{R_r} c_j \cos(\bullet)\theta_i \right). \quad (4.12b)$$

Symbol $(\bullet) = 0, 1, \dots, \Phi$ in equations 4.12. Equation 4.8 defines the motion of the ring gear in terms of modal participation factors a_n and b_n , which can be substituted into equation 4.2 to obtain the ring-gear response in the rotating coordinate system.

4.2.2 Equation of Motion for Planet Gears

Forces acting on the i^{th} planet due to planet-ring mesh force F_{rp} can be expressed in the rotating coordinate system as

$$\mathbf{F}_{rp_i} = k_{rp} \Delta_{rp} (-\sin\phi, \cos\phi, r_p)^T. \quad (4.13)$$

By considering the d'Alembert forces due to accelerations, we can write a force balance equation for the i^{th} planet gear of mass m_p and moment of inertia I_p (about z axis). Thus,

$$\begin{aligned} \mathbf{M}_{p_i} \ddot{\mathbf{q}}_{p_i} &= \mathbf{F}_{rp_i} + \mathbf{F}_{p_i} + \mathbf{F}_{sp_i} \\ &= k_{rp} \Delta_{rp} (-\sin\phi, \cos\phi, r_p)^T + \mathbf{F}_{p_i} + \mathbf{F}_{sp_i}, \end{aligned} \quad (4.14)$$

where matrix $\mathbf{M}_{p_i} = \text{diag}(m_{p_i}, m_{p_i}, I_{p_i})$, $m_{p_i} = m_p$ for $i \neq \Gamma$ and $m_{p_i} = m_p - m_b$ for $i = \Gamma$, $I_{p_i} = I_p$ for $i \neq \Gamma$ and $I_{p_i} = I_p - I_b$ for $i = \Gamma$, Γ is the index of the planet containing a defective bearing, m_b is the bearing inner-race mass, I_b is the bearing moment of inertia, $\mathbf{F}_{sp_i} = -(\mathbf{K}_{22}^{sp})_i \mathbf{q}_{p_i} - (\mathbf{K}_{21}^{sp})_i \mathbf{q}_s$ is the sun-planet mesh force and

$$\mathbf{F}_{p_i} = \begin{cases} \mathbf{F}_{cp_i} = -(\mathbf{K}_{22}^{cp})_i \mathbf{q}_{p_i} - (\mathbf{K}_{21}^{cp})_i \mathbf{q}_c & \text{if } i \neq \Gamma \\ \mathbf{F}_{bp_i} = -\mathbf{K}_{22}^{bp} \mathbf{q}_{p_i} - \mathbf{K}_{21}^{bp} \mathbf{q}_b & \text{if } i = \Gamma \end{cases}. \quad (4.15)$$

Matrices $\mathbf{K}_{22}^{bp} = \mathbf{K}_{11}^{bp}$ and $\mathbf{K}_{21}^{bp} = (\mathbf{K}_{12}^{bp})^T$. \mathbf{F}_{cp_i} and \mathbf{F}_{bp_i} are the carrier-planet and bearing-planet forces respectively.

Equation 4.15 describes the connection between the i^{th} planet, carrier and defective bearing inner-race. If i^{th} planet contains a defective bearing, i.e. $i = \Gamma$, then the planet is connected to the inner race of the defective bearing; but if the planet does not contain a defective bearing, i.e. $i \neq \Gamma$, then it is directly connected to the carrier. Substitution of equation 4.5 into 4.14 leads to

$$\mathbf{M}_p \ddot{\mathbf{q}}_{p_i} + k_{rp} \left\{ \mathbf{K}_{11}^{rp} \mathbf{q}_{p_i} + (\mathbf{K}_{12}^{rp})_i \begin{pmatrix} \mathbf{a} \\ \mathbf{b} \end{pmatrix} \right\} = \mathbf{F}_{p_i} + \mathbf{F}_{sp_i}, \quad (4.16)$$

where $(\mathbf{K}_{12}^{rp})_i = (\mathbf{K}_{21}^{rp})_i^T$ and

$$\mathbf{K}_{11}^{rp} = \begin{pmatrix} \sin^2\phi & -\sin\phi\cos\phi & -r_p\sin\phi \\ & \cos^2\phi & r_p\cos\phi \\ \text{symm.} & & r_p^2 \end{pmatrix}.$$

4.2.3 Equation of Motion for the Inner Race of Defective Bearing

Forces acting on the inner race of a defective bearing are due to the planet gear and carrier. If $\mathbf{F}_{\mathbf{b}p_i}$ is the force due to the planet gear and $\mathbf{F}_{\mathbf{b}c}$ is the force due to the carrier, then force equilibrium on the defective bearing inner-race is

$$\mathbf{M}_{\mathbf{b}}\ddot{\mathbf{q}}_{\mathbf{b}} = \mathbf{F}_{\mathbf{b}p_i} + \mathbf{F}_{\mathbf{b}c}, \quad (4.17)$$

where $\mathbf{M}_{\mathbf{b}} = \text{diag}(m_b, m_b, I_b)$. The forces acting on the defective bearing inner-race are

$$\mathbf{F}_{\mathbf{b}p_i} = \begin{pmatrix} -k_{bp}^r(x_b - x_{p_i}) \\ -k_{bp}^t(y_b - y_{p_i}) \\ 0 \end{pmatrix} \quad (4.18a)$$

and

$$\mathbf{F}_{\mathbf{b}c} = \begin{pmatrix} -k_{bc}^r(x_b - x_c \cos \alpha_i - y_c \sin \alpha_i) \\ -k_{bc}^t(y_b + x_c \sin \alpha_i - y_c \cos \alpha_i - r_c \theta_c) \\ -k_{bc}^\theta \theta_b \end{pmatrix}, \quad (4.18b)$$

where k_{bp}^r and k_{bp}^t are the radial and tangential stiffness between planet gear and defective bearing, and k_{bc}^r , k_{bc}^t and k_{bc}^θ are the radial, tangential and torsional stiffness between carrier and defective bearing.

Substitution of equations 4.18 into 4.17 yields

$$\mathbf{M}_{\mathbf{b}}\ddot{\mathbf{q}}_{\mathbf{b}} + \left(\mathbf{K}_{11}^{\mathbf{b}p} + \mathbf{K}_{22}^{\mathbf{c}b} \right) \mathbf{q}_{\mathbf{b}} + \mathbf{K}_{12}^{\mathbf{b}p} \mathbf{q}_{p_i} + \mathbf{K}_{21}^{\mathbf{c}b} \mathbf{q}_{\mathbf{c}} = 0, \quad (4.19)$$

where $\mathbf{K}_{11}^{\mathbf{b}p} = \text{diag}(k_{bp}^r, k_{bp}^t, 0)$, $\mathbf{K}_{12}^{\mathbf{b}p} = -\mathbf{K}_{11}^{\mathbf{b}p}$, $\mathbf{K}_{22}^{\mathbf{c}b} = \text{diag}(k_{bc}^r, k_{bc}^t, k_{bc}^\theta)$, and

$$\mathbf{K}_{21}^{\mathbf{c}b} = \begin{pmatrix} -k_{bc}^r \cos \alpha_i & -k_{bc}^r \sin \alpha_i & 0 \\ k_{bc}^t \sin \alpha_i & -k_{bc}^t \cos \alpha_i & -k_{bc}^t r_c \\ 0 & 0 & 0 \end{pmatrix}.$$

4.2.4 Equations of Motion for Carrier and Sun Gear

Equations of motion for carrier and sun gear are similar to the ones derived by Lin and Parker^[86], since in both formulations these components are treated as rigid bodies. The only difference in the carrier equation is due to the inclusion of the defective-bearing inner-race in the present analysis. So, if $i = \Gamma$ then the carrier is connected to a defective-bearing inner-race and if $i \neq \Gamma$ then the carrier is connected to the i^{th} planet. Hence,

equation for the carrier is

$$\begin{aligned} \mathbf{M}_c \ddot{\mathbf{q}}_c + \left\{ \mathbf{K}_B + \mathbf{K}_{11}^{cb} + \sum_{i=1:z}^{i \neq \Gamma} (\mathbf{K}_{11}^{cp})_i \right\} \mathbf{q}_c + \mathbf{K}_{12}^{cb} \mathbf{q}_b \\ + \sum_{i=1:z}^{i \neq \Gamma} \{ (\mathbf{K}_{12}^{cp})_i \mathbf{q}_{p_i} \} = 0 \end{aligned} \quad (4.20)$$

and equation for the sun gear is

$$\mathbf{M}_s \ddot{\mathbf{q}}_s + \left\{ \mathbf{K}_B + \sum_{i=1}^z (\mathbf{K}_{11}^{sp})_i \right\} \mathbf{q}_s + \sum_{i=1}^z \{ (\mathbf{K}_{12}^{sp})_i \mathbf{q}_{p_i} \} = 0, \quad (4.21)$$

where $\mathbf{M}_c = \text{diag}(m_c, m_c, I_c)$, $\mathbf{M}_s = \text{diag}(m_s, m_s, I_s)$, $\mathbf{K}_B = \text{diag}(k_b^x, k_b^y, 0)$ is the stiffness matrix of bearings supporting sun and carrier, and k_b^x and k_b^y are the support stiffness in x and y directions. Mesh stiffness matrices are defined in the appendix C.

4.2.5 Equation of Motion for the Combined System

The equation of motion of the combined system in the fixed coordinate system ($X_f Y_f Z_f$ in figure 4.1) can be written as

$$\mathbf{M}_{\text{sys}} \ddot{\bar{\mathbf{q}}} + \bar{\mathbf{K}}_{\text{sys}} \bar{\mathbf{q}} = \bar{\mathbf{F}}, \quad (4.22)$$

where \mathbf{M}_{sys} is the system mass matrix, $\bar{\mathbf{K}}_{\text{sys}}$ is the system stiffness matrix in the fixed coordinate system, $\bar{\mathbf{F}}$ is the external force matrix and $\bar{\mathbf{q}}$ is the matrix containing the components' coordinates in the fixed coordinate system. Since all the system components are axi-symmetric (about Z axis), mass matrices in the fixed and the rotating coordinate systems are same. System stiffness matrix, $\bar{\mathbf{K}}_{\text{sys}}$, will vary with time due to a continuous change in the planet position caused by the carrier rotation. To avoid this time-varying stiffness in equation 4.22, we can take advantage of the cyclic symmetry of the structure and formulate the equation of motion in the coordinate system XYZ (figure 4.1) which is rotating with the carrier. Now, the system coordinate matrix (\mathbf{q}) in the rotating coordinate system becomes

$$\mathbf{q} = \mathbf{T} \bar{\mathbf{q}} \quad \text{or} \quad \bar{\mathbf{q}} = \mathbf{T}^T \mathbf{q}, \quad (4.23)$$

where \mathbf{T} is the transformation matrix (defined in appendix C). Substitution of equation 4.23 into 4.22 and multiplying the equation by \mathbf{T} yields

$$\mathbf{M}_{\text{sys}}\ddot{\mathbf{q}} + \omega_c \mathbf{C}_L \dot{\mathbf{q}} + (\mathbf{K}_{\text{sys}} - \omega_c^2 \mathbf{K}_c) \mathbf{q} = \mathbf{F}, \quad (4.24)$$

where $\mathbf{F} = (\mathbf{F}_s, \mathbf{F}_r, \mathbf{F}_{p_1}, \dots, \mathbf{F}_{p_z}, \mathbf{F}_b, \mathbf{F}_c)^T = \mathbf{T}\bar{\mathbf{F}}$, $\mathbf{K}_{\text{sys}} = \mathbf{T}\bar{\mathbf{K}}_{\text{sys}}\mathbf{T}^T$, \mathbf{C}_L is a skew-symmetric Coriolis matrix, and \mathbf{K}_c is the centripetal matrix. Carrier speed ω_c for a typical wind-turbine planetary-drive is small (typically 10-15 rpm). At such low speeds, the effects of Coriolis and centripetal terms are small and are neglected in the current analysis (see appendix D for an explanation). Hence, equation 4.24 becomes

$$\mathbf{M}_{\text{sys}}\ddot{\mathbf{q}} + \mathbf{K}_{\text{sys}}\mathbf{q} = \mathbf{F}, \quad (4.25)$$

where $\mathbf{q} = (\mathbf{q}_s, \mathbf{q}_r, \mathbf{q}_{p_1}, \dots, \mathbf{q}_{p_z}, \mathbf{q}_b, \mathbf{q}_c)^T$ and $\mathbf{q}_r = (\mathbf{a}, \mathbf{b})^T$. Substituting $\mathbf{q} = \mathbf{u}e^{i\omega t}$ (where $i^2 = -1$) and $\mathbf{F} = 0$ into equation 4.25 gives

$$-\omega^2 \mathbf{M}_{\text{sys}}\mathbf{u} + \mathbf{K}_{\text{sys}}\mathbf{u} = 0. \quad (4.26)$$

See appendix C for the formulation of \mathbf{M}_{sys} and \mathbf{K}_{sys} . Equation 4.26 is the eigenvalue problem and its solution gives us the system natural frequencies $\Omega_1, \Omega_2, \dots, \Omega_N$ and mode-shapes $\mathbf{u}^{(1)}, \mathbf{u}^{(2)}, \dots, \mathbf{u}^{(N)}$ associated with each natural frequency. The corresponding modal matrix is $\mathbf{U} = (\mathbf{u}^{(1)}, \mathbf{u}^{(2)}, \dots, \mathbf{u}^{(N)})$ with $\mathbf{u}^{(r)} = (\mathbf{u}_s^{(r)}, \mathbf{u}_r^{(r)}, \mathbf{u}_{p_1}^{(r)}, \dots, \mathbf{u}_{p_z}^{(r)}, \mathbf{u}_b^{(r)}, \mathbf{u}_c^{(r)})^T$ for $r = 1$ to N and $\mathbf{u}_r^{(r)} = (u_{a_0}^{(r)}, \dots, u_{a_\Phi}^{(r)}, u_{b_0}^{(r)}, \dots, u_{b_\Phi}^{(r)})^T$. N is the number of modes.

4.3 Derivation of Frequency-Response Function

Substitution of $\mathbf{q} = \mathbf{U}\eta$ and $\mathbf{F} = \mathbf{U}\mathbf{Q}$ into equation 4.25 and pre-multiplication with \mathbf{U}^T gives an uncoupled equation in terms of generalized coordinates η .

$$\ddot{\eta}(t) + \mathbf{\Omega}\eta = \mathbf{Q}, \quad (4.27)$$

where $\mathbf{\Omega} = \text{diag}(\Omega_1^2, \dots, \Omega_N^2)$ and \mathbf{Q} is the generalized force matrix. From equation 4.27 a generalized equation for r^{th} coordinate, with modal damping factor ξ_r , can be written as

$$\ddot{\eta}_r + 2\xi_r \Omega_r \dot{\eta}_r + \Omega_r^2 \eta_r = Q_r. \quad (4.28)$$

Now consider a defect located at an angle γ in the rotating coordinate system on inner race, outer race or rolling element of a planet bearing with position angle θ^* (figure 4.4(a)).

Table 4.1: Model parameters for a typical 2MW wind-turbine planetary drivetrain (number of planets, $z = 3$). Symbols r , R , m and I take the subscript s for sun, p_i for i^{th} planet, r for ring and c for carrier.

Parameter	Sun	Planet	Ring	Carrier
Base radius (r), mm	144.2	265.6	675.3	436.6
Pitch radius (R), mm	153.6	283	743.3	-
Face-width (ℓ), mm			325	
Density (ρ), kg/m ³			7800	
Mass (m), kg	188	638	958	374
Inertia (I), kg.m ²	2.2	25.5	617.4	35.6
Parameter	Planet bearing			
Number of rollers (Z_b)			16	
Roller radius (r_b), mm			27	
Pitch radius (R_b), mm			156.5	
Inner-race mass (m_b), kg (including planet pin)			410	
Inertia (I_b), kg.m ²			10.6	
Material			Steel	
Ring gear thickness (h), mm			75	
Mesh stiffness, N/m			$k_{sp} = k_{rp} = 5 \times 10^8$	
Ring support stiffness, N/m ³			$K_r = 10^8/\ell, K_\theta = 5 \times 10^8/\ell$	
Carrier coupling stiffness, N/m			$k_{cb}^{r,t} = 2 \times 10^8, k_{cp}^{r,t} = 10^8$	
Planet bearing stiffness, N/m			$k_{bp}^{r,t} = 3 \times 10^8$	
Support stiffness, N/m			$k_b^{x,y} = 10^8$	

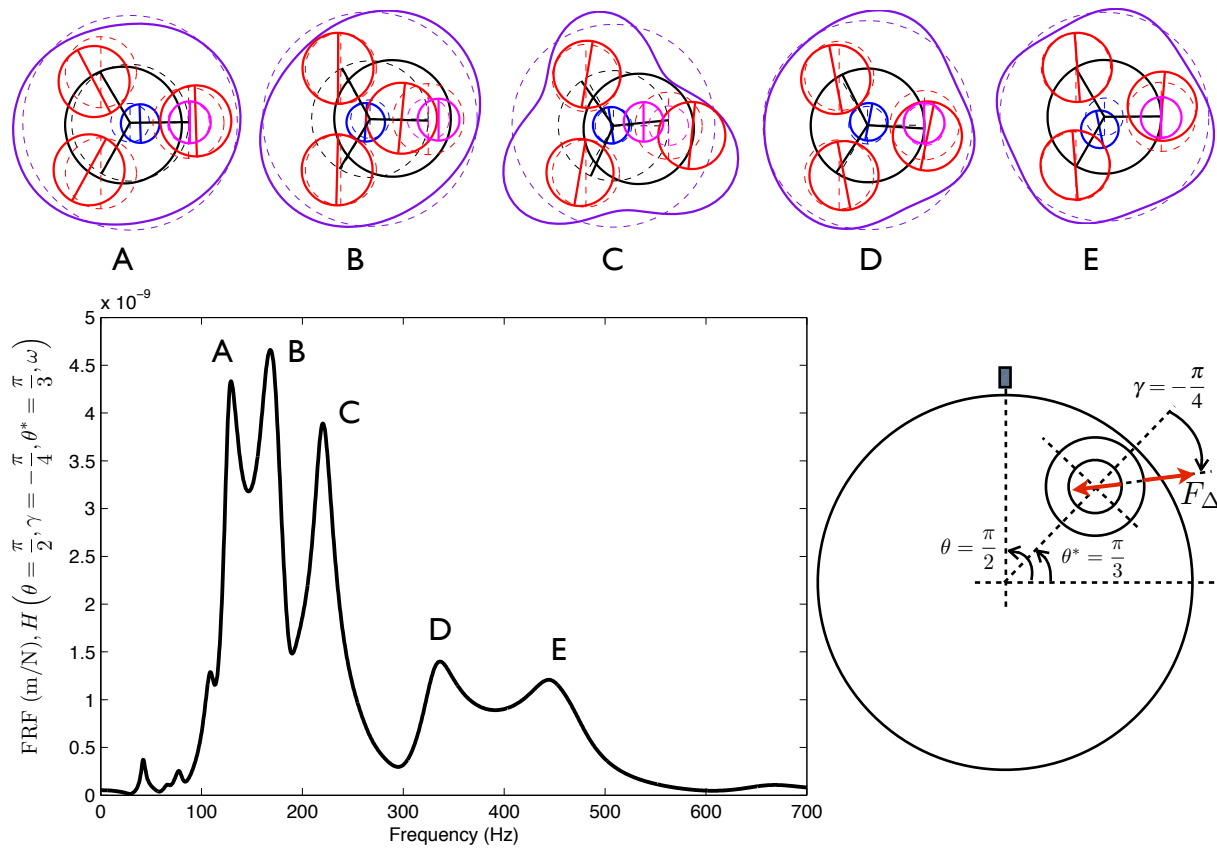


Figure 4.3: An example of the frequency-response function of a planet-bearing fault with (A,B,C,D,E) five dominant mode-shapes for $\theta = \frac{\pi}{2}$, $\theta^* = \frac{\pi}{3}$ and $\gamma = -\frac{\pi}{4}$. Ring gear deforms in all the five dominant modes.

Due to the dynamic interaction between the defect and the rolling elements, a force F_Δ is applied to the i^{th} planet gear ($i = \Gamma$) as well as the defective-bearing inner-race in opposite directions. Therefore,

$$\mathbf{F}_{\mathbf{p}_i} = F_\Delta(\cos\gamma, \sin\gamma, 0)^T \quad (4.29a)$$

and

$$\mathbf{F}_{\mathbf{b}} = -\mathbf{F}_{\mathbf{p}_i}. \quad (4.29b)$$

Using $\mathbf{Q} = \mathbf{U}^T \mathbf{F}$, a generalized force for the r^{th} coordinate can be calculated as

$$\begin{aligned} Q_r &= (\mathbf{u}_{p_i}^{(r)})^T \mathbf{F}_{\mathbf{p}_i} + (\mathbf{u}_{\mathbf{b}}^{(r)})^T \mathbf{F}_{\mathbf{b}} \\ &= (u_{pb_x}^{(r)} \cos\gamma + u_{pb_y}^{(r)} \sin\gamma) F_\Delta, \end{aligned} \quad (4.30)$$

where $\mathbf{u}_{p_i}^{(r)} = (u_{p_{i_x}}^{(r)}, u_{p_{i_y}}^{(r)}, u_{p_{i_\theta}}^{(r)})^T$, $\mathbf{u}_{\mathbf{b}}^{(r)} = (u_{b_x}^{(r)}, u_{b_y}^{(r)}, u_{b_\theta}^{(r)})^T$ and $u_{pb(\bullet)}^{(r)} = u_{p_i(\bullet)}^{(r)} - u_{b(\bullet)}^{(r)}$. Substitution of equation 4.30 into 4.28 gives

$$\ddot{\eta}_r + 2\xi_r \Omega_r \dot{\eta}_r + \Omega_r^2 \eta_r = (u_{pb_x}^{(r)} \cos\gamma + u_{pb_y}^{(r)} \sin\gamma) F_\Delta. \quad (4.31)$$

Putting $\eta_r(t) = \eta_r(\omega)e^{i\omega t}$ and $F_\Delta(t) = F_\Delta(\omega)e^{i\omega t}$ into equation 4.31 leads to

$$\eta_r(\omega) = \left(\frac{u_{pb_x}^{(r)} \cos\gamma + u_{pb_y}^{(r)} \sin\gamma}{\Omega_r^2 - \omega^2 + 2i\xi_r \omega \Omega_r} \right) F_\Delta(\omega). \quad (4.32)$$

Now, using $\mathbf{q} = \mathbf{U}\eta$ and the transformation matrix defined by equation 4.23, we can calculate the modal participation factors for the ring gear in the fixed coordinate system $X_f Y_f Z_f$. Hence,

$$\bar{a}_n(\omega) = C_{n\theta^*} \sum_{r=1}^N u_{a_n}^{(r)} \eta_r(\omega) - S_{n\theta^*} \sum_{r=1}^N u_{b_n}^{(r)} \eta_r(\omega) \quad (4.33a)$$

and

$$\bar{b}_n(\omega) = S_{n\theta^*} \sum_{r=1}^N u_{a_n}^{(r)} \eta_r(\omega) + C_{n\theta^*} \sum_{r=1}^N u_{b_n}^{(r)} \eta_r(\omega), \quad (4.33b)$$

where $C_{(\bullet)} = \cos(\bullet)$ and $S_{(\bullet)} = \sin(\bullet)$. From equations 4.33 and 4.2, ring-gear response in the radial and tangential directions are obtained and corresponding frequency-response

functions (FRFs) are also calculated. FRF for the ring-gear radial-response is

$$\begin{aligned}
 H(\gamma, \theta^*, \theta, \omega) &= \frac{\bar{W}_r(\theta, \omega)}{F_\Delta(\omega)} = \frac{\sum_{n=0}^{\Phi} \{\bar{a}_n(\omega)C_{n\theta} + \bar{b}_n(\omega)S_{n\theta}\}}{F_\Delta(\omega)} \\
 &= \sum_{r=1}^N \frac{u_{pb_x}^{(r)} \cos\gamma + u_{pb_y}^{(r)} \sin\gamma}{\Omega_r^2 - \omega^2 + 2l\xi_r\omega\Omega_r} \sum_{n=0}^{\Phi} [\{C_{n\theta}C_{n\theta^*} \\
 &\quad + S_{n\theta}S_{n\theta^*}\} u_{a_n}^{(r)} + \{S_{n\theta}C_{n\theta^*} - C_{n\theta}S_{n\theta^*}\} u_{b_n}^{(r)}]. \quad (4.34)
 \end{aligned}$$

FRF given by equation 4.34 is a function of the position angles of the fault (γ), the carrier (θ^*), and the measurement point (θ). Figure 4.3 shows an example of the FRF calculated for $\theta = \frac{\pi}{2}$, $\theta^* = \frac{\pi}{3}$ and $\gamma = -\frac{\pi}{4}$. The damping $\xi_r = 0.05$ for all coordinates r , this value of 5% is commonly used in structural vibration problems. The exact value of the damping does not really influence the outcome of the method developed here. Model parameters are listed in table 4.1. Ring gear deforms in all the dominant modes (A, B, C, D, E) and it does not behave as a rigid body. Therefore, flexibility of the ring is important for the accurate response prediction. If both $u_{pb_x}^r$ and $u_{pb_y}^r$ are zero in equation 4.34, FRF will be zero. This is because the presence of a fault will apply an impulsive force to the inner and the outer raceways, which will cause the defective-bearing inner-race and the planet gear to move apart. Hence, all the modes in which there is no relative motion between a defective bearing and the planet gear containing this defective bearing will not be present in the response spectrum. This is also confirmed by figure 4.3 in which all the dominant modes have relative displacement between the planet gear and the defective-bearing inner-race.

4.4 Vibration Signatures of Planet-Bearing Faults

In the previous section we have observed that the FRF of a planet-bearing fault is the function of fault-position angle and carrier-rotation angle. As a fault rotates around the bearing centre and the bearing rotates with the carrier, these angles change and as a result, FRF changes. This complicates the response calculation as for each impact between a rolling element and a fault, we have a different FRF. In the following paragraph, we discuss our approach of response calculation for the system with time-varying FRF.

The impact force produced when rolling elements strike a localized fault is modelled as an impulse train shown in figure 4.4. The frequency of the impulse train ω_d is the characteristic fault frequency and its value depends on the bearing geometry and operating

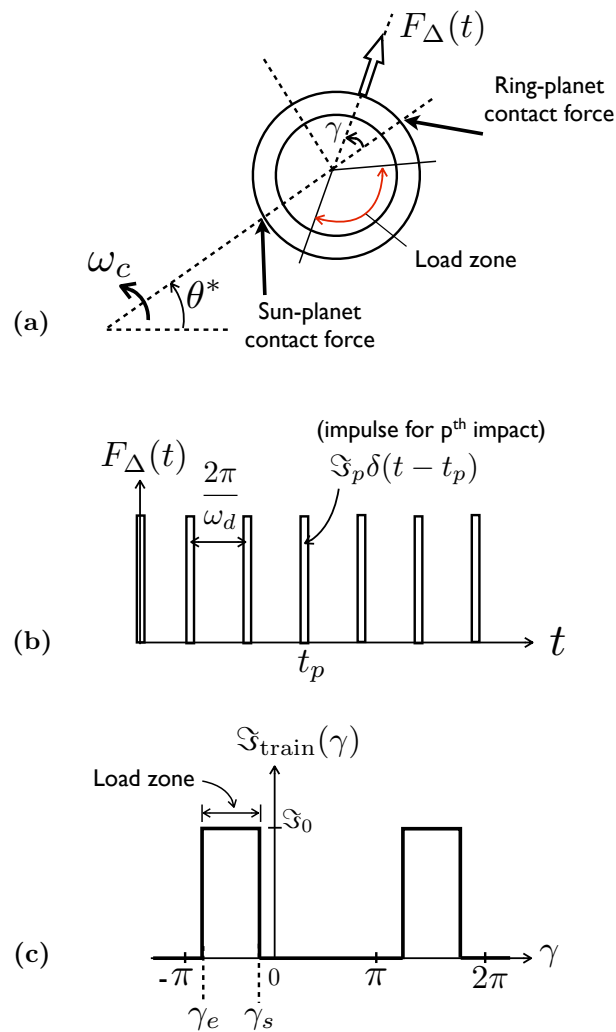


Figure 4.4: (a) Free-body diagram of a planet bearing showing formation of load zone; (b) A train of impulses due to bearing fault; (c) Impulse-train function showing non-zero impulse value inside a load zone and zero impulse value outside a load zone.

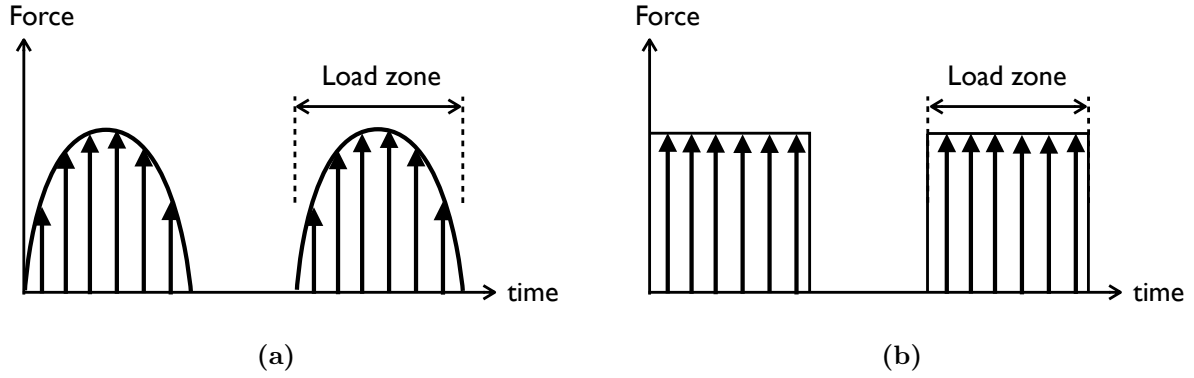


Figure 4.5: (a) Impulse train with impulse proportional to rolling-element load, (b) Impulse train with impulse proportional to rolling-element speed

speed. This impulse train can be represented by

$$F_{\Delta}(t) = \sum_{p=0}^{\infty} \mathfrak{S}_p \delta(t - t_p), \quad (4.35)$$

where \mathfrak{S}_p is the impulse due to p^{th} impact and $t_p (= 2\pi p/\omega_d)$ is the time at which p^{th} impact occurs. If the impulse-response function for the p^{th} impact is $h_p(t)$, radial response of the ring gear at angle θ due to p^{th} impact can be calculated using convolution theorem as

$$\bar{w}_r^p(\theta, t) = \int_0^t \mathfrak{S}_p \delta(s - t_p) h_p(t - s) ds = h_p(t - t_p) \mathfrak{S}_p. \quad (4.36)$$

The combined response for all the impacts can be written as

$$\bar{w}_r(\theta, t) = \sum_{p=0}^{\infty} \bar{w}_r^p(\theta, t) = \sum_{p=0}^{\infty} h_p(t - t_p) \mathfrak{S}_p. \quad (4.37)$$

Fourier transform of equation 4.37 gives us the response in frequency domain. Thus,

$$\begin{aligned} \bar{W}_r(\theta, \omega) &= \int_{-\infty}^{+\infty} \bar{w}_r(\theta, t) e^{-i\omega t} dt = \sum_{p=0}^{\infty} \mathfrak{S}_p \int_{-\infty}^{\infty} h_p(t - t_p) e^{-i\omega t} dt = \sum_{p=0}^{\infty} H_p(\omega) e^{-i\omega t_p} \mathfrak{S}_p \\ &= \sum_{p=0}^{\infty} H(\gamma_p, \theta^* = \omega_c t_p, \theta, \omega) e^{-i\omega t_p} \mathfrak{S}_p, \end{aligned} \quad (4.38)$$

where γ_p is the position angle of the fault relative to carrier at the time t_p .

The next step is to determine the impulse \mathfrak{S}_p due to the p^{th} impact. According to McFadden and Smith^[90], impacts generated when a rolling element passes through a

localized fault are proportional to the contact force acting on the rolling element (figure 4.5a). In the current analysis, however, we use an impulse train (figure 4.5b) based on the assumption that the impulse due to a bearing fault is: (i) proportional to the speed of the rolling element and independent of contact force inside the load zone, and (ii) zero outside the load zone. We provide a theoretical and an experimental justification to this assumption later in section 4.7. Impulse due to the p^{th} impact can be described as

$$\mathfrak{S}_p = \mathfrak{S}_{\text{train}}(\gamma_p), \quad (4.39)$$

where $\mathfrak{S}_{\text{train}}$ is the impulse-train function. Planetary bearings are radially loaded, which results in load-zone formation as shown in the figure 4.4. If γ_s and γ_e represent the start and end of loaded zone, the impulse-train function can be expressed in terms of γ using Fourier series. Thus

$$\mathfrak{S}_{\text{train}}(\gamma) = \mathfrak{S}_0 \sum_{m=-\infty}^{\infty} \epsilon_m e^{im\gamma}, \quad (4.40)$$

where \mathfrak{S}_0 is the impulse inside the load zone and $\epsilon_m = \frac{-C_m\gamma_s + C_m\gamma_e - i(-S_m\gamma_s + S_m\gamma_e)}{2\pi im}$. For the results presented in this chapter we have used $\gamma_s = 0$ and $\gamma_e = -\pi$, i.e., size of the load zone is assumed to be 180° . This assumption is made just for simplicity, and the analytical model developed in chapter is valid for the load zone of any size. The size of the load zone does not influence the frequencies associated with the vibration signatures of planet-bearing faults described later, it only influences the amplitudes at those frequencies. For $\gamma_s = 0$ and $\gamma_e = -\pi$, ϵ_m becomes

$$\epsilon_m = \begin{cases} 0 & \text{for } m \text{ even} \\ -1/i\pi m & \text{for } m \text{ odd} \\ 1/2 & \text{for } m = 0. \end{cases} \quad (4.41)$$

Substitution of equations 4.39 and 4.40 into equation 4.38 yields

$$\bar{W}_r(\theta, \omega) = \sum_{p=0}^{\infty} \sum_{m=-\infty}^{\infty} H(\gamma_p, \theta^* = \omega_c t_p, \theta, \omega) e^{-i\omega t_p} \mathfrak{S}_0 \epsilon_m e^{im\gamma_p}. \quad (4.42)$$

Equation 4.42 gives us the frequency response of a ring gear at angle θ in the presence of a localized planet-bearing fault. Other parameters used for the results presented in this chapter are $\mathfrak{S}_0 = 1$ Ns, $\xi_r = 0.05$ and $\omega_c = 10$ rpm.

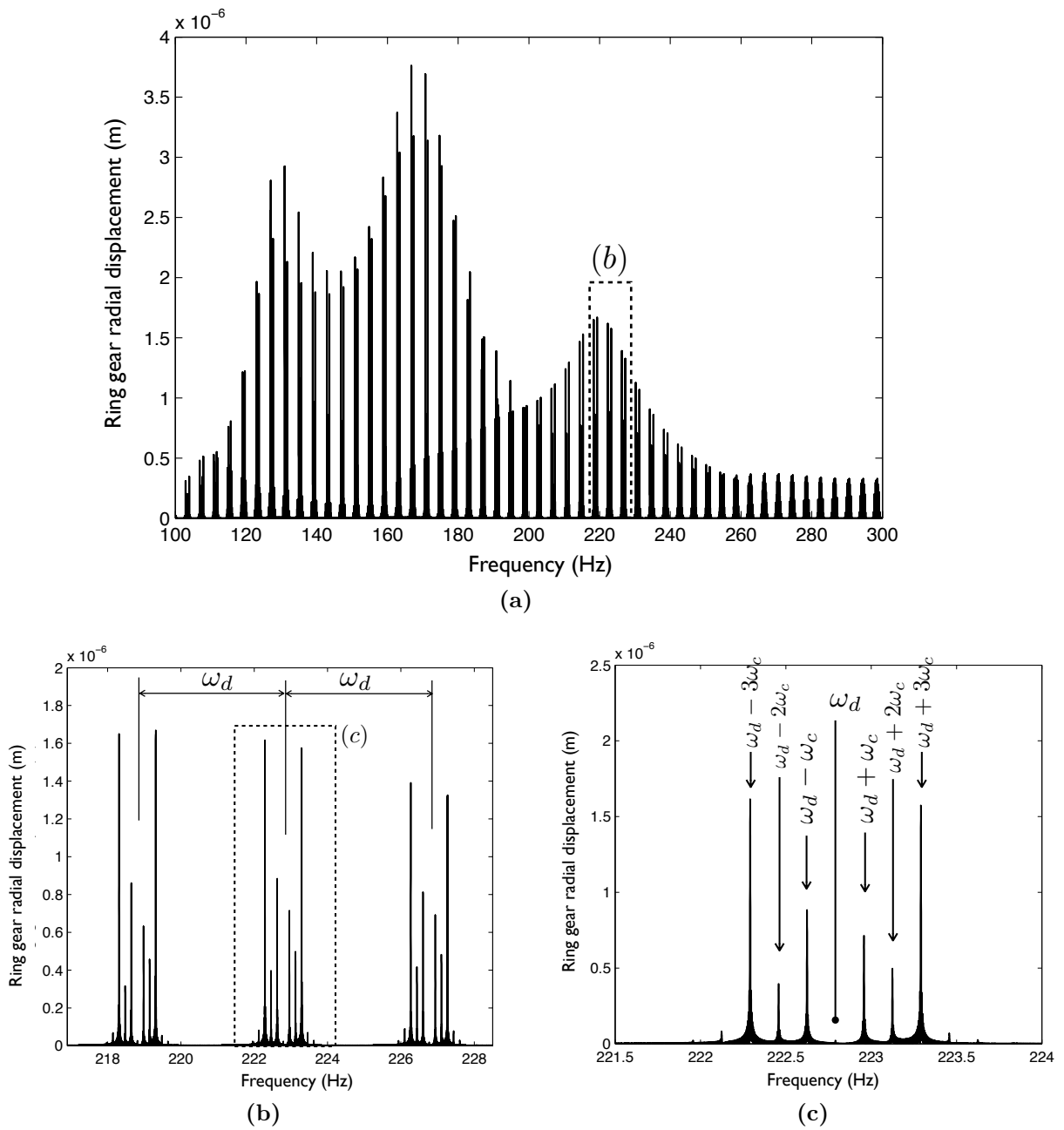


Figure 4.6: Analytical vibration signature of a planet-bearing inner-race fault located at an angle $\gamma_0 = -\pi/4$, (a) frequency response, (b) clusters of peaks separated by ω_d , (c) sidebands within a cluster separated by carrier frequency ω_c .

4.4.1 Fault Located on an Inner Race

A localized fault located on inner race of a planet bearing does not move relative to carrier and bearing load-zone. Therefore, position angle of the fault relative to carrier for p^{th} impact (γ_p) remains constant for all the impacts, i.e.,

$$\gamma_p = \gamma_0 \quad \text{for all } p. \quad (4.43)$$

Here γ_0 is the fault-location angle. Substitution of equation 4.43 into 4.42 yields

$$\bar{W}_r(\theta, \omega) = \sum_{p=0}^{\infty} \sum_{m=-\infty}^{\infty} H(\gamma_0, \theta^* = \omega_c t_p, \theta, \omega) e^{-i\omega t_p} \mathfrak{S}_0 \epsilon_m e^{im\gamma_0}. \quad (4.44)$$

Equation 4.44 gives us the vibration signature of a planet-bearing inner-race fault. Characteristic fault-frequency (ω_d), in equation 4.44, for an inner-race fault is defined as

$$\omega_d = \frac{z_b}{2} (\omega_p - \omega_c) \left(1 + \frac{r_b}{R_b} \right). \quad (4.45)$$

Here, z_b is the number of rolling elements in a planet bearing, r_b is the radius of a rolling element, and R_b is the planet-bearing pitch radius.

Let us take an example of a wind turbine planetary drivetrain with parameters defined in table 4.1. One of the planet bearings has a localized inner-race fault. Figure 4.6 shows the vibration response at a measurement point fixed on the ring gear ($\theta = \pi/2$) calculated using equation 4.44. The response contains clusters of peaks separated by characteristic fault-frequency ω_d . This is because the Fourier transform of a time-domain impulse-train is an impulse train in frequency domain. The period of time-domain impulse-train due to bearing inner-race fault is $2\pi/\omega_d$, which results in the frequency separation of ω_d between two consecutive clusters in figure 4.6. Each cluster contains several sidebands separated by the carrier rotation frequency ω_c . These sidebands are caused by the amplitude and frequency modulation of the signal due to carrier rotation. Measurement point is fixed on the ring gear, but the fault is rotating with the carrier with a speed ω_d . This continuous relative motion between the measurement point and the fault results in time-varying vibration transmission-path, which generates modulation sidebands separated by the speed of the fault relative to the measurement point (ω_c). This is analogous to Doppler effect.

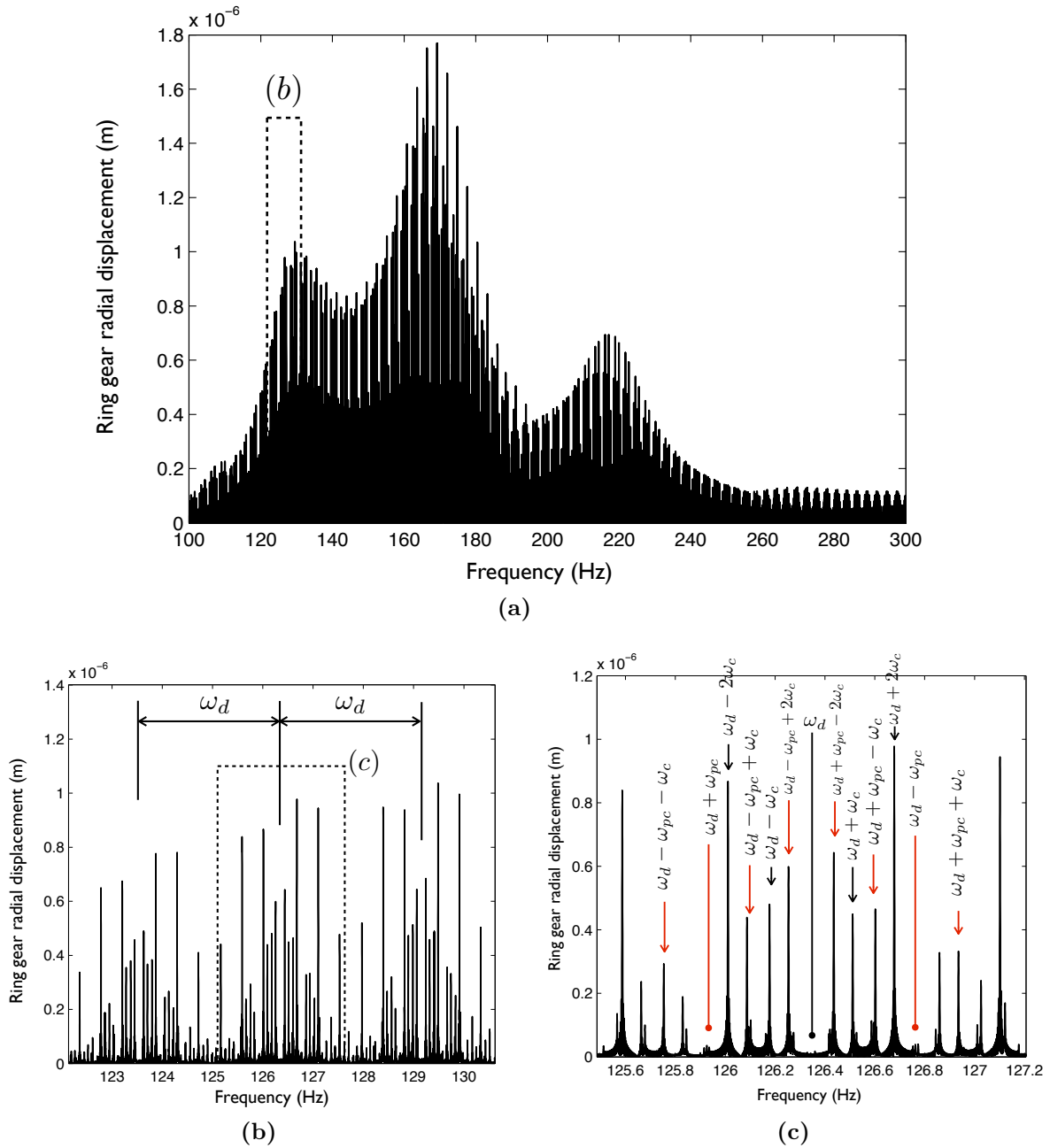


Figure 4.7: Analytical vibration signature of a planet-bearing outer-race fault, (a) frequency response, (b) clusters of peaks separated by ω_d , (c) sidebands within a cluster separated by the planet frequency relative to carrier ω_{pc} and the carrier frequency ω_c .

4.4.2 Fault Located on an Outer Race

Outer race of a planet bearing is fixed to a planet gear. Sometimes planet gear itself acts as the outer race. A fault located on an outer race of a planet bearing rotates with the planet gear with a speed ω_{pc} ($= \omega_p - \omega_c$) relative to carrier. Therefore, position angle of the fault relative to carrier for p^{th} impact becomes

$$\gamma_p = \omega_{pc} t_p = 2\pi p \frac{\omega_{pc}}{\omega_d}. \quad (4.46)$$

Characteristic fault-frequency for an outer-race fault is defined as

$$\omega_d = \frac{z_b}{2} (\omega_p - \omega_c) \left(1 - \frac{r_b}{R_b} \right). \quad (4.47)$$

Substitution of equations 4.46 and 4.47 into equation 4.42 gives us the vibration signature of a planet-bearing outer-race fault.

Figure 4.7 shows the vibration response calculated at a measurement point fixed on the ring gear ($\theta = \pi/2$). Again, like the previous case, response contains clusters (of peaks) separated by the characteristic fault-frequency ω_d , and within each cluster we have several sidebands. But, unlike the inner-race defect signature, we now have two families of sidebands: first with peaks separated by ω_c , and second with peaks separated by ω_{pc} . The first family of sidebands is caused by the variation in vibration transmission-path. The second family of sidebands is caused by two additional sources.

First source is the amplitude modulation caused by the variation in impulse magnitude as the fault passes through the load zone. According to the impulse train of figure 4.5b, impulse inside the load zone is non zero and impulse outside the load zone is zero. Due to this variation in impulse magnitude, the vibration signal gets modulated by the impulse-train defined by equation 4.40 and we get modulation sidebands separated by ω_{pc} .

Second source is the amplitude modulation caused by the variation in impulse direction. Vibration is transmitted from the defective planet-bearing to the ring gear through the mesh spring between the planet and the ring gears. An outer-race fault rotates relative to this mesh spring with a frequency ω_{pc} . Impulse due a fault acts along the position angle of the fault. When the impulse is parallel to the mesh spring, maximum force transmission takes place; and when the impulse is perpendicular to the mesh spring, minimum force transmission takes place. This variation in the force transmission results in modulation sidebands separated by the frequency ω_{pc} .

4.4.3 Fault Located on a Rolling Element

A localized fault located on a rolling element generates two impulses during one rotation of the rolling element - one when it strikes the inner race and other when it strikes the outer race. In this analysis, we assume that the two impulses are identical in magnitude. Similar to the outer-race fault, a fault located on a rolling element rotates relative to the carrier. The position angle of a rolling element fault relative to the carrier is

$$\gamma_p = \Omega t_p = 2\pi p \frac{\Omega}{\omega_d}, \quad (4.48)$$

where Ω is the speed of the planet-bearing cage relative to the carrier. Characteristic fault-frequency for a rolling-element fault is

$$\omega_d = (\omega_p - \omega_c) \left(\frac{R_b}{r_b} - \frac{r_b}{R_b} \right). \quad (4.49)$$

Substitution of equations 4.48 and 4.49 into equation 4.42 gives us the vibration signature of a localized fault located on a rolling element of a planet bearing.

Figure 4.8 shows the vibration response calculated at the ring gear. The response is similar to the outer-race fault with two families of sidebands caused by three modulation sources. The only difference is that in the case of a rolling-element fault, sidebands due to variation in impulse magnitude and direction are separated by Ω not ω_{pc} . This is because a rolling-element fault moves relative to the load zone and the ring-planet mesh-spring with frequency Ω .

4.4.4 Sources of Modulation Sidebands

In the previous three sections (4.4.1, 4.4.2 and 4.4.3), we have observed that the vibration signatures of planet-bearing inner-race, outer-race and rolling-element faults are complicated because of the presence of various modulation sidebands. In the following paragraphs we summarize the sources of these modulation sidebands.

- *Variation in impulse magnitude.* This is caused by the rotation of a fault relative to a load zone. Load zone of a planet bearing is fixed relative to the carrier, and a fault rotates with a speed ω_{pc} (if located on the outer race) or Ω (if located on a rolling element) relative to the carrier. This results in a relative rotation between the fault and the load zone. Impulse magnitude is non zero when the fault is inside the load zone, and impulse magnitude is zero when the fault is outside the load zone (figure 4.5b). This change in impulse magnitude modulates the defect signal and

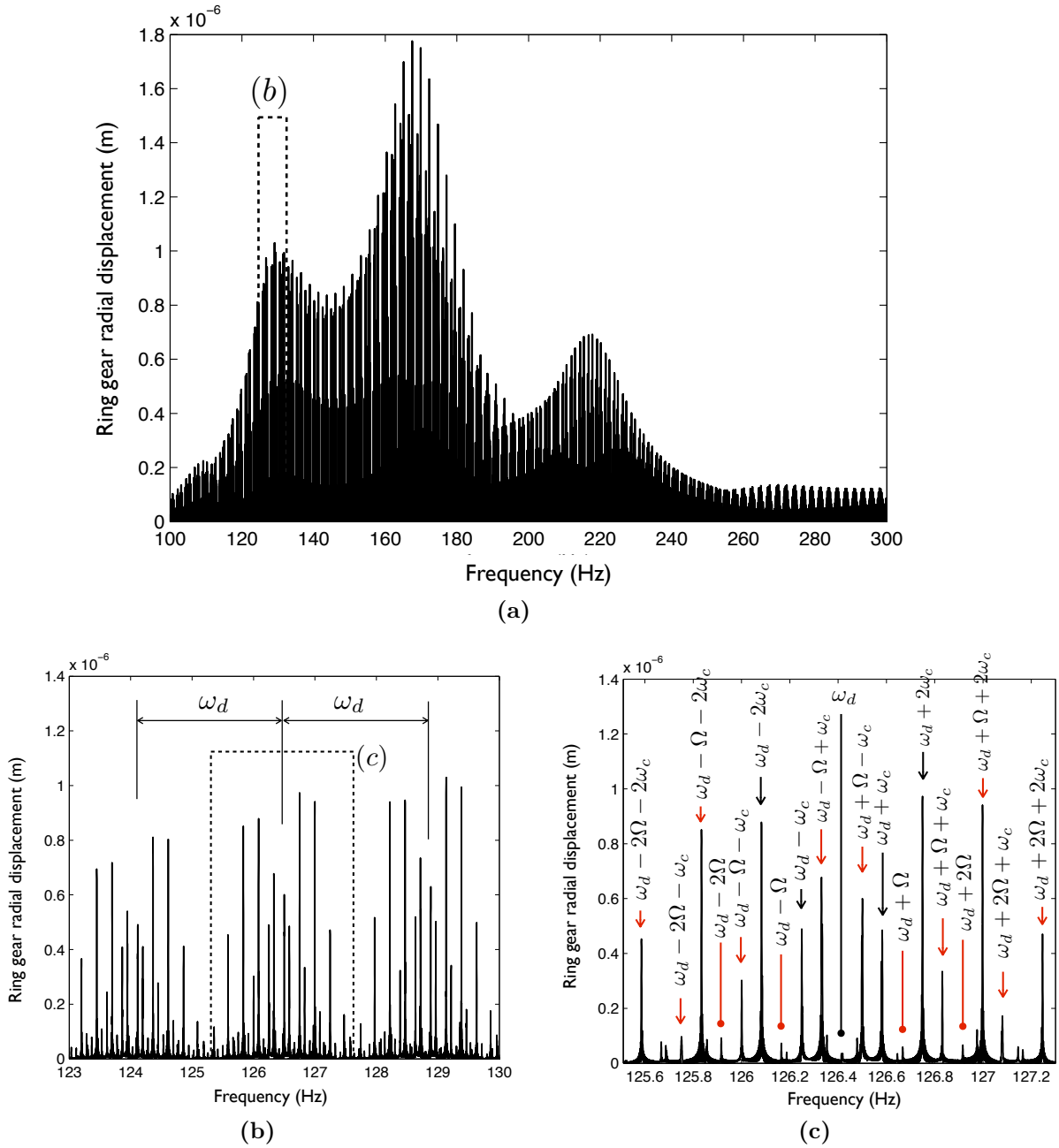


Figure 4.8: Analytical vibration signature of a planet-bearing rolling-element fault, (a) frequency response, (b) clusters of peaks separated by ω_d , (c) sidebands within a cluster separated by the frequency of the planet-bearing cage relative to carrier Ω and the carrier frequency ω_c .

generates sidebands separated by the integer multiples of ω_{pc} (for outer-race fault) and Ω (for rolling-element fault). In the frequency-response spectrum we get peaks at $p\omega_d + m\omega_{pc}$ (for outer-race fault) and $p\omega_d + m\Omega$ (for rolling-element fault), where integer $p \geq 0$ and m is any integer including zero.

- *Variation in impulse direction.* When a rolling element strikes a fault, the direction of the impulse vector is along the position angle of the fault. In a planet bearing, fault rotates with a speed ω_{pc} (if located on outer race) or Ω (if located on a rolling element) relative to carrier. Ring-planet mesh-spring is always aligned with the line-of-action of the gear pair, which is fixed relative to the carrier. Ring-gear response is maximum when the impulse vector is parallel to the ring-planet mesh, ring-gear response is minimum when the impulse vector is perpendicular to the ring-planet mesh. Therefore, as the fault rotates relative to the ring-planet mesh, ring-gear response varies sinusoidally with frequency ω_{pc} (for outer-race fault) and Ω (for rolling-element fault); and we get a pair of sidebands at $p\omega_d \pm \omega_{pc}$ (for outer-race fault) and $p\omega_d \pm \Omega$ (for rolling-element fault).
- *Variation in vibration transmission-path.* This is caused by the rotation of carrier. Defective bearing rotates with the carrier relative to a measurement point (fixed on the ring gear) with a speed ω_c . This relative rotation changes the vibration transmission-path between a planet-bearing fault and a measurement point. This variation in the vibration transmission path results in amplitude-modulation sidebands separated by carrier frequency ω_c and we get peaks at $p\omega_d \pm n\omega_c$, where integer $n \geq 0$. Relative motion between the fault and the measurement point also results in frequency modulation of the signal and we get sidebands separated by the relative speed ω_c , but these sidebands are less pronounced compared to the amplitude-modulated sidebands because the impulse duration is small.

For the case of an inner-race fault, the fault does not move relative to the load zone or the ring-planet mesh and the only source of modulation is due the variation in vibration transmission-path caused by the carrier rotation. For the case of an outer-race fault, all the three sources of modulation are present. By combining all the three sources of modulation described above, we can define the sideband behaviour within each cluster of figure 4.7 by $p\omega_d + (m \pm 1)\omega_{pc} \pm n\omega_c$. Similarly, all the three sources of modulation are present in the case of a rolling-element fault and the sideband behaviour can be described by $p\omega_d + (m \pm 1)\Omega \pm n\omega_c$.

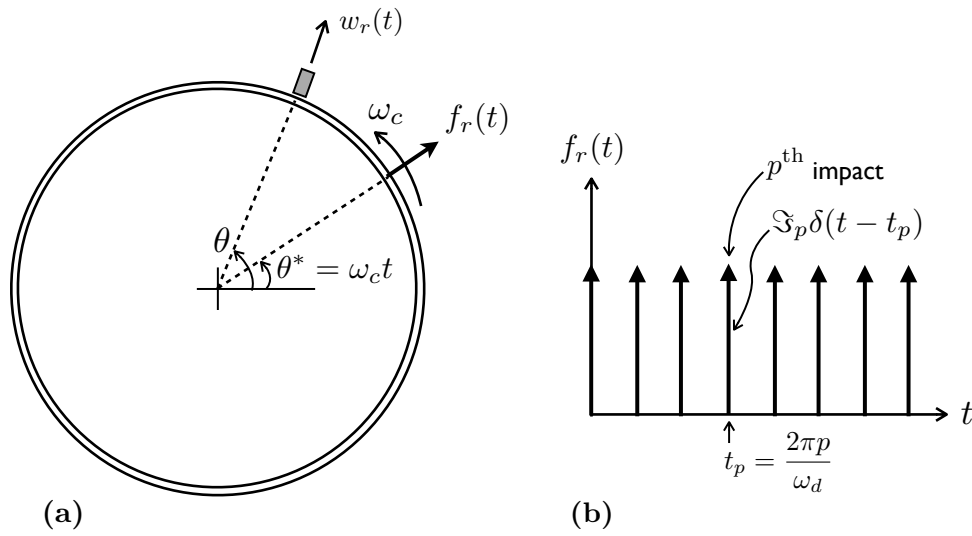


Figure 4.9: (a) An elastic ring excited by an impulse train moving with a constant speed ω_c . (b) Impulse train with frequency ω_d exciting the elastic ring.

4.5 Influence of Ring-Gear Flexibility on the Sideband Behaviour

In section 4.4.4 we have identified various sources of modulation sidebands present in the vibration signature of planet-bearing faults. In this section we examine how the flexibility of the ring gear influences the sideband behaviour of planet-bearing faults.

Let us first take a simple example where an elastic ring is excited by an impulse train (figure 4.9). Including modal damping in equation 4.3 we get the equation of motion of the ring in terms of modal participation factors as

$$\ddot{a}_n + 2\xi_n\omega_n\dot{a}_n + \omega_n^2 a_n = \frac{1}{M_n} \int_0^{2\pi} \{f_r \cos(n\theta) + c_n f_\theta \sin(n\theta)\} d\theta \quad (4.50a)$$

and

$$\ddot{b}_n + 2\xi_n\omega_n\dot{b}_n + \omega_n^2 b_n = \frac{1}{M_n} \int_0^{2\pi} \{f_r \sin(n\theta) - c_n f_\theta \cos(n\theta)\} d\theta. \quad (4.50b)$$

Substituting $a_n(t) = a_n(\omega)e^{i\omega t}$, $b_n(t) = b_n(\omega)e^{i\omega t}$, $f_r = F(\omega)e^{i\omega t}\delta(\theta - \theta^*)$, and $f_\theta = 0$ into equation 4.50 gives

$$a_n(\omega) = \frac{\cos(n\theta^*)}{M_n(\omega_n^2 - \omega^2 + 2i\xi_n\omega_n\omega)} F(\omega) \quad (4.51a)$$

and

$$b_n(\omega) = \frac{\sin(n\theta^*)}{M_n(\omega_n^2 - \omega^2 + 2i\xi_n\omega_n\omega)} F(\omega). \quad (4.51b)$$

Here, θ^* is the force application angle. Using equations 4.51 and 4.2 we obtain the FRF between the excitation point and the measurement point located at an angle θ on the ring,

$$H(\omega) = \frac{W_r(\omega)}{F(\omega)} = \sum_{n=0}^{\infty} \frac{\cos(n\theta^*)\cos(n\theta) + \sin(n\theta^*)\sin(n\theta)}{M_n(\omega_n^2 - \omega^2 + 2\iota\xi_n\omega_n\omega)}. \quad (4.52)$$

Ring is subjected to an impulse train, which can be described as

$$f_r(t) = \sum_{p=0}^{\infty} \mathfrak{S}_p \delta(t - t_p). \quad (4.53)$$

Using convolution theorem, ring-gear response in the radial direction can be calculated as

$$w_r(t) = \sum_{p=0}^{\infty} h_p(t - t_p) \mathfrak{S}_p. \quad (4.54)$$

Following from equation 4.38, Fourier transform of the above equation gives

$$W_r(\omega) = \sum_{p=0}^{\infty} H(\omega, \theta^* = \omega_c t_p) e^{-\iota\omega t_p} \mathfrak{S}_p, \quad (4.55)$$

where $t_p = 2\pi p/\omega_d$. Using equation 4.52, $\cos(x) = (e^{\iota x} + e^{-\iota x})/2$, $\sin(x) = (e^{\iota x} - e^{-\iota x})/2\iota$, and assuming unit impulse for all p i.e. $\mathfrak{S}_p = 1$ for all p , equation 4.55 can be simplified as

$$W_r(\omega) = \sum_{p=0}^{\infty} \sum_{n=0}^{\infty} \frac{(\cos(n\theta) - \iota\sin(n\theta))e^{-\iota(\omega - n\omega_c)t_p} + (\cos(n\theta) + \iota\sin(n\theta))e^{-\iota(\omega + n\omega_c)t_p}}{2M_n(\omega_n^2 - \omega^2 + 2\iota\xi_n\omega_n\omega)}. \quad (4.56)$$

From equation 4.56 ring-gear response at $\theta = 0$ can be calculated as

$$W_r(\omega) = \sum_{p=0}^{\infty} \sum_{n=0}^{\infty} \frac{e^{-2\pi\iota p(\omega - n\omega_c)/\omega_d} + e^{-2\pi\iota p(\omega + n\omega_c)/\omega_d}}{2M_n(\omega_n^2 - \omega^2 + 2\iota\xi_n\omega_n\omega)}. \quad (4.57)$$

Equation 4.57 describes the vibration response of an elastic ring (figure 4.9) excited by an impulse train. From equation 4.57, it is clear that the response contains clusters (of peaks) separated by ω_d and within each cluster there are sidebands separated by ω_c .

In order to determine the function governing the amplitudes of central peaks ($p\omega_d$) within each cluster, we put $n = 0$ in equation 4.57 which gives

$$W_r^{p\omega_d}(\omega) = \sum_{p=0}^{\infty} W_{p\omega_d}(\omega) e^{-2\pi\iota p\omega/\omega_d}, \quad (4.58)$$

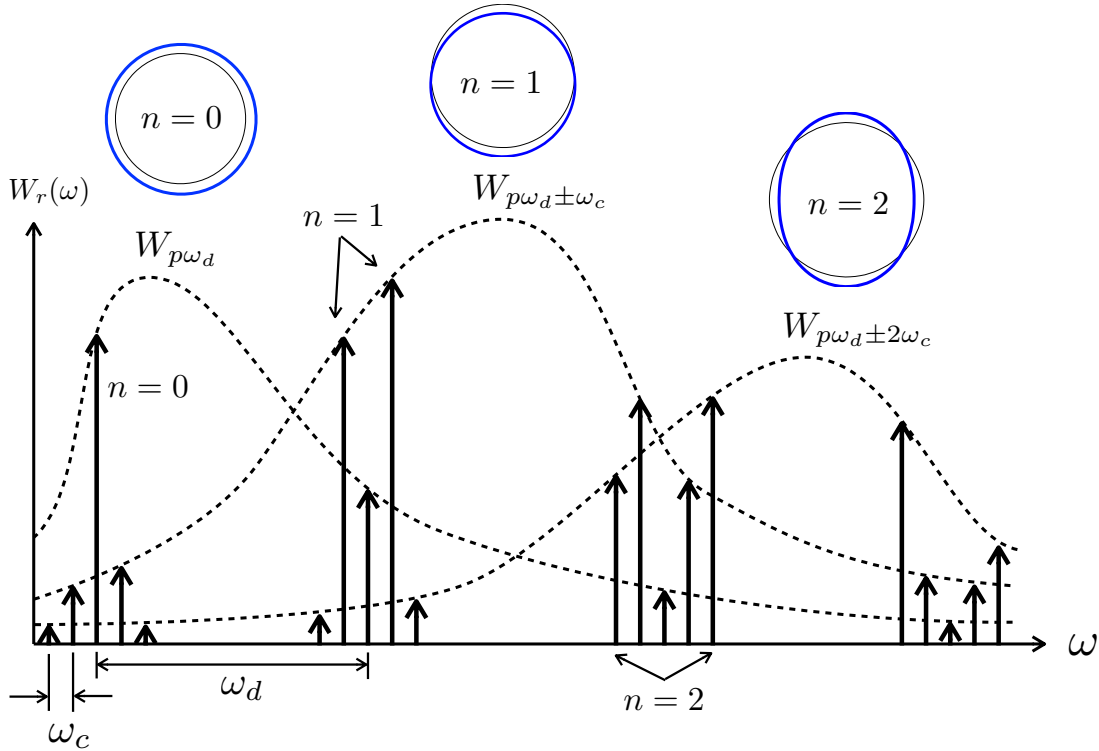


Figure 4.10: Frequency response of an elastic ring excited by a moving impulse-train. Clusters of sidebands along with their envelope functions show that the amplitude of n^{th} sideband is governed by the n^{th} ring mode

where $W_{p\omega_d}(\omega)$ is the function governing the amplitudes of peaks at $p\omega_d$ given by

$$W_{p\omega_d}(\omega) = \frac{1}{2M_0(\omega_0^2 - \omega^2 + 2i\xi_0\omega_0\omega)}. \quad (4.59)$$

Similarly, we can derive expressions for the functions governing amplitudes of first ($p\omega_d \pm \omega_c$) and second ($p\omega_d \pm 2\omega_c$) sidebands as

$$W_{p\omega_d \pm \omega_c}(\omega) = \frac{1}{2M_1(\omega_1^2 - \omega^2 + 2i\xi_1\omega_1\omega)} \quad (4.60a)$$

and

$$W_{p\omega_d \pm 2\omega_c}(\omega) = \frac{1}{2M_2(\omega_2^2 - \omega^2 + 2i\xi_2\omega_2\omega)}. \quad (4.60b)$$

Functions described in equations 4.59 and 4.60 are shown in figure 4.10 along with the corresponding sidebands. The simple example described here clearly suggests that the amplitudes of peaks corresponding to the n^{th} sideband ($p\omega_d \pm n\omega_c$) are governed by the n^{th} ring-gear mode. This is because of the rotation of vibration modes relative to the measurement point fixed on the ring. Rotation of the first vibration mode (breathing

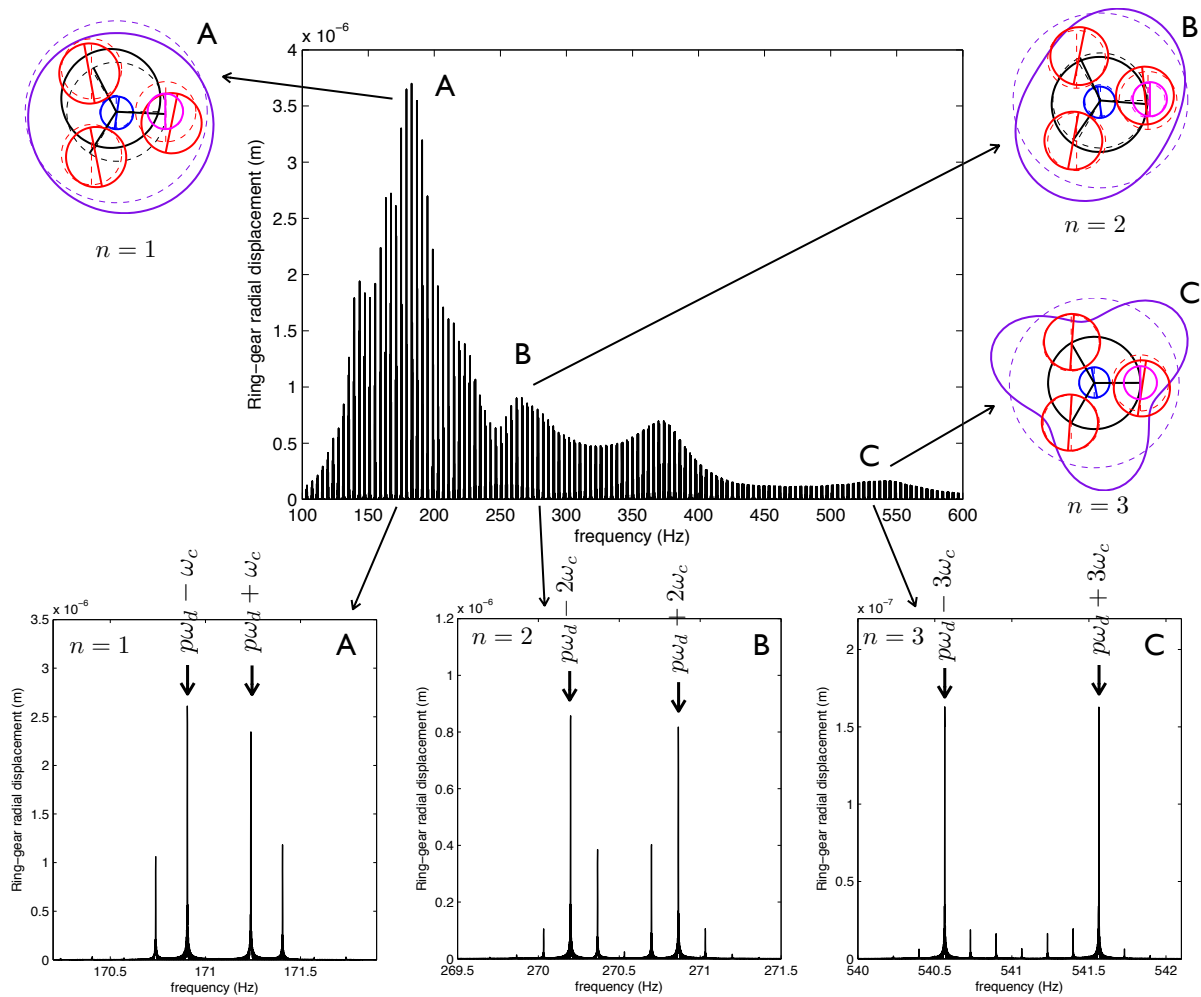


Figure 4.11: Variation in the sideband behaviour of a planet-bearing inner-race fault with frequency. n^{th} sideband dominates near the n^{th} ring-gear mode. Examples are shown for A ($n = 1$), B ($n = 2$) and C ($n = 3$) with respective mode shapes.

mode) with respect to a fixed point on the ring does not lead to any modulation and hence there are no sidebands. Along the same lines, rotation of the second vibration mode results in one modulation cycle per rotation and we get sidebands corresponding to $n = 1$. Rotation of the third vibration mode results in two modulation cycles per rotation and we get sidebands corresponding to $n = 2$, and so on.

Sideband behaviour of a planet-bearing fault is more complicated than this simple example as the vibration modes of an elastic ring-gear are coupled with the epicyclic-drivetrain modes. Figure 4.11 shows the ring-gear response of the planetary drive of table 4.1 in the presence of a planet-bearing inner-race fault. We have increased the thickness of the ring to 2.5 times the value mentioned in the table to create more frequency separation in the vibration modes of the ring. As with the simple example above, the

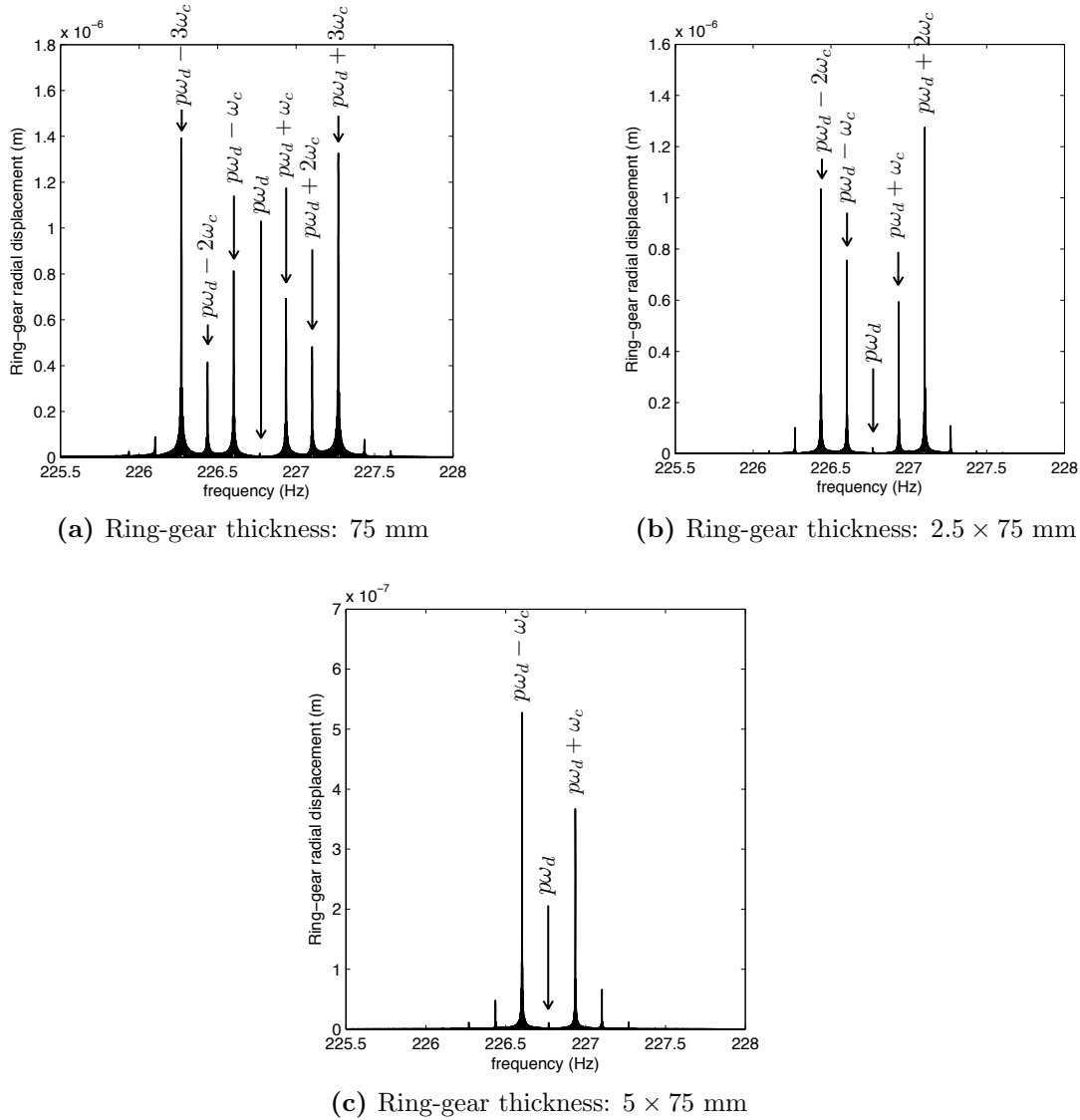


Figure 4.12: Influence of ring-gear thickness on the sideband pattern. Higher-order sidebands disappear as we increase the ring-gear thickness: (a) three dominant sidebands for a thickness of 75 mm; (b) two dominant sidebands for a thickness of 2.5×75 mm; and (c) only one dominant sideband for a thickness of 5×75 mm.

amplitudes of sidebands are governed by the corresponding ring-gear modes. For example, modes near 180 Hz are governed by the second ($n = 1$) ring-gear mode and the clusters in this region are dominated by $n = 1$ sidebands ($p\omega_d \pm \omega_c$). Similarly, mode near 270 Hz is governed by the third ($n = 2$) ring-gear mode and as a result the clusters in this region are dominated by $n = 2$ sidebands ($p\omega_d \pm 2\omega_c$).

As we increase the ring-gear thickness, the frequencies of ring-gear modes increase. This results in small contributions at low frequency range from the higher-order ring modes and the amplitudes of higher-order sidebands decrease. Figure 4.12 shows the sideband behaviour for three ring-gear thickness values. As we increase the thickness, amplitudes of higher order sidebands decrease.

Based on the above discussions we can draw the following conclusions.

- Ring-gear modes govern the relative amplitudes of the sidebands in a fault signature.
- Sideband behaviour changes as we move across the frequency range because of the shift in dominant ring-gear mode.
- Number of dominant sidebands at low frequency range in a fault signature depends on the thickness of the ring gear. As we increase the thickness, higher-order sidebands disappear.

4.6 Experimental Validation of Fault Signatures

In this section, we validate the theoretically predicted fault signatures against the experiments performed in collaboration with Whitely^[127]. The experimental test-rig is designed by Whiteley^[127]. We briefly describe the test-rig and discuss three test results for inner-race and outer-race faults. See Whitely^[127] for a detailed description of test-rig design and more experimental results.

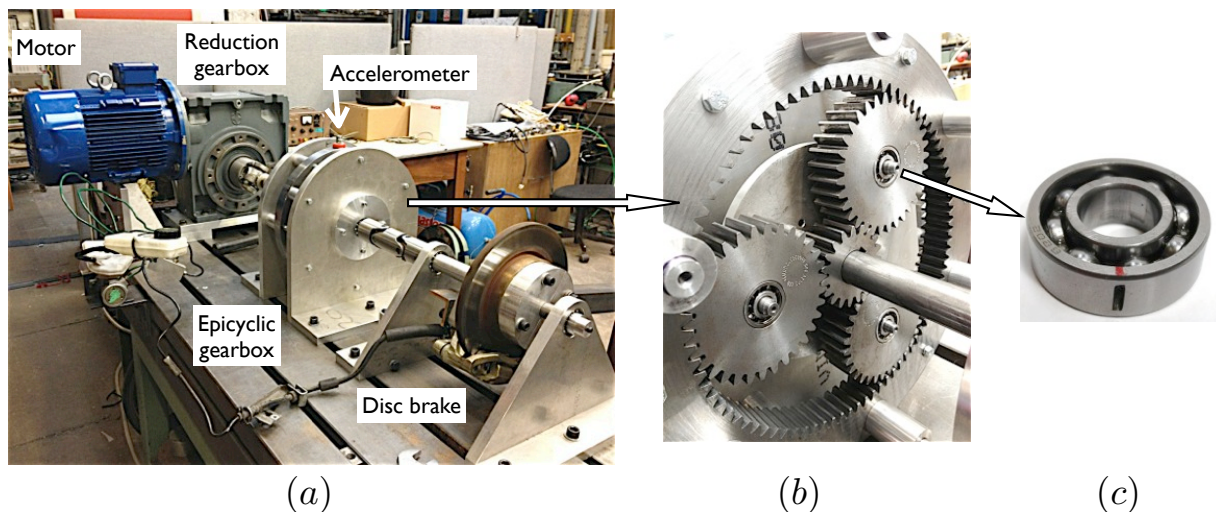
We perform the experiments on an epicyclic test-rig (figure 4.13) consisting of a variable speed motor (5.5 kW rated power), a reduction gearbox (1:30 speed ratio), a planetary gearbox (about one-fifth of a typical wind turbine planetary gear stage and parameters listed in table 4.2), and a disc-brake system to provide reaction torque. A localized defect (3 mm wide) is introduced to one of the ball bearings supporting a planet gear using spark erosion technique.

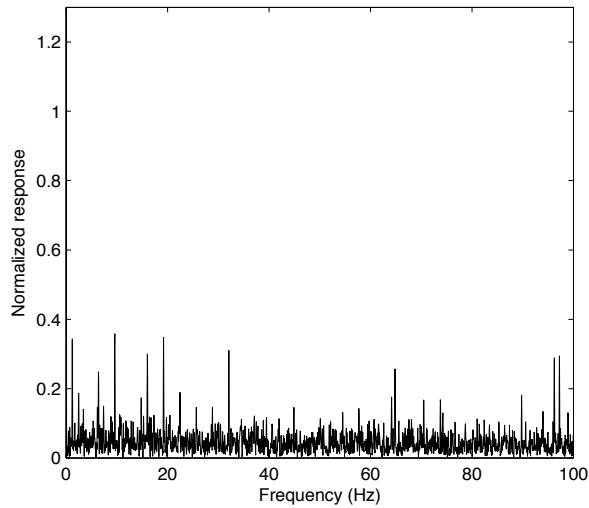
Tests are conducted at the carrier speeds of 72 and 96 rpm and carrier torque of 350 Nm. For the given bearing geometry (table 4.2b) and carrier speeds, characteristic fault frequency ω_d for ball bearing is 15.4 Hz (for $\omega_c = 72$ rpm) and 20.6 Hz (for $\omega_c = 96$ rpm) for the inner-race defect, and 9.5 Hz (for $\omega_c = 72$ rpm) and 12.7 Hz (for $\omega_c = 96$ rpm)

Table 4.2: Parameters of the planetary gearbox used in the test rig

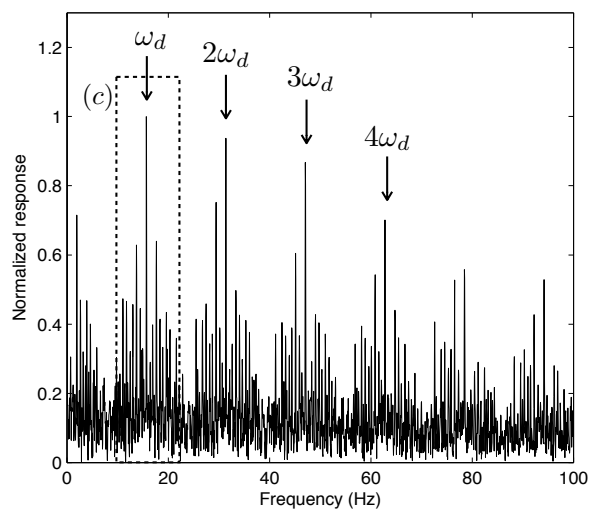
(a) Epicyclic gears				
Parameter	Sun	Planet	Ring	Carrier
Number of teeth	19	32	83	-
Base radius, mm	26.68	45.11	117	76.5
Pitch radius, mm	28.5	48	124.5	-
Face-width, mm			30	
Density, kg/m ³		7800		
Number of planets		3		

(b) Planet bearing		
	Ball bearing	Roller bearing
Number of balls	8	11
Rolling-element radius, mm	3	5.5
Pitch radius, mm	12.65	12.5

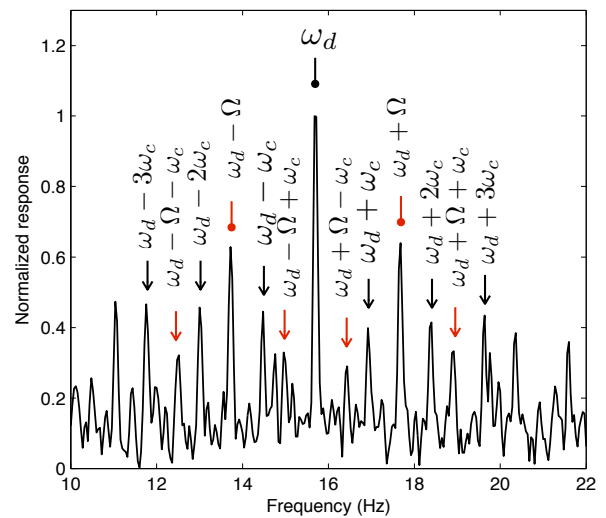
**Figure 4.13:** (a) Planetary test rig; (b) Epicyclic drivetrain used in the test rig; (c) Planet bearing with a localized outer-race fault (a through rectangular hole)



(a) Healthy bearing



(b) Faulty bearing



(c) Faulty bearing

Figure 4.14: (a) Measured vibration response of a healthy planet ball-bearing. (b) Measured vibration signature of a planet bearing inner-race defect, for a carrier speed of 72 rpm, containing clusters of peaks separated by ω_d . (c) Sidebands within a cluster.

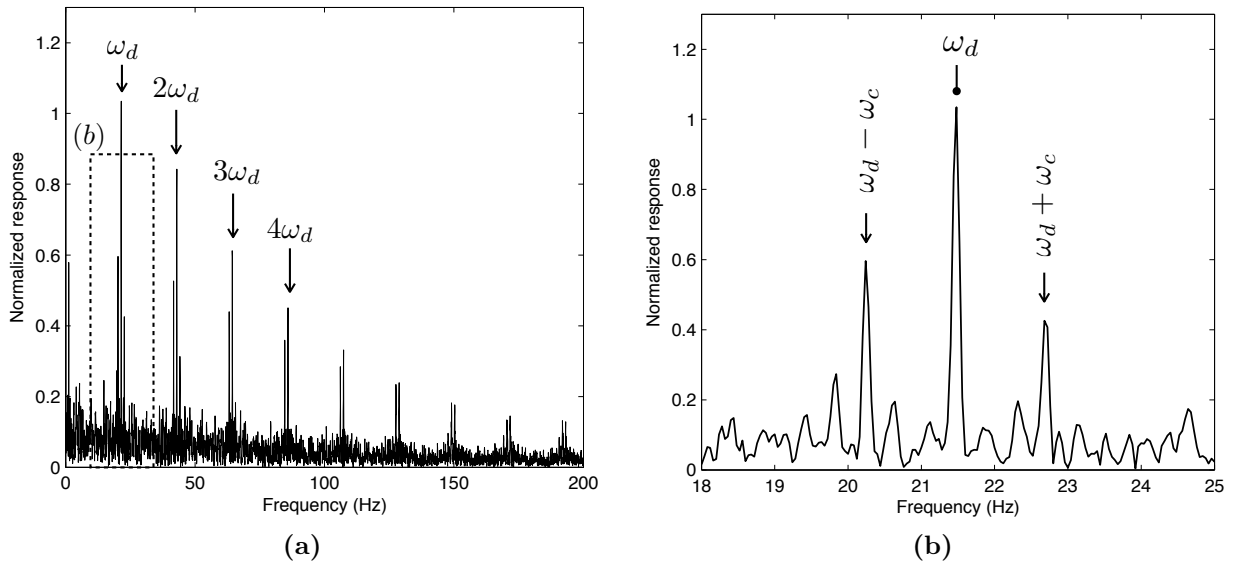


Figure 4.15: Measured vibration signature of a planet-bearing (cylindrical roller) inner-race fault for a carrier speed of 72 rpm (a) Clusters of peaks separated by ω_d (b) Sidebands within a cluster

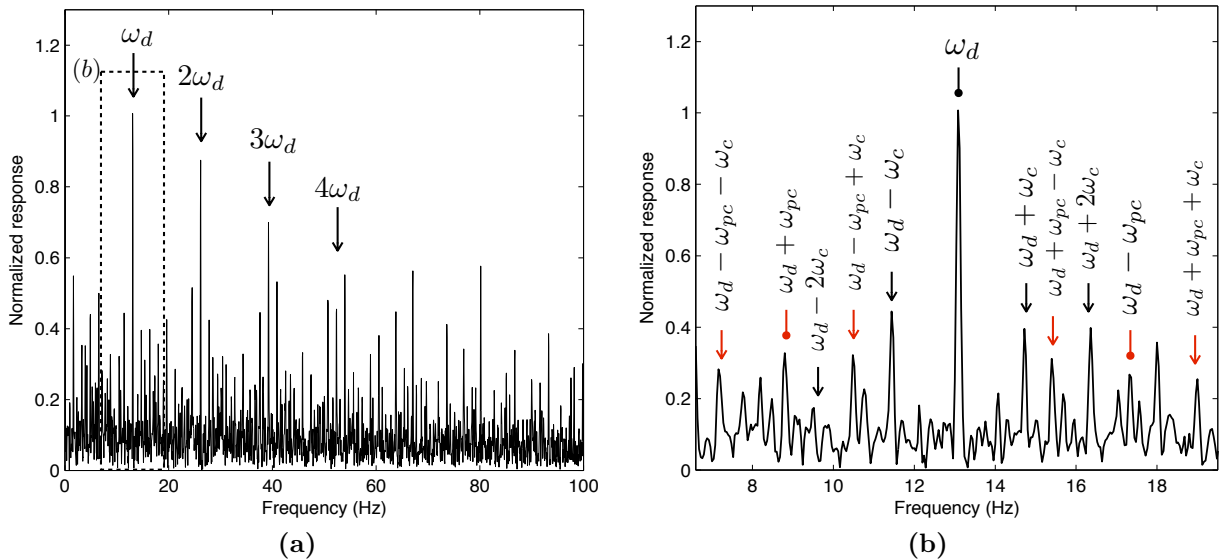


Figure 4.16: Measured vibration signature of a planet bearing outer-race defect for a carrier speed of 96 rpm (a) Clusters of peaks separated by ω_d (b) Sidebands within a cluster

for the outer-race defect. For roller bearing, ω_d is 21 Hz (for $\omega_c = 72$ rpm) and 28 Hz (for $\omega_c = 96$ rpm) for inner-race fault. The response is measured by an accelerometer mounted on the ring gear. The accelerometer signal is high-pass filtered with cut-off frequency 30 kHz and then envelope analysis was carried out on the filtered response. The envelope signal is then converted into frequency domain using MATLAB's FFT algorithm.

Figure 4.14b shows the measured frequency response for an inner-race fault. As predicted by the theoretical model, the measured response contains clusters (of peaks) separated by ω_d and sidebands separated by ω_c within each cluster (figure 4.14c). These clusters of sidebands are not present in the case of a healthy gearbox, i.e., gearbox without a planet bearing defect as shown in figure 4.14a. In addition to the sidebands separated by ω_c , we also get some sidebands which are spaced by the cage frequency of the planet bearing relative to the carrier (Ω), which we do not get from the analytical simulations. In the analytical model, we assume that each impact between rolling-elements and inner-race fault is identical because inner-race fault does not move relative to the load zone. If there is a slight variation in the rolling-element diameters (due to manufacturing tolerance) then these impacts will no longer be same for all the rolling elements, and will vary periodically with the frequency Ω . This is because the same rolling element hits the inner-race fault after the time-interval of $2\pi/\Omega$. A periodic variation in the impulses results in the amplitude modulation of the signal, and we get sidebands at $\omega_d \pm \Omega$.

Figure 4.15 shows the measured vibration signature of a more precise cylindrical-roller bearing with an inner-race fault. The manufacturing tolerance on rolling-element diameters is much less than the ball bearing of previous case. In this case, we only get the sidebands separated by the carrier frequency ω_c as predicted by the theoretical model.

We also carried out experiments for outer-race faults. Figure 4.16 shows the measured frequency response containing a peak at the fault frequency ω_d and modulation sidebands. Again, as predicted by the theoretical model, the measured response contains primary sidebands separated by ω_{pc} and each primary sideband along with the central peak (at ω_d) has secondary sidebands separated by carrier frequency ω_c . The sources of these modulation sidebands are already discussed in section 4.4.4.

The experimental results presented in this section show that all the sources of modulation sidebands discussed in section 4.4.4, which we identified using an analytical model, are real and can be used to detect various faults in planet bearings.

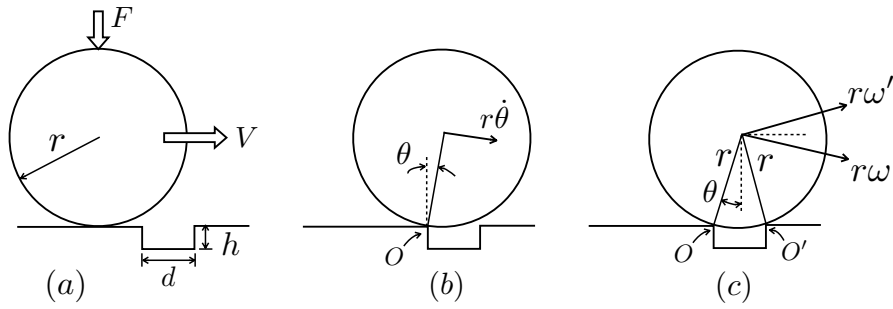


Figure 4.17: Different stages of a rolling element passing through a narrow localized fault with a constant horizontal speed: (a) before entering the fault; (b) after entering the fault; and (c) at the time of impact.

4.7 Impulse Generated by a Localized Bearing-Fault

In section 4.4 we make an assumption that the impulses generated when a rolling element passes through a localized fault are proportional to the speed with which the rolling element is traveling and independent of the contact force acting on the rolling element during the impact. In this section we provide a justification to this assumption. McFadden and Smith^[90] propose an analytical model to calculate the vibration response of a fixed-axis bearing containing localized faults. In that model, authors make an assumption that the impulse generated when a rolling element passes through a fault is proportional to the contact force acting on the rolling element. They do not mention any speed dependence of this impulse. This assumption is widely used in papers related to bearing-fault diagnostics (e.g. ^[90,104,118,131]) during the last 30 years, but none of these papers provide any scientific justification to this assumption. Therefore, in this section we check the validity of this assumption and explore the relationship between the impulse generated by a defect and rolling-element contact-force and speed.

4.7.1 Theoretical Impulse Calculation

Let us consider a rolling element of mass m and radius r travelling with a speed V and a force F is acting on it (figure 4.17(a)). It passes through a rectangular fault of width d and depth h . The width of the fault is sufficiently small so that the rolling element never touches its bottom surface, i.e., $d < 2\sqrt{2rh}$. The speed of the rolling element is below a critical value of $\sqrt{Fr/m}$ (see appendix E for derivation) which ensures that the rolling element does not loose contact with the left edge of the fault before the impact. After the rolling element enters the fault, the speed of its centre of mass at an angle θ becomes $r\dot{\theta}$ (figure 4.17(b)). If we assume that the rolling element is moving with a

constant horizontal speed V then

$$r\dot{\theta}\cos\theta = V \implies \dot{\theta} = \frac{V}{r\cos\theta}. \quad (4.61)$$

The angle at the time of impact between the rolling element and the right edge of the fault is given by

$$\cos\theta = \sqrt{1 - \frac{1}{4} \frac{d^2}{r^2}}. \quad (4.62)$$

If the fault is small compared to the radius of the rolling element then $d^2/r^2 \ll 1$; therefore, $\cos\theta \approx 1$ and angular velocity of the rolling element just before the impact $\omega \approx V/r$ (from equation 4.61). Let us now determine the angular velocity just after the impact. Using conservation of angular momentum about point O' (figure 4.17(c)), we get

$$mr^2\omega (\cos^2\theta - \sin^2\theta) + I\omega = (I + mr^2) \omega', \quad (4.63)$$

where ω' is the angular velocity of the rolling element just after the impact and $I = \frac{2}{5}mr^2$ is the moment of inertia of the rolling element. Substituting θ from equation 4.62 into 4.63 and solving for ω' yields

$$\omega' = \omega \left(1 - \frac{5}{14} \frac{d^2}{r^2} \right). \quad (4.64)$$

For narrow faults $\omega' \approx \omega$. We can now obtain the impulse in the vertical direction (\mathfrak{S}_v) which is equal to the change in linear momentum of the rolling element just before and after the impact. Therefore,

$$\mathfrak{S}_v = mr\omega'\sin\theta - (-mr\omega\sin\theta) = mrs\sin\theta (\omega' + \omega). \quad (4.65)$$

Putting $\omega' \approx \omega$, $\omega \approx V/r$ and $\sin\theta = d/(2r)$ into equation 4.65 gives

$$\mathfrak{S}_v = mV \frac{d}{r}. \quad (4.66)$$

Similarly impulse in the horizontal direction is obtained which comes out to be zero. Equation 4.66 clearly shows that the impulse generated, when a rolling element passes through a narrow fault, is proportional to the speed of the rolling element and independent of the applied load, as long as the speed is below $\sqrt{Fr/m}$. In appendix E, we show that if the speed of the rolling element is above $\sqrt{Fr/m}$ then the impulse depends on the applied load. However, for a planet bearing of a typical wind turbine gearbox, linear speed of a rolling element is much less than this critical value.

A problem similar to this can also be found in the railway-vibration literature, where

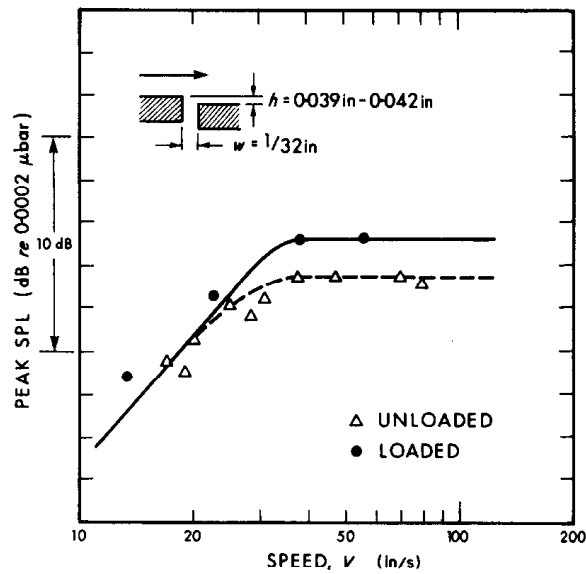
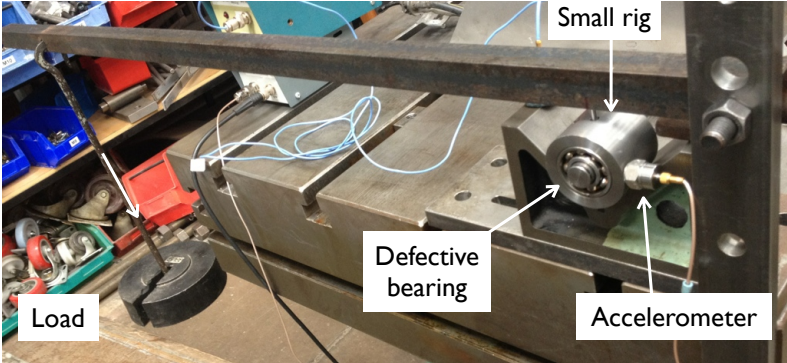


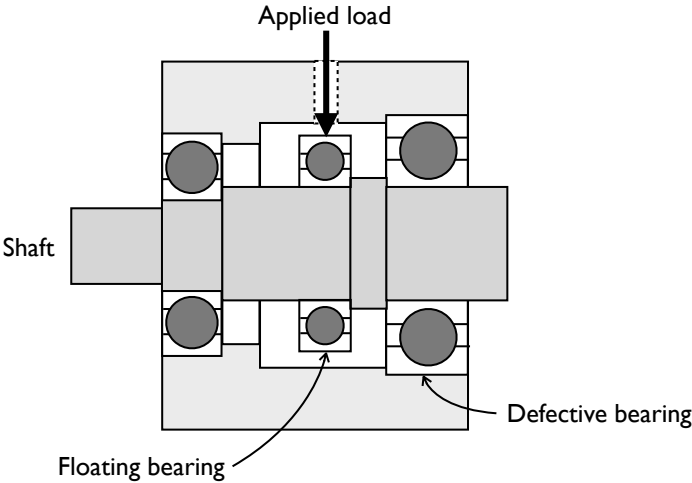
Figure 4.18: Effect of static axle-load on the peak impact-sound pressure-level for a rail joint (reproduced from Ver et. al. [125]). At low speeds, sound pressure is independent of axle load. At high speeds, sound pressure depends on axle load.

rail-wheel impacts are caused by joints in the railways, wheel flats etc. Ver et. al. [125] investigate the impact noise generated by various wheel and rail discontinuities. Their experimental analysis reveal that for a level joint the impact noise is proportional to the speed of a train and independent of its weight, as long as the train speed is below a critical value (figure 4.18). When they increase the train speed above this critical value, impact noise becomes weight dependent and speed independent. They also derive the expression for the critical speed in terms of wheel and train mass, which is consistent with the simple analysis described above. Similar observations are found by Steenbergen [117]. All these railway vibration studies are in agreement with the impulse calculation described above.

At this point, we have two theories: first is based on the McFadden and Smith [90] assumption which suggests that the impulses generated by a localized fault are proportional to the load acting on a rolling element; second is based on simple momentum-based calculations and railway-vibration literature which suggests that the impulses are proportional to the speed and independent of the load. So, the two theories are in disagreement with each other. The question is which one should we use to predict the vibration signatures of planet bearings. We carry out an experimental analysis to find out the answer to this question.



(a) Experimental setup



(b) Small rig design

Figure 4.19: Experimental setup used to measure the impulse generated by a localized bearing-fault. Lever mechanism is used to vary the applied load and the shaft in the small rig is driven by a hand drill.

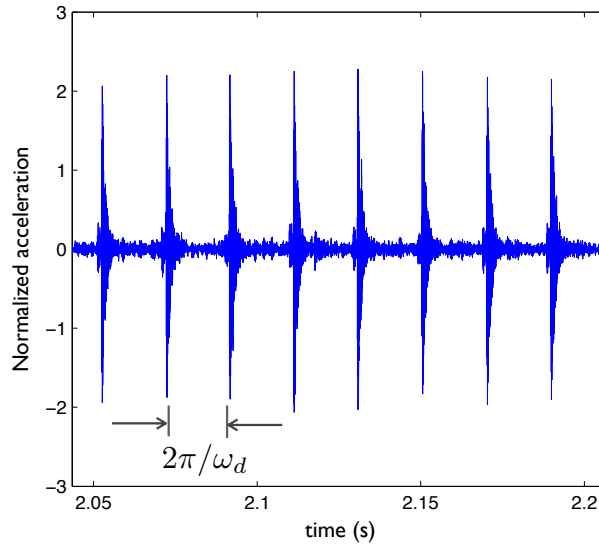


Figure 4.20: Typical acceleration signal measured by an accelerometer located near the outer race of the faulty bearing. Each peak represents an impulse response due to a bearing fault.

4.7.2 Experimental Determination of Impacts Generated by a Localized Fault

Figure 4.19 shows the experimental setup used to determine the impacts generated by a localized fault. The setup consists of a small rig with three bearings (figure 4.19). The two bearings located at the ends support a shaft containing a floating bearing. One of the end bearings (faulty bearing) contain a localized inner-race fault. A lever mechanism, with 1:10 leverage ratio, is used to apply a constant radial load to the floating bearing. This load is shared by the faulty bearings and the other end bearing. Different radial loads can be applied to the faulty bearing by adding different weights to the lever arm. An accelerometer is mounted near the outer race of the faulty bearing. The small rig is driven by a variable-speed hand-drill. Experiments are carried out at two speeds ($V = 0.18$ m/s and 0.52 m/s) and five loads ($F = 170, 320, 460, 580$ and 740 N).

Figure 4.20 shows a typical response measured by the accelerometer. The response contains periodic impulses, separated by a time interval of $2\pi/\omega_d$, generated when rolling elements pass through the fault. The vibration transmission path between the fault and the measurement point remains constant as the locations of both the fault and the accelerometer are fixed. Therefore, the response is not modulated and all the impulses in the response signal (figure 4.20) are of the same magnitude. We calculate the average magnitude of these impulses for different loads and speeds.

Figure 4.21 shows the variation of normalized impulse with the contact force acting on

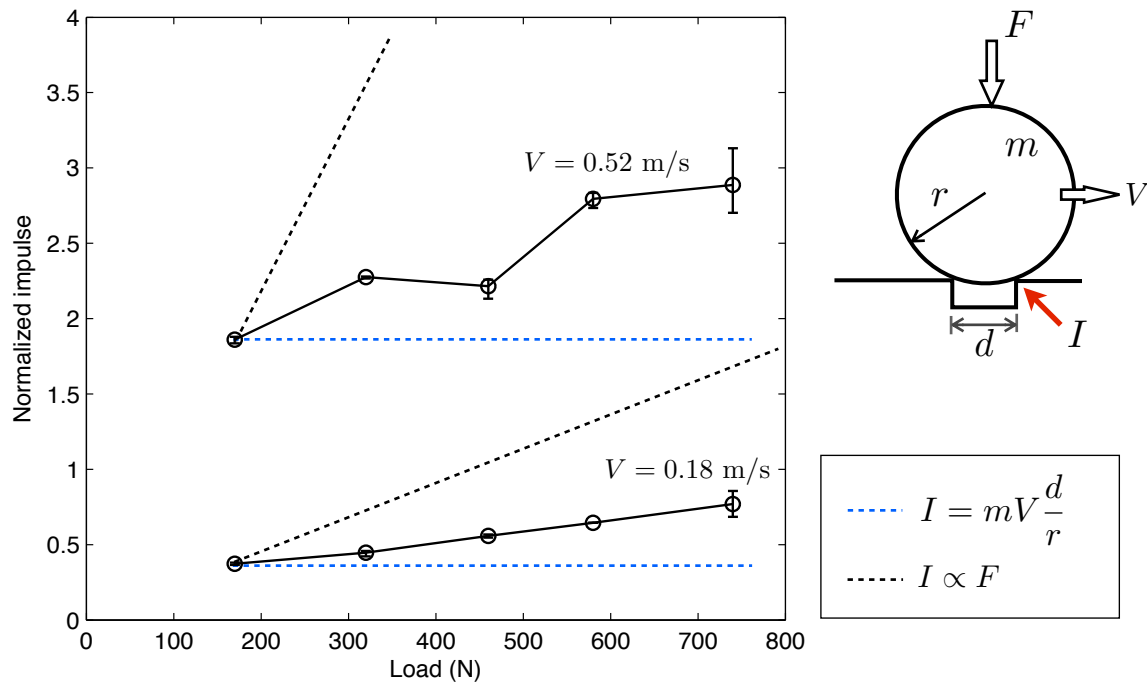


Figure 4.21: Measured variation in the impulse generated by a bearing fault with the applied load at two rolling-element speeds. Theoretical impulse values predicted from the speed-dependence (dotted blue) and load-dependence (dotted black) theories are also shown.

a rolling element at the time of impact for two different speeds. Each data point shows the spread and the mean calculated for 10 different runs. It is clear from the figure that the impulse is more sensitive to speed than load. Experimental data shows that the impulse is proportional to $V^{1.4}$, but more experiments should be performed at wide range of speed values to accurately calculate this relationship. Figure 4.21 also shows the theoretical impulses predicted by the two theories: load dependence and speed dependence. Since the measured acceleration is proportional to the impulse and does not give us the impulse magnitude directly, we have used the first data point at each speed to normalize the impulse values predicted by the two theories.

The experimental results presented in this section clearly suggest that the impulse generated by a localized narrow-fault depends primarily on the speed of a rolling element. There is some load dependence but it is secondary compared to the speed dependence.

4.7.3 Reason Behind Secondary Load-Dependence

In the previous section, we have observed that the impulse generated by a localized fault depends primarily on the rolling-element speed. This observation can be explained using the simple impulse calculation described in section 4.7.1 (equation 4.66). We also found

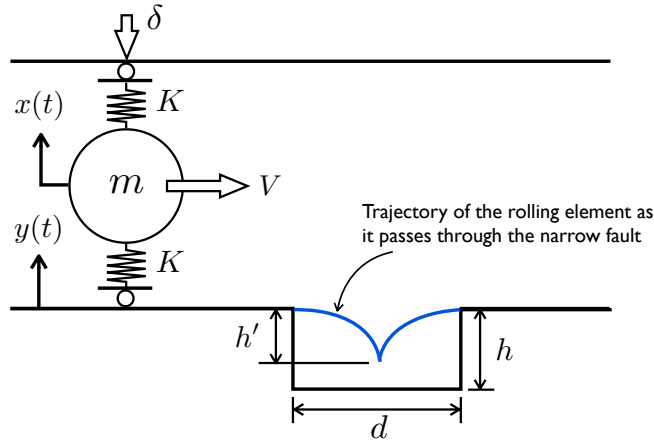


Figure 4.22: A rolling element of radius r with nonlinear contact springs passing through a narrow fault of width d and depth h such that $d < 2\sqrt{2rh}$, i.e., the rolling element never touches the bottom of the fault.

that impulse increases with the load acting on a rolling element during the time of impact, although the variation with the load is secondary compared to the speed. None of the existing theories explain this secondary load-dependence of impulse. Therefore, in this section, we analyze the influence of various factors on the impulse calculation to find out the reason behind this secondary load-dependence.

4.7.3.1 Nonlinear Contact-Stiffness

Contact stiffness between a rolling element and raceways is governed by the Hertzian contact theory and it is a nonlinear function of load. As the applied load on a rolling element varies, its contact stiffness changes. In this section, we evaluate the influence of this nonlinear contact stiffness on the impulse generated by a localized fault.

Let us consider a rolling element travelling with a constant horizontal speed between two surfaces representing inner and outer raceways (figure 4.22). The rolling element is connected to the raceways by springs representing the contact stiffness. The initial static compression in each of these contact springs is $\delta/2$ which is caused by the application of a constant force F . The values of the contact stiffness are calculated for the constant applied load F . The trajectory of rolling-element's centre of mass, when it passes through the fault, is shown in the figure 4.22 and can be expressed as

$$y(t) = \begin{cases} -\frac{V^2}{2R}t^2 & \text{for } 0 \leq t < \frac{d}{2V} \\ -\frac{(d-Vt)^2}{2R} & \text{for } \frac{d}{2V} \leq t < \frac{d}{V}. \end{cases} \quad (4.67)$$

Equation 4.67 is based on the assumption that the rolling element never loses contact

with the fault, and we have already established that this is true for a rolling element located within the load zone of a typical wind-turbine planetary-bearing. We can now write the equation of motion for the rolling element as

$$\ddot{x}(t) + \Omega^2 x(t) = \frac{K}{m} y(t), \quad (4.68)$$

where $\Omega = \sqrt{2K/m}$ and y is given by equation 4.67. Solution of equation 4.68 is

$$x(t) = \frac{1}{\Omega} \int_0^t \frac{K}{m} y(\tau) \sin\{\Omega(t - \tau)\} d\tau. \quad (4.69)$$

Substituting y from equation 4.67 into 4.69 and solving the integral yields

$$x(t) = \frac{1}{2} \left[-\frac{(Vt - d)^2}{2R} + \frac{V^2}{R\Omega^2} \{1 - \cos(\Omega t)\} - \frac{dV}{R\Omega} \sin \left\{ \Omega \left(t - \frac{d}{2V} \right) \right\} \right]. \quad (4.70)$$

Total force in the spring between the rolling element and upper raceway is $K \{x(t) + \delta/2\}$, and the static force (by ignoring the rolling element dynamics) in the spring is $K \{\delta/2 + y(t)/2\}$. The dynamic force in the upper spring can be calculated by subtracting the static force from the total force. Therefore,

$$F_{\text{dyn}} = K \left(x(t) - \frac{y(t)}{2} \right), \quad (4.71)$$

where $x(t)$ is defined by equation 4.70. The trajectory of the rolling-elements centre of mass when it comes in contact with the right edge of the fault is defined by $y(t) = -\frac{(d-Vt)^2}{2R}$ (from equation 4.67). Since we are interested in the impulse when a rolling element strikes the right edge of the fault, we substitute $y(t) = -\frac{(d-Vt)^2}{2R}$ into equation 4.71. The substitution gives

$$F_{\text{dyn}} = -\frac{K}{2} \left[\frac{V^2}{R\Omega^2} \{1 - \cos(\Omega t)\} + \frac{dV}{R\Omega} \sin \Omega \left(t - \frac{d}{2V} \right) \right]. \quad (4.72)$$

For our test bearing, Ω is of the order of 10^6 rad/s. Thus, the magnitude of the first (cosine) term in the above equation will be much smaller compared to the magnitude of the second (sine) term. Neglecting the first term in equation 4.72 and making a substitution $\hat{t} = t - d/(2V)$ yields

$$F_{\text{dyn}} = \frac{K}{2} \frac{dV}{R\Omega} \sin(\Omega \hat{t}). \quad (4.73)$$

Equation 4.73 gives us the dynamic force when the rolling element strikes the right edge of the fault. In order to calculate the impulse generated during the impact, we

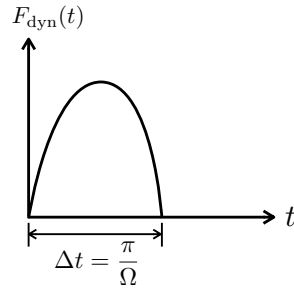


Figure 4.23: An impact-force pulse due to a bearing fault

integrate the positive half-cycle of the sinusoidal dynamic force (figure 4.23). Therefore, the impulse is given by

$$\mathfrak{S} = \int_0^{\pi/\Omega} \frac{K}{2} \frac{dV}{R\Omega} \sin(\Omega\hat{t}) \, d\hat{t} = mV \frac{d}{R}. \quad (4.74)$$

Impulse given by equation 4.74 is independent of the contact stiffness K and is same as the one calculated without considering the contact stiffness. This shows that the contact stiffness does not influence the impulse value. Since contact stiffness is a function of the applied load, impulse is independent of the applied load. The simple analysis described here shows that the nonlinear behaviour of the contact stiffness does not explain the secondary load-dependence of the impact generated by a fault.

One assumption we make in the analysis described above is that the rolling element is always loaded. But in some cases, if a fault is wide enough, rolling element might become unloaded as it enters the fault. We now analyse the influence of this unloading behaviour on the impulse value.

Let us first consider an inertia based approach. Impulse generated during the impact in the vertical direction is proportional to the vertical velocity of a rolling element just before the impact. If the horizontal speed of the rolling element is constant then for any position angle θ

$$r\dot{\theta}\cos\theta = V, \quad (4.75)$$

which gives

$$\dot{\theta} = \frac{V}{r\cos\theta}. \quad (4.76)$$

Using the above expression for $\dot{\theta}$ we can calculate the rolling-element speed in the vertical direction as

$$V_{\text{vertical}} = r\dot{\theta}\sin\theta = V\tan\theta, \quad (4.77)$$

where θ varies from 0 (at the point of entry into the fault) to $d/(2r)$ (at the point of

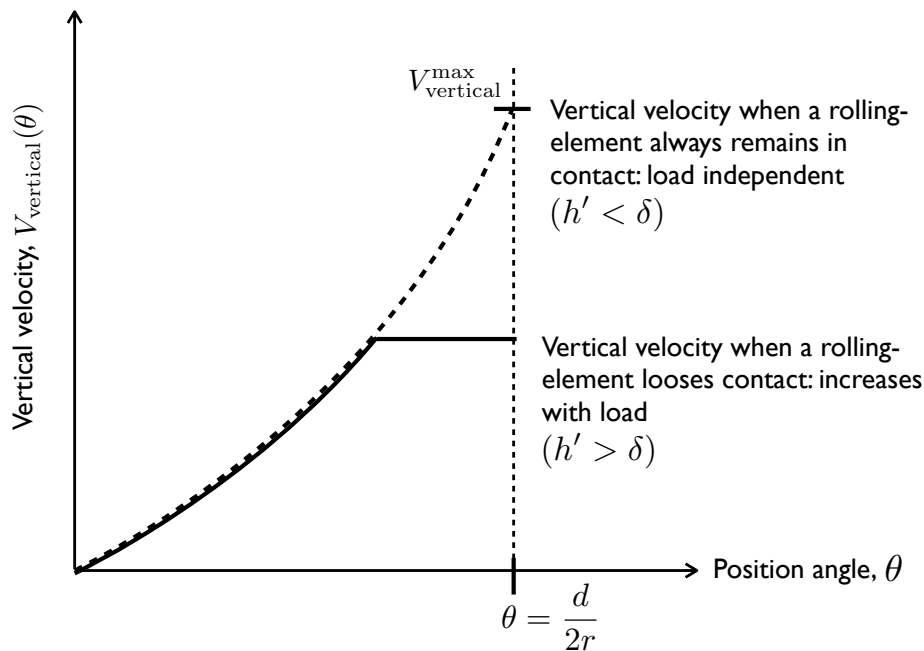


Figure 4.24: Variation in the vertical velocity of a rolling element with its position angle as it passes through the fault

impact). Figure 4.24 shows the variation of the vertical velocity with position angle θ . If the vertical displacement ($h' = d^2/(8r)$ from equation 4.67) of the rolling element as it passes through the fault is less than the static deflection of the rolling element ($h' < \delta$) then the rolling element never becomes completely unloaded and vertical velocity at the time of impact is $V_{\text{vertical}}^{\text{max}} \approx Vd/(2r)$. However, if the vertical displacement is greater than the static deflection ($h' > \delta$) then the rolling element becomes completely unloaded. Once the rolling element is unloaded, its velocity remains constant in the absence of any contact force. In this case, the vertical velocity of the rolling element just before the impact is less than $V_{\text{vertical}}^{\text{max}}$. The position angle θ , at which the rolling element becomes unloaded, is governed by the applied load. As we increase the applied load, static deflection in the contact spring increases and the rolling element has to travel further into the fault before it becomes completely unloaded. This reduces the difference between the vertical velocity just before the impact and $V_{\text{vertical}}^{\text{max}}$ (figure 4.24). Hence, the vertical velocity of the rolling element increases with the load, and this results in an increase in the impulse. But as the load is increased beyond a point when the static deflection in the rolling element is more than the maximum vertical displacement, the vertical velocity before the impact stays constant at the value $V_{\text{vertical}}^{\text{max}}$ and impulse becomes load independent. A qualitative variation in the impulse with the applied load is shown in figure 4.25.

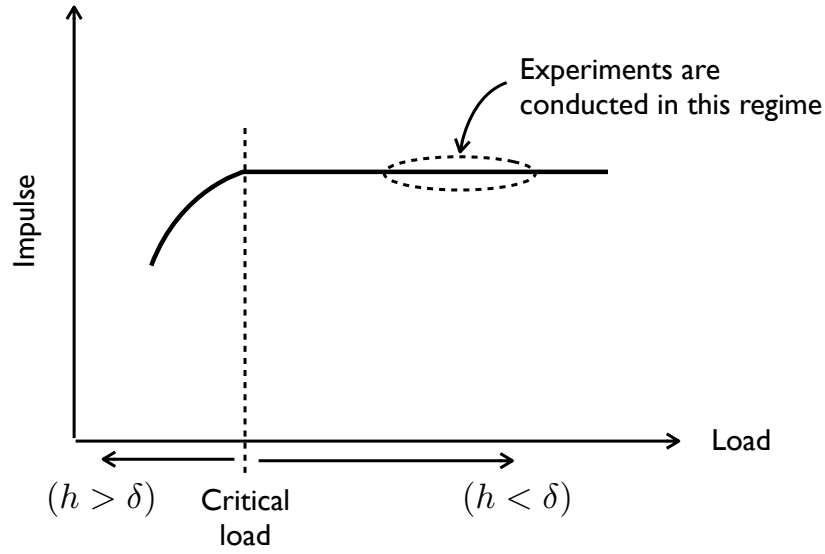


Figure 4.25: Qualitative variation in the impulse due a bearing fault with the applied load. The regime in which experiments of section 4.7.2 were conducted is also shown.

A similar conclusion can be derived by using a stiffness-based static approach. Let us consider a spring with a constant stiffness K , representing the rolling element, travelling with a constant horizontal speed. Initial compression in the spring is δ due to the applied load and initial spring force is $K\delta$. If the initial compression is greater than the maximum vertical displacement of the rolling element as it passes through the fault ($\delta > h'$) then the compression in the spring as it enters the fault becomes $\delta - h'$, and spring force becomes $K(\delta - h')$ (figure 4.26). Change in the static spring force as the spring passes through the fault is

$$\Delta F_{\text{spring}} = Kh', \quad (4.78)$$

which is independent of δ and hence independent of the applied load. Next, let us consider another case where the static deflection in the spring is less than the maximum vertical displacement. In this case, the spring becomes completely unloaded when it enters the fault and the spring force becomes zero. The change in the spring force is

$$\Delta F_{\text{spring}} = K\delta. \quad (4.79)$$

Since δ is a function of the applied load, ΔF_{spring} also depends on the applied load. Hence, we get the impulse load-dependence similar to figure 4.25.

The qualitative analysis described here shows that the load dependence of the impulse can only be explained if a fault is big enough for a rolling element to become completely

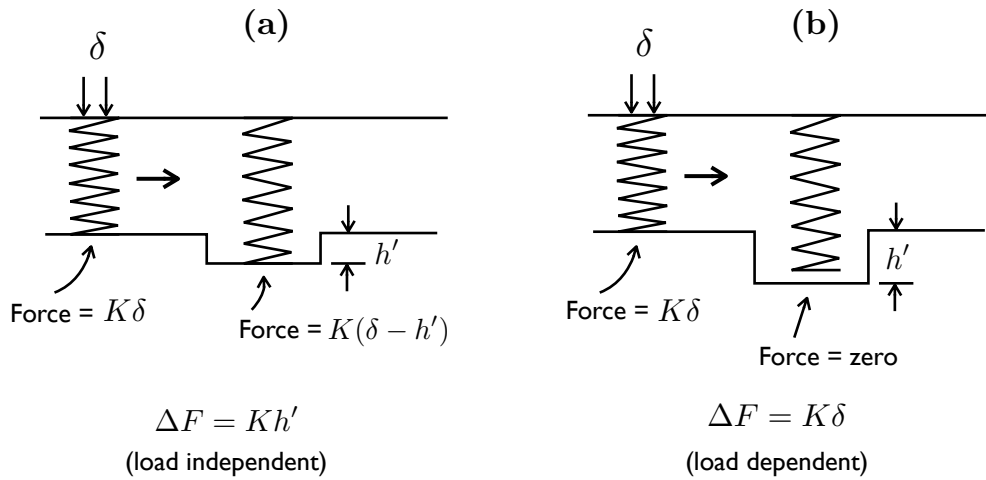


Figure 4.26: A spring representing a rolling element passing through a fault. (a) Initial compression in the spring is more than the maximum vertical displacement of the rolling element. (b) Initial compression in the spring is less than the maximum vertical displacement of the rolling element.

unloaded. For our test bearing this is not the case. The static deflection of a rolling element of our test bearing at the contact force of 300 N is 70 μm and the maximum vertical displacement of a rolling element when it enters the fault is about 40 μm which is less than the static deflection. As a result, a rolling element in the test bearing never becomes completely unloaded and the secondary load-dependence of the impulse which we observed in the experimental analysis cannot be explained by the theory described in this section.

4.7.3.2 Interaction Between Cage and Rolling-Elements

Impulse described by equation 4.66 is based on the assumption that the rolling element travels with a constant horizontal speed. But under the application of a vertical load, rolling element will accelerate as it enters the fault. Let us now remove this assumption of constant horizontal speed and calculate the expression for the impulse.

Consider a rolling element at a position angle θ . We assume that the rolling element is rotating without any sliding about the contact point O with an angular speed $\dot{\theta}$ and an angular acceleration $\ddot{\theta}$ (figure 4.27). Balancing the moments about the contact point O gives

$$(I + mr^2) \ddot{\theta} = Fr \sin \theta. \tag{4.80}$$

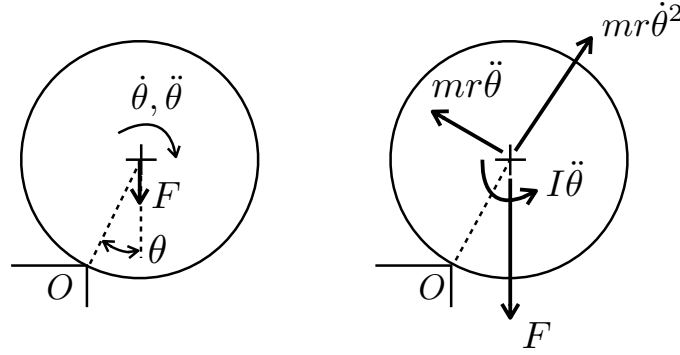


Figure 4.27: Acceleration and forces acting on a rolling element as it enters the fault (before impact).

Substituting $I = \frac{2}{5}mr^2$ into the above equation and solving for $\ddot{\theta}$ yields

$$\ddot{\theta} = \frac{5F}{7mr} \sin\theta. \quad (4.81)$$

Using

$$\ddot{\theta} = \frac{\partial \dot{\theta}}{\partial t} = \frac{\partial \dot{\theta}}{\partial \theta} \dot{\theta} \implies \dot{\theta} \partial \dot{\theta} = \ddot{\theta} \partial \theta = \frac{5F}{7mr} \sin\theta \partial \theta, \quad (4.82)$$

we can obtain the angular speed of the rolling element at an angle θ as

$$\int_{\omega_0}^{\omega} \dot{\theta} d\dot{\theta} = \frac{5F}{7mr} \int_0^{\theta} \sin\theta d\theta \implies \omega = \sqrt{\omega_0^2 + \frac{10F}{7mr} (1 - \cos\theta)}, \quad (4.83)$$

where $\omega_0 = V/r$ is the angular speed of the rolling element before it enters the fault. Substituting $\cos\theta \approx 1 - \frac{d^2}{8r^2}$, angle at the time of impact, into the above equation gives the angular speed just before the impact as

$$\omega = \sqrt{\omega_0^2 + \frac{5F}{28mr} \left(\frac{d^2}{r^2} \right)}. \quad (4.84)$$

We have already calculated the angular speed just after the impact using the conservation of angular momentum, which is defined by equation 4.64. Now, we can determine the impulse in the vertical direction as

$$\mathfrak{S} = mr\omega' \sin\theta - (-mr\omega \sin\theta) = mr(\omega' + \omega) \sin\theta. \quad (4.85)$$

Substituting ω' from equation 4.64 and assuming that the fault is small, i.e., $d^2/r^2 \ll 1$, we can simplify equation 4.85 as

$$\mathfrak{S} = md\omega. \quad (4.86)$$

Putting the value of ω from equation 4.84 into the above equation gives

$$\mathfrak{S} = m \frac{d}{r} \sqrt{V^2 + \frac{5Fd^2}{28mr}}. \quad (4.87)$$

Equation 4.87 contains both the load and the speed terms, which explains the load and the speed dependence of the impulse. Now let us check whether this equation also gives us the primary speed and the secondary load dependence, which we observed in the experimental data. For our test bearing: $r = 3$ mm, $d = 1$ mm, and $m = 10^{-3}$ kg. Putting these values into equation 4.87 gives

$$\mathfrak{S} = \frac{10^{-3}}{3} \sqrt{V^2 + 0.06F}, \quad (4.88)$$

and for $V = 0.52$ m/s (maximum rolling-element speed for the experiments described in section 4.7.2), above expression becomes

$$\mathfrak{S} = \frac{10^{-3}}{3} \sqrt{0.27 + 0.06F}. \quad (4.89)$$

Clearly, for $F = 100$ N (which is less than the minimum rolling-element force used in the experiments of figure 4.21) the load term dominates the above equation and the influence of rolling-element speed on the impulse becomes secondary. This contradicts with the experimental observation.

The analysis we have done so far suggests that if the horizontal speed of a rolling element is kept constant when it passes through a fault then the impulse depends on the speed and not on the applied load. On the other hand, if we allow a rolling element to accelerate freely under the application of an applied load as it passes through the fault then the impulse depends on both the applied load and the speed, but the load dependence is more prominent compared to the speed dependence. A rolling element in a bearing is constrained by a cage. As the rolling element tries to accelerate under the application of a vertical load, cage resists its changing speed. Therefore, the acceleration of the rolling element depends on the applied load as well as resistance force between the rolling element and the cage. In the following paragraphs, we investigate the influence of this rolling-element-cage interaction on the impulse.

Let us consider a rolling element at an angle θ inside a fault (figure 4.28). The rolling element is connected to a linear spring with spring constant k_{cage} representing the stiffness between the rolling element and a cage pillar. Speed of the cage inside a bearing is determined by the rolling elements, if the cage is driven by the rolling elements. A small change in the speed of a rolling element passing through a fault will not influence the cage speed significantly, as all other rolling elements travel with a constant speed.

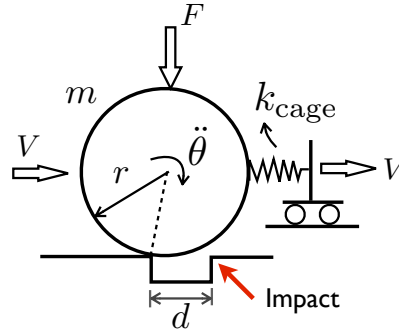


Figure 4.28: A rolling element passing through a bearing fault and connected to a cage pillar with a linear spring

Therefore, in our simplified model we assume that the other end of the spring is travelling with a constant horizontal speed V . If the fault is small then the horizontal displacement of the rolling element can be approximated by $r\theta$, and the compression in the cage spring becomes $r\theta - Vt$. Using this, we can write down a force balance equation for the rolling element as

$$(I + mr^2) \ddot{\theta} = Fr\theta - k_{\text{cage}}r(r\theta - Vt). \quad (4.90)$$

Assuming that the damping in the system is high enough so that the small oscillations in θ die out quickly, we can calculate the steady-state value of θ from the above equation,

$$\theta = \frac{k_{\text{cage}}V}{k_{\text{cage}}r - F}t. \quad (4.91)$$

By differentiating the above equation, we obtain the angular speed of the rolling element just before the impact as

$$\omega = \dot{\theta} = \frac{k_{\text{cage}}V}{k_{\text{cage}}r - F}. \quad (4.92)$$

Substituting ω from equation 4.92 into the impulse equation 4.86 we get

$$\begin{aligned} \mathfrak{S} &= mV \frac{d}{r} \left(\frac{k_{\text{cage}}r}{k_{\text{cage}}r - F} \right) \\ &= mV \frac{d}{r} \left(1 + \frac{F}{k_{\text{cage}}r - F} \right). \end{aligned} \quad (4.93)$$

Equation 4.93 includes two terms: the first term is same as equation 4.66 which explains the speed dependence of the impulse, and the second term explains the load dependence of the impulse. Figure 4.29 compares the impulse predicted by equation 4.93 with the experimental data discussed in section 4.7.2 for two values of cage stiffness. The first data point at each speed is used to normalize the analytically predicted values. Impulse values

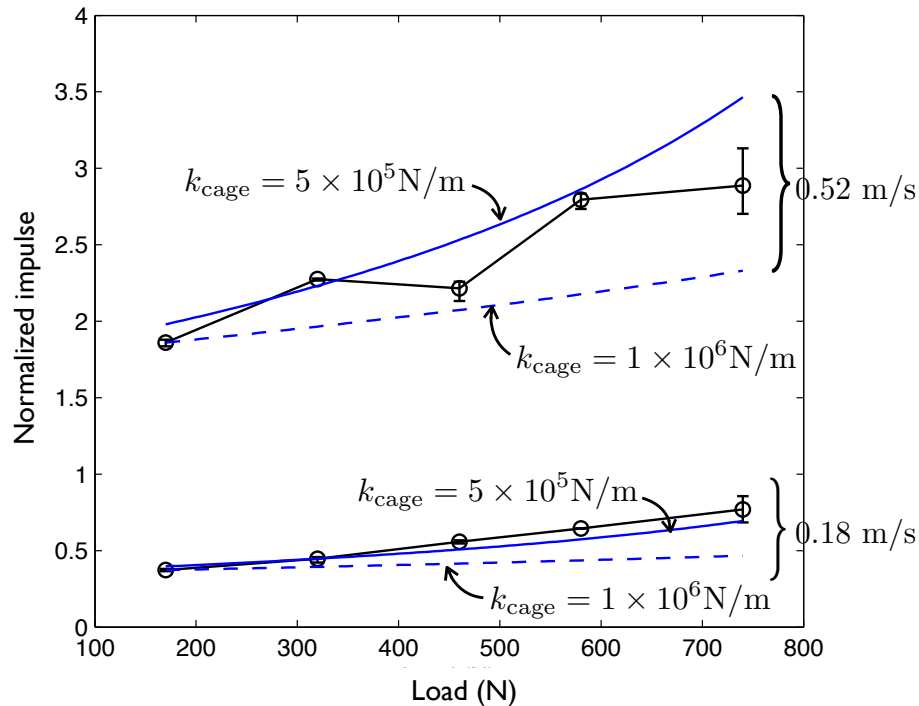


Figure 4.29: Measured variation in the impulse generated by a bearing fault with the applied load (black) along with the impulse variation predicted by the cage-interaction model for two values of cage stiffness (blue).

predicted by equation 4.93 show a trend similar to the experimental data and exhibit both primary speed-dependence and secondary load-dependence.

While deriving equation 4.93, we assume that there is no clearance between the rolling element and the cage. This is a reasonable assumption because these impacts occur inside a load zone, and rolling elements drive the cage within a load zone of a bearing. Therefore, all the clearance between a rolling element and a cage is already taken by the rolling element when it enters the load zone.

4.7.4 Effect of Impulse Calculation on the Vibration Signatures of Planet-Bearing Faults

In the previous section we have observed that the impulse due to a localized bearing fault depends primarily on the rolling-element speed. There is some load dependence but it is secondary compared to speed dependence. This observation undermines the commonly used assumption that the impulse due to a bearing fault is proportional to the load acting on a rolling element at the time of impact. In this section we investigate how this new observation influences the sideband pattern of planet-bearing faults described in section 4.4.

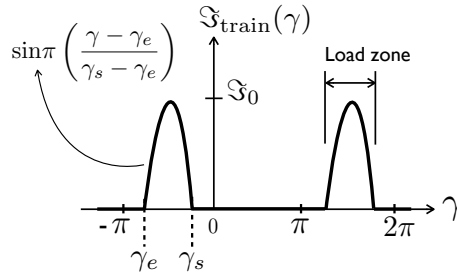


Figure 4.30: Load-dependent impulse-train function

Figure 4.5 shows two impulse trains. The first impulse train is “load dependent” as it is based on the assumption that the impulse is proportional to the contact force acting on a rolling element. The contact force acting on a rolling element inside a load zone is parabolic, therefore the impulse train due to a bearing fault takes the form shown in figure 4.5a. The second impulse train (figure 4.5b) is “speed dependent”. For this impulse train, the impulse values inside the load zone are constant as they are proportional to the rolling-element speed. The impulse values outside the load zone are zero as the rolling-element speed is greater than the critical speed required for speed dependence*.

Sideband pattern of a planet-bearing outer-race fault for the speed-dependent impulse-train is shown in figure 4.31a (see section 4.4 for how it is calculated). In order to determine the sideband pattern for the load-dependent impulse-train, we just have to replace the impulse-train function defined by equation 4.39 of section 4.4 by the impulse-train function of figure 4.30. The rest of the analysis remains unchanged. The impulse-train function of figure 4.30 can be described by

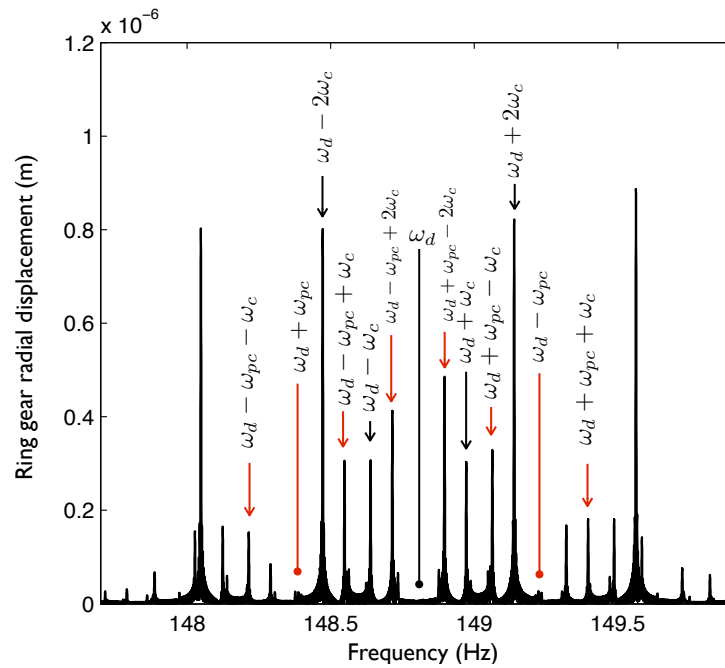
$$\mathfrak{S}_{\text{train}}(\gamma) = \mathfrak{S}_0 \sum_{m=-\infty}^{\infty} \epsilon_m e^{im\gamma}, \quad (4.94)$$

where \mathfrak{S}_0 is the maximum value of the impulse inside the load zone and

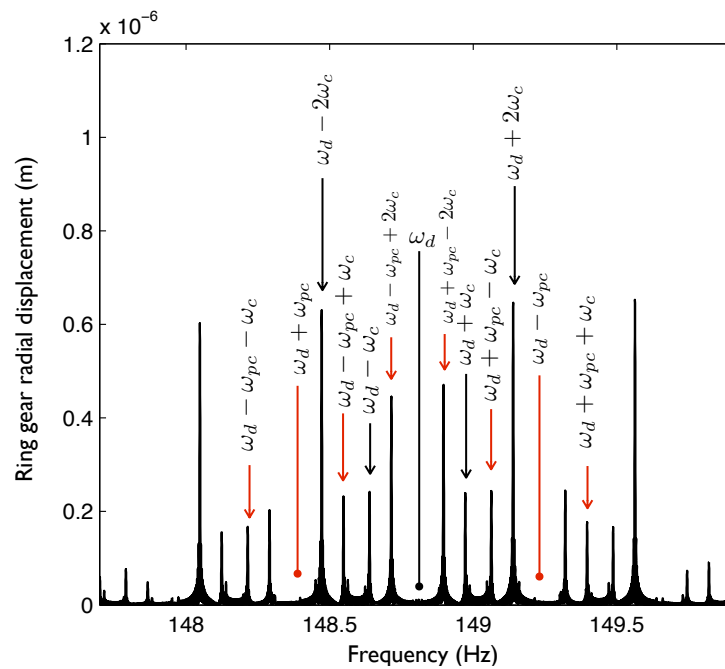
$$\epsilon_m = \frac{-C_{m\gamma_s} - C_{m\gamma_e} + \iota(S_{m\gamma_s} + S_{m\gamma_e})}{2(\gamma_s - \gamma_e) \{m^2 - \pi^2/(\gamma_s - \gamma_e)^2\}}. \quad (4.95)$$

Equation 4.95 is based on the assumption that contact force inside a load zone can be approximated by a sinusoidal function (figure 4.30). If the size of a load zone is 180° then

*Critical speed is proportional to the square root of load. Since the load outside a load zone is zero, critical speed is also zero. This makes the impulse load-dependent and we get zero impulse values outside a load zone.



(a)



(b)

Figure 4.31: Analytical vibration signature of a planet-bearing outer-race defect: (a) calculated using speed-dependent impulse-train, (b) calculated using load-dependent impulse-train. The frequencies of sidebands are same in both cases (a) and (b), but the amplitudes are different.

substituting $\gamma_s = 0$ and $\gamma_e = -\pi$ into equation 4.95 gives

$$\epsilon_m = \begin{cases} \frac{1}{\pi(1-m^2)} & \text{for } m \text{ even} \\ \frac{\iota}{4m} & \text{for } m = \pm 1 \\ 0 & \text{for } m \text{ odd and } m \neq \pm 1. \end{cases} \quad (4.96)$$

Using the impulse-train function defined by equation 4.94 in the analysis described in section 4.4 we determine the sideband pattern (figure 4.31b) for the load-dependent impulse-train. By comparing the two sideband patterns of figure 4.31 we observe that:

1. the frequencies of the sidebands are identical in both cases;
2. the amplitudes of the sidebands are different in both cases.

The two impulse trains are defined in terms of Fourier series. The frequencies in the two Fourier series are same but the magnitudes of the Fourier terms in the two equations are different. This explains why the frequencies of the sidebands in the two cases are same but the amplitudes are different.

This result directly influences the condition-monitoring and fault-detection algorithms used in wind turbines. In most of these algorithms, variations in the sideband amplitudes are recorded over time and the condition of a bearing is determined based on the changes in these amplitudes. If a change in the sideband amplitude is detected, we must know whether it is due a change in the operating speed or load or fault size. In order to answer this question and to determine the condition of a bearing, it is crucial to know how these sideband amplitudes vary with operating speed, load and fault size.

4.8 Conclusions

We develop an analytical model of a planetary drivetrain, including flexible ring-gear and defective planet-bearing, to determine the vibration signatures of localized planet-bearing faults. Following are the main conclusions.

- Vibration signatures of planet-bearing faults contain several modulation sidebands. We identify all the sources of modulation and provide an explanation for their formation.
- Sideband behaviour of a planet bearing with an inner-race fault can be described by $p\omega_d \pm n\omega_c$, where p and n are positive integers. Sidebands spaced by ω_c are due to the variation in vibration transmission-path caused by the carrier rotation.

-
- Sideband behaviour of an outer-race fault can be described by $p\omega_d + (m \pm 1)\omega_{pc} \pm n\omega_c$, where m is an integer. In this case, three sources of modulation sidebands are present: (i) variation in impulse magnitude as a defect passes through the load zone; (ii) variation in the angle between impulse vector and ring-planet mesh; and (iii) variation in the vibration transmission-path caused by the carrier rotation.
 - Sideband behaviour of a rolling-element fault can be described by $p\omega_d + (m \pm 1)\Omega \pm n\omega_c$. As with the outer-race fault, all the three sources of modulation are present.
 - Amplitudes of modulation sidebands in a fault signature are governed by the vibration modes of ring gear, and these amplitudes change as we move across the frequency range.
 - Theoretically predicted vibration signatures of planet-bearing faults are in close agreement with the experimental results.
 - We have shown both theoretically and experimentally that the impulse due to a localized bearing fault depends primarily on the rolling-element speed and almost independent of the applied load.

Chapter 5

Conclusions and Future Work

This chapter summarizes the findings of this research and provides some suggestions for future work. The headlines are: (i) skidding is predicted using simple analytical methods; (ii) sideband analysis is used to detect planet-bearing faults; (iii) impulse due to a bearing fault is independent of load. Further work is needed in five key areas: incorporation of non-Newtonian lubrication in skidding model; skidding analysis under realistic time-varying operating conditions; inclusion of cage clearance into skidding model; detection of bearing faults under time-varying speeds; and determination of vibration signatures for non-rectangular faults.

5.1 Conclusions

This research addresses two key issues in wind turbine gearboxes: skidding in high-speed bearings and detection of localized faults in planet bearings.

5.1.1 Skidding in high-speed bearings

High-speed bearings of wind-turbine gearboxes operate at high speeds and low loads which make them prone to skidding. Skidding occurs when the traction forces between rolling elements and raceways are not sufficient to overcome drag and inertial forces acting on a rolling element. Skidding is known to cause high subsurface shear stress and can lead to premature bearing failure.

Unlike the classical fatigue failure mechanism, for which we have well-established theories to calculate bearing life, skidding mechanism in bearings is not well understood. Most of the work done on ball-bearing skidding until now has been focused on axially-loaded bearings operating under constant operating conditions. Wind turbine bearings, however,

operate under combined axial and radial loads and time-varying operating conditions. In this research, we study the skidding behaviour of ball bearings under both axial and radial loads as well as time-varying speeds. We present a dynamic model, which includes gyroscopic effects, to analyse the roll-slip dynamics of rolling-elements in a ball bearing for a wide range of operating conditions. Following are the main conclusions of this work.

1. For bearings operating under constant axial loads and constant speeds, skidding occurs when operating load is less than the minimum load required to prevent skidding. The value of this minimum load depends on bearing geometry, lubricant, and operating speed. We provide simple equations to calculate this minimum load.

$$\int_{-a}^a \int_{-b}^b \eta(x'', y'') dx'' dy'' \geq \frac{\pi h C_D \rho (\omega_c^{\text{th}} r_p)^2 r^2}{4 \Delta u_{\max}}$$

and

$$\int_{-a}^a \int_{-b}^b \eta(x'', y'') dx'' dy'' \geq \frac{G_0 h}{\Delta u_{\max}}.$$

2. For bearings operating under combined axial and radial loads, skidding occurs when a rolling-element enters a load-zone. The extent of the skidding inside a load-zone can be reduced by increasing the applied load, but it is not possible to completely eliminate skidding. We propose a simple analytical method to calculate the extent of skidding inside a load-zone.

$$\left| -\vartheta^3 + \frac{3}{2} \theta_L \vartheta^2 \right| \geq \frac{3 I \omega_b^{\text{th}} \omega_c^{\text{th}} \tan^2 \beta \theta_L^2}{8 r \mu_{AB} F_e^{\max}}$$

and

$$\left| \frac{3}{2} \theta_L \Theta^2 - \Theta^3 + \vartheta^3 - \frac{3}{2} \theta_L \vartheta^2 \right| \geq \frac{\pi a b I \omega_b^{\text{th}} \omega_c^{\text{th}} \theta_L^2 \tan \beta}{4 \mu_{BC} F_e^{\max} \Phi(a, b)}.$$

3. For bearings operating under constant axial loads and time-varying speeds, skidding occurs if the frequency or the amplitude of speed fluctuation is more than a critical value. These critical values increase with applied load. We derive a simple equation to predict these critical values of the frequency and the amplitude of speed fluctuation.

$$\Omega \Delta \omega \leq \frac{2 \mu_e F_a (r_i + r_o)}{z I_c \sin \beta \left(1 - \frac{\cos \beta}{r_p / r} \right)} - \frac{C_D}{2 I_c} \pi \rho r_p^3 r^2 \omega_0^2 \left(1 - \frac{\cos \beta}{r_p / r} \right).$$

We also demonstrate that skidding could occur under time-varying speeds even if the applied load is well above the minimum load required to avoid skidding predicted by the constant-speed skidding criterion.

4. This research shows that the mechanism of skidding changes with operating conditions. Any skidding prevention criterion derived for constant axial loads and constant speeds is not applicable for combined loading conditions or time-varying speeds.

This work explains the skidding behaviour of ball bearings under a wide range of operating conditions using a detailed dynamic model as well as approximate closed-form solutions. The closed-form solutions described above: (i) help us to determine whether a bearing will skid under given operating conditions without having to run the full numerical model; (ii) provide a direct relationship between bearing geometrical parameters and skidding; (iii) are computationally cheap and, therefore, can be implemented in a bearing design tool. The methods developed in this research will help bearing designers to improve the reliability of wind turbine bearings by predicting the amount of skidding at the design stage.

5.1.2 Detection of localized faults in planet bearings

Localized faults in planet bearings are difficult to detect using vibration measurements because of their complicated and time-varying vibration transmission path. A fault located inside a planet bearing rotates around the bearing centre and it also rotates with the carrier. This double rotation results in a complicated vibration transmission path. Most of the work done on bearing fault diagnostics until now has been focused on fixed-axis bearings and no work has been done on planet bearing faults so far. In this research, we develop a dynamic model of a planetary drive to understand the vibration behaviour of localized planet bearing faults. The dynamic model contains a flexible ring gear and a defective bearing with localized faults. The model is used to derive vibration signatures of planet bearing faults located on inner-race, outer-race, and rolling-elements. Following are the main conclusions of this work.

1. Vibration signature of a planet bearing inner-race fault contains modulation sidebands separated by carrier frequency. The source of this modulation is carrier rotation. As a carrier rotates inside a planetary drive, the vibration transmission path between a fault and an accelerometer located on ring gear changes. This change in the transmission path results in modulation.

2. Vibration signature of a planet-bearing outer-race fault contains additional sidebands separated by planet frequency relative to carrier. This modulation is caused by two additional sources: variation in impulse train as a fault moves in and out of the load zone, and variation in the angle between a fault and a ring-planet contact line.
3. Frequencies of these modulation sidebands are kinematic frequencies which are governed by the geometry of a planetary drive and operating speed. Amplitudes of these modulation sidebands are governed by the geometry as well as the impulse generated when a rolling-element passes through a fault.
4. This research shows theoretically as well as experimentally that the impulse generated when a rolling-element passes through a localized narrow fault primarily depends on the rolling-element speed. There is some load dependence but it is secondary compared to speed dependence. This undermines the assumption, commonly used in bearing-fault-diagnostics literature, that these impulses are proportional to the load acting on a rolling-element during the time of impact. This finding is important for algorithms used for condition monitoring of bearings. Most of these algorithms record the variation in the sideband amplitudes with time. Since the sideband amplitudes depend on the impulse, it is important to know whether a change in the amplitude is caused by a change in the speed, or the load, or the fault size.

This research will improve existing condition-monitoring and fault-detection algorithms. Wind turbine gearbox maintenance costs can also be reduced by detecting a fault at an early stage.

5.2 Future work

Future work that follows directly from this research falls into two main areas: (i) future work on bearing skidding; and (ii) future work on planet-bearing fault-detection.

5.2.1 Future work on bearing skidding

1. The traction model described in section 3.2.3 is based on two assumptions: (i) lubricant is a Newtonian fluid and (ii) contact is elastohydrodynamic (EHD). Newtonian fluid assumption is valid as long as the contact stress between rolling-elements and

raceways is less than the Eyring stress. If the contact stress is greater than the Eyring stress, lubricant starts to exhibit non-Newtonian behaviour (figure 2.7). The operating contact stress in a typical wind turbine high-speed bearing is close to the Eyring stress and in some cases it is even higher. According to Johnson and Tevaarwerk^[70], this non-Newtonian behaviour of a fluid can be described by equation 2.6. Further investigation could be done to find out how this non-Newtonian traction behaviour of a lubricant changes the roll-slip dynamics of a rolling-element. The dynamic model of section 3.2.2 will remain unchanged. Only the traction equation 3.21 will need to be replaced by equation 2.6. According to figure 2.7, Newtonian equation over predicts the traction when the contact stress is more than the Eyring stress. Therefore, it is expected that the minimum load required to avoid skidding will be slightly more for a non-Newtonian fluid.

Another assumption made in the current analysis is that of the EHD lubrication regime with no metal-to-metal contact. Lubrication contact regime is determined by a film parameter (defined by equation 2.8) which is the ratio of film thickness and surface roughness of contacting solids. If the surface roughness is of the same order or greater than the film thickness generated between contacting solids, asperity contact occurs. Surface roughness of rolling-elements and raceways of wind turbine bearings is significantly less than lubricant film-thickness generated under normal operation, and the EHD contact assumption is valid. Although in extreme loading events, asperity contact might occur because of the reduction in film thickness, and as a result the traction behaviour of a lubricant might change from EHD contact regime to mixed-lubrication regime (figure 2.9). Johnson, Greenwood and Poon^[68] provide a mathematical theory based on statistical distribution of surface asperities to calculate the traction forces in mixed-lubrication regime. The further work could focus on extending the current research by replacing the EHD traction model by the mixed-lubrication model and evaluate the change in the skidding characteristics. Like the non-Newtonian case, the dynamic model would remain unchanged.

2. In this research we have demonstrated the effect of time-varying speed on the skidding behaviour of a ball-bearing, but the analysis is limited to axially loaded bearings. Further work could be done to extend the current work on time-varying speeds to bearings operating under combined axial and radial loads. Another limitation of the current analysis is that the frequency and the amplitude of speed variation are assumed to be constant. In a wind turbine these parameters change with time. Speed variation in a wind turbine often includes multiple frequencies such as blade passing frequency and its higher harmonics, gear meshing frequencies etc. Further

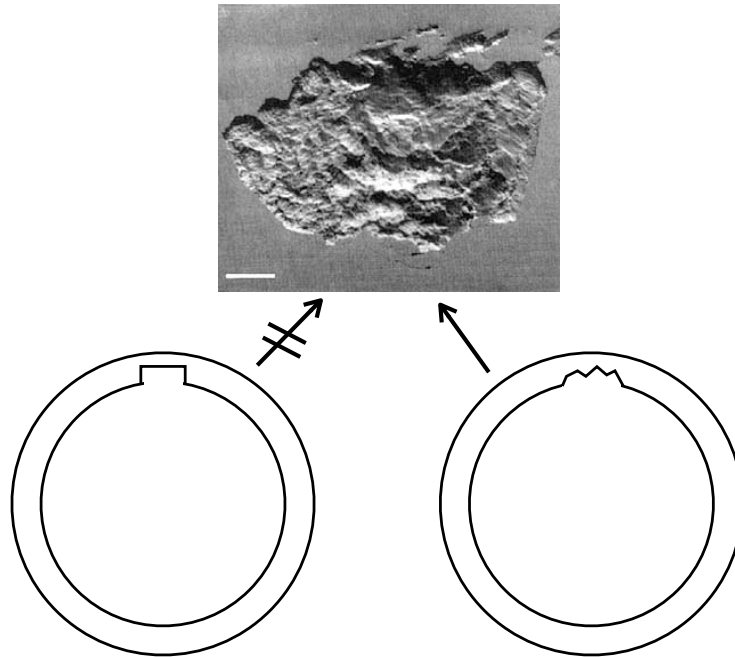


Figure 5.1: A real bearing fault with non-rectangular profile. Source: Kuhnell^[80]

analysis could be performed to quantify the effect of variation in speed fluctuation frequency and amplitude on skidding behaviour. The two further investigations proposed here can be performed using the bearing dynamic model described in this work as the model itself does not have limitations mentioned above. However, the closed-form solutions to predict occurrence of skidding will not be applicable and should be re-derived for the proposed operating conditions.

3. The dynamic model, used to predict skidding, developed in this research ignores clearance between cage and rolling-elements. Cage clearance might not influence the skidding behaviour under constant axial loads and constant speeds as roll-slip response of each rolling-element is identical, but under combined loading conditions and time-varying speeds cage clearance might have some influence on the skidding behaviour. Further investigation could be done to quantify the influence of cage clearance on skidding behaviour.

5.2.2 Future work on planet-bearing fault-detection

1. Vibration signatures of planet bearing faults presented in this work are derived for constant operating speed and load. As we have mentioned earlier, loads and speeds in wind turbines vary with time. How does this variation in speed and load alter

the vibration signatures of planet bearing faults? This question could be addressed in future work. Implementation of load variation in the existing dynamic model of planetary drivetrain is straight forward as the load influences only the impact generated by a fault and the frequency-response function derived in section 4.3 remains unchanged. Implementation of speed variation is not as straight forward as load variation. Speed variation will cause the rotating coordinate system (of section 4.2.5) to accelerate and this will add an extra term to the equation of motion of the system. Hence, the frequency-response function must be re-derived to take into account this angular acceleration.

2. The vibration signatures of planet bearing faults derived in the current research are limited to rectangular faults with crisp boundaries. Real faults, however, do not have well-defined shapes (figure 5.1). Further investigation could be performed on the impact characteristics of faults of different shapes and sizes, and how they influence the sideband behaviour. We expect the frequencies of the sidebands to remain unchanged as long as these faults are localized because the modulation frequencies are kinematic frequencies and are independent of the impulse generated by a fault. Amplitudes of the sidebands are likely to change as they are influenced by the impulse generated by a fault. The current work could also be extended to include distributed faults. Distributed faults have random shapes and, unlike a localized fault, it would be difficult to derive a closed-form expression for the impact generated by a distributed fault. Perhaps a stochastic approach could be developed to predict the fault response envelope by taking into account the random distribution of asperities in a distributed fault.

Appendix A

Comparison of Minimum Loads Required to Avoid Drag-Sliding and Gyroscopic-Spinning

Equations 3.38a and 3.38b give us the two loads: (i) minimum load required to avoid drag-sliding, and (ii) minimum load required to avoid gyroscopic-spinning. In this section, we identify the parameters which determine which of these two loads will be greater than the other.

Let us calculate the ratios of the right-hand-sides of the equations 3.38a and 3.38b such that

$$\mathfrak{R} = \left(\frac{G_0 h}{\Delta u_{max}} \right) / \left(\frac{\pi h C_D \rho (\omega_c^{th} r_p)^2 r^2}{4 \Delta u_{max}} \right) \quad (\text{A.1})$$

The left-hand-sides of equations 3.38a and 3.38b increase monotonically with the applied load F_a ; therefore, if \mathfrak{R} is greater than one then the load required to avoid gyroscopic-spinning will be greater than the load required to avoid drag-sliding, and if \mathfrak{R} is less than one then the load required to avoid drag-sliding will be greater.

Now, let us simplify equation A.1 by substituting $G_0 = \frac{m r_p \omega_i^2}{20} \left(1 - \frac{\cos \beta}{r_p/r} \right)^2 \left(1 + \frac{\cos \beta}{r_p/r} \right) \sin \beta$, $\omega_c^{th} = \left(1 - \frac{\cos \beta}{r_p/r} \right) \frac{\omega_i}{2}$, and $m = \frac{4}{3} \pi r^3 \rho_b$. The substitution leads to

$$\mathfrak{R} = \frac{16 \rho_b r \sin \beta}{15 \rho r_p C_D} \left(1 + \frac{\cos \beta}{r_p/r} \right). \quad (\text{A.2})$$

For steel bearings $\rho_b = 7800 \text{ kg/m}^3$, for a typical lubricant $\rho \approx 900 \text{ kg/m}^3$, and the

drag-coefficient for a ball $C_D = 0.47$. Substituting these values into equation A.2 gives

$$\mathfrak{R} \approx 20 \frac{r}{r_p} \sin \beta \left(1 + \frac{\cos \beta}{r_p/r} \right). \quad (\text{A.3})$$

Equation A.3 shows that the value of the ratio \mathfrak{R} only depends upon the bearing geometry parameters (r , r_p , and β) and not on the operating speed. Therefore, the bearing geometry alone determines which of the two loads (to avoid drag-sliding or to avoid gyroscopic-spinning) will be higher.

Appendix B

Equations of Motion of a Continuous Elastic Ring

In this section, we derive equations of motion of a continuous elastic ring. The derivation is adapted from the work by Rao^[105] and Huang and Soedel^[63]. The effects of rotary inertia and transverse shear deformation are neglected in the analysis.

Figure B.1a shows a free-body diagram of a section of the ring. Balancing the forces in the radial and tangential directions gives

$$\rho AR_r \ddot{w}_r = f_r - P + \frac{\partial F}{\partial \theta} - K_r b R_r w_r \quad (\text{B.1a})$$

and

$$\rho AR_r \ddot{w}_\theta = f_\theta + F + \frac{\partial P}{\partial \theta} - K_\theta b R_r w_\theta, \quad (\text{B.1b})$$

where P is the tensile force and F is the shear force. Moment balance about an axis normal to the plane of the ring gives

$$\frac{\partial M}{\partial \theta} + F R_r = 0, \quad (\text{B.2})$$

where M is the bending moment. Consider an element located at a distance x from the neutral axis of the ring (figure B.1b). If the axial stress in the element is σ then the bending moment and tensile force can be described by

$$M = \iint_A \sigma x dA \quad (\text{B.3a})$$

and

$$P = \iint_A \sigma dA, \quad (\text{B.3b})$$

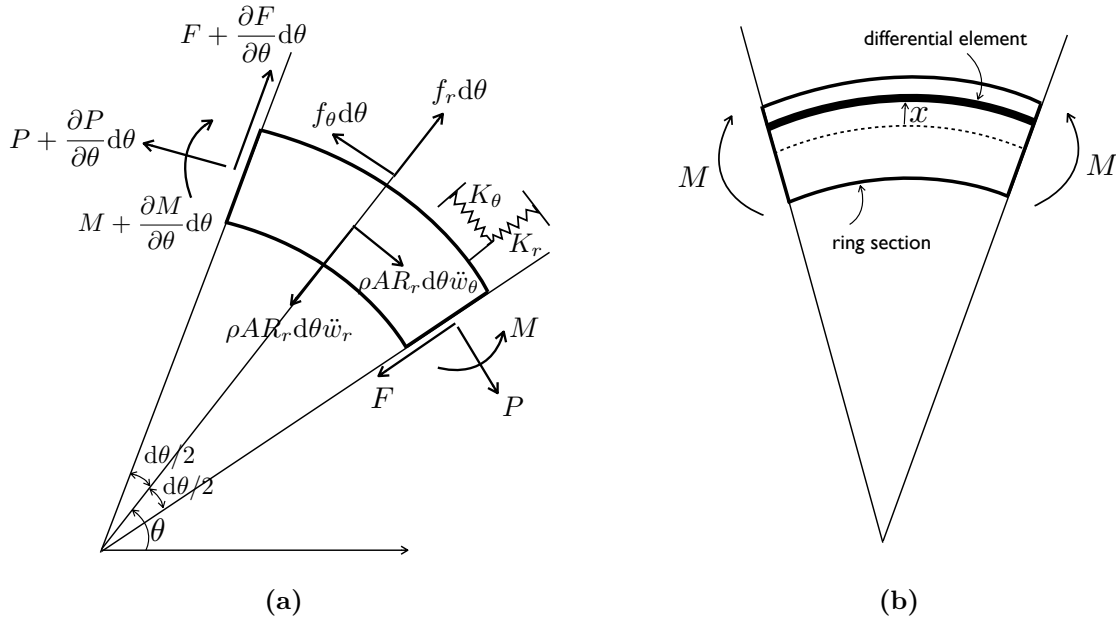


Figure B.1: (a) Free-body diagram of a ring showing all the forces acting on a section; (b) Differential element at a distance x from the neutral axis of the ring.

and the strain in the element can be defined by^[105]

$$\epsilon = \frac{1}{R_r} \left\{ w_r + w'_\theta + \frac{x}{R_r} (w'_\theta - w''_r) \right\}. \quad (\text{B.4})$$

From equations B.3 and B.4 and using $\sigma = E\epsilon$, bending moment and tensile force can be calculated as

$$M = \frac{E\ell h^3}{12R_r^2} (w'_\theta - w''_r) \quad (\text{B.5a})$$

and

$$P = \frac{EA}{R_r} (w_r + w'_\theta). \quad (\text{B.5b})$$

Substituting equations B.2 and B.5 into B.1 gives us the equations of motion of a continuous elastic ring, which are

$$\frac{Eh^3\ell}{12R_r^3} (w_r''' - w_\theta'') - \frac{Eh\ell}{R_r} (w_r' + w_\theta'') + \rho A R_r \ddot{w}_\theta + K_\theta \ell R_r w_\theta = f_\theta \quad (\text{B.6a})$$

and

$$\frac{Eh^3\ell}{12R_r^3} (w_r'''' - w_\theta''') + \frac{Eh\ell}{R_r} (w_\theta' + w_r) + \rho A R_r \ddot{w}_r + K_r \ell R_r w_r = f_r. \quad (\text{B.6b})$$

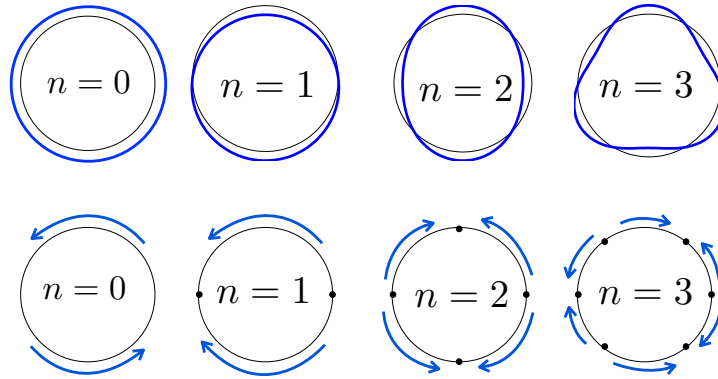


Figure B.2: Vibration modes of an elastic ring. Top row represents inextensional modes. Bottom row represents extensional modes.

Since w_r and w_θ are periodic with respect to θ , they can be expressed in terms of Fourier series as

$$w_r(\theta, t) = \sum_n w_{r,n}(t) e^{in\theta} \quad (\text{B.7a})$$

and

$$w_\theta(\theta, t) = \sum_n w_{\theta,n}(t) e^{in\theta}. \quad (\text{B.7b})$$

To obtain the natural frequencies we substitute $w_{r,n}(t) = W_{r,n} e^{i\omega_n t}$ and $w_{\theta,n}(t) = W_{\theta,n} e^{i\omega_n t}$ into equations B.7, and substitute equation B.7 into B.6 with $f_r = f_\theta = 0$. Natural frequencies of the ring are described by the equation^[63]

$$\omega_n^4 + c_2 \omega_n^2 + c_0 = 0, \quad (\text{B.8})$$

where

$$\begin{aligned} c_2 &= -K_1 - \frac{K_r + K_\theta}{\rho h}, \\ c_0 &= K_2 + \frac{n^2 E h^3}{12 \rho^2 h^2 R_r^4} (n^2 K_\theta + K_r) + \frac{E h}{\rho^2 h^2 R_r^2} (n^2 K_r + K_\theta) + \frac{K_r K_\theta}{\rho^2 h^2}, \\ K_1 &= \frac{n^2 + 1}{\rho h R_r^2} \left(\frac{n^2 E h}{12 R_r^2} + E h \right), \\ K_2 &= \frac{n^2 (n^2 - 1)^2 E^2 h^4}{R_r^6 \rho^2 h^2} \frac{1}{12}. \end{aligned}$$

Equation B.8 has two distinct roots for each n . One of the two roots represents predominantly an inextensional mode and the other root represents an extensional mode (figure B.2). Frequencies of extensional modes are generally an order of magnitude higher than the fre-

Table B.1: Comparison of natural frequencies of the ring of table 4.1 calculated using complete theory (inextensional and extensional, equation B.8) and inextensional only theory (equation B.10).

	Inextensional only (Hz)	Complete theory (Hz)	
		Inextensional	Extensional
n=0	0	0	1004.3
n=1	0	0	1420.7
n=2	72.70	72.63	2247.7
n=3	205.63	205.38	3179.5
n=4	394.27	393.76	4146.0
n=5	637.62	636.75	5127.7

frequencies of inextensional modes^[63]. Therefore, the analysis can be simplified by ignoring the extensional vibration of the ring. Using the inextensional assumption $w_r = -w'_\theta$, a simplified expression for the frequencies of inextensional modes can be obtained as^[63]

$$\omega_n'^2 = \frac{n^2(n^2 - 1)^2 E h^2}{12 \rho R_r^4 (n^2 + 1)} + \frac{K_r n^2 + K_\theta}{\rho h (n^2 + 1)}. \quad (\text{B.10})$$

Table B.1 shows the natural frequencies of the free ring, with parameters defined in table 4.1, calculated using equations B.8 and B.10. The frequencies of inextensional modes calculated using equation B.10 are in close agreement with the frequencies of inextensional modes calculated using equation B.8. The frequencies of extensional modes are an order of magnitude higher than the frequencies of inextensional modes. This suggests that the inextensional ring assumption made in section 4.2.1 is reasonable, and the frequencies of the ring can be calculated using equation B.10 for $n > 0$. The modes associated with $n = 0$ are: (i) rotational mode with zero frequency, and (ii) breathing mode. The breathing mode involves the extension of the ring, and its frequency is obtained from equation B.8 as

$$\omega_n'^2 = \frac{1}{2} \left\{ \frac{K_r + K_\theta}{\rho h} + \frac{E}{\rho R_r^2} + \sqrt{\left(\frac{K_r + K_\theta}{\rho h} + \frac{E}{\rho R_r^2} \right)^2 - \frac{4K_\theta}{\rho^2 h^2} \left(\frac{Eh}{R_r^2} - K_r \right)} \right\}. \quad (\text{B.11})$$

Appendix C

Matrices of the Planetary Model

This section details the matrices used in the planetary model of section 4.2.

Mass-Matrix Terms. System mass matrix is given by

$$\mathbf{M}_{\text{sys}} = \text{diag}(\mathbf{M}_s, \mathbf{M}_r, \mathbf{M}_r, \underbrace{\mathbf{M}_{p_1}, \dots, \mathbf{M}_{p_z}}_{\text{for } z \text{ planets}}, \mathbf{M}_b, \mathbf{M}_c), \quad (\text{C.1})$$

where

$$\mathbf{M}_{(\bullet)} = \text{diag}(m_{(\bullet)}, m_{(\bullet)}, I_{(\bullet)}) \quad \text{for } (\bullet) = s, p_i, b \text{ and } c,$$

and

$$\mathbf{M}_r = \text{diag}(M_0, M_1, \dots, M_n).$$

Stiffness-Matrix Terms. System stiffness matrix is given by

$$\mathbf{K}_{\text{sys}} = \begin{pmatrix} \mathbf{K}_B + \sum_{i=1}^Z (\mathbf{K}_{11}^{\text{sp}})_i & 0 & \dots & (\mathbf{K}_{12}^{\text{sp}})_i & \dots & 0 & 0 \\ & [\omega_r^*] + k_{rp} \mathbf{K}_{22}^{\text{rp}} & \dots & k_{rp} (\mathbf{K}_{21}^{\text{rp}})_i & \dots & 0 & 0 \\ & & \ddots & \vdots & & \vdots & \vdots \\ & & & k_{rp} \mathbf{K}_{11}^{\text{rp}} + \mathbf{K}_i^* + (\mathbf{K}_{22}^{\text{sp}})_i & \dots & (\mathbf{K}_{21}^{\text{bp}})_{i=\Gamma} & (\mathbf{K}_{21}^{\text{cp}})_{i \neq \Gamma} \\ & & & & \ddots & \vdots & \vdots \\ & \text{symm.} & & & & \mathbf{K}_{11}^{\text{bp}} + \mathbf{K}_{22}^{\text{sb}} & \mathbf{K}_{21}^{\text{cp}} \\ & & & & & & \mathbf{K}_B + \mathbf{K}_{21}^{\text{cb}} + \sum_{i=1:Z} (\mathbf{K}_{11}^{\text{cp}})_i \end{pmatrix},$$

where $[\omega_r^*] = \text{diag}(\omega_r, \omega_r)$, and $\mathbf{K}_i^* = (\mathbf{K}_{22}^{\text{cp}})_i$ if $i \neq \Gamma$, $\mathbf{K}_i^* = \mathbf{K}_{22}^{\text{bp}}$ if $i = \Gamma$.

Component stiffness matrices are:

$$(\mathbf{K}_{11}^{\text{sp}})_i = k_{sp} \begin{pmatrix} S_{(\alpha_i - \phi)}^2 & -S_{(\alpha_i - \phi)} C_{(\alpha_i - \phi)} & -r_p S_{(\alpha_i - \phi)} \\ & C_{(\alpha_i - \phi)}^2 & r_p C_{(\alpha_i - \phi)} \\ \text{symm.} & & r_s^2 \end{pmatrix};$$

$$\begin{aligned}
(\mathbf{K}_{12}^{\text{sp}})_i &= k_{sp} \begin{pmatrix} S_{(\alpha_i-\phi)} S_\phi & S_{(\alpha_i-\phi)} C_\phi & -r_p S_{(\alpha_i-\phi)} \\ -C_{(\alpha_i-\phi)} S_\phi & -C_{(\alpha_i-\phi)} C_\phi & r_p C_{(\alpha_i-\phi)} \\ -r_s S_\phi & -r_s C_\phi & r_s r_p \end{pmatrix}; \\
(\mathbf{K}_{22}^{\text{sp}})_i &= k_{sp} \begin{pmatrix} S_\phi^2 & -S_\phi C_\phi & -r_p S_\phi \\ & C_\phi^2 & -r_p C_\phi \\ \text{symm.} & & r_p^2 \end{pmatrix}; \\
(\mathbf{K}_{21}^{\text{sp}})_i &= (\mathbf{K}_{12}^{\text{sp}})_i^T; \\
(\mathbf{K}_{11}^{\text{cp}})_i &= \begin{pmatrix} k_{cp}^r C_{\alpha_i}^2 + k_{cp}^t S_{\alpha_i}^2 & (k_{cp}^r - k_{cp}^t) S_{\alpha_i} C_{\alpha_i} & -k_{cp}^t r_c S_{\alpha_i} \\ & k_{cp}^r S_{\alpha_i}^2 + k_{cp}^t C_{\alpha_i}^2 & k_{cp}^t r_c C_{\alpha_i} \\ \text{symm.} & & k_{cp}^t r_c^2 \end{pmatrix}; \\
(\mathbf{K}_{12}^{\text{cb}})_i &= (\mathbf{K}_{21}^{\text{cb}})_{k_{bc} \Rightarrow k_{cp}}^T; \\
\mathbf{K}_{11}^{\text{cb}} &= (\mathbf{K}_{11}^{\text{cp}})_{i=\Gamma}^{k_{cp} \Rightarrow k_{cb}}; \\
\mathbf{K}_{22}^{\text{cp}} &= \text{diag}(k_{cp}^r, k_{cp}^t, 0); \\
\mathbf{K}_{12}^{\text{cb}} &= (\mathbf{K}_{21}^{\text{cb}})_{i=\Gamma}^T.
\end{aligned}$$

Symbol $[\bullet]^{(\bullet)} \Rightarrow \odot$ or $[\bullet]_{(\bullet)} \Rightarrow \odot$ means that the term (\bullet) should be replaced by \odot in the matrix $[\bullet]$.

Transformation Matrix. Coordinate transformation matrix from fixed coordinate-system $(X_f Y_f Z_f)$ to rotating coordinate-system (XYZ) is given by

$$\mathbf{T} = \text{diag}(\mathbf{T}_1, \mathbf{T}_2, \underbrace{\mathbf{T}_1, \dots, \mathbf{T}_1}_{\text{for } \mathbf{z} \text{ planets}}, \mathbf{T}_1, \mathbf{T}_1), \quad (\text{C.3})$$

where

$$\begin{aligned}
\mathbf{T}_1 &= \begin{pmatrix} C_{\theta^*} & S_{\theta^*} & 0 \\ -S_{\theta^*} & C_{\theta^*} & 0 \\ 0 & 0 & 1 \end{pmatrix}; \\
\mathbf{T}_2 &= \begin{pmatrix} \mathbf{T}_a & \mathbf{T}_{ab} \\ -\mathbf{T}_{ab} & \mathbf{T}_b \end{pmatrix}; \\
\mathbf{T}_a &= \mathbf{T}_b = \text{diag}(1, C_{\theta^*}, C_{2\theta^*}, \dots, C_{\Phi\theta^*}); \\
\mathbf{T}_{ab} &= \text{diag}(0, S_{\theta^*}, S_{2\theta^*}, \dots, S_{\Phi\theta^*}).
\end{aligned} \quad (\text{C.4})$$

Appendix D

Effect of Coriolis and Centripetal Terms on the Natural Frequencies

In section 4.2.5, we assume that at small speeds the effect of Coriolis and centripetal terms on the dynamic response of a planetary drive are small and can be neglected. In this section we justify this assumption by showing that the natural frequencies of a wind-turbine planetary-drive do not change much due to the Coriolis and centripetal terms for typical wind-turbine operating speeds.

Following from section 4.2.5, equation of motion of a planetary drive in the fixed coordinate-system is

$$\mathbf{M}_{\text{sys}}\ddot{\bar{\mathbf{q}}} + \bar{\mathbf{K}}_{\text{sys}}\bar{\mathbf{q}} = \bar{\mathbf{F}}. \quad (\text{D.1})$$

System coordinates in the fixed coordinate-system can be defined in terms of system coordinates in the rotating coordinate-system (using equation 4.23) as

$$\bar{\mathbf{q}} = \mathbf{T}^T \mathbf{q}. \quad (\text{D.2})$$

Substituting equation D.2 into equation D.1 gives

$$\mathbf{M}_{\text{sys}}\ddot{\mathbf{q}} + \omega_c \mathbf{C}_L \dot{\mathbf{q}} + (\mathbf{K}_{\text{sys}} - \omega_c^2 \mathbf{K}_c) \mathbf{q} = \mathbf{F}, \quad (\text{D.3})$$

where

$$\mathbf{C}_L = \frac{1}{\omega_c} \mathbf{T} \mathbf{M}_{\text{sys}} \dot{\mathbf{T}}^T \quad (\text{D.4})$$

is the Coriolis matrix and

$$\mathbf{K}_c = -\frac{1}{\omega_c^2} \mathbf{T} \mathbf{M}_{\text{sys}} \ddot{\mathbf{T}}^T \quad (\text{D.5})$$

is the centripetal matrix.

Substituting expressions of \mathbf{M}_{sys} (from equation C.1) and \mathbf{T} (from equation C.3) into equations D.4 and D.5 yields

$$\mathbf{C}_L = \text{diag} \left(\mathbf{C}_L^s, \mathbf{C}_L^r, \underbrace{\mathbf{C}_L^{p_1}, \dots, \mathbf{C}_L^{p_z}}_{\text{for } z \text{ planets}}, \mathbf{C}_L^b, \mathbf{C}_L^c \right) \quad (\text{D.6a})$$

and

$$\mathbf{K}_c = \text{diag} \left(\mathbf{K}_c^s, \mathbf{K}_c^r, \underbrace{\mathbf{K}_c^{p_1}, \dots, \mathbf{K}_c^{p_z}}_{\text{for } z \text{ planets}}, \mathbf{K}_c^b, \mathbf{K}_c^c \right). \quad (\text{D.6b})$$

Sub-matrices in equation D.6a are defined as

$$\mathbf{C}_L^{(\bullet)} = \begin{pmatrix} 0 & -m_{(\bullet)} & 0 \\ m_{(\bullet)} & 0 & 0 \\ 0 & 0 & 0 \end{pmatrix} \quad \text{for } (\bullet) = s, p_i, b \text{ and } c, \quad (\text{D.7a})$$

$$\mathbf{C}_L^r = \begin{pmatrix} 0 & \mathbf{C}_L^{12} \\ -\mathbf{C}_L^{12} & 0 \end{pmatrix}, \quad (\text{D.7b})$$

and

$$\mathbf{C}_L^{12} = -\text{diag} (0, M_1, 2M_2, \dots, nM_n). \quad (\text{D.7c})$$

Sub-matrices in equation D.6b are defined as

$$\mathbf{K}_c^{(\bullet)} = \begin{pmatrix} m_{(\bullet)} & 0 & 0 \\ 0 & m_{(\bullet)} & 0 \\ 0 & 0 & 0 \end{pmatrix} \quad \text{for } (\bullet) = s, p_i, b \text{ and } c, \quad (\text{D.8a})$$

$$\mathbf{K}_c^r = \begin{pmatrix} \mathbf{K}_c^{11} & 0 \\ 0 & \mathbf{K}_c^{11} \end{pmatrix}, \quad (\text{D.8b})$$

$$\mathbf{K}_c^{11} = \text{diag} (0, M_1, 4M_2, \dots, n^2M_n). \quad (\text{D.8c})$$

Substituting $\mathbf{q} = \mathbf{q}_0 \exp(\lambda t)$ and $\mathbf{F} = 0$ into equation D.3 we get the eigenvalue problem, which is given by

$$\mathbf{A}\mathbf{U} = \lambda\mathbf{U}. \quad (\text{D.9})$$

Matrices in equation D.9 are defined as

$$\mathbf{A} = \begin{pmatrix} 0 & 1 \\ -\mathbf{M}_{\text{sys}}^{-1}\mathbf{K}_{\text{sys}} + \omega_c^2\mathbf{M}_{\text{sys}}^{-1}\mathbf{K}_c & -\omega_c\mathbf{M}_{\text{sys}}^{-1}\mathbf{C}_L \end{pmatrix}$$

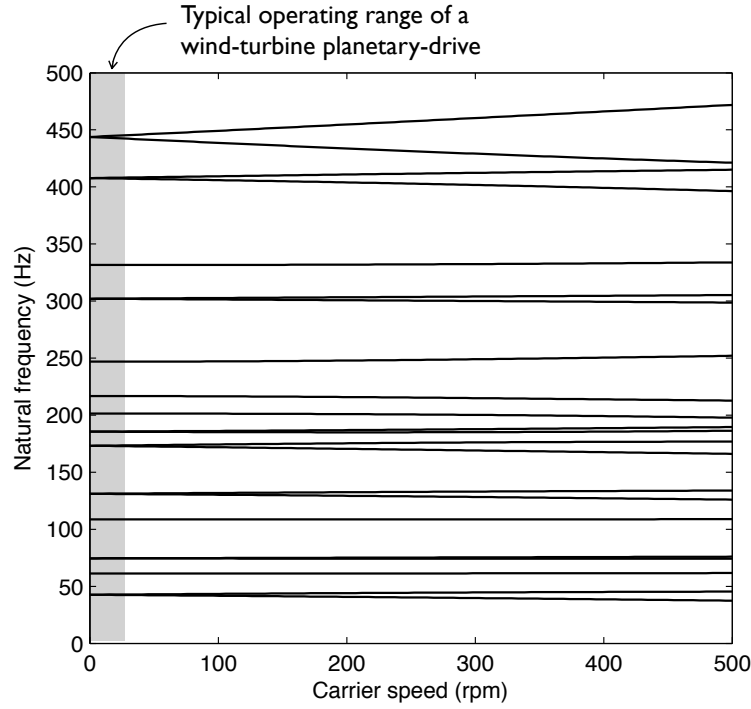


Figure D.1: Variation in the natural frequencies of a planetary drive with carrier speed caused by the Coriolis and the centripetal terms.

and

$$\mathbf{U} = (\mathbf{q}_0, \lambda \mathbf{q}_0)^T.$$

Solution of equation D.9 gives us the eigenvalues λ and eigenvectors \mathbf{U} . Figure D.1 shows the variation in natural frequencies (upto 500 Hz) of the planetary drive of table 4.1 with the carrier speed ω_c . The translational modes bifurcate into two frequencies for non-zero carrier speeds due to Coriolis term. Clearly the variation in the natural frequencies of the planetary drive are small and can be ignored for the typical operating speeds of a wind turbine. For the applications involving large rotational speeds, however, changes in the natural frequencies can be large and must be accounted for.

Appendix E

Critical Speed of a Rolling Element Passing Through a Fault

Consider a rolling element of radius r and mass m passing through a narrow localized fault (figure E.1(a)). Forces acting on the rolling element after it enters the fault are shown in the free-body diagram of figure E.1(b). Balancing the forces in the normal direction gives

$$F_1 = F \cos \theta - mr\omega^2, \quad (\text{E.1})$$

where F_1 is the reaction force acting on the rolling element. To insure that the rolling element does not lose contact with the left edge of the fault before the impact, reaction force F_1 must be greater than zero from the time the rolling element enters the fault until it hits the right edge of the fault. Therefore,

$$F_1 \geq 0 \implies F \cos \theta \geq mr\omega^2. \quad (\text{E.2})$$

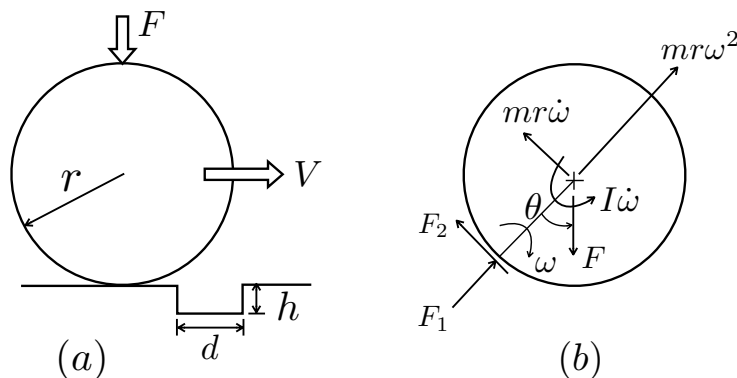


Figure E.1: (a) A rolling element passing through a narrow localized fault; (b) Forces acting on a rolling element after it enters the fault.

Angular velocity of the rolling element at an angle θ is given by equation 4.83. Substituting equation 4.83 into E.2 yields

$$V^2 \leq \frac{Fr}{7m}(17\cos\theta - 10). \quad (\text{E.3})$$

For a narrow fault ($d^2/r^2 \ll 1$) $\cos\theta \approx 1$. Substituting this into equation E.3 gives the expression for the critical speed as

$$V \leq \sqrt{\frac{Fr}{m}}. \quad (\text{E.4})$$

Speed defined by equation E.4 is the maximum speed a rolling element can have to always maintain contact with the left edge of the fault until it hits the right edge.

Next we derive the expression for the impulse when the speed of a rolling element is above the critical speed. From equation E.3, the angle at which the rolling element loses contact with the left edge is

$$\theta_1 = \cos^{-1} \left(\frac{10 + \frac{7mV^2}{Fr}}{17} \right), \quad (\text{E.5})$$

and the speed of the rolling element at that angle is

$$\omega_1 = \sqrt{\omega_0^2 + \frac{10F}{7mr}(1 - \cos\theta_1)}. \quad (\text{E.6})$$

After the rolling element loses contact with the left edge, the only force acting on it is the applied force F . Hence, its vertical speed just before the impact becomes

$$V_{\text{vertical}}^2 = r^2\omega_1^2\sin^2\theta_1 + \frac{2Fr}{m}(\cos\theta_1 - \cos\theta_0), \quad (\text{E.7})$$

where θ_0 is the angle at which impact occurs, and is given by $\cos\theta_0 \approx 1 - d^2/(8r^2)$. Substituting the expression of θ_0 into equation E.7 gives

$$V_{\text{vertical}}^2 = r^2\omega_1^2\sin^2\theta_1 + \frac{2Fr}{m} \left(\cos\theta_1 - 1 + \frac{d^2}{8r^2} \right). \quad (\text{E.8})$$

Following from equations 4.86 and E.8, impulse in the vertical direction can be calculated as

$$\mathfrak{S} = 2mV_{\text{vertical}} = 2m\sqrt{r^2\omega_1^2\sin^2\theta_1 + \frac{2Fr}{m} \left(\cos\theta_1 - 1 + \frac{d^2}{8r^2} \right)}. \quad (\text{E.9})$$

Equation E.9 suggests that the impulse, for the case when the rolling-element speed is

above the critical speed, depends on the load acting on the rolling element.

If the force acting on a rolling element is zero, for example unloaded zone of a bearing, then the angle at which the rolling element loses contact is $\theta_1 = 0$ (from equation E.3). Substituting $\theta_1 = 0$ into equation E.9 gives

$$\mathfrak{S} = m \frac{d}{r} \sqrt{\frac{Fr}{m}}. \quad (\text{E.10})$$

Equation E.10 shows that in the unloaded zone of a bearing, impulse due to a fault depends on the load acting on a rolling element and not its speed. Since the load is zero, impulse is zero.

References

- [1] Bearing failures and their causes. SKF. Product information 401.
- [2] New bearing doctor catalogue. www.nsk.com. NSK.
- [3] Romax Technology Ltd. www.romaxtech.com. Nottingham, UK.
- [4] *Wind Power. Renewable energy technologies: Cost analysis series*, volume 1: Power Sector. International Renewable Energy Agency, June 2012.
- [5] J. Antoni and R. Randall. Unsupervised noise cancellation for vibration signals: part i, evaluation of adaptive algorithms. *Mechanical Systems and Signal Processing*, 18(1):89–101, 2004.
- [6] J. Antoni and R. Randall. Unsupervised noise cancellation for vibration signals: part ii, a novel frequency-domain algorithm. *Mechanical Systems and Signal Processing*, 18(1):103–117, 2004.
- [7] M. H. Arafa and M. M. Megahed. Evaluation of spur gear mesh compliance using the finite element method. *Proceedings of the Institution of Mechanical Engineers, Part C: Journal of Mechanical Engineering Science*, 213(6):569–579, 1999.
- [8] R. August and R. Kasuba. Torsional vibrations and dynamic loads in a basic planetary gear system. *ASME, Transactions, Journal of Vibration, Acoustics, Stress, and Reliability in Design*, 108:348–353, 1986.
- [9] S. Bair. *High-pressure rheology for quantitative elastohydrodynamics*. Elsevier Science Ltd, 2007.
- [10] C. Barus. Isothermals, isopiestic and isometrics relative to viscosity. *Am. J. Sci*, 45(266):87–96, 1893.
- [11] I. Bercea, S. Cretu, and D. Nelias. Analysis of Double-Row Tapered Roller Bearings, Part I-Model. *Tribology Transactions*, 46(2):228–239, 2003.

- [12] M. Blanco. The economics of wind energy. *Renewable and Sustainable Energy Reviews*, 13(6):1372–1382, 2009.
- [13] R. J. Boness. Minimum Load Requirements for the Prevention of Skidding in High Speed Thrust Loaded Ball Bearings. *Journal of lubrication technology*, 103:35, 1981.
- [14] R. J. Boness and C. R. Gentle. Ball motion in thrust loaded ball bearings. *Wear*, 35(1):131–148, 1975.
- [15] M. Botman. Epicyclic gear vibrations. In *American Society of Mechanical Engineers, Design Engineering Technical Conference, Washington, DC, Sept. 17-19, 1975, 5 p.*, volume 1, 1975.
- [16] D. E. Brewe and B. J. Hamrock. Simplified solution for elliptical-contact deformation between two elastic solids. *ASME, Transactions, Series F-Journal of Lubrication Technology*, 99:485–487, 1977.
- [17] C. Bujoreanu, S. Crețu, and D. Nelias. Scuffing Behaviour in Angular Contact Ball-Bearings. *FASCICLE VIII, Tribology*, ISSN 1221-4590, 2003.
- [18] F. Chaari, W. Baccar, M. S. Abbas, and M. Haddar. Effect of spalling or tooth breakage on gearmesh stiffness and dynamic response of a one-stage spur gear transmission. *European Journal of Mechanics-A/Solids*, 27(4):691–705, 2008.
- [19] F. Chaari, T. Fakhfakh, and M. Haddar. Dynamic analysis of a planetary gear failure caused by tooth pitting and cracking. *Journal of Failure Analysis and Prevention*, 6(2):73–78, 2006.
- [20] F. Chaari, T. Fakhfakh, and M. Haddar. Analytical modelling of spur gear tooth crack and influence on gearmesh stiffness. *European Journal of Mechanics-A/Solids*, 28(3):461–468, 2009.
- [21] F. Chaari, T. Fakhfakh, R. Hbaieb, J. Louati, and M. Haddar. Influence of manufacturing errors on the dynamic behavior of planetary gears. *The International Journal of Advanced Manufacturing Technology*, 27(7):738–746, 2006.
- [22] L. Chang, T. F. Conry, and C. Cusano. Analysis of High-Speed Cylindrical Roller Bearings Using a Full Elastohydrodynamic Lubrication Model Part 2: Results. *Tribology Transactions*, 33(2):285–291, 1990.
- [23] G. Chaturvedi and D. Thomas. Bearing fault detection using adaptive noise cancelling. *ASME, Transactions, Journal of Mechanical Design*, 104:280–289, 1982.

-
- [24] F. K. Choy, V. Polyshchuk, J. J. Zakrajsek, R. F. Handschuh, and D. P. Townsend. Analysis of the effects of surface pitting and wear on the vibration of a gear transmission system. *Tribology International*, 29(1):77–83, 1996.
- [25] W. J. Crecelius. User’s Manual for Steady State and Transient Thermal Analysis of a Shaft-Bearing System (SHABERTH)., 1978.
- [26] S. Creju, I. Bercea, and N. Mitu. A dynamic analysis of tapered roller bearing under fully flooded conditions part 1: theoretical formulation. *Wear*, 188(1-2):1–10, 1995.
- [27] S. Creju, N. Mitu, and I. Bercea. A dynamic analysis of tapered roller bearings under fully flooded conditions part 2: results. *Wear*, 188(1-2):11–18, 1995.
- [28] A. W. Crook. The Lubrication of Rollers. *Phil. Trans. Roy. Soc., London, Series A, Mathematical and Physical Sciences*, 250(981):387–409, 1958.
- [29] A. W. Crook. The Lubrication of Rollers II. Film Thickness with Relation to Viscosity and Speed. *Phil. Trans. Roy. Soc., London. Series A, Mathematical and Physical Sciences*, 254(1040):223–236, 1961.
- [30] A. W. Crook. The Lubrication of Rollers III. A Theoretical Discussion of Friction and the Temperatures in the Oil Film. *Phil. Trans. Roy. Soc., London. Series A, Mathematical and Physical Sciences*, 254(1040):237–258, 1961.
- [31] A. W. Crook. The Lubrication of Rollers IV. Measurements of Friction and Effective Viscosity. *Phil. Trans. Roy. Soc., London. Series A, Mathematical and Physical Sciences*, 255(1056):281–312, 1963.
- [32] F. Cunliffe, J. Smith, and D. Welbourn. Dynamic tooth loads in epicyclic gears. *Journal of Engineering for Industry*, 96:578, 1974.
- [33] G. L. Doll. Tribological challenges in wind turbine technology. In *Wind turbine tribology seminar, Colorado, USA*, November 2011.
- [34] T. Eritenel and R. G. Parker. Modal properties of three-dimensional helical planetary gears. *Journal of Sound and Vibration*, 325(1-2):397–420, 2009.
- [35] C. R. Evans and K. L. Johnson. Regimes of traction in elastohydrodynamic lubrication. *Proceedings of the Institution of Mechanical Engineers. Part C. Mechanical engineering science*, 200(5):313–324, 1986.

-
- [36] C. R. Evans and K. L. Johnson. The rheological properties of elastohydrodynamic lubricants. *Proceedings of the Institution of Mechanical Engineers. Part C. Mechanical engineering science*, 200(5):303–312, 1986.
- [37] C. R. Gentle and A. Cameron. Some granular aspects of EHL traction. *Wear*, 27(1):71–81, 1974.
- [38] J. Greenwood. An extension of the grubin theory of elastohydrodynamic lubrication. *Journal of Physics D: Applied Physics*, 5(12):2195, 2002.
- [39] R. W. Gregory, S. L. Harris, and R. G. Munro. Dynamic behaviour of spur gears. In *Proceedings*, volume 1963, page 207, 1964.
- [40] A. Grubin. Central scientific research institute for technology and mechanical engineering. *Moscow, Book*, 30, 1949.
- [41] P. Gupta. Modeling of instabilities induced by cage clearances in ball bearings. *Tribology Transactions*, 34(1):93–99, 1991.
- [42] P. K. Gupta. Transient ball motion and skid in ball bearings. *ASME-ASLE Joint Lubrication Conference, Montreal, Canada*, Paper no. 74-Lub-9, 1974.
- [43] P. K. Gupta. Dynamics of rolling element bearings. part iii: Ball bearing analysis. *ASME-ASLE Joint Lubrication Conference Minneapolis, Minn.*, Paper no. 78-Lub-32, 1978.
- [44] P. K. Gupta. Dynamics of rolling element bearings. part iv: Ball bearing results. *ASME-ASLE Joint Lubrication Conference Minneapolis, Minn.*, Paper no. 78-Lub-33, 1978.
- [45] P. K. Gupta. On the Dynamics of a Tapered Roller Bearing. *Journal of Tribology*, 111:278, 1989.
- [46] O. Gustafsson and T. Tallian. Detection of damage in assembled rolling element bearings. *ASLE transactions*, 5(1):197–209, 1962.
- [47] B. Hahn, M. Durstewitz, and K. Rohrig. Reliability of wind turbines. *Wind Energy*, pages 329–332, 2007.
- [48] J. C. Hamer, R. S. Sayles, and E. Ioannides. An experimental investigation into the boundaries of smearing failure in roller bearings. *Journal of Tribology*, 113(1):102–109, 1991.

- [49] B. J. Hamrock and W. J. Anderson. Arched-outer-race ball-bearing considering centrifugal forces. *NASA TN D-6765*, 1972.
- [50] B. J. Hamrock and D. Dowson. *Ball bearing lubrication*. Wiley New York, 1981.
- [51] A. D. Hansen and L. H. Hansen. Wind turbine concept market penetration over 10 years (1995-2004). *Wind Energy*, 10(1):81–97, 2007.
- [52] S. L. Harris. Dynamic loads on the teeth of spur gears. *Proceedings of the Institution of Mechanical Engineers*, 172(1958):87–112, 1958.
- [53] T. A. Harris. An analytical method to predict skidding in high speed roller bearings. *Tribology Transactions*, 9(3):229–241, 1966.
- [54] T. A. Harris. On the Effectiveness of Hollow Balls in High-Speed Thrust Bearings. *Tribology Transactions*, 11(4):290–294, 1968.
- [55] T. A. Harris. An analytical method to predict skidding in thrust-loaded, angular-contact ball bearings. *ASME Journal of Lubrication Technology*, 93:17–24, 1971.
- [56] T. A. Harris. Ball Motion in Thrust-Loaded, Angular Contact Bearings with Coulomb Friction. *Journal of Lubrication Technology, Transactions of the ASME*, pages 32–38, 1971.
- [57] H. Hertz. On the contact of elastic solids. *J. Reine Angew. Mathematik*, 92:156–171, 1881.
- [58] T. HIDAKA, Y. Terauchi, and M. Fujii. Analysis of dynamic tooth load on planetary gear. *Bulletin of JSME*, 23(176):315–323, 1980.
- [59] F. Hirano. Motion of a ball in angular-contact ball bearing. *Tribology Transactions*, 8(4):425–434, 1965.
- [60] F. Hirano and H. Tanoue. Motion of a ball in a ball bearing. *Wear*, 4(3):177–197, 1961.
- [61] L. Houpert. Cagedyn: A contribution to roller bearing dynamic calculations part i: Basic tribology concepts. *Tribology Transactions*, 53(1):1–9, 2009.
- [62] L. Houpert. Cagedyn: A contribution to roller bearing dynamic calculations part ii: Description of the numerical tool and its outputs. *Tribology Transactions*, 53(1):10–21, 2009.

- [63] S. C. Huang and W. Soedel. Effects of coriolis acceleration on the free and forced in-plane vibrations of rotating rings on elastic foundation. *Journal of sound and vibration*, 115(2):253–274, 1987.
- [64] J. Ignacio Amasorrain, X. Sagartzazu, and J. Damián. Load distribution in a four contact-point slewing bearing. *Mechanism and Machine Theory*, 38(6):479–496, 2003.
- [65] M. Inalpolat and A. Kahraman. A theoretical and experimental investigation of modulation sidebands of planetary gear sets. *Journal of Sound and Vibration*, 323(3-5):677–696, 2009.
- [66] M. Inalpolat and A. Kahraman. A dynamic model to predict modulation sidebands of a planetary gear set having manufacturing errors. *Journal of Sound and Vibration*, 329(4):371–393, 2010.
- [67] K. Johnson. *Contact mechanics*. Cambridge university press, 1987.
- [68] K. Johnson, J. Greenwood, and S. Poon. A simple theory of asperity contact in elastohydro-dynamic lubrication. *Wear*, 19(1):91–108, 1972.
- [69] K. L. Johnson. Regimes of elastohydrodynamic lubrication. *Journal of Mechanical Engineering Science*, 12:9–16, 1970.
- [70] K. L. Johnson and J. L. Tevaarwerk. Shear behaviour of elastohydrodynamic oil films. *Proceedings of the Royal Society of London. Series A, Mathematical and Physical Sciences*, 356(1685):215–236, 1977.
- [71] A. B. Jones. The Mathematical Theory of Rolling-Element Bearings. *Mechanical Design and Systems Handbook*, 1956.
- [72] A. B. Jones. Ball motion and sliding friction in ball bearings. *ASME Trans*, 81:1–12, 1959.
- [73] A. B. Jones. A general theory for elastically constrained ball and radial roller bearings under arbitrary load and speed conditions. *Journal of Basic Engineering*, 82(2):309–320, 1960.
- [74] J. M. Jonkman, S. Butterfield, W. Musial, and G. Scott. *Definition of a 5-MW reference wind turbine for offshore system development*. National Renewable Energy Laboratory, 2009.

-
- [75] A. Kahraman. Load sharing characteristics of planetary transmissions. *Mechanism and Machine Theory*, 29(8):1151–1165, 1994.
- [76] A. Kahraman. Natural modes of planetary gear trains. *Journal of Sound Vibration*, 173:125–130, 1994.
- [77] A. Kahraman, A. Kharazi, and M. Umrani. A deformable body dynamic analysis of planetary gears with thin rims. *Journal of sound and vibration*, 262(3):752, 2003.
- [78] R. Kasuba and J. W. Evans. An extended model for determining dynamic loads in spur gearing. *ASME, Transactions, Journal of Mechanical Design*, 103:398–409, 1981.
- [79] P. S. Kliman. High Speed Ball Bearings-Limitation and Thrust Requirements. (1963) *ASLE, 18th ASLE Annual Meeting, New York*, 1963.
- [80] B. Kuhnell. Wear in rolling element bearings and gears- how age and contamination affect them. *Machinery Lubrication*, pages 62–64, 2004.
- [81] A. Leblanc and D. Nelias. Ball Motion and Sliding Friction in a Four-Contact-Point Ball Bearing. *Journal of Tribology*, 129:801, 2007.
- [82] A. Leblanc and D. Nelias. Analysis of Ball Bearings with 2, 3 or 4 Contact Points. *Tribology Transactions*, 51(3):372–380, 2008.
- [83] H. Li and Z. Chen. Overview of different wind generator systems and their comparisons. *IET Renewable Power Generation*, 2(2):123–138, 2008.
- [84] N. T. Liao and J. F. Lin. Ball bearing skidding under radial and axial loads. *Mechanism and Machine Theory*, 37(91):113, 2002.
- [85] N. T. Liao and J. F. Lin. Rolling-sliding analysis in ball bearing considering thermal effect. *Tribology Transactions*, 49(1):1–16, 2006.
- [86] J. Lin and R. G. Parker. Analytical characterization of the unique properties of planetary gear free vibration. *Journal of Vibration and Acoustics*, 121:316, 1999.
- [87] G. Marsh. Wind turbines: How big can they get? *Refocus*, 6(2):22–28, 2005.
- [88] P. McFadden and J. Smith. Vibration monitoring of rolling element bearings by the high-frequency resonance techniquea review. *Tribology international*, 17(1):3–10, 1984.

- [89] P. McFadden and J. Smith. The vibration produced by multiple point defects in a rolling element bearing. *Journal of Sound and Vibration*, 98(2):263–273, 1985.
- [90] P. D. McFadden and J. D. Smith. Model for the vibration produced by a single point defect in a rolling element bearing. *Journal of Sound and Vibration*, 96(1):69–82, 1984.
- [91] P. D. McFadden and J. D. Smith. An explanation for the asymmetry of the modulation sidebands about the tooth meshing frequency in epicyclic gear vibration. *Proceedings of the Institution of Mechanical Engineers. Part C. Mechanical engineering science*, 199(1):65–70, 1985.
- [92] D. McMillan and G. Ault. Quantification of condition monitoring benefit for offshore wind turbines. *Wind Engineering*, 31(4):267–285, 2007.
- [93] C. R. Meeks and L. Tran. Ball Bearing Dynamic Analysis Using Computer Methods Part I: Analysis. *Journal of Tribology*, 118:52, 1996.
- [94] W. Musial, S. Butterfield, and B. McNiff. Improving wind turbine gearbox reliability. In *Proceedings of the European Wind Energy Conference*. Citeseer, 2007.
- [95] D. Nelias, I. Bercea, and N. Mitu. Analysis of Double-Row Tapered Roller Bearings, Part II—Results: Prediction of Fatigue Life and Heat Dissipation. *Tribology Transactions*, 46(2):240–247, 2003.
- [96] F. Oyague, D. Gorman, and S. Sheng. Nrel gearbox reliability collaborative experimental data overview and analysis. In *Windpower Conference and Exhibition*, 2010.
- [97] R. G. Parker. A physical explanation for the effectiveness of planet phasing to suppress planetary gear vibration. *Journal of sound and vibration*, 236(4):561–573, 2000.
- [98] R. G. Parker, V. Agashe, and S. M. Vijayakar. Dynamic response of a planetary gear system using a finite element/contact mechanics model. *Journal of Mechanical Design*, 122:304, 2000.
- [99] M. Pasdari and C. R. Gentle. Effect of lubricant starvation on the minimum load condition in a thrust-loaded ball bearing. *A S L E Transactions*, 30(3):355–359, 1987.

- [100] M. Pimsarn and K. Kazerounian. Efficient evaluation of spur gear tooth mesh load using pseudo-interference stiffness estimation method. *Mechanism and machine theory*, 37(8):769–786, 2002.
- [101] H. Polinder, F. Van der Pijl, G. De Vilder, and P. Tavner. Comparison of direct-drive and geared generator concepts for wind turbines. *Energy conversion, IEEE transactions on*, 21(3):725–733, 2006.
- [102] J. V. Poplawski, D. R. Atwell, M. J. Lubas, and V. Odessky. Predicting steady-state temperature, life, skid, and film thickness in a greased preloaded hybrid ball bearing. *Journal of Engineering for Gas Turbines and Power*, 118:443, 1996.
- [103] J. V. Poplawski and A. Mauriello. Skidding in lightly loaded, high speed ball thrust bearings. (1969) *ASME Paper No 69-LubS-20*, 1969.
- [104] R. Randall. *Vibration-based condition monitoring: industrial, aerospace and automotive applications*. Wiley, 2011.
- [105] S. Rao. *Vibration of continuous systems*. Wiley, 2007.
- [106] A. Ray. Monitoring rolling contact bearings under adverse conditions. In *2nd International Conference of Vibrations in rotating Machinery, Institution of Mechanical Engineers, Cambridge*, pages 1–4, 1980.
- [107] J. V. Rensselaar. Wind Turbines: Solving gearbox problems from the ground up. www.stle.org, Cover story, June 2010. *Tribology & Lubrication Technology*.
- [108] O. Reynolds. On the theory of lubrication and its application to mr. beauchamp tower’s experiments, including an experimental determination of the viscosity of olive oil. *Proceedings of the Royal Society of London*, 40(242-245):191–203, 1886.
- [109] J. Ribrant and L. Bertling. Survey of failures in wind power systems with focus on Swedish wind power plants during 1997-2005. In *IEEE Power Engineering Society General Meeting, 2007*, pages 1–8, 2007.
- [110] S. Sassi, B. Badri, and M. Thomas. A numerical model to predict damaged bearing vibrations. *Journal of Vibration and Control*, 13(11):1603, 2007.
- [111] N. Sawalhi and R. Randall. Simulating gear and bearing interactions in the presence of faults: Part i. the combined gear bearing dynamic model and the simulation of localised bearing faults. *Mechanical Systems and Signal Processing*, 22(8):1924–1951, 2008.

-
- [112] A. Selvaraj and R. Marappan. Experimental analysis of factors influencing the cage slip in cylindrical roller bearing. *The International Journal of Advanced Manufacturing Technology*, 53(5):635–644, 2011.
- [113] J. Smith. Vibration monitoring of bearings at low speeds. *Tribology International*, 15(3):139–144, 1982.
- [114] J. D. Smith. *Gear noise and vibration*. Marcel Dekker, Inc., 2003.
- [115] F. Spinato, P. Tavner, G. Van Bussel, and E. Koutoulakos. Reliability of wind turbine subassemblies. *Renewable Power Generation, IET*, 3(4):387–401, 2009.
- [116] G. Stachowiak and A. Batchelor. *Engineering tribology*. Butterworth-Heinemann, 2005.
- [117] M. Steenbergen. The role of the contact geometry in wheel–rail impact due to wheel flats. *Vehicle System Dynamics*, 45(12):1097–1116, 2007.
- [118] N. Tandon and A. Choudhury. An analytical model for the prediction of the vibration response of rolling element bearings due to a localized defect. *Journal of Sound and Vibration*, 205:275–292, 1997.
- [119] N. Tandon and A. Choudhury. A review of vibration and acoustic measurement methods for the detection of defects in rolling element bearings. *Tribology International*, 32(8):469–480, 1999.
- [120] P. J. Tavner, G. J. W. Van Bussel, and F. Spinato. Machine and converter reliabilities in wind turbines. In *The 3rd IET International Conference on Power Electronics, Machines and Drives*, pages 127–130. IET, 2006.
- [121] B. Tower. First report on friction experiments. *Proceedings of the Institution of Mechanical Engineers*, 34(1):632–659, 1883.
- [122] B. Tower. Research committee on friction, second report on friction experiments. *Proceedings of the Institution of Mechanical Engineers*, 36(1):58–70, 1885.
- [123] W. Tu, Y. Shao, and C. Mechefske. An analytical model to investigate skidding in rolling element bearings during acceleration. *Journal of Mechanical Science and Technology*, 26(8):2451–2458, 2012.
- [124] G. Van Bussel and M. Zaaijer. Reliability, availability and maintenance aspects of large-scale offshore wind farms, a concepts study. In *Proceedings of MAREC*, pages 119–126, 2001.

-
- [125] I. L. Ver, C. S. Ventres, and M. M. Myles. Wheel/rail noise part iii: Impact noise generation by wheel and rail discontinuities. *Journal of Sound and Vibration*, 46(3):395–417, 1976.
- [126] M. F. While. Rolling element bearing vibration transfer characteristics: Effect of stiffness. *Journal of Applied Mechanics*, 46(3):677–684, 1979.
- [127] P. E. Whiteley. Fault detection in wind turbine bearings. *Fourth Year Project Report, Cambridge University Engineering Department*, May 2012.
- [128] R. J. K. Wood. Tribology and corrosion aspects of wind turbines. In *Wind energy - Challenges for Materials, Mechanics and Surface Science*, IOP, London. IOP, 2010.
- [129] X. Wu and R. G. Parker. Modal properties of planetary gears with an elastic continuum ring gear. *Journal of Applied Mechanics*, 75:031014, 2008.
- [130] E. Yau, H. R. Busby, and D. R. Houser. A Rayleigh-Ritz approach to modeling bending and shear deflections of gear teeth. *Computers & Structures*, 50(5):705–713, 1994.
- [131] C. T. Yiakopoulos, K. C. Gryllias, and I. A. Antoniadis. Rolling element bearing fault detection in industrial environments based on a k-means clustering approach. *Expert Systems with Applications*, 38(3):2888–2911, 2011.